



**Hemodynamic analysis of flow near cerebral aneurysms:  
Insight into aneurysm formation and effect of intervention**

A

Dissertation

Presented to

the Faculty of the Department of Mechanical Engineering

University of Houston

In Partial Fulfillment

of the Requirements for the Degree

Doctor of Philosophy

in Mechanical Engineering

by

Aishwarya Rao Mantha

May 2012



## Acknowledgements

The road to getting my Ph.D. has neither been easy nor conventional. I lost hope many a time during this journey; sometimes it was because of the long distance, sometimes it was my own mind hoodwinking me into believing that it was not possible for someone in my situation, thousands of miles away from the university environs coupled with the responsibilities and fun that come with motherhood. There was no motivation. And then, during the lowest times of my life, I found myself moving, and inching towards the finish line. Surprisingly, it did not feel like any effort at all and how could it, I was being carried towards the goal, by someone; no not God, although he means as much to me as God. He is my advisor, Prof Ralph Metcalfe. And I dedicate this thesis and my entire research work in the field of science to him.

Saying that I could not have gotten this without his help would be a gross understatement. He taught me how good computational work is done and gave me complete liberty to express my opinion during our brainstorming sessions that were indeed quite stimulating and productive. With his enthusiasm, his inspiration, and his great efforts to explain things clearly and simply, he helped to make computational fluid dynamics fun for me. Throughout my thesis-writing period, he provided encouragement, sound advice, good teaching, good company, and lots of good ideas. I would have been lost without him. It has been an honor to be his Ph.D. student.

Special thanks to my committee, Dr. Kleis, Dr. Franchek, Dr. Naghavi, Dr. Hartley and Dr. Larin for their support, guidance and helpful suggestions. Their guidance has served me well and I owe them my heartfelt appreciation.

Members of my lab also deserve my sincerest thanks, their friendship and assistance has meant more to me than I could ever express. I could not complete my work without invaluable friendly assistance of Mircea Ionescu and Andres Hernandez. Thank you Pranab, Priyanka, Priya, Max, and Oumama for bringing mirth into otherwise a serious work environment.

I wish to thank my parents, Mantha Ramadevi and Col. M.V. Subbarao. They bore me, raised me, supported me, taught me, and loved me. Their love provided my inspiration and was my driving force. I owe them everything and wish I could show them just how much I love and appreciate them. The reason why I could fly high was because they were the wind beneath my wings. My husband, Ajish Potty's infinite love and encouragement allowed me to finish this journey. He already has my heart so I will just give him my heartfelt "thanks". I would like to thank my two lovely and inspirational grandmothers; they love life and live it to the fullest. I could not have done this without the unconditional help of my very good friend and my mentor Pradeep Dhoorjaty, who was there for me during all the times of need. He indeed is my true friend. My brothers, Bhargav and Swaroop, who took it upon themselves to make sure I was not at peace till I finished my thesis, and also for being my best friends! Smitha deserves my heartfelt gratitude for being the mother of my son while I was working on my thesis and for being my very good friend. I have deep appreciation for In laws for taking care of my son while I was away in Houston. And lastly and most importantly, my son, Advait Govind, who is the reason for my happiness and who gives meaning to my life!

**Hemodynamic analysis of flow near cerebral aneurysms:  
Insight into aneurysm formation and effect of intervention**

An Abstract

of a

Dissertation

Presented to

the Faculty of the Department of Mechanical Engineering

University of Houston

In Partial Fulfillment

of the Requirements for the Degree

Doctor of Philosophy

in Mechanical Engineering

by

Aishwarya Rao Mantha

May 2012

## **Abstract**

The purpose of this study is to investigate the role of hemodynamics in the initiation and progression of cerebral aneurysms. It is composed of two major sections, where the first part attempts at understanding the hemodynamic cause and effect linkages leading to aneurysm formation and it is shown that low and oscillatory shear could lead to aneurysm initiation. The second part consists of hemodynamic analysis inside the aneurysm. It is shown that stable flow patterns exist inside the aneurysm with distinct influx and efflux zones that remain unchanged during the cardiac cycle; application of this knowledge will aid in better design of flow diverting devices.

In my Master's thesis, it was demonstrated that low and oscillatory wall shear stresses (WSS) correlated with the aneurysm sites. This work is summarized and then a careful critique of some newer aneurysm formation theories involving high WSS and wall shear stress gradients (WSSG) and how they relate to the AFI (aneurysm formation indicator, proposed by our group) is presented.

Second, a numerical experiment is performed to demonstrate the potential drawbacks of using WSSG and its variations as a hemodynamic indicator. Effects of various meshing schemes and resolutions are investigated systematically and the sensitivity of WSSG to image acquisition and reconstruction is demonstrated, along with its potential for misleading interpretation.

Third, robustness and sensitivity of the proposed AFI is demonstrated by analyzing the effects of ageing reflected by the change in waveform shape as a result of degeneration of arterial tone. It is shown that AFI indeed captures the differences in the waveforms of an older and a younger adult.

Fourth, hemodynamic influences on aneurysm stability under realistic physiological conditions are explored, and contrary to what has been reported in the literature, we have shown that flow patterns inside the aneurysm are relatively stable and insensitive to pulsatility. Two aneurysm types were considered: sidewall (paraclinoid) and bifurcation (basilar tip), with three specimens of each obtained from human patients via clinical 3D digital subtraction angiography. We identified stable large-scale flow patterns in the aneurismal flows. This knowledge of flow patterns is applied towards better design of stents and other flow diverting devices. In addition, potential use of hemodynamic simulations in clinical application is also established.

# Table of Contents

	Page
Acknowledgements.....	iv
Abstract.....	vii
Table of Contents.....	ix
List of Figures.....	xii
List of Tables.....	xxii
<b>1. Introduction.....</b>	<b>1</b>
1.1. Aneurysms.....	2
1.1.1. Aortic Aneurysm.....	2
1.1.2. Cerebral Aneurysm.....	3
1.2. Types of Intracranial Aneurysms.....	5
1.3. Detection of Aneurysms.....	6
1.4. Treatment Options.....	11
<b>2. Background and Literature survey.....</b>	<b>14</b>
2.1. Pathogenesis of Cerebral aneurysms.....	15
2.2. Hemodynamics and Cerebral Aneurysms.....	18
2.2.1. Hemodynamic Experiments.....	18
2.2.2. Computational Hemodynamic Modeling.....	19
<b>3. Endothelial Cells and Wall Shear Stress.....</b>	<b>26</b>
3.1. Endothelial Cells and Flow Disturbances.....	27
3.2. Models of Cellular Transport: Two Phase Model of Blood.....	29
3.3. Indicators proposed in Literature.....	31

3.3.1.	Low Oscillatory WSS theory .....	31
3.3.2.	High Wall Shear Stress Theory.....	43
3.4.	Summary and Conclusions .....	51
<b>4.</b>	<b>The Wall Shear Stress Gradient Problem .....</b>	<b>53</b>
4.1.	Working with Gradient .....	54
4.2.	Numerical Experiment: Flow in an elliptical pipe.....	59
4.3.	Numerical Analysis.....	61
4.4.	Other issues with WSSG.....	69
<b>5.</b>	<b>Waveform Analysis.....</b>	<b>77</b>
5.1.	The Characteristic Idealized Waveforms.....	81
5.2.	The Hoi Waveform: Real Human Data .....	90
5.3.	The Azhim Waveform .....	96
5.4.	Discussion.....	102
5.5.	Conclusions.....	105
<b>6.</b>	<b>Stability of Flow inside the aneurysm .....</b>	<b>107</b>
6.1.	Previous Work .....	108
6.2.	Identification of Large Scale Structure .....	111
6.3.	Pulsatile Flow Simulations .....	114
6.3.1.	Ostium Flow.....	115
6.3.2.	Waveform Independence .....	117
6.3.3.	Additional case.....	118
6.4.	Discussion.....	119
6.5.	Conclusions.....	124

<b>7. Summary and Conclusions</b> .....	126
7.1. Key Results and Conclusions.....	126
7.2. Recommendations for Future Work.....	132
<b>8. References</b> .....	137
<b>Appendix A (Flow in Curved pipes)</b> .....	162
<b>Appendix B (The Models and Assumptions)</b> .....	171
<b>Appendix C (Enlarged Plots from Chapter 4)</b> .....	180

## List of Figures

Figure 1.1. Depiction of (A) healthy human artery, (B) TAA and (C) AAA [Source: <a href="http://www.nhlbi.nih.gov/health/dci/Diseases/arm/arm_types.html">http://www.nhlbi.nih.gov/health/dci/Diseases/arm/arm_types.html</a> ]. .....	3
Figure 1.2. Circle of Willis, showing the major arteries supplying blood to the brain. Aneurysms are also shown in the regions where they most commonly form. ....	4
Figure 1.3. Classification of intracranial aneurysms. (Source: <a href="http://www.thebni.com/.../images/aneurysm8_sm_new.gif">www.thebni.com/.../images/aneurysm8_sm_new.gif</a> ). .....	6
Figure 1.4. (A) Sketch illustrating catheter placement in a blood vessels leading to the brain and the injection of a contrast agent or dye. (B, C, D) Show typical CT angiography image of cerebral arteries with aneurysms. (Source: <a href="http://brainavm.uhnres.utoronto.ca/images/malformations/aneurysm/3-D-angio.jpg">http://brainavm.uhnres.utoronto.ca/images/malformations/aneurysm/3-D-angio.jpg</a> ).....	8
Figure 1.5. Shows colored computed tomography (CT) scan of a subarachnoid brain hemorrhage (green) caused by rupture of a cerebral aneurysm. This is anthropological plane projection. (Source: <a href="http://www.sciencephoto.com/media/255517/enlarge#">http://www.sciencephoto.com/media/255517/enlarge#</a> ). .....	10
Figure 1.6. Two views of an MRI image showing a cranial aneurysm .....	11
Figure 1.7. Shows A schematic of the treatment of an intracranial aneurysm by surgical clipping. ....	12
Figure 1.8. (a) Treatment of an intracranial aneurysm by endovascular coiling. Anteroposterior vertebral subtraction angiograms in a 61-year-old woman showing a 12-mm basilar aneurysm before treatment. (b) Treatment of intracranial aneurysms by endovascular coiling. This is after the placement of four Guglielmi detachable coils. (c) An illustration of embolization. ....	13
Figure 2.1. Shows a schematic of the anatomy of an artery .....	15

Figure 3.1. A, B, C: Lateral views (DSA) of three sidewall aneurysms of the paraclinoid internal carotid artery. The aneurysms vary in their orientation to the vessel axis. In A (case I) the aneurysm dome extends more distally than proximally, in B (case II), the dome is extends more proximally than distally (as opposed to A) and in C (case III) the dome extends equally in both directions. Insets in A and C show the aneurysms in tangential projections according to their orientation laterally (A), and medially (C). D, E, F: The 3-dimensional computational domain that was obtained from 3D angiography of the three aneurysms is shown. Figures D and F are aligned in the same orientation as in the insets of A and C. G, H, I: Geometries in identical projection to D,E,F respectively after artificial removal of the aneurysms using a smoothing algorithm. The inset in Figure G, oriented according to the intial DSA (A), was chosen to highlight the effects of wall shear stress at the ostium plane for case-I. This orientation is identical to Figure J showing the ostium “en face”. J, K, L: “En face” projections of the aneurysm ostium (transparent grids). ..... 33

Figure 3.2. Contour plot of the Aneurysm Formation Indicator (AFI) at systolic deceleration. The blue color corresponds to complete reversal in WSS, green corresponds to a 90° rotation of WSS and red implies that the instantaneous WSS vector aligns with the reference value, the temporal average of WSS. Panels (A), (B) and (C) correspond to cases I, II and III respectively. The insets show the location of the aneurysms. The most significant values of this indicator tend to correlate with the area of subsequent aneurysm development. .... 34

Figure 3.3. CFD in 3D models of simulated asymmetry of outflow. Results of WSS are shown with high outflow pressure in the right posterior cerebral artery and superior cerebellar artery. Insets: Real patient data, A: pre-aneurysm B: Post-aneurysm.....	36
Figure 3.4. Contours of WSS for the evolving aneurysm.....	37
Figure 3.5. Representative examples of the six constant (planar) parametric models.....	38
Figure 3.6. Contours of wall shear stress (WSS) for the reference bifurcation and each of the corresponding parametric models. ....	39
Figure 3.7. Contours of WSS for the reference arterial network and parametric idealization of this vasculature for a Reynolds number of 400, with (a) WSS in reference network, (b) WSS in parametric model. Arrows indicate regions of high and low WSS.	40
Figure 3.8. Schematic of the ACA/OA junction. Arrow shows the direction of blood....	41
Figure 3.9. (A) ACA/OA branch. (B) Magnified view of the apical area. Note the juxta-depression. (C) Degeneration of intimal pad, medial VSMC is decreased in number. (D) Thinning and dilation of the juxta-apical depression. (E) Outward bulging. The internal elastic lamina has completely disappeared. (F)A schematic of early aneurysm development. (G) Advanced aneurysm with the involvement of the intimal pad. ....	43
Figure 3.10. (A) Schematic of the methodology. (B) Procedure to surgically create the bifurcation. (C) Mapping of CFD results onto the histological images.....	44
Figure 3.11. (A) Patient specific data.(B, C) contours of WSS with and without the increase of viscosity and BV. (D, E) contours of OSI with and without the increase in BV and viscosity.....	48

Figure 3.12. A show the patient specific artery. B shows the geometry of the artery after artificially removing the aneurysm. C shows the meshing scheme. Waveform is indicated in Figure 3.15(D). Contours of AFI, GON and OSI are shown in E,F,G respectively..... 50

Figure 4.1. Wall shear stress gradient observed with variable angles of the realistic left coronary artery models generated at peak systolic phase of 0.4s. Arrows display the wall shears tress gradient distributions, with a large region of the low magnitude present in a  $120^0$  model and a small region in a  $73^0$  model..... 55

Figure 4.2. Contours of WSS for the case 1. Inset represents where the aneurysm eventually developed. The graph shows the values of WSSG and WSS along the regions shown in inset 2. .... 56

Figure 4.3. Top panel shows a sample topography map, middle panel shows the values of shear stresses and bottom panel shows the histograms of the WSS and WSSG from the CFD model..... 57

Figure 4.4. Schematic of flow in an elliptical pipe ..... 59

Figure 4.5. Schematic of the cross-section. .... 59

Figure 4.6. Shows different meshes used in the numerical experiment. Case 1(A, B) is the structured mesh with progressively refined boundary layer mesh. Case 2 (C, D) shows hexahedral meshing scheme, but adaptive mesh refinement has been used. Case 3(E, F) shows progressively refined hexahedral elements. Case 4(G, H) is progressive refinement of tetrahedral meshing scheme without the boundary layer mesh..... 63

Figure 4.7. Plots A, B, C, D show WSS plots at the circumference of the CS plot shown above for all the Case 1, 2, 3 and 4..... 66

Figure 4.8. Shows convergence plots of WSSG and their comparison with the analytic solution. A,B,C,D are for four cases respectively. Zones of maximum error for BL mesh are indicated by arrows. ....	66
Figure 4.9. (A) shows cross sections along which the WSSG was plotted. (B) plot showing convergence in the axial direction.....	68
Figure 4.10. (A) Contours of WSS for sidewall case 1 (B) contours of WSSG. Arrows indicate where aneurysm eventually formed. Unstructured meshes with adaptive mesh refinement were used. About 2 Million tetrahedral elements were used to define the computational domain.....	69
Figure 4.11. Image acquisition through MS-CT, C-arm CT, FP-CT and Micro-CT at two sample planes (near the struts and at the connector plane).....	71
Figure 4.12. Right panel shows magnified image after pre-processing in Amira. Left panel shows contours of velocity. Bottom panel shows contours of WSS for FP-CT and Micro-CT respectively.....	73
Figure 4.13. Case-I (A) 3D-DSA image directly obtained from human patient. (B) 3D surface reconstruction showing a large side-wall aneurysm. (C,D) Two views showing the reconstructed artery (green) and ostium surface (red) superimposed on the original DSA image. (E) Final mesh of the geometry after excision. ....	75
Figure 5.1. Left panel showing pressure and velocity waveform. Right panel shows correlations between velocity and pressure and FAI and PAI.....	79
Figure 5.2. A schematic of flow waveform for an old and young adult depicting the key points in the cardiac cycle.....	80

Figure 5.3. Two characteristic waveforms, with different deceleration slope, Wave1 and Wave 4 respectively. The blue circles indicate the important phases in cycle where the results are plotted. .... 82

Figure 5.4. Schematic of flow pattern and associated pressure and WSS distributions relevant to arterial hemodynamics: flow in a curved tube. .... 83

Figure 5.5. Contours of velocity magnitude overlaid with secondary velocity vectors for wave1 and wave 4 taken at ED, PS, and MSD1 AND MSD2 respectively. Inset shows the location of the cross-section. Stagnation zone is shown by the arrow..... 84

Figure 5.6. Contours of WSS for critical times in cycle for Wave 1 and 4. Inset shows the ostium plane (region connecting the two necks of aneurysm). Accordingly, the region of interest in the pre-aneurysm geometry is indicated by the ovals. .... 86

Figure 5.7. Contours of AFI for wave 1 and wave 4. Inset shows the ostium plane(region connecting the two necks of aneurysm). Accordingly, the region of interest in the pre-aneurysm geometry is indicated by the ovals. .... 88

Figure 5.9: Comparison of the CCA and ICA Waveforms for female vs. male..... 91

Figure 5.10: The averaged waveform of CCA, ICA and ECA..... 92

Figure 5.11. Waveform of the ICA for older and younger adult. The blue and red dots indicate regions of interest where the results have been plotted. These will be denoted as end diastole, peak systole, second peak, first systolic deceleration 1(SD1), second systolic deceleration (SD2). .... 93

Figure 5.1. Contours of axial velocity overlaid by the secondary velocity for Old and Young waveform at End diastole, Peak systole, SD1 and SD2..... 93

Figure 5.13. Contours of WSS at critical phases of cardiac cycle for Young and Old adult waveform. .... 94

Figure 5.14. Contours of AFI for Older and Young adult. .... 95

Figure 5.15. A sample waveform characterizing the key features. The dashed line represent young adult and the bold line represents older adult..... 97

Figure 5.16. Averaged waveform comparing exercise (bold) vs. non exercise (dashed) younger adults (left and older adults (right respectively). .... 97

Figure 5.17. Waveform of young active adult and old sedentary adult. The blue dots indicate the key phases in the cardiac cycle where the data will be plotted. .... 98

Figure 5.18. Shows contours of axial velocity overlaid with secondary velocity vectors for younger (top panel) and older adults (bottom panel). .... 99

Figure 5.19. Shows contour plots of WSS for active younger and sedentary older adult. .... 100

Figure 5.20. Contours of AFI for active younger and sedentary adults respectively. .... 101

Figure 5.21. Waveform of the CCA showing subject specific, older adult, young adult. .... 103

Figure 5.22. 66-year-old woman with high-grade atherosclerotic stenosis of proximal right internal carotid artery and parvus–tardus waveforms in mid internal carotid artery. .... 104

Figure 6.1. Streamlines that have been started from the same points at the inlet plain are shown. (A) Lateral view of the sidewall aneurysm, (B) Figure A rotated anticlockwise by 90o, (C) Anterior Posterior view of Basilar tip, (D) Figure C rotated 90o. Blue arrows indicate flow direction. .... 112

Figure 6.2. The basic aneurismal flow patterns are characterized by streamlines and velocity vectors for Sidewall Case 1 (A) and Bifurcation Case 2 (B). The three streamlines for each Case are color coded according to their velocity magnitude at their intersection with the ostium plane: peak influx velocity (pink), peak efflux velocity (white), small normal velocity (green). These pink, white and green streamlines are identical to those shown for the two Cases in Figure 2. The velocity vectors are displayed in cross-sectional planes approximately aligned with the peak influx and efflux streamlines. The green streamlines, being closer to the core of the ostium vortex, capture the helical motion of the fluid particles passing through it..... 114

Figure 6.3. Volumetric flow rates across the parent artery, ostium plane, and other arterial branches for Sidewall Case 1 and Bifurcation Case 2. .... 115

Figure 6.4. Contour plots of flow velocity normal to the ostium plane for Sidewall Case 1 (A – D) and Bifurcation Case 2 (F – I) at end diastole (A,C,F,H) and mid-systolic deceleration (B,D,G,I), with blue indicating influx and red, efflux. Figs. C,D,H, & I are normalized to show the size of the influx & efflux zones and to emphasize the relative stability of these zones over the pulsatile cycle. Figs. E & J show movement of the virtual boundary separating the influx & efflux zones at three times in the pulsatile cycle: end diastole (red), peak systole (green), and mid-systolic deceleration (blue). Black arrow (Fig. 4.4 A) shows parent artery flow direction for Sidewall Case 1. For bifurcation aneurysms, the parent artery flow direction is normal to the viewing plane. .... 116

Figure 6.5. Overlaid velocity vectors in the same plane as Figure 4.2 at three different phases of the cycle: end diastole (red), peak systole (green), mid-systolic deceleration

(blue) for Sidewall Case 1 (A) and Bifurcation Case 2 (B). There is relatively little change in direction at points of highest velocity over the cycle. .... 117

Figure 6.6. Figure A,B,D,E,G,H show the influx and efflux zones for the three sidewall cases respectfully. C,F,I show the corresponding waveforms. .... 118

Figure 6.7. A,B,C shows the contours of velocity normal to the ostium plane at three different phases of cycle; end diastole, peak systole and systolic deceleration. Letter I, E on figure 4.7A indicate influx and efflux zone. Figure 4.7 D shows the ostium plane on the aneurysm. .... 119

Figure 6.8. Shows the influx and efflux zones of all the aneurysm cases studies herein at the two critical phases of the cycle. To orient the reader, the cross-sectional plots can be seen to the left. .... 120

Figure 7.1. Contours of WSSG, OSI and AFI for sidewall aneurysm case 1. .... 127

Figure 7.2. Contours of AFI was the three cases studies here in. D, E, F show the pre-aneurysmal artery overlaid with the artery where aneurysm is present to clearly indicate the region of interest. Regions of aneurysm sites (A, B, C) are indicated by black arrows. Inset shows Wave 4. .... 130

Figure 7.3. Shows the influx and efflux zones of all the aneurysm cases studies herein at the two critical phases of the cycle. To orient the reader, the cross-sectional plots can be seen to the left. .... 131

Figure 7.4. Multiscale modeling framework for IA evolution combining structural, hemodynamic, and signaling pathway analysis. (Adapted from Ho et al., 2011). .... 135

Figure A.1. Flow form used by Tomai & Yanishita (1997) for simulating intermittent flow in curved tubes. .... 164

Figure A.2. Secondary flow streamlines for $\kappa = 393$ , $\alpha = 27$ , $\eta = 0$ and $\delta = 1/2$ . (From Tomai & Yanishita 1997). .....	165
Figure A.3. (a) The vessel segment. The inflow plane is at the front. (b) The finite-element mesh. Four representative cross-sections have been indicated: (a) halfway down first bend, (b) end of first bend/beginning of second bend, (c) halfway down second bend and (d) end of second bend. Hoogerstraten et al. (1996). .....	166
Figure A.4. The geometric model of the S-shaped artery .....	167
Figure A.5. A photograph of a transparent human right coronary artery .panel A. from which the shape of the multiple bend adopted in the present study was traced out .panel B., and a three-dimensional mesh model of the vessel used in the computational analyses of blood flow and transport of LDL from flowing blood to the vessel wall: panel C. ...	169
Figure A.6. The effect of Reynolds number on the distribution of LDL concentration at the luminal surface of the multiple bend. Note that at $Re = 200$ at which no adverse flow formed distal to the apex of the inner wall of the acute second bend, the highest LDL surface concentration appeared as a long stripe in the common median plane of the multiple bend, whereas at $Re = 500$ and $900$ at which an adverse flow formed as a result of flow separation at the apex of the inner wall of the bend, the highest LDL surface concentration appeared as a pair of spots located symmetrically on both sides of the common median plane. ....	170
Figure B.1. Final meshes of the 6 different aneurysm models used on the study. ....	175
Figure B.2. Temporal convergence plot. ....	176
Figure B.3. Shows the volumetric flow waveform used for the simulations.....	178

## List of Tables

Table 3.1: A brief summary of the drawbacks of potential indicators of aneurysm initiation.....	51
Table 4.1: Details of meshing scheme and refinement procedure and computational costs and times of all the cases run for the numerical experiment.....	64
Table 5.1: Key features differentiating old vs. young adult .....	80
Table A.1: OSI values computed at different cross-sections (refer Figure A.4). .....	168
Table B.1: Shows the cases and various meshes used for each case. ....	175

# Chapter 1

## 1. Introduction

Interest in vascular diseases is augmented by the fact that vascular diseases are the leading cause of death in western societies. Cerebrovascular disease, coronary artery disease, and heart failure are principal examples of cardiovascular disease that have significant clinical impact and present a major scientific challenge for the development of effective therapies due to its complexity and difficulty in early detection. Research on the treatment and cure of cardiovascular disease is being conducted on many fronts, ranging from basic research on understanding the physiological triggers for the disease to applied clinical practice, and from genetic therapy to various forms of surgical therapy, such as vascular implants and semi-invasive procedures. The disease is multi-factorial (having various causes) and multi-faceted (having various symptoms).

Hemodynamics -- which concerns blood flow in the vessels and its interaction with the vessel wall -- derives from the fact that much of the physiological and pathological behavior of the arterial wall results from mechanical (as opposed to purely biological) factors (e.g., pressure and wall shear stress), which, in turn, are controlled by the fluid mechanics of blood. Prominent examples of disease stemming directly from abnormal hemodynamics in regions of disturbed flow are *aneurysms* and *atherosclerosis*. Understanding the ways in which the flow of blood and the associated physical forces interact with the vessel wall and tissue is, therefore, indispensable in analyzing the genesis, progression, diagnosis and treatment of cardiovascular disease.

In this work blood flow in aneurysms was modeled based on real data from patients detected with cerebral aneurysms. This dissertation focuses on mathematical modeling of *arterial hemodynamics* with the intent of understanding the formation, progression, diagnosis and possible treatment options for cerebral aneurysms, a blood flow-associated disease. The section that follows presents a brief overview of aneurysms, their types, and detection and also briefly discusses the existing treatment techniques.

## **1.1. Aneurysms**

An aneurysm is an abnormal dilatation of an artery. Aneurysms can be broadly classified into two main types, aortic and cerebral aneurysm, depending on their location in the human body. Aortic and cerebral aneurysms occur in the aorta and brain, respectively while aneurysms that occur in arteries other than aorta and the brain arteries are termed peripheral aneurysms.

### **1.1.1. Aortic Aneurysm**

The two types of aortic aneurysms are: Abdominal aortic aneurysm (AAA) and thoracic aortic aneurysm (TAA). The abdominal aorta is the more common site for an aneurysm to develop (Figure 1.1). The primary risk factors of AAA include atherosclerosis, hypertension and smoking. Other risk factors include trauma to the arterial wall, infection and congenital defects of the arterial wall. Most AAAs occur below the level of the renal artery and are proximate to the bifurcation of the aorta as well as the proximal ends of the iliac arteries. Stasis of blood within the aneurysm can lead to thrombus formation along the arterial wall. Peripheral emboli can develop, causing arterial insufficiency. Once an aneurysm forms it often increases in size and consequently

the chances of rupture also increase. Aneurysm rupture can lead to severe complications where 60% of patients either die or suffer permanent disability.

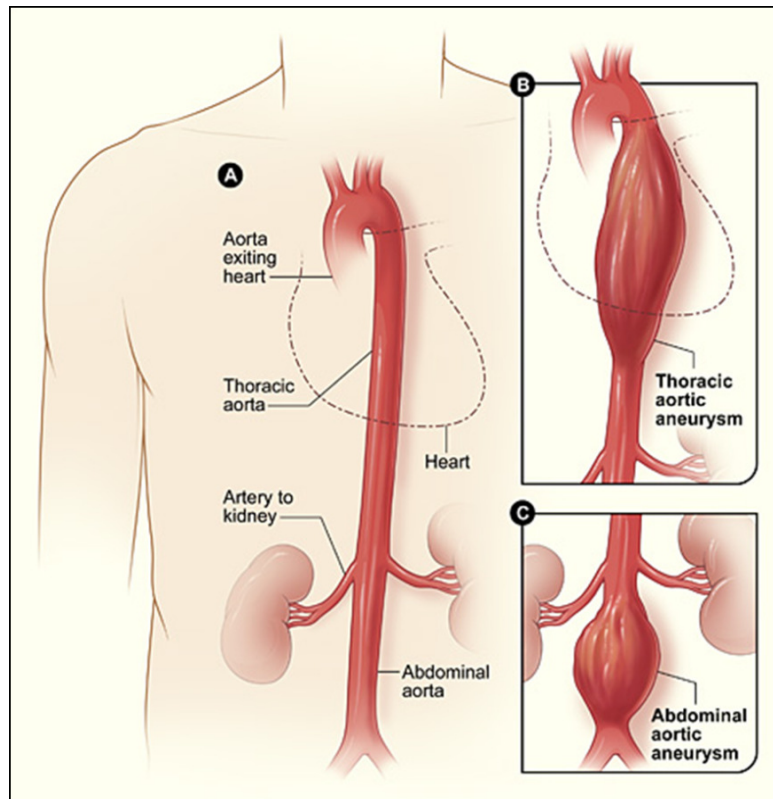


Figure 1.1. Depiction of (A) healthy human artery, (B) TAA and (C) AAA [Source: [http://www.nhlbi.nih.gov/health/dci/Diseases/arm/arm\\_types.html](http://www.nhlbi.nih.gov/health/dci/Diseases/arm/arm_types.html)].

TAA occurs in the chest portion of the aorta. In a common type of TAA, the walls of aorta weaken and a section near the heart enlarges causing a failure of the valve between the heart and aorta thereby resulting in blood to leakage back to the heart. TAA's are typically detected from a chest CT scan performed for other medical reasons.

### 1.1.2. Cerebral Aneurysm

In order to understand the types of cerebral or brain aneurysms it is important to know the vascular system in the brain (Figure 1.2). The head and brain receive arterial blood via the carotid arteries, which originate at the aortic arch. At the base of the ear, the

carotid artery branches into internal and external branches. The external carotid supplies the face, scalp and skull. The internal carotid artery supplies the brain itself. It is divided into an intracranial part, which consists of the carotid siphon traversing the base of the skull (cranium), and an extra-cranial part, which branches into the middle cerebral, anterior cerebral and posterior cerebral arteries to form the Circle of Willis. This is shown in Figure 1.2 (adapted from Vega et al., 2002).

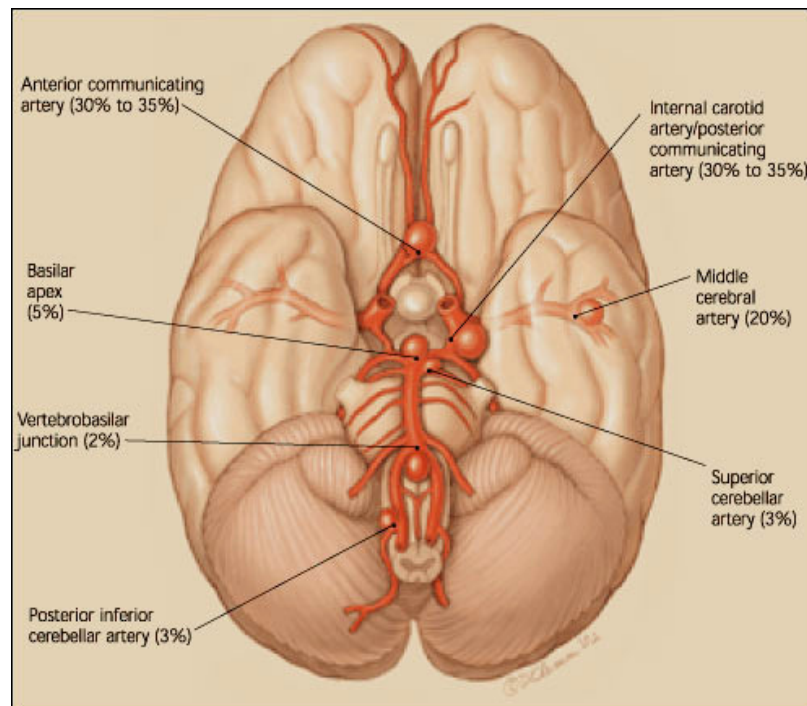


Figure 1.2. Circle of Willis, showing the major arteries supplying blood to the brain. Aneurysms are also shown in the regions where they most commonly form.

A cerebral aneurysm is a dilatation of an artery (Figure 1.2) in the brain that commonly arises at a branch site on a parent artery. These aneurysms are usually detected after rupture, which usually produces subarachnoid hemorrhage (SAH). Among the various signs and symptoms, the sentinel headache is often the earliest warning sign of incipient rupture. Less frequently, intracranial aneurysms are discovered incidentally during neuroradiologic examinations performed for some other diagnostic purposes.

## 1.2. Types of Intracranial Aneurysms

There are four basic types of intracranial aneurysms, categorized according to their etiopathogenesis and histology (Figure 1.3. Goldman et al. 1999):

- **Saccular:** Ninety percent of intracranial aneurysms are saccular or “berry-shaped” and develop as a thin-walled sac protruding from the arteries of the Circle of Willis or its major branches. According to their size, saccular aneurysms can be grouped into three types: small (<10 mm), large (10– 25 mm), and giant (>25 mm). According to their neck width (ostium size), they are further classified into (1) small neck (<4 mm) and (2) large neck (>4 mm). These anatomical features are crucial in deciding the therapeutic approach and the intraoperative risk. They occur at the branching points of the large blood vessels at the base of the brain. Saccular aneurysm formation, thus, is a gradual process occurring over years and risk of rupture increases with age.
- **Fusiform:** Fusiform aneurysms are usually caused by atherosclerosis (also known as atherosclerotic aneurysm), and typically occur in older patients. They can lead to mass effect or ischemia, but rupture is uncommon. Atherosclerotic aneurysms occur in people who have wide-spread atherosclerotic disease or "hardening of the arteries." Instead of rupturing, fusiform aneurysms cause symptoms similar to a stroke by compressing the surrounding brain or by shedding debris that blocks the blood vessels away from the aneurysm.
- **Mycotic:** Mycotic aneurysms are very rare and develop from infection in the arterial wall, often deriving from bacterial endocarditis.

- **Traumatic aneurysms:** They are formed when an accident injures a cerebral blood vessel. The damaged blood vessel weakens at the site of injury and may eventually burst.

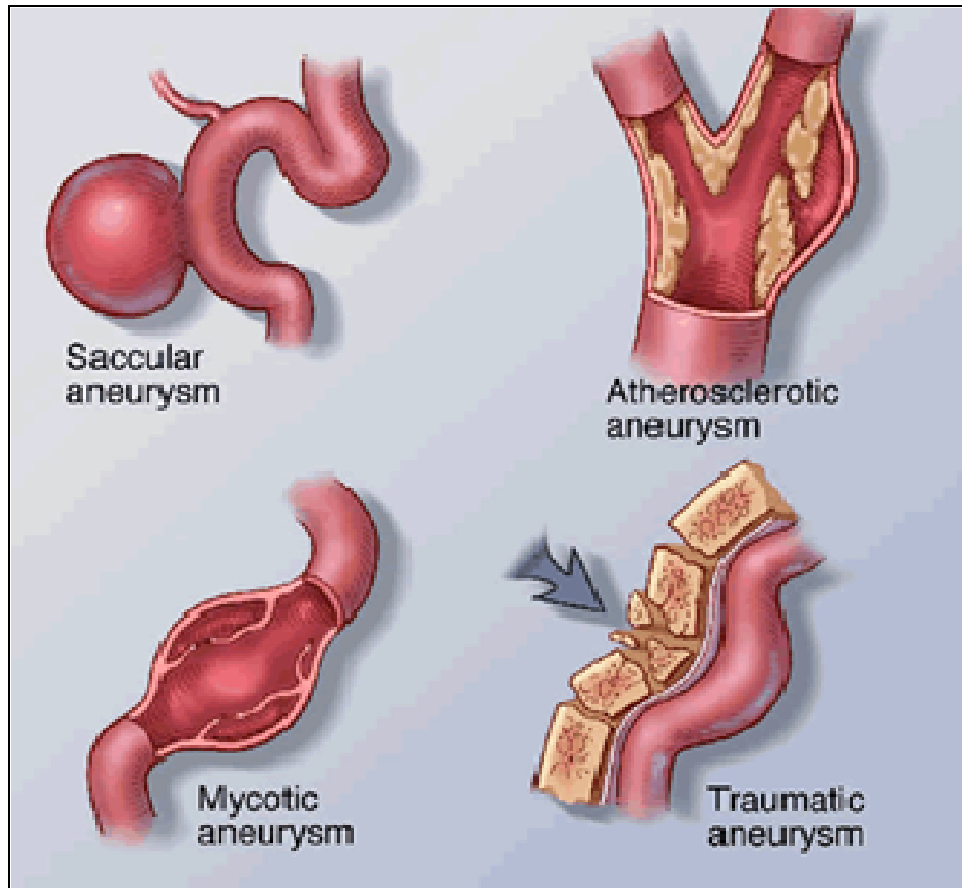


Figure 1.3. Classification of intracranial aneurysms. (Source: [www.thebni.com/.../images/aneurysm8\\_sm\\_new.gif](http://www.thebni.com/.../images/aneurysm8_sm_new.gif)).

### 1.3. Detection of Aneurysms

The most commonly used aneurysm diagnostics are: 1) Angiography 2) Computed Tomography (CT) scan, 3) Magnetic Resonance Imaging (MRI), and 4) Magnetic Resonance Angiography (MRA). In certain cases, the doctor may choose a combination of these technologies for detection as one particular detection tool may not be sufficient. For example, fusiform atherosclerotic aneurysms usually arise from elongated tortuous

arteries. CT scans or angiographies fail to capture accurately the shape of these aneurysms owing to the presence of severe atherosclerotic lesions and thrombus. These aneurysms also do not have significantly identifiable necks. MRI is helpful in delineating the relationship between vessels and adjacent structures such as the brainstem and cranial nerves.

**Angiography:** Technically adequate cerebral angiography is essential in the assessment of non-traumatic SAH (Figure 1.4 adapted from Zhang et al. 2010). This requires visualizing the entire intracranial circulation. A patent (open) intracranial aneurysm is visualized as a contrast-filled out-pouching that commonly arises from an arterial wall or bifurcation. The circle of Willis and the MCA bifurcation are common locations (Zouaoui et al., 1997).

Thrombosed aneurysms usually appear normal on angiographic studies. Aneurysms should be distinguished from vascular loops. Vascular loops are caused by overlapping projections of a 3-dimensional vessel onto a 2-dimensional image. Typically, they appear denser than an aneurysm and can be identified using multiple views. When cerebral angiography demonstrates more than one aneurysm, determining which lesion is the most likely rupture site is important.

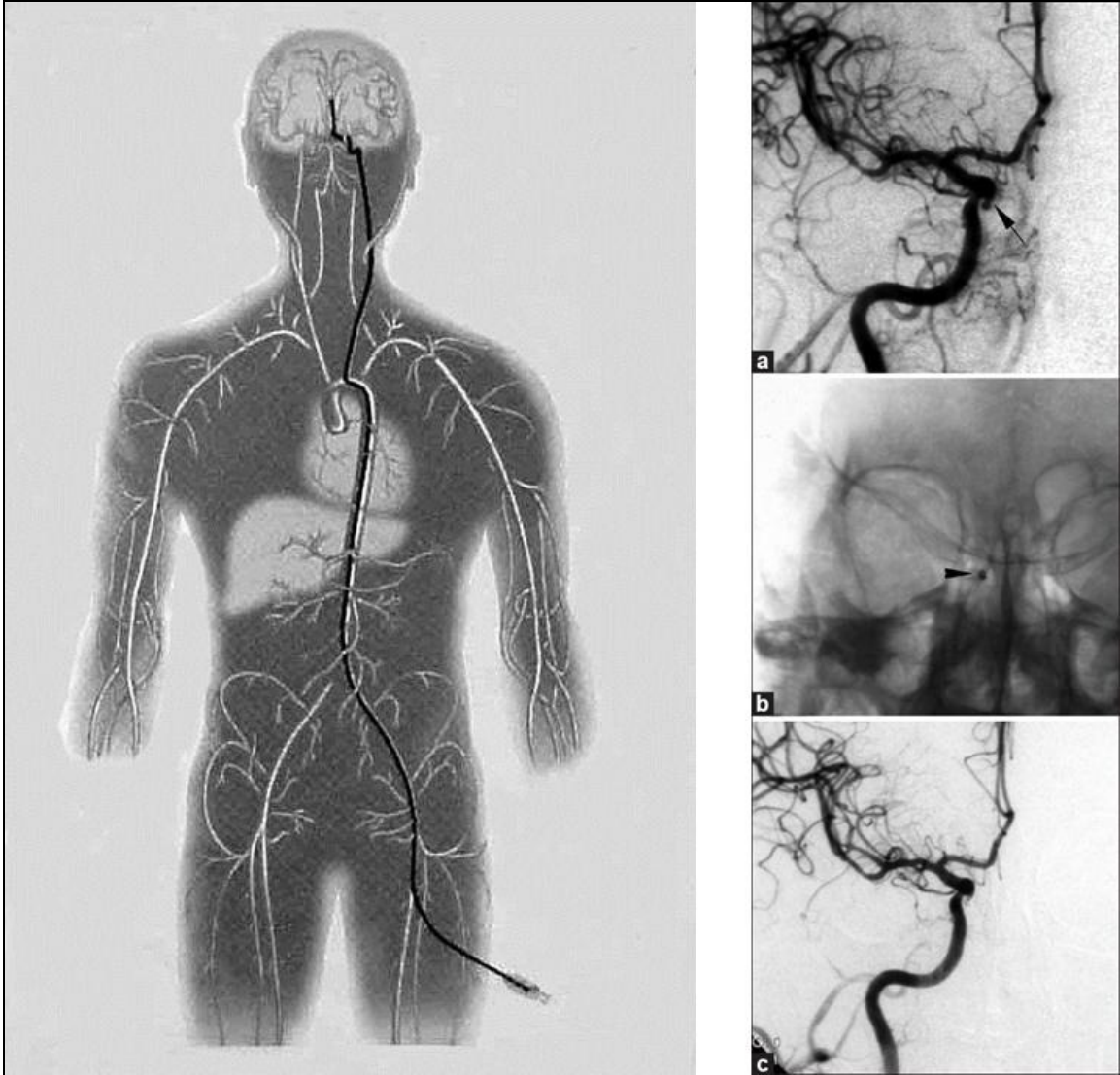


Figure 1.4. (A) Sketch illustrating catheter placement in a blood vessels leading to the brain and the injection of a contrast agent or dye. (B, C, D) Show typical CT angiography image of cerebral arteries with aneurysms. (Source: <http://brainavm.uhnres.utoronto.ca/images/malformations/aneurysm/3-D-angio.jpg>).

**Computed tomography scan** (Figure 1.5): Bone erosion is a characteristic feature that can be observed in long-standing lesions that arise near the skull base. On a non-contrast CT scan, the typical non-thrombosed aneurysm appears as a well-delineated isodense-to-slightly hyperdense mass located somewhat eccentrically in the subarachnoid space (Wardlaw et al. 2000). Patent aneurysms enhance intensely and quite uniformly following administration of intravenous contrast material. Angiographic-like

images of the cerebral vasculature can be obtained using rapid contrast infusion and thin-section dynamic CT scanning. Various 3-dimensional display techniques, including shaded surface display, volume rendering, and maximal intensity projection, are used to complement the conventional images. Such studies provide multiple projections of anatomically complex vascular lesions, such as giant aneurysms (S Aoki et al., 1999). The accuracy of high-resolution axial CT scan in the diagnosis of cerebral aneurysms 3 mm and larger has been reported to be about 97%. Partially thrombosed aneurysms have a patent lumen inside a thickened often partially calcified wall. The residual lumen and outer rim of the aneurysm may enhance strongly following contrast administration.

The presence of SAH may complicate the appearance of aneurysms in a CT scan. The reported ability of CT scan to detect SAH caused by ruptured cerebral aneurysms in the acute phase is about 95% (Kallenberg et al., 2011). SAH may quickly spread diffusely throughout the cerebrospinal fluid (CSF) spaces, providing little clue to its site of origin.

Hemorrhage located predominantly within the inter-hemispheric fissure is common with anterior communicating artery aneurysms. Intra-ventricular blood can be helpful in localizing ruptured aneurysms.

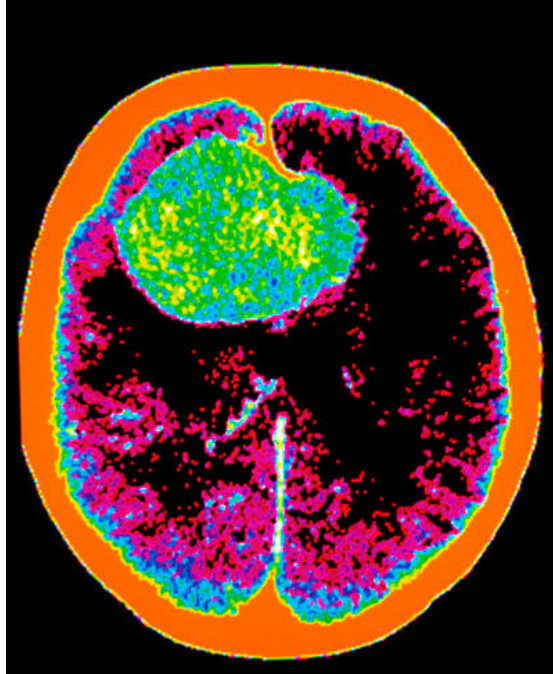


Figure 1.5. Shows colored computed tomography (CT) scan of a subarachnoid brain hemorrhage (green) caused by rupture of a cerebral aneurysm. This is anthropological plane projection. (Source: <http://www.sciencephoto.com/media/255517/enlarge#>).

**Magnetic resonance imaging** (Figure 1.6): Aneurysm appearance on MRI is highly variable and may be quite complex. The signal depends on the presence, direction, and rate of flow, as well as the presence of clots and calcification within the aneurysm itself.

Patent aneurysms can produce different signals on routine MRI studies, depending on specific flow characteristics and pulse sequences used. The typical patent aneurysm lumen with rapid flow shows high-velocity signal loss. Variations in signals may also be observed due to the presence of turbulence. Intravenous contrast typically does not enhance patent aneurysms with high flow rates, but wall boundaries can be preserved. Contrast in the intravascular space also often increases artifacts observed with rapid intraluminal flow.

**Magnetic resonance angiography** (Figure 1.6): The motion of flowing blood, together with background stationary tissue, can be used to create images of the cerebral

vasculature (Horikoshi et al., 1994). The images can be viewed as individual thin sections (source images) or can be re-projected in the form of flow maps or MRAs. Two standard MRA techniques currently used to reconstruct aneurysms are phase-contrast (PC) studies and time-of-flight (TOF) acquisitions.

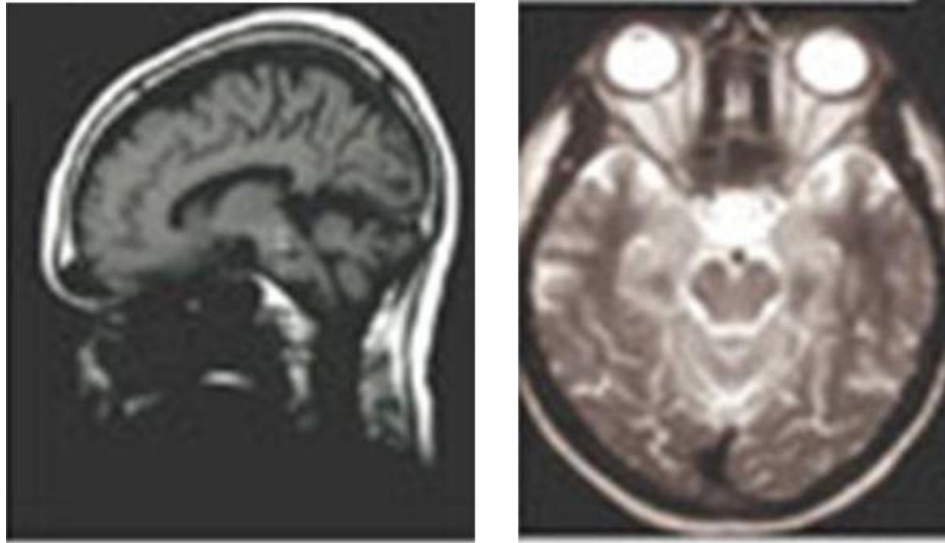


Figure 1.6. Two views of an MRI image showing a cranial aneurysm.

## 1.4. Treatment Options

After detection of a brain aneurysm, a neurovascular expert decides on the treatment options -- surgical clipping or minimally-invasive endovascular coiling are the typical techniques employed for treatment. Additional details on these methods used to treat patients suffering from SAH or aneurysms will be discussed in this section.

**Surgical Clipping** (Figure 1.7): This procedure involves placing a clip across the neck of the aneurysm to exclude blood circulation within the aneurysm while not occluding normal vessels. For the procedure, the surgeon removes a section of the skull to get to the aneurysm, places a small metal clip, secures the bone in its original position,

and closes the wound. The operative mortality rate is less than 5%, when surgery is performed with all available aids.

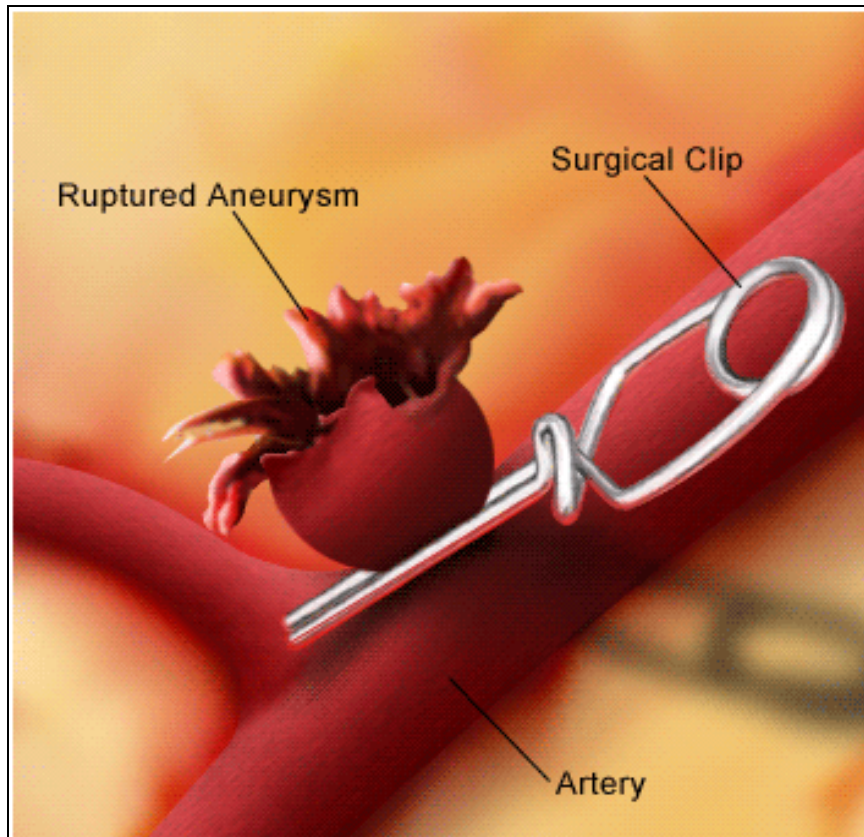


Figure 1.7. Shows A schematic of the treatment of an intracranial aneurysm by surgical clipping.

**Endovascular Coiling** (Figure 1.8): During the past decade, minimally invasive methods have been developed to treat intracranial aneurysms. This endovascular procedure does not require surgery – the physician inserts a catheter into the patient’s femoral artery in the leg. Using fluoroscopic imaging, the physician can visualize the patient’s vascular system, and navigate the catheter to the brain and into the aneurysm (Figure 1.4 A). Platinum coils are then deployed at the site of the aneurysm to block blood flow and prevent rupture. The most common coils used in endovascular procedures are platinum Guglielmi detachable coils (GDC). The coils are made of platinum since

they can be seen using X-rays and are sufficiently flexible to conform to the shape of the aneurysm.

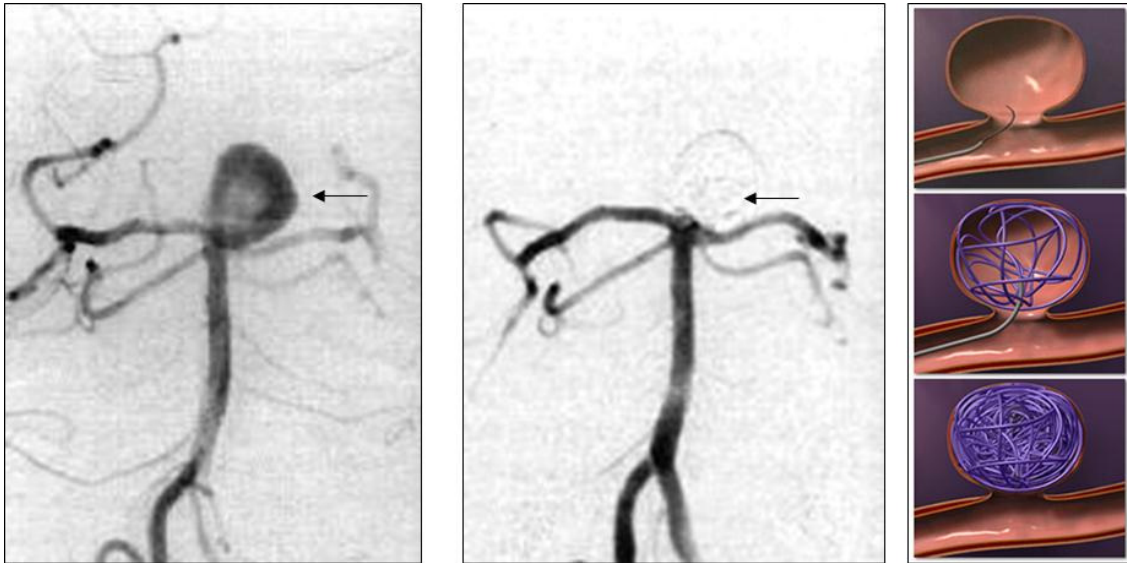


Figure 1.8. (a) Treatment of an intracranial aneurysm by endovascular coiling. Anteroposterior vertebral subtraction angiograms in a 61-year-old woman showing a 12-mm basilar aneurysm before treatment. (b) Treatment of intracranial aneurysms by endovascular coiling. This is after the placement of four Guglielmi detachable coils. (c) An illustration of embolization.

The decision to perform surgery or to use endovascular methods is a decision made by the neurosurgeon and the endovascular radiologists as a team based on which approach best suits each patient's aneurysm. The treatment option depends greatly on the age of the patient and the location of the aneurysm. Younger patients tend to undergo surgical clipping because coiling has a high recurrence rate. In most major aneurysm centers, most cases are still obliterated by surgical clipping, but coiling is being used more frequently due to less hospital stay, shorter recovery times, and lower risk of death or serious complications.

## Chapter 2

### 2. Background and Literature survey

Atherosclerosis has been associated with the formation of abdominal aortic aneurysms. Factors, such as cigarette smoking, heavy alcohol consumption or certain medications, gender, diet, genetic make-up, etc., that are known to promote atherosclerosis and hypertension are correlated also with the formation of cerebral aneurysms.

Several cases of familial intra-cranial aneurysms have also been reported in the literature. However, pathogenesis of cerebral aneurysms, although studied very extensively, is poorly understood. Endogenous factors like elevated arterial blood pressure, the anatomy of the Circle of Willis, and hemodynamic factors (wall pressures and shear stresses) -- especially at aneurysm-prone locations such as vessel bifurcations and (as shown later in this study) points of large arterial curvature -- are all involved in the initiation, growth and rupture of aneurysms. The specific roles of these factors and the details of the specific mechanisms leading to aneurysm growth continue to be subjects of active research. Even to this day many theories have been propounded that attempt to explain the initiation of cerebral aneurysms.

The aim of this chapter is to review the important theories and hypotheses proposed in the literature to account for the causes and mechanisms of aneurysm growth.

## 2.1. Pathogenesis of Cerebral aneurysms

A previous history of atherosclerosis in the artery is an important indicator of possible locations for the formation of abdominal aortic aneurysms. However, that is not the case with cerebral aneurysms. One of the first studies done towards understanding the cause of aneurysm formation was by Eppinger (1887). He claimed that the congenital defects that arise at the arteries that have defective elastic layers are more prone to aneurysm formation. He proposed that these defects are further augmented over time, which could lead to aneurysm formation. Hackel (1928) confirmed this theory and concluded that these degenerative changes are critical in the development of an aneurysm. Intra-cranial vessels feature an exceptionally thick internal elastica layer, which has heavily strained borders, and a relatively thin or no middle layer (media). The inner layer separates with aging (Figure 2.1 shows a schematic of arterial anatomy). The gaps between the elastica and surrounding tissue layers may become filled with collagen and fine elastic fibrils. The presence of these tissues can cause the wall to lose some of its elasticity, thereby promoting the possibility of aneurysm growth.

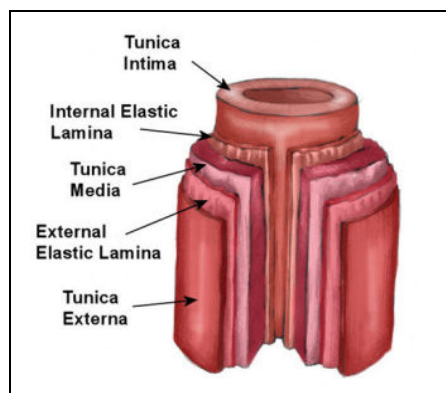


Figure 2.1. Shows a schematic of the anatomy of an artery

Forbus (1930) concluded, from his survey of arteries in 14 children and 9 adults, that aneurysms can be acquired over time from a combination of degeneration of the elastica through prolonged stretching and hypertension and the medial defects in the arterial layers. Glynn (1940) noted that the most common type of aneurysms are saccular. Medial defects at the bifurcation points on the Circle of Willis were found in 81% of patients with aneurysms and 80% of those without. 50% of cerebral arteries from patients under 2 years of age showed medial defects, whereas 91% of the 32 adult specimen showed such defects.

Glynn subjected these samples (obtained from cadavers) of bifurcated arteries to pressures ranging 400-600 mm Hg; at these levels of pressure no localized bulging (indicating aneurysms) could be visually discerned. Superficially, this may suggest the irrelevance of high hemodynamic pressures to aneurysmal growth, but it is quite possible that, the arteries being necrotic and in an unphysiological state, the unsupported elastic elements of the vessel wall could withstand such high pressures (far higher than has ever been recorded in the physiologic range). It has been suggested that the greater frequency with which aneurysms occur in the Circle of Willis in comparison with other muscular arteries is probably due to the differences in the elastic tissue in these arteries. Glynn observed that while aneurysms on the coronary and mesenteric arteries are very rare, medial defects are commonly seen at systemic sites. He concluded that medial defects are not significant in aneurysm growth. In contrast, Richardson and Hyland (1941) inferred, after reviewing 118 cases of SAH's, that while medial defects do play role in aneurysms development, it is another unrecognized, acquired lesion which causes

degeneration of elastic tissue. Vaguely suggesting that aneurysms result from progressive degeneration of the artery as a result of some local injury.

The next major work done in this area aimed specifically at the aneurysms that formed at arterial bifurcations. Stehbens (1959, 1960 and 1962) was of the opinion that a “true” aneurysm is formed by the weakening of the components of the vessel wall that undergo extensive structural degenerative change. In their early stages, walls seem more translucent than the adjacent artery. A localized reduction of tensile strength occurs at the apex of the vessel wall, permitting a small dilatation. Areas of wall thinning and funnel-shaped dilatations have been observed in infants and animals. Electron microscopic studies of early aneurysmal changes show loss of elastic tissue and the presence of considerable cellular debris.

Similar histologic observations have been made in atherosclerosis. One theory that was beginning to evolve was the possible correlation of atherosclerosis to cerebral aneurysm formation. Chyatte (1999) performed a detailed histologic analysis of aneurysm tissue from 23 unruptured and 2 ruptured aneurysms and compared these specimens with 11 control basilar arteries harvested at autopsy. Through this comparative process, he tried to identify the presence of certain chemical secretions or components such as macrophages and monocytes in the tissues with aneurysms. Immunohistochemistry indicated the presence of these components in large quantities; this is also typical of tissues undergoing inflammation. He concluded that extensive inflammatory and immunological reactions are common in unruptured intra-cranial aneurysms and may be related to aneurysm formation and rupture. However, it still remains to be established if aneurysm growth and aneurysm initiation have two different mechanisms or if the same

mechanism governs initiation, growth and rupture of a cerebral aneurysm. Towards this end, several hemodynamics-based theories have been proposed that shed some light on the possible hemodynamic variables leading to aneurysm rupture.

## **2.2. Hemodynamics and Cerebral Aneurysms**

Growth and rupture of an aneurysm can be explained mechanically and pathologically on the basis of wall structure, lumen hemodynamics and extramural factors. In the next section, a brief summary of hemodynamic experiments and numerical simulations, pertaining to aneurysm studies, is reported.

### **2.2.1. Hemodynamic Experiments**

Experimental studies typically involve modeling the artery using a glass tube, with a bulge representing the aneurysm. Water or a water-glycerol mixture is generally used as the fluid and flow measurements are taken either invasively or non-invasively. Various techniques have been used to emulate physiological conditions.

Some of the early work focused on modeling abdominal aortic aneurysms. Liepsch et al. (1987) conducted experimental studies of lateral aneurysms and measured velocities non-invasively using the laser Doppler method. They found that in steady flow, the maximum velocities in the aneurysms were around 2% of the mean flow. On the other hand, in unsteady flow the velocities were as high as 13%. These results varied with the fluid used to model the blood. Using the measured velocity profiles near the wall, they were able to estimate the wall shear stress and found that stress levels are sensitive to the manner in which the flow varies with time. Subsequently, Fukushima et al. (1989) carried out an experimental and computational analysis of pulsatile flows at varying flow rates

and aneurysm lengths. They observed a recessing vortex within the aneurysm, which became highly unsteady when the pulse frequency, flow velocities or aneurysm length were increased. With decreasing amplitude of the oscillatory (zero-mean) flow component flow structure approached that of steady flow. Their experimental model's results were in good agreement with their computational results. Using the latter model, it was found that peak wall shear stresses occur at the distal end of the aneurysm during the time of peak flow rate.

### **2.2.2. Computational Hemodynamic Modeling**

Early studies mostly relied on experiments; however the growth of computational abilities has led to a composite approach based on both methods. One of the first attempts at computational modeling of cerebral aneurysms was undertaken by Perktold et al. (1984). It was a two dimensional model. Under pulsatile flow conditions, a vortex was seen to develop in the aneurismal sac, whose structure and strength were strongly dependent on the phase of the cycle. However, as will be shown in the subsequent chapters, the flow inside the aneurysm is highly three dimensional and 2-D simulations fail to capture key features of flow in the aneurysm. Perktold et al. (1989) extended this analysis to pulsatile flow and compared results obtained from Newtonian and non-Newtonian fluid models. They concluded that in a “large artery under physiological flow conditions there is no essential difference in the results”. This result is very important towards simplifying the model of blood flow in a large artery. Löw (1993) and Perktold et al. (1993) considered incompressible, pulsatile, three-dimensional non-Newtonian flow in models having rigid and distensible aneurysm walls. Some differences were observed

between the rigid and compliant wall models during the systolic period, but the maximum displacement of the aneurysmal wall was minimal (about 6% of the diameter).

Gonzalez et al. (1992), using images of a cerebral aneurysm in the middle cerebral artery obtained from angiography, constructed a two-dimensional finite element model of the region. Three cases were presented in which the size of the aneurysm opening (ostium) was varied. It was noted that the rapid changes in the direction of the impinging blood flow during the cardiac cycle must produce significant hemodynamic stresses on endothelial layer of the artery. Variations in shear stress arising from directional change, rather than magnitude change, may cause more damage to the artery than high, but unidirectional, stresses. This observation led the authors to conclude that the directional recirculation and the resulting oscillating wall shear stress were the etiology of the aneurysm. Another important finding was that the major changes in hemodynamics occurred at the neck and not at the dome of the aneurysm, as was previously believed. This finding implied that if the neck of the aneurysm is not completely eliminated during treatment, the risk of recurrence or rupture still exists. Finally, since larger aneurysms have more complex flow patterns, treatment is correspondingly more complicated.

Kumar & Naidu (1996) reported on their findings of hemodynamics in an aneurysm where the degree of dilatation of an aneurysm was varied between 0.25, 0.50, and 0.75, while the inlet diameter was held constant at 1. In their two-dimensional model, a recirculation region within the aneurysm was observed and the vortices grew with time. Separation and reattachment locations of the vortex were seen to move further away from the aneurysm as the dilatation was increased. Similarly, pressure variations away from the central axis grew more prominent as the dilatation or time increased. Wall shear stress

magnitudes were found to increase significantly with increasing dilatation and time with the maximum values found at the necks. It was therefore concluded that the hemodynamics were highly sensitive to the degree of dilatation.

Burleson et al. (1995) presented several simulations of lateral aneurysms in which the shape of the aneurysm ostium were varied. Half-spherical, spherical, and pear-shaped aneurysms were modeled in which the width of the aneurysm ostium was set equal to the artery diameter or twice the artery diameter. Again, this was a 2-D model. Under these conditions, Burleson et al. noticed that blood entered the aneurysm from the distal end and exited along the aneurysm wall, resulting in a low-velocity counterclockwise recirculation zone. The half-spherical aneurysm had a smaller recirculation zone than the other two shapes. Volume flow into the aneurysm increased with increasing ostium width, but decreased with increasing Reynolds number. Maximum shear stresses were found to be at the distal end of the ostium and were the highest for the spherical aneurysm. An increase in ostium width increased the shear stress for the spherical and half-spherical aneurysms but decreased the shear stress for the pear-shaped aneurysms. The authors concluded that the rupture of an aneurysm occurs at the point of maximum hemodynamic stress and that the aneurysm size, shape, ostium width, and Reynolds number have a significant impact on these stresses. However, as will be shown in the subsequent chapters, the flow inside the aneurysm is highly three dimensional and 2-D simulations fail to capture key features of flow in the aneurysm.

One of the treatment options that was suggested in the mid 1990's was the placement of self-expanding stents. They were a minimally invasive alternative option for the more invasive surgical treatments. Aenis et al. (1997) modeled a lateral aneurysm with and

without the placement of a stent using an idealized and symmetrical three-dimensional model. For the non-stented model, except during the minima of flow rate, the flow activity inside the aneurysm was an order of magnitude lower than the flow in the parent vessel and was highest during systole and maximum flow rate. At systolic acceleration, fluid entered the aneurysm at the proximal end and exited near the distal end. This reversed after a vortex was formed and the flow was in the deceleration stage. They also observed a secondary vortex, which was strongest at peak flow rate and forced the fluid to leave the aneurysm through the middle of the neck. The main vortex was present throughout the cycle and moved closer to the parent vessel as the flow decelerated. This vortex growth and movement generated significant fluctuations, which were highest at the distal neck and alternated in direction each cycle. Consequently, the highest shear stresses were observed at the distal neck even though the stresses were high at the proximal neck. The vortex observed in the non-stented model disappeared completely in the stented model. Flow that entered through the pores of the stents wound around the filaments and remained local. Therefore, there was hardly any motion within the aneurysm sac. Shear stresses in the sac were consequently lowered but flow around the stent filaments caused high shear stresses in those regions. Based on their results, even though the shear stresses at the proximal and distal necks were higher than in the non-stented model, a different location for stent placement along with a different stent density would have attenuated the stresses. Flow activity, shear rates, and high pressures were found to be dependent on the density of the stent filaments and pore density. Finally, it was demonstrated that placing a stent without providing structural support to the parent vessel would not lead to satisfactory results.

There have been experimental studies that have corroborated these numerical results. Liou et al. (1997) studied blood flow in saccular aneurysms of various sizes at a bifurcation site. Type A was created to simulate a late stage aneurysm, Type B was of medium size and Type C was created to simulate an aneurysm still in its initial stages. A vortex was found to be fully developed in the first type but was relatively weak. Type B had the strongest vortex and Type C did not have a fully formed vortex. There was found to be a range of aneurysm size above which the forced vortex inside the aneurysm is weak and below it there is not enough space within the aneurysm for such a vortex.

To study the efficacy of endovascular coiling, Groden et al. (2001) constructed an approximate 3-D model of an aneurysm at the bifurcation site. Simulations were performed assuming the blood to be Newtonian and wall to be rigid. A total of four cases were presented; One with no intervention, with 20% filling, 12% filling and 12% and partial clot formation. It was seen that the platinum coils immediately relieved the influx of pulsating blood and allowed for clotting. The occlusion process was seen to be dependent on the density of the coils. The 20% volume density platinum coil mesh was determined to be appropriate.

Based on the work done, Baoshun et al. (2000) deemed it necessary to characterize aneurysms based on maximum diameter, neck diameter, height, aspect-ratio, bottle-neck factor, bulge location, volume, surface area, Gaussian mean curvatures, iso-parametric ratio and convexity ratio. By categorizing these aneurysms based on the indices mentioned above it became possible to predict what treatment modalities could be effective for these aneurysms. This study was first of its kind in terms of quantifying seemingly arbitrary geometries of human cerebral aneurysms sacs. However, there were a

few limitations to this study. Saccular aneurysms are the most common kind of cerebral aneurysms but they do not constitute the entire spectrum of intra-cranial aneurysms. Fusiform aneurysms vary quite substantially in shape when compared to the saccular aneurysm, but these were not included in the study. Further, the comparison of idealized geometries of aneurysms to that of real patient data was solely by visual inspection: That may not be accurate enough.

One of the first studies that actually used patient specific models by extracting the CTA data and preprocessing followed by solving for the Navier-Stokes (NS) equations simulations was done by Torri et al. (2001). Data from 4 patients was extracted and the computational domain was defined. A Womersley profile was used to model the pulsatility. Secondary flow was observed due to the arterial curvatures, and depending on the location of the branch, flow impingement was observed to be strong in some geometries and weaker in the others. This showed that the shear stresses are dependent on the artery shape, local flow conditions, and the position of the branch.

Using rotational angiography with 3-D reconstruction, or computed rotational angiography, Steinman et al. (2003) was able to develop a computational mesh that resembled the actual cerebral artery. During the systolic peak the slip-streams inserted into the flow showed more mixing as it entered the aneurysm through the proximal neck. Swirling motion resulted in a rotating vortex which persisted throughout the cycle. However, by the end of diastole, little mixing was observed in the parent vessel. Two counter-rotating vortices were present throughout the cycle in the aneurysm, with more mobile vortices forming during deceleration. Cycle-averaged wall shear stress corroborated the effect of the flow impinging on the neck of the aneurysm and

decelerating into the aneurysm. The authors also calculated the oscillatory shear index to locate the regions experiencing highly disturbed flow. These regions were identified at the boundaries of the high shear regions, indicating that there was change in shear stress over the cardiac cycle at those locations. High oscillatory shear indices were also found at the most interior part of the aneurysm when compared with the parent artery. Even though their model was of a lateral aneurysm in which, according to previous studies, flow is supposed to enter through the distal neck and exit through the proximal neck, based on the streamline analysis, the authors observed high-speed flow impacts on the aneurysm causing several vortices to develop. This observation again demonstrated the importance of the geometry of the artery in hemodynamics. However, note that stream lines and path lines streak lines are not the same for unsteady flow, and analyzing the stream lines to understand flow behavior for an unsteady case can be misleading.

While extensive research was being done to understand flow inside the aneurysm, computational models were beginning to evolve that targeted developing a better understanding of the hemodynamics involved in the initiation of aneurysms. Seminal work in this area was done by our group as part of my Master's thesis (Mantha et al., 2006, Karmonik et al., 2006b). As a consequence of the work done, two different schools of thought evolved proposing two different hemodynamic mechanisms that lead to aneurysm formation. In the following chapter, a brief summary of the Master's thesis work will be presented, followed by a comparison of each of the theories.

## Chapter 3

### 3. Endothelial Cells and Wall Shear Stress

It has been suggested in the literature (Nerem et al., 1981; Okani and Yoshida, 1993, 1994, 1995; Ziegler et al., 1981, 1995) that hemodynamic wall effects resulting from disturbances in the flow trigger biological processes leading to degeneration of the vessel wall – intimal thickening or thrombus formation – and that the analysis of certain specific hemodynamic parameters will lead to a better understanding of these processes and the precise identification of arterial segments prone to flow-related diseases. Flow disturbances locally aggravate the endothelium and may lead to the dysfunction of endothelial cells, monocyte deposition, elevated wall permeability to macro-molecules, particle migration to the vessel wall, smooth muscle cells (SMC) proliferation, etc. These aggravating flow events are greatly influenced by the geometry of the blood vessel and by the temporal variation of the flow-rate (i.e. the input waveform). Numerous experimental and computational studies of blood flow in model tubes, with bends and bifurcations, have been published (see appendix A). Studies relating particle deposition to hemodynamic flow variables have been performed by modeling blood as a two-phase colloidal fluid. The local time-averaged wall shear stress (WSS), the near-wall pressure gradient, and critical particle deposition rate form the basis of various indicators proposed in the literature. Wall compliance, wall strain, and non-Newtonian viscosity are typically assumed to be secondary factors, and hence neglected; this is likely a conservative assumption (see appendix B).

Some indicators have been independently proposed in the literature that attempt to quantify the flow disturbance effect and link it to the onset of various flow diseases. These indicators were proposed in the context of intimal thickening and atherosclerosis, although some recent ones target aneurysm formation: Mantha et al, 2006 and Meng et al. 2008; The first published research that attempts to correlate hemodynamic parameters to the biological response of endothelial cells leading to aneurysm formation was proposed by our group (Mantha et al., 2006).

In this chapter, we first review the biochemical responses of endothelial cells to different flow stimuli, and then conduct a critical survey of the various indicators that have been proposed in the literature related to atherosclerosis and aneurysm formation.

### **3.1. Endothelial Cells and Flow Disturbances**

In general, endothelial cell morphology and orientation are sensitive to WSS. These cells do not respond to the flow immediately; rather the morphological changes in these cells occur as a result of sustained disturbances in the flow patterns. Even under steady flow conditions, it takes several hours for endothelial cells to adapt to a change in the hemodynamic forces in the vicinity of the cells, although responses are seen within the nucleus of the cell almost immediately. Zielger et al. (1981, 1995) demonstrated a relationship between the time for shape change in EC and WSS induced by a particular flow field. It took 24 hours for the change in the conformation of endothelial cells (EC) when exposed to a steady shear stress of  $3 \text{ N/m}^2$ . The affected cells tended to have an elongated shape in the direction of the flow field. This change in shape increased the cells permeability to several serum substrates, either through the inter-cellular junctions called the endothelial clefts or by vesicular transport through the sub-endothelium.

Okano and Yoshida (1993, 1994, and 1995) exposed ECs to low WSS and observed increased cellular activity: cell permeability increased, which, in turn, made these regions susceptible to lipid deposition. These cells were seen to have a polygonal shape. Healthy arterial blood flow in reality is highly pulsatile in nature. The arterial segments which are prone to aneurysm formation or atherosclerosis experience dynamic changes in magnitudes and directions of flow variables during the cardiac cycle. These arteries were found to be characterized by regions of recirculating flow and regions where the local velocities are oscillatory in nature. Helmlinger (1991) studied the effects of oscillatory flow on the morphology of Bovine aortic ECs (BAEC) cultured on a flat plate. He exposed these cells to sinusoidal flow with a positive mean, and observed that the cells indeed elongated in the direction of flow. However, when the mean flow was of zero magnitude, the cells oriented in random directions, but did not show any degenerative response to the shear stresses. The morphology of these cells can be gauged in terms of a “shape index” (SI) and their angle of orientation (AO). Under static or no-flow conditions, ECs exhibit an elongated shape, but with random orientations. When exposed to flow, they elongated in the direction of flow. Therefore, the directional changes in WSS and the duration of change play a major role in the AO and SI of ECs. Disorganized ECs have decreased peripheral actin (a protein found in muscle that together with myosin functions in muscle contraction) and increased fiber numbers (thick myosin bundles or filaments). These cells exhibited high monocyte adhesion in the regions of flow disturbances. Kataoka et al. (1998) studied ECs exposed to one-way, reciprocating and alternating flow directions. For one-way flow, they found marked cellular elongation. For reciprocating flow, the elongation was not very substantial although the cells oriented

with the direction of flow. When exposed to orthogonal flow, that is when the cells alignment was orthogonal to the direction of flow, these cells did not elongate but approximately re-oriented themselves in the direction of flow. In all the cases, there was a predilection of ECs to orient themselves in the direction of flow.

### **3.2. Models of Cellular Transport: Two Phase Model of Blood**

To quantify cellular transport of blood elements such as platelets in computational studies, some of the common techniques that have been applied are 1) Lagrangian tracking of individual particles (looking at fluid motion through the movement of fluid particles through space and time. Plotting the positions would give the pathlines.) 2) Mass transfer-type Eulerian calculations, using a pre-determined rate of surface deposition (looking fluid motion by focusing on specific points in the space through which the fluid flows, in time).

Karino et al. (1989) visualized the fluid mechanics of neutrally buoyant spheres in hardened and transparent arteries. The maximum deposition occurred adjacent to vortex centers (vortices forming close to the wall) and the minimum at reattachment points. The deposition of these spheres near the vortex centers is not surprising as the particles tend to cluster near the vortex center and fluid replenishment only affects the particles outside the vortex.

Barber et al. (1998) focused on particulate adhesion to human umbilical vein EC. Adhesion was seen to be dependent on the Reynolds number. This in-vitro observation is consistent with the distribution of monocytes/macrophages in normo-cholesterolemic (normal blood pressure) animals and lesions in hyper-cholesterolemic (high blood

pressure) animals. Smaller branches such as intercostals do not create significant secondary flows and have relatively low levels of intimal monocytes due to little or no variation in the direction of WSS. In contrast, larger branches such as celiac and superior mesenteric arteries produce significant secondary flows that enable monocyte transport to the endothelial surface. In the regions of low oscillatory flow, an elevated concentration of chemo-attractants was also observed. Presence of chemo-attractants is a mechanism of cell signaling in response to endothelial injury.

Deng et al. (1994, 1995) numerically studied the concentration distributions of low-density lipoproteins (LDL) in regions of flow disturbances under steady state conditions. They assumed that the walls were semi-permeable, and macromolecular uptake was modeled using a fixed filtration rate (suction normal velocity). Surface concentration of LDL was found to be highest at the re-attachment points. Lei et al. (1999) explored the wall shear stress gradient (WSSG) as a possible basis for macromolecular permeability in the celiac junction, based on permeability data from Herrmann et al. (1994). Buchanan (1999) also explored shear stress gradient-dependent LDL wall permeability: He proposed the following parameter:

$$WSSG = \left[ \left( \frac{\partial \tau_m}{\partial n} \right)^2 + \left( \frac{\partial \tau_n}{\partial n} \right)^2 \right]^{1/2}, \quad (3.1)$$

where  $\tau_m$  and  $\tau_n$  are the diagonal components of the WSSG tensor that cause widening and shrinking of cellular gaps. The non-dimensionalized form of this parameter is:

$$WSSG_{nd} = \frac{d_o}{T \tau_o} \int_0^T WSSG dt, \quad (3.2)$$

where  $T$ = Cardiac cycle time period,  $d_0$ = inlet diameter,  $\tau_0$ = Poiseuille type WSS at the inlet corresponding to the mean flow rate. The use of WSSG as a possible index will be further explored in the following sections.

### **3.3. Indicators proposed in Literature**

Based on the EC response to wall shear stress, two different theories have been proposed that correlate aneurysm formation with changes in WSS: (a) the low oscillatory WSS theory, and (b) the high WSS and WSSG theory. These are discussed below.

#### **3.3.1. Low Oscillatory WSS theory**

In my Master's thesis (Mantha MS Thesis 2006, Mantha et al. 2006), an attempt was made to identify hemodynamic factors contributing to aneurysm formation. Models of intra-cranial sidewall aneurysms obtained from clinical three-dimensional digital subtraction angiograms were used in computational hemodynamic simulations. A geometrically realistic approximation of the artery prior to aneurysm formation was constructed. Unsteady-flow simulations performed for these arterial segments led to a new hemodynamic indicator: Aneurysm Formation Indicator (AFI), the cosine of a reference value of wall shear stress and instantaneous wall shear stress. The indicator was found to correlate well with locations of aneurysm formation.

3D DSA image data of three paraclinoid aneurysms were retrospectively obtained from imaging studies done as part of diagnostic evaluations. Data were obtained with C-arm systems (Axiom Artis; Siemens, Medical Systems, Erlangen, Germany). For the virtual reconstruction of the parent artery across the aneurysm ostium, a software plugin developed in-house for the Siemens image post processing workstation Leonardo was

utilized (Karmonik et al., 2006). Figures 3.1(A, B, C) show the 3D-DSA images for the three cases. The arterial geometries obtained from patients, as described above, were converted to a stereolithographic file format and transferred to a geometric modeling and computational mesh generating software code, Gambit<sup>®</sup> (Fluent, Inc.). After some smoothing and geometric remodeling, computational meshes of various degrees of refinement were generated (see Appendix A for more details).

The three cases studied involved sidewall aneurysms in the carotid artery with differing orientations and are shown in Figures 3 (D, E, F) from a perspective that emphasizes the presence of the aneurysm. The corresponding pre-aneurysm geometries, after artificial excision of the aneurysm, are shown in Figures 3(G, H, I) as indicated by white arrows. The geometries of these models are essentially identical to those in Figures 3 (D, E, F) away from the aneurysm site, and are smoothly connected across the aneurysm segment, minimizing geometric artifacts. Another perspective, normal to a plane cutting through the ostium, is shown in Figures 3 (J, K, L).

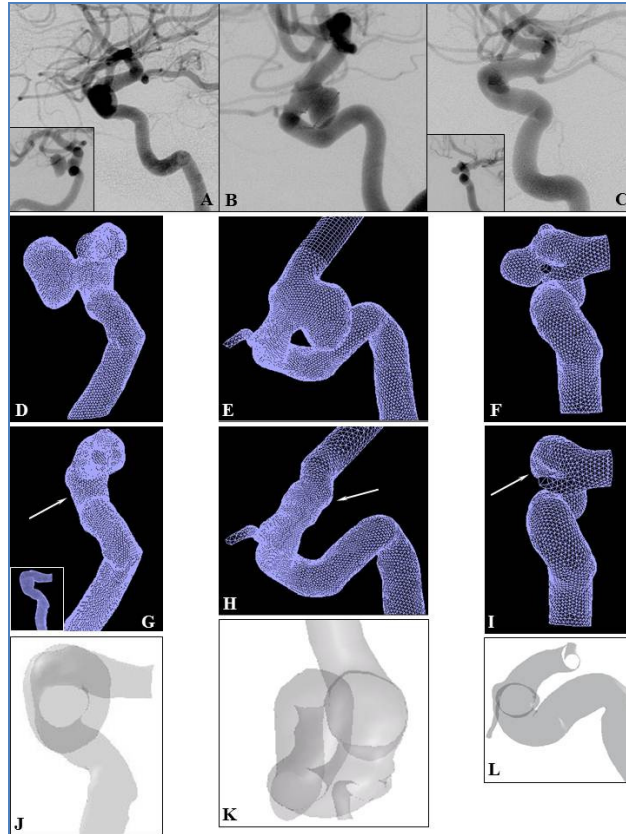


Figure 3.1. A, B, C: Lateral views (DSA) of three sidewall aneurysms of the paraclinoid internal carotid artery. The aneurysms vary in their orientation to the vessel axis. In A (case I) the aneurysm dome extends more distally than proximally, in B (case II), the dome extends more proximally than distally (as opposed to A) and in C (case III) the dome extends equally in both directions. Insets in A and C show the aneurysms in tangential projections according to their orientation laterally (A), and medially (C). D, E, F: The 3-dimensional computational domain that was obtained from 3D angiography of the three aneurysms is shown. Figures D and F are aligned in the same orientation as in the insets of A and C. G, H, I: Geometries in identical projection to D,E,F respectively after artificial removal of the aneurysms using a smoothing algorithm. The inset in Figure G, oriented according to the initial DSA (A), was chosen to highlight the effects of wall shear stress at the ostium plane for case-I. This orientation is identical to Figure J showing the ostium “en face”. J, K, L: “En face” projections of the aneurysm ostium (transparent grids).

An important aspect of the study was that not only were three different aneurysm geometries analyzed, but also the “pre-aneurysmal” geometry was emulated by excising the aneurysm (via a smoothing algorithm). Despite the considerable differences among the three cases – in the details of the arterial curvature, aneurysm size and shape -- strong similarities among the three were seen, in both pre- and post-aneurysmal flows. In particular, we observed that at the aneurysm location (a) secondary flows are prominent,

(b) pressures are elevated at the outer bend of the arterial walls (at the aneurysm location), and (c) shear stresses were oscillatory. As discussed earlier, previous studies have shown that low and oscillatory WSS has a deleterious effect on the arterial wall. In order to capture this we developed the AFI, given by the cosine of the angle ( $\cos \theta$ ) between the instantaneous WSS and a reference value. As A principal reference value, we have used the time-averaged WSS ( $WSS_{av}$ ). This correlated well with the location of eventual aneurysm formation as shown in fig 3.2.

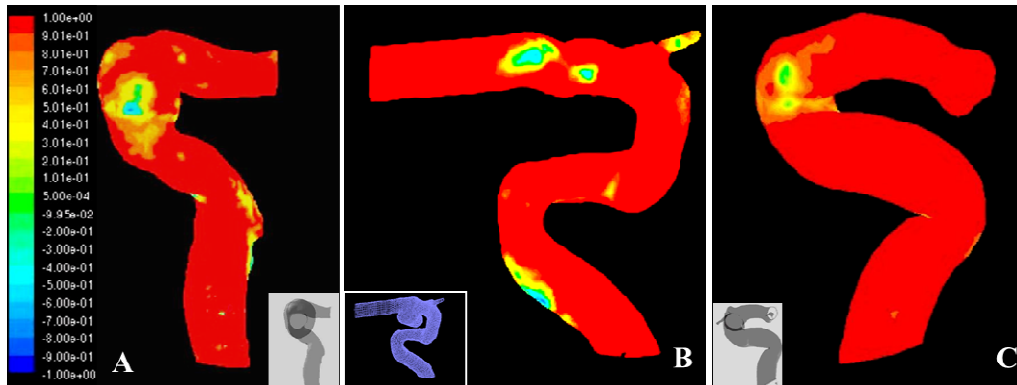


Figure 3.2. Contour plot of the Aneurysm Formation Indicator (AFI) at systolic deceleration. The blue color corresponds to complete reversal in WSS, green corresponds to a  $90^\circ$  rotation of WSS and red implies that the instantaneous WSS vector aligns with the reference value, the temporal average of WSS. Panels (A), (B) and (C) correspond to cases I, II and III respectively. The insets show the location of the aneurysms. The most significant values of this indicator tend to correlate with the area of subsequent aneurysm development.

While the quantitative aspects of the flow (WSS) showed expected differences across the (three) different aneurysm geometries, the common features showed promise in terms of the possible development of a generalized model for aneurysm genesis. The application of AFI has demonstrated a possible correlation between low, oscillatory WSS and aneurysm genesis. This relationship can be explained through two mechanisms. First, low WSS causes increased permeability of endothelial cells to low-density lipoproteins (LDL). Infiltration of LDL into the intima-media layer triggers inflammatory responses in

the vessel wall. Second, oscillatory WSS provides a conducive environment for enhanced adhesion of monocytes and macromolecules to the wall and deposition of platelets. All these biochemical processes can lead to progressive degeneration of the arterial vessel wall.

Szymanski et al. (2008) studied the effect of impinging flow on endothelial cells. They designed a T-chamber mimicking the bifurcation and exposed the bovine aortic endothelial cells (BAEC) to this flow, with  $WSS > 40 \text{ dynes/cm}^2$  and  $WSSG > 300 \text{ dynes/cm}^3$ . After 24-72 hours under flow, the cells around the stagnation zone maintained polygonal shapes; however cell density was reduced. In contrast, cells exposed to high WSS and WSSG were elongated, aligned parallel to flow and at higher density, implying that the cells migrated from the stagnation point in response to impinging flow, as a result of which lower EC density was observed at the regions of low WSS. They concluded that low WSS is responsible for the depletion of the EC, and WSSG was responsible for the migration of the cells to the region of high WSS. In addition, they also showed that high WSS and high WSSG did not directly cause EC damage.

Doenitz et al. (2010) were fortunate to get access to a real patient data set of an artery before and after the formation of aneurysm (ref Figure 3.2). Within 44 days, they observed de novo genesis and rupture of an aneurysm of the basilar artery of the patient. They performed CFD analysis on the 3D models of the artery. Based on the results they proposed a mechanism of genesis of fast growing aneurysms. 3-D models were built using computed tomography angiographic slices. A Non-Newtonian model of blood was used with shear dependent dynamic viscosity. They investigated hemodynamic flow

variables such velocity, pressures and WSS. From their simulations and analysis, they found low WSS in the region where aneurysm eventually formed (Figure 3.3). The pressures were indeed slightly higher at the bifurcation point. In addition they concluded that regions of high WSS had no relevance to aneurysm formation.

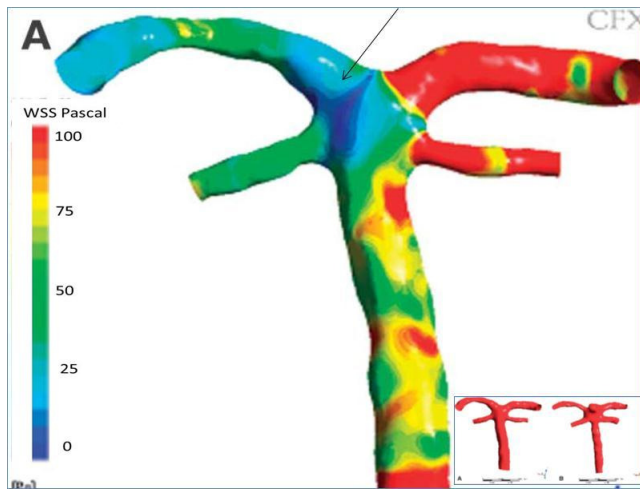


Figure 3.3. CFD in 3D models of simulated asymmetry of outflow. Results of WSS are shown with high outflow pressure in the right posterior cerebral artery and superior cerebellar artery. Insets: Real patient data, A: pre-aneurysm B: Post-aneurysm.

Watton et al. (2011) developed a fluid-solid growth model (FSG) of saccular aneurysm-evolution. It utilized a two-layered structural model of the internal carotid artery and accounted for the degradation of elastinous constituents and growth and remodeling of the collagen fabric. The perturbation to the geometry altered the hemodynamic environment. Subsequent degradation was explicitly linked to regions of low WSS (fig 3.4).

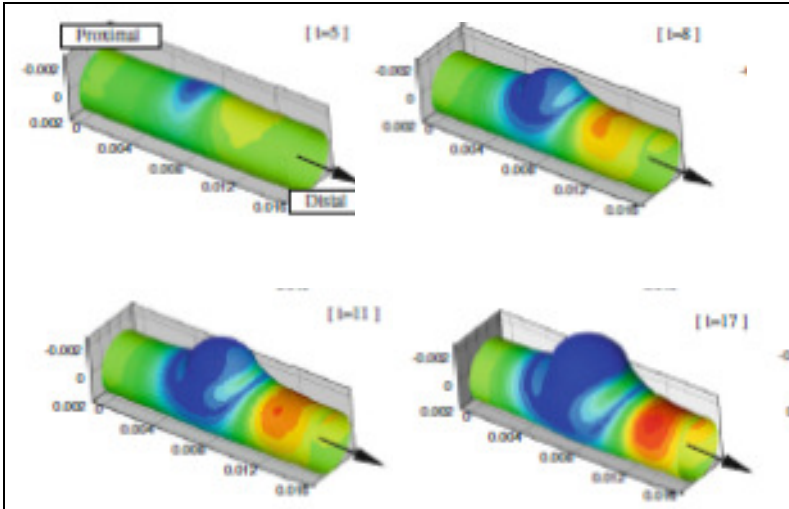


Figure 3.4. Contours of WSS for the evolving aneurysm.

In a study similar to Doenitz et al. (2010), Zakaria et al. (2007) constructed three parametric models (Figure 3.5) of arterial bifurcations, to capture all the geometric features identified as common to cerebral bifurcations in the complex transition from parent to daughter branches. In their simulations, maximum differences in the WSS were found to be less than 8% for all the models.

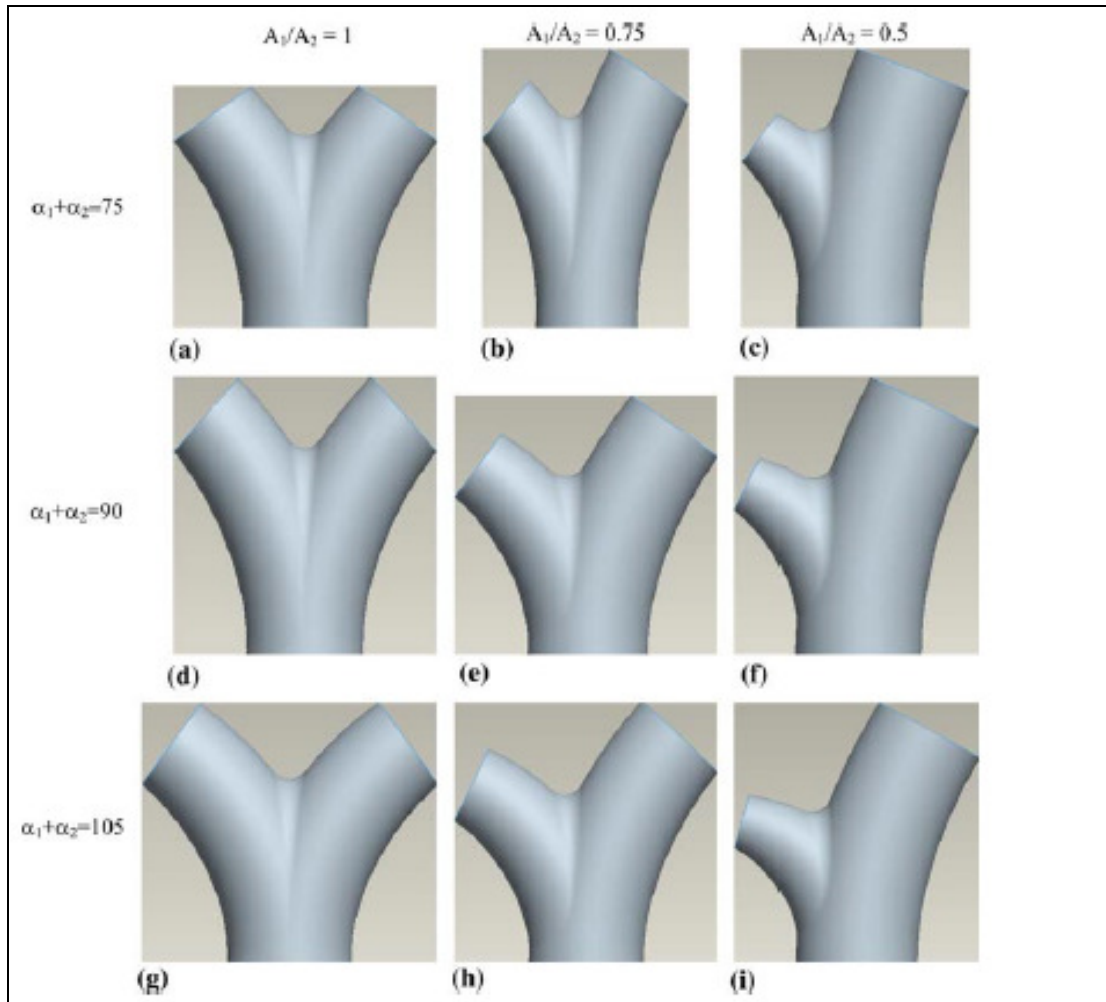


Figure 3.5. Representative examples of the six constant (planar) parametric models.

The results of the simulations showed very low WSS at the apex, but corresponding increase in the WSS at the branches. However, the high WSS found at the branch points was still within the physiologically healthy range. Regions of low WSS produced a stagnation zone (Figure 3.6).

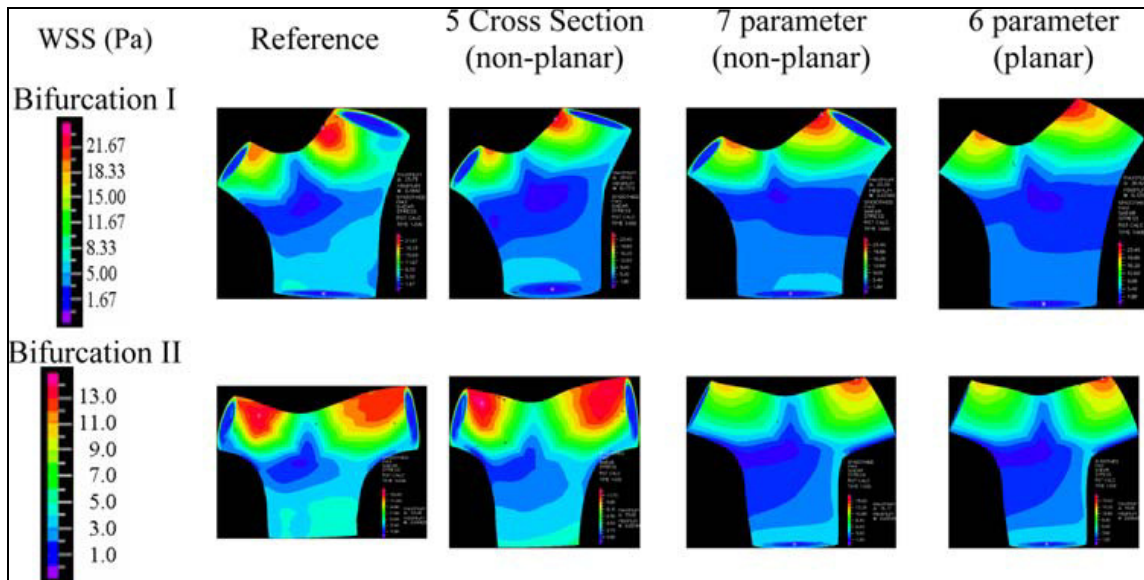


Figure 3.6. Contours of wall shear stress (WSS) for the reference bifurcation and each of the corresponding parametric models.

Analysis of a real bifurcation model yielded similar results. The stagnation zone formed at the apex of the aneurysm can move due to the pulsatility of the vessel wall and the angle formed by the branches. This creates a region of low, oscillatory WSS at and near the apex, as well as regions of high WSS near the branches, due to the accelerating flow (Figure 3.7).

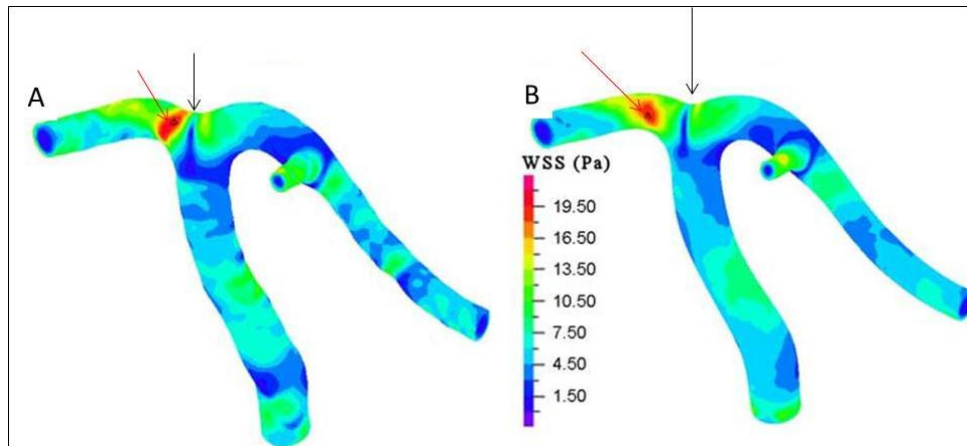


Figure 3.7. Contours of WSS for the reference arterial network and parametric idealization of this vasculature for a Reynolds number of 400, with (a) WSS in reference network, (b) WSS in parametric model. Arrows indicate regions of high and low WSS.

Consequently, there are regions of high WSS *gradients* in the transition region. The increase in WSS, however, is still within physiologically acceptable levels. In contrast, in regions at and near the apex, the WSS is below physiologically normal levels and is known to cause a deleterious effect on the wall, as was shown experimentally by Hazama et al. (1986). They ligated the left common carotid artery and the posterior branch of both renal arteries of 22-male rats. Ten-age matched untreated rats were used as control studies. Three months later, saline was perfused through the left ventricle of the animals at 37C, followed by 4% paraformaldehyde in 0.1M phosphate buffer. The circle of Willis was carefully removed from the brain and immersed in saline fixative at 4C for twelve hours. The specimens were then washed and semi-thin sections containing anterior communicating artery (ACA), stem and branch, and olfactory artery (OA) were cut at 1 $\mu$ m thickness and stained with 1% toluidine blue. Nomenclature of the parts of ACA/OA is shown in Figure 3.8. It was observed that in the control studies the OA branch was larger than the OA in diameter.

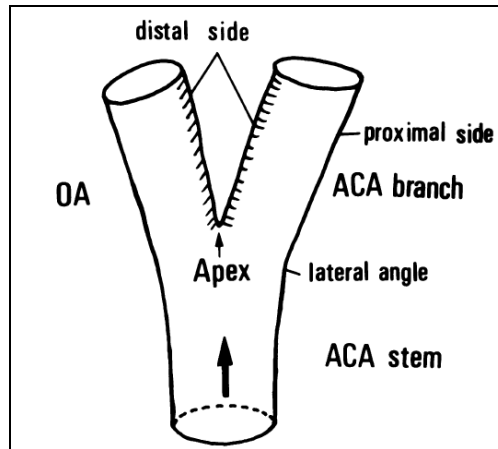


Figure 3.8. Schematic of the ACA/OA junction. Arrow shows the direction of blood.

The wall apex consisted of normal arterial components, that is, EC, elastic lamina, smaller sized medial smooth muscle cells, and thin adventitial fibrous connective tissue. Apical medial defects were not found. They also found existence of an intimal pad on the distal side of the apex, although the size of the intimal pad varied. In the experimental animals, the most prominent feature was thinning of media with or without dilation of the wall on the distal side of the ACA branch adjacent to the apex. Eight of the 22 cases showed dilation of the arterial wall. In the study it was shown that aneurysm initiation occurred not at the apex itself but rather very close to it. Based on the earlier studies of flow simulation in bifurcating aneurysms, this region typically has a stagnation zone or very low WSS. The initiation seemed to be associated with a degeneration of the elastic lamina at the intimal pad. The interior elastic lamina showed thinning, fragmentation, duplication and disappearance. The neighboring area showed a shallow depression associated with thinning. Such changes were augmented by the experimental treatment and developed with advancing age (Figure 3.9). This experiment confirmed that the

regions where the maximum damage to the vessel wall occurred were where WSS were very low.

This is somewhat contradictory to the studies done by the Meng group (2007, 2008, 2009, and 2011), in which correlations were reported between regions of high WSS found adjacent to the apex (at the branch) and aneurysm initiation. As mentioned earlier, the study performed by our group (Mantha et al., 2006) was the first computational study towards correlating hemodynamic variables and factors leading to pathogenesis of cerebral aneurysms by simulating pre- and post- aneurysm environment. After this work appeared, two divergent theories (low WSS and high WSS) evolved, concerning the possible causality between hemodynamic factors and vessel wall injury. In the next section, the theory of high WSS is discussed.

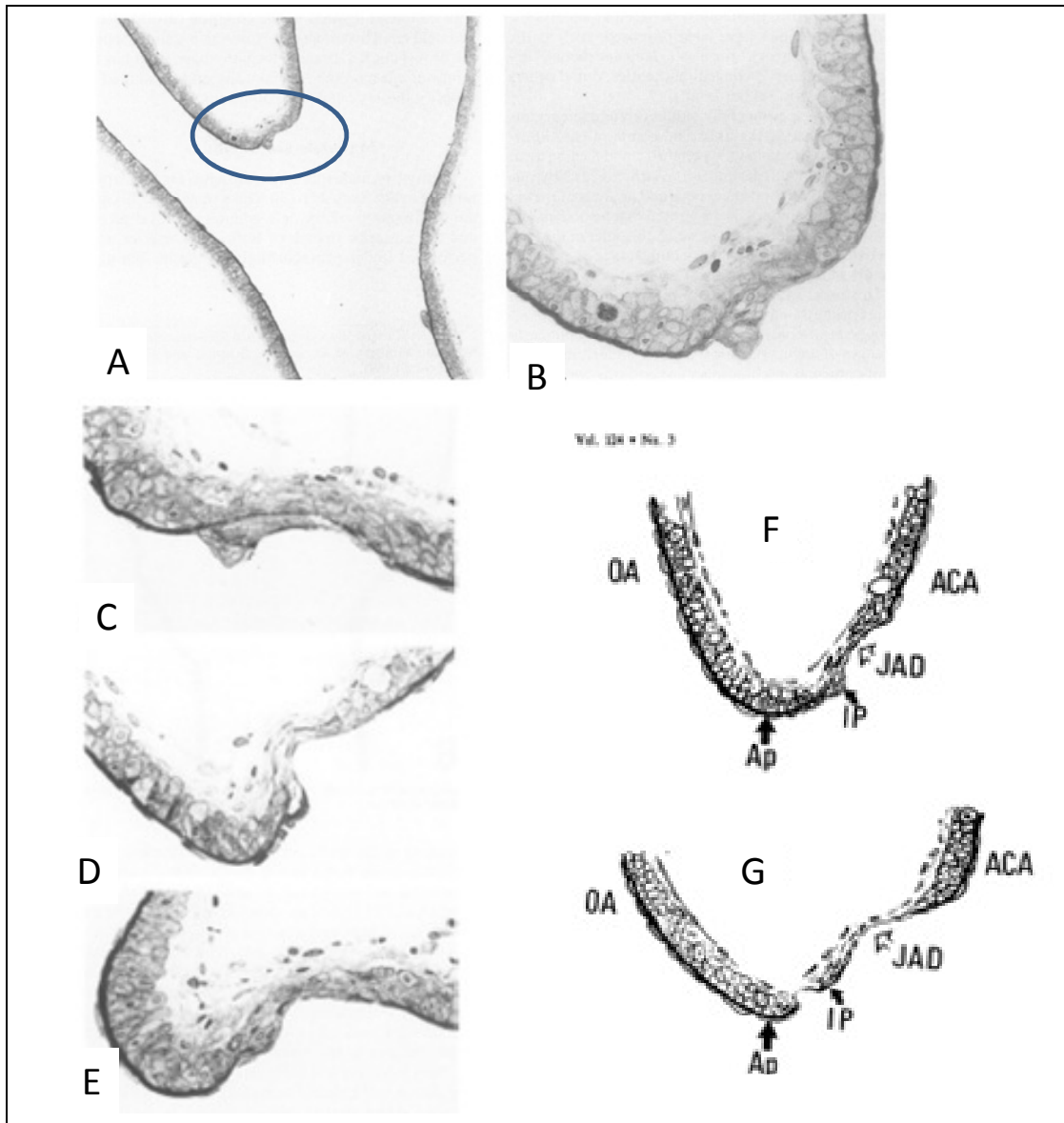


Figure 3.9. (A) ACA/OA branch. (B) Magnified view of the apical area. Note the juxta-depression. (C) Degeneration of intimal pad, medial VSMC is decreased in number. (D) Thinning and dilation of the juxta-apical depression. (E) Outward bulging. The internal elastic lamina has completely disappeared. (F) A schematic of early aneurysm development. (G) Advanced aneurysm with the involvement of the intimal pad.

### 3.3.2. High Wall Shear Stress Theory

Meng et al. (2006) created an arterial bifurcation from native common carotid arteries in two dogs and angiographically imaged them, one after two weeks and the other after

two months. They characterized the local morphological changes in response to the specifically manipulated hemodynamics. CFD simulations were later performed on the two geometries, and mapped the results from the CFD studies onto the histological images (Figure 3.10).

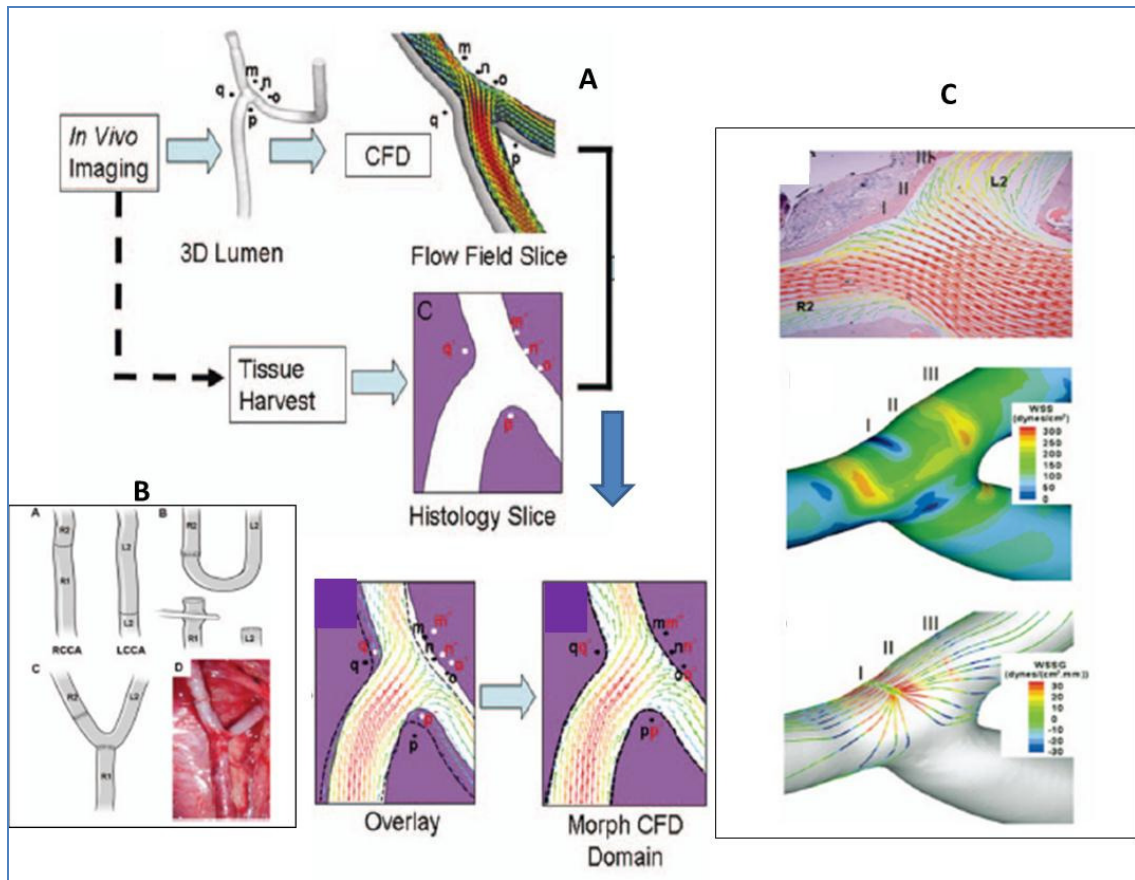


Figure 3.10. (A) Schematic of the methodology. (B) Procedure to surgically create the bifurcation. (C) Mapping of CFD results onto the histological images.

They divided the region into three segments: Region (I), the impingement region where an intimal pad developed, a region of low WSS; Region (II), the acceleration region where the groove (very small out pouch) developed; and Region (III), which showed normal morphology. The pad and groove formation were considered the indications of early aneurysm development. An increase in the elastin-collagen was seen

at the intimal pad, and the groove was characterized by disrupted endothelium and thinned media and depletion of VSMC. They concluded that the regions of high WSS and WSSG were responsible for the creation of a groove that leads to early aneurysm initiation.

The study failed to explain why there is a certain predilection for an aneurysm to form only at one branch as the regions of high WSS are seen at both the branches of the artery. Note that regions of high WSS are seen on both the branches of the bifurcation, and therefore this region of high WSS is not unique. In fact, aneurysms are known to form at the apices, which are regions of low, oscillatory WSS. In addition, Region I is seen to be very small, and the histology results vary along a larger area. It is possible an overlap exists between region I and II, making it harder to conclude which morphological changes correspond to what region in the CFD simulations.

Gao et al. (2008) subjected nine female New Zealand white rabbits to sham, unilateral or bilateral common carotid ligation to produce varying degrees of compensatory basilar artery flow increase. They quantified the destructive structural changes at the basilar terminus and correlated them with the increase in flow. The basilar artery flow rate was increased by 105% to 900% maximum. All the rabbits presented nascent aneurysm formation indicated by a bulge with thinned media and absent internal elastic lamina near the basilar terminus. To determine if there was a correlation between the aneurysm-initiating destructive modeling and the increase in the flow rate, they measured the luminal length along the bulge, the length of the wall exhibiting thinned media, and the maximum length of EC loss (including the bulge). These lengths were then normalized by the BA diameter prior to ligation. The product of the three was indicated as the

nascent aneurysm index (NAI) to reflect the overall degree and severity of destructive modeling. NAI is defined as the ratio of the product of bulge length, media thinning length, and IEL loss length to the square of BA diameter before ligation.

NAI was defined by a multiplicative combination of the three so with any one of them missing, the NAI would be zero, meaning no aneurysm is formed. The computed NAI correlated strongly with flow rate increase, with  $R^2 = 0.91$ . Due to ligation, and the compensatory mechanism in the Circle of Willis, increased flow in the BA was observed. This resulted in higher flow impingement which further elevated the wall shear stresses and wall shear stress gradient in the hemodynamic “danger zone”. This hemodynamic insult was speculated to trigger local maladaptive vascular remodeling leading to aneurysm initiation. The drawback of this study is that such high increases in the flow are not present as a result of any major arterial disease. The eventual increase in WSS seen here is thus not physiologically present in the human arterial network, making it difficult to assess the relevance of these results to clinical aneurysms.

As an extension to this work, Metaxa et al. (2008) performed an experiment to study endothelial cell response to high WSS. The increase in EC proliferation was initially linear from 15 to 50 dynes/cm<sup>2</sup> and changed to more than 6 fold at 50-100 dynes/cm<sup>2</sup>. Furthermore, staining revealed a decrease in the apoptosis with increasing WSS. Immunostaining revealed increased endothelial nitric oxide synthase (eNOS) production with increasing WSS. They concluded that very high WSS that occurs at the apices of the bifurcation directly stimulates EC proliferation, and this stimulation is dependant on the nitric oxide (NO) signaling mechanism. The regulation of this behavior by NO offered a direct connection to physiological risk factors that are known to precede aneurysm

formation in this hemodynamic environment. Again, the levels of WSS found in these arterial regions do not go as high as 100 dynes/cm<sup>2</sup>. Also at WSS less than 40dynes/cm<sup>2</sup> is considered to have an athero-protective effect on the vessel wall (Helminger et al., 1995).

In a study by Singh (2009), an attempt was made to correlate the effects of smoking and hypertension on WSS and OSI at the location of aneurysm formation. The methodology used was similar to Mantha et al. (2006). Two intracranial aneurysms (IA) were artificially removed from the patient specific arterial geometry. Smoking and hypertension were modeled by increasing the viscosity of the blood by 6% and increasing the blood volume (BV) by 8.1%. High values of WSS (>15 dynes/cm<sup>2</sup>) were observed at the location. An increase in viscosity and BV did not change the values of OSI (Figure 3.11). They concluded that long-term exposure to high WSS may result in increased risk to IA development. Note that the regions of low WSS near the bifurcation, and interestingly, the regions of high WSS that they point out are still within the physiologically relevant values of WSS.

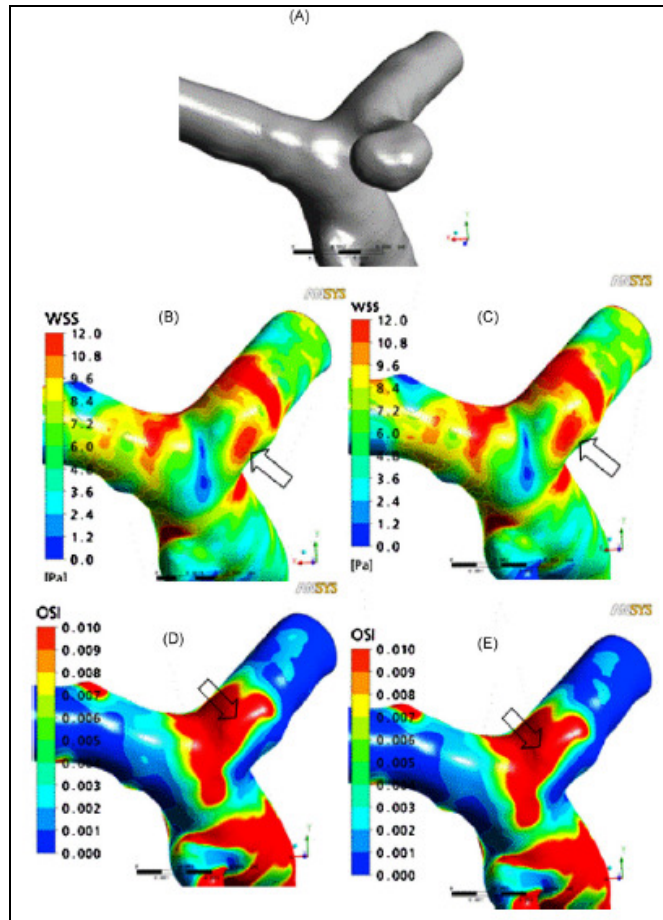


Figure 3.11. (A) Patient specific data.(B, C) contours of WSS with and without the increase of viscosity and BV. (D, E) contours of OSI with and without the increase in BV and viscosity.

Dolan et al. (2011), investigated the role of positive and negative WSSG and elevated WSS, using a flow chamber with constant-height channels to create regions of uniform WSS and converging and diverging channels to create positive and negative WSSG respectively. Cultured bovine aortic endothelial cells were subjected to  $35 \text{ dynes/cm}^2$  and  $284 \text{ dynes/cm}^2$  with and without WSSG for 24 and 36h. High WSS inhibited EC alignment to the flow direction. Positive WSSG ( $+980 \text{ Pa/m}$ ) inhibited alignment and stimulated apoptosis and proliferation whereas negative WSSG ( $-1120 \text{ Pa/m}$ ) promoted alignment and suppressed proliferation and apoptosis. The major drawback of this study was that it did not consider the effect of pulsatility. It is well known that pulsatility tends

to shift the regions of WSSG, implying that the same region can experience both positive and negative WSSG, as in the case of arterial curvature.

Based on the earlier work on WSSG by Meng, Shimoganya et al. (2009) performed numerical simulations on a patient specific data by artificially removing the aneurysm to create pre-aneurysm environment. They based their work on the theory of WSSG affecting the EC proliferation. They proposed an indicator called the Gradient Oscillatory Number (GON). They also did a comparative analysis of the indicators proposed, including AFI. The study concluded that GON correlated better with aneurysm formation (Figure 3.12). However, the waveform used was unrealistic and not patient specific. The new hemodynamic index focused on the fluctuations of hemodynamic forces on the ECs. If  $f$  is given as the WSS, then  $f_p$  and  $f_q$  are the unit vectors tangential to the surface, and perpendicular to each other, where  $f_p$  is the time averaged WSS and  $f_q$  is perpendicular to the time averaged WSS.  $G$  is defined as the spatial WSSG, given by

$$G = \left( \frac{\partial f_p}{\partial p}, \frac{\partial f_q}{\partial q} \right), \quad (3.3)$$

These components are said to generate tension and compression forces on the endothelial cells.

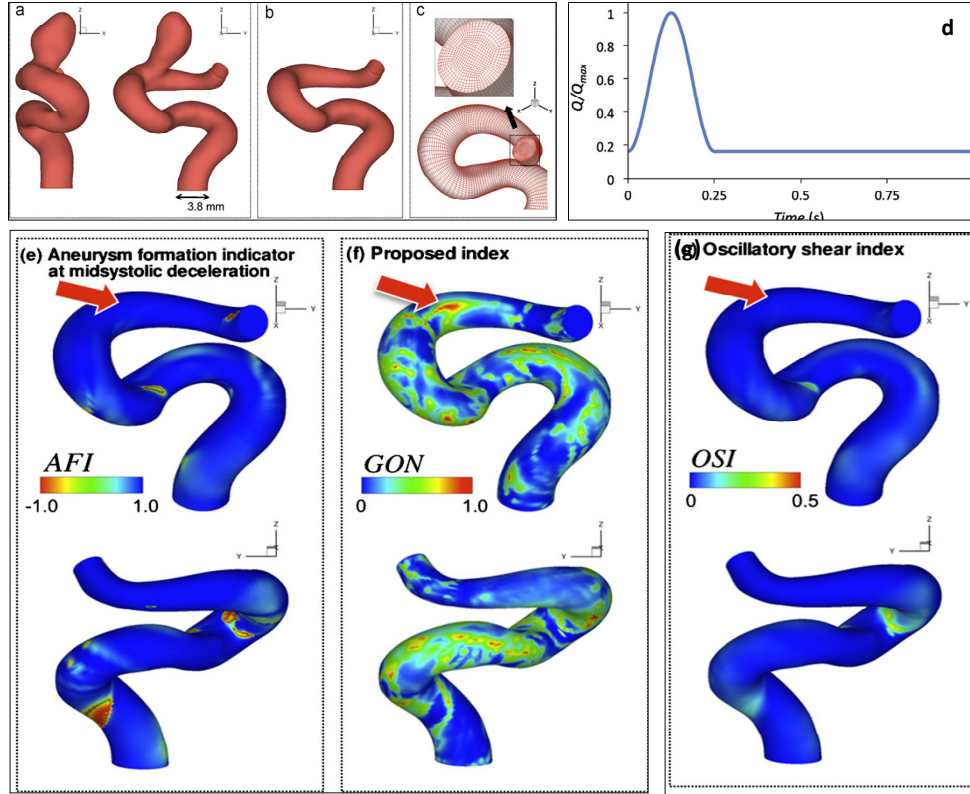


Figure 3.12. A show the patient specific artery. B shows the geometry of the artery after artificially removing the aneurysm. C shows the meshing scheme. Waveform is indicated in Figure 3.15(D). Contours of AFI, GON and OSI are shown in E,F,G respectively.

Thus to quantify the degree of oscillating tension/compression forces, they calculated a new hemodynamic index called the GON index defined as

$$GON = 1 - \frac{\int_0^T |G| dt}{\int_0^T |G| dt} \quad (0 \leq GON \leq 1). \quad (3.4)$$

Use of an idealistic waveform, and being limited to only one arterial geometry were the major drawbacks of the study. In addition, as seen in the figure 3.12, there are various locations in the artery which have high values of GON, in other words, various false positives.

Another concern with such analyses is that WSSG is a highly sensitive fluid dynamic variable, sensitive to the resolution of the mesh, the scheme of the mesh used (tetrahedral vs. structured mesh, use of boundary layer vs. adaptive meshing scheme). It is also very sensitive to inherent resolution artifacts resulting from image acquisition. The drawbacks of the use of WSSG as a potential hemodynamic indicator will be explicated upon in the next chapter.

### 3.4. Summary and Conclusions

In the previous sections we have discussed various theories proposed in the literature regarding aneurysm initiation. A table containing a summary of the drawbacks of each theory is presented.

Table 3.1: A brief summary of the drawbacks of potential indicators of aneurysm initiation.

High WSS	Low WSS
1. In the CFD simulations, regions of High WSS were not found to be high enough to illicit deleterious response from vessel wall.	1. AFI, based on low oscillatory WSS, fails to distinguish regions of aneurysm formation from regions of atherosclerosis.
2. In the experimental studies, the regions of high WSS are very close to the disturbed flow region, so the histological examination for inflammatory or remodeling response is not conclusive.	
3. WSSG is highly sensitive to mesh scheme, resolution, image acquisition techniques as well as image reconstruction procedure, making it unreliable (shown in next chapter).	2. A simple indicator based on WSS is not sufficient to take into account the complex physio-chemical responses that occur at the wall after injury.
4. GON is a complex index, that is based on WSSG calculation and it will be shown that it is a highly unreliable hemodynamic quantity	

Two theories have been proposed in the literature that link hemodynamic variable to aneurysm formation: Low Oscillatory WSS and High WSS and WSSG. Further experimental validation has to be performed, and use of more arterial geometries for computational studies is necessary, to achieve a consensus on which better predicts the initiation and progression off aneurysm. In the next section, we further delve into the details of the CFD simulations that could shed more light into the complex variable that is now being popularly used, namely the WSSG.

## Chapter 4

### 4. The Wall Shear Stress Gradient Problem

Wall shear stress gradient (WSSG) has become a popular hemodynamic index in the past decade. Regions of “disturbed flow” are now considered not only to be areas of low and oscillatory shear stress but also regions with high WSSG. Through experiments it was found that high positive shear stress gradients encourage endothelial cell migration, thereby rendering the region with low EC density prone to flow associated diseases (Meng et al., 2009). However, a study done by Frangos et al. (2007) claimed that it is not the spatial changes in the WSS to which ECs are most sensitive; it is temporal fluctuations that cause EC damage. A consensus still needs to be reached in this regard and it is still a subject of contention. Based on the experimental results, numerical studies were performed wherein the WSSG or its derived quantities were used as a possible index. Shimogonya et al. (2009) proposed the GON, briefly discussed in the previous chapter, based on the WSSG. WSSG is a second order derivative fluid dynamic variable, sensitive to inherent resolution artifacts resulting from image acquisition and in some cases, the computational procedure for the arterial reconstruction. In addition, it is also sensitive to the resolution of the mesh, the meshing scheme (tetrahedral vs. structured mesh, use of boundary layer vs. adaptive meshing scheme). The drawbacks of the use of WSSG as a potential hemodynamic indicator will be elucidated in this chapter. First, a brief summary of the studies done in the past related to WSSG will be presented; numerical simulations will be emphasized (it will be explained that taking derivatives of real experimental data boosts noise levels in most cases). Second, we will demonstrate

the inherent complexities of this variable by setting up a unique problem of a flow in an ellipse whose analytical solution is derived and will be compared against the numerical solution. Note that this chapter does not argue about the effect the WSSG on endothelial cells. Vast research has been done to show the change in the health of EC exposed to WSSG. The aim is to present the numerical errors associated with the computation of WSSG and the caution needed to ensure a stable, accurate calculation including during the use of commercially available software.

#### **4.1. Working with Gradient**

Chaichana et al. (2011) investigated the hemodynamic effect of variations in the angles of left coronary artery, based on simulated and realistic coronary artery models. Twelve models were used, consisting of four realistic and eight simulated geometries with the latter having different angular variations. They quantified the effect of these variations on the hemodynamic indices such as the WSSG and used this indicator to define disturbed flow regions. CFD software ANSYS was used to solve the equations and the WSSG was calculated using the previous definition (chapter 3, equation 3.1). They concluded that since regions of low WSS covered a smaller area of disturbed flow, while regions of WSSG covered a larger region of disturbed flow where the atherosclerotic regions were seen, WSSG is a better hemodynamic indicator of atherosclerosis initiation (Figure 4.1).

Kulcsar et al. (2011) aimed to examine the hemodynamic micro-environment related to aneurysm initiation at certain arterial segments that later developed an aneurysm. They reconstructed the angiographic data of three patients before a true aneurysm developed.

Flow in these arterial geometries was simulated by using finite volume modeling. The WSS and WSSG were analyzed (Figure 4.2).

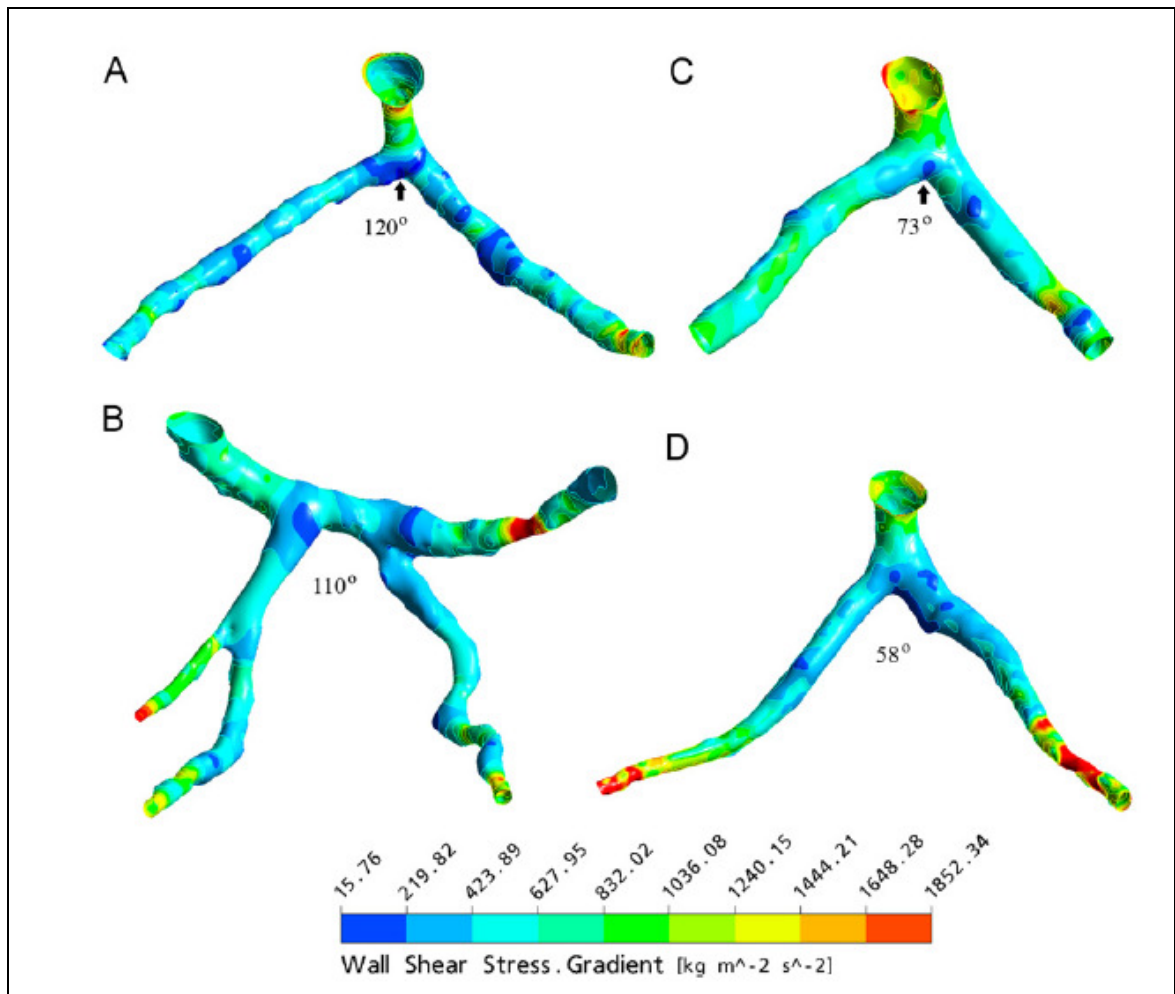


Figure 4.1. Wall shear stress gradient observed with variable angles of the realistic left coronary artery models generated at peak systolic phase of 0.4s. Arrows display the wall shears tress gradient distributions, with a large region of the low magnitude present in a  $120^\circ$  model and a small region in a  $73^\circ$  model.

They concluded that a combination of high WSS at the regions of aneurysm formation along with high WSSG found at those regions contributed to aneurysm formation. This was in accordance with the clinical follow up. As with all these studies, it is very difficult to understand what really contributed to aneurysm formation as the WSS levels found in those regions have been within the physiological range; further, as will be

shown in the next section, numerical calculations of WSSG using commercially available software can be quite tricky.

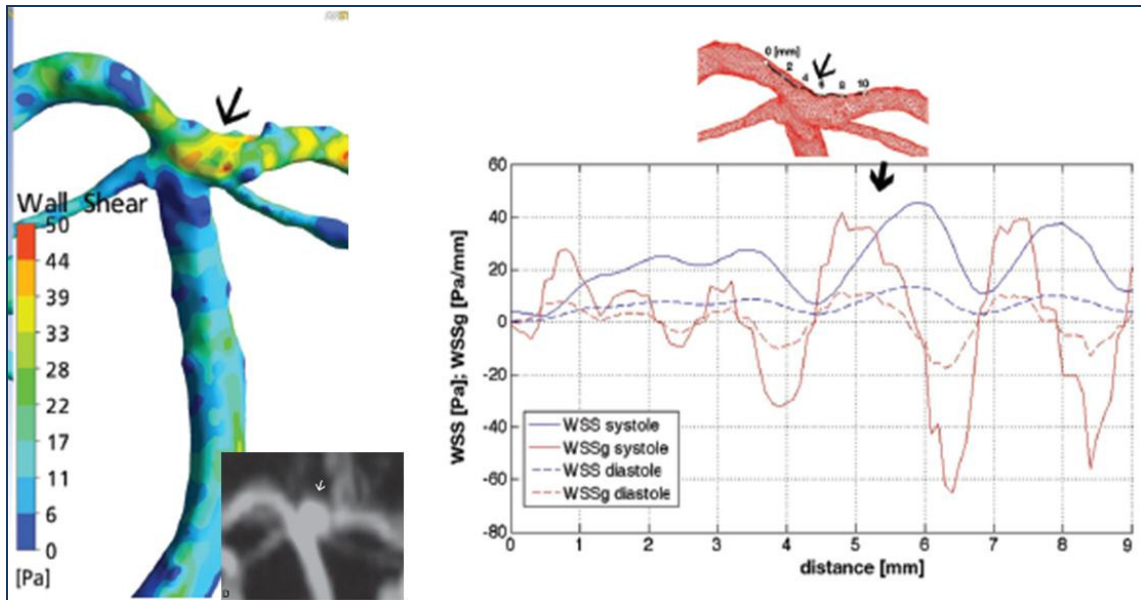


Figure 4.2. Contours of WSS for the case 1. Inset represents where the aneurysm eventually developed. The graph shows the values of WSSG and WSS along the regions shown in inset 2.

Some studies (Brown et al., 2010) involved experiments to investigate the combined effect of two physical stimuli on endothelial cells: (i) microstructured tissue culture polystyrene substrate that is known to produce changes in cell shape and orientation and, (ii), the laminar shear stress in a parallel plate chamber. These effects were evaluated in a parallel plate flow chamber and in a CFD model. The topography was different for the three studies: aligned cells on ridges, nonaligned cells on planar tissue culture, and nonaligned cells with high pillars. Significant differences were found in cell shape and orientation on the different micro-structured surfaces. Based on the CFD model they found the aligned cell monolayers experienced significantly lower spatial gradients.

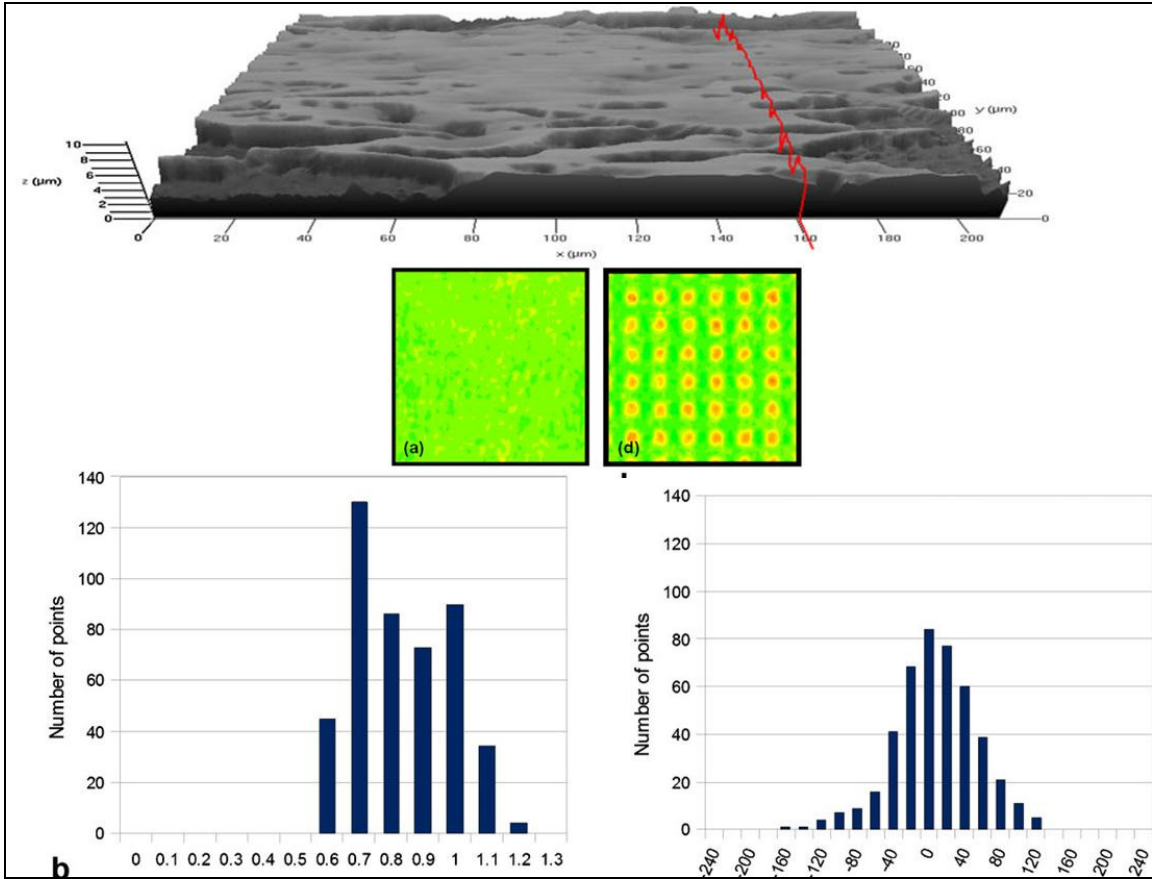


Figure 4.3. Top panel shows a sample topography map, middle panel shows the values of shear stresses and bottom panel shows the histograms of the WSS and WSSG from the CFD model.

This is a typical example of studies that have attempted to combine experimental results with a CFD model in which values such as WSS and WSSG are computed (Figure 4.3). Although it is reasonable to compare EC behavior with hemodynamic calculations from a CFD model, it gets tricky when this kind of comparison is made at such fine scales. In addition to potential resolution problems the experimental data may be accurate, however, errors in such cases can also stem from failing to achieve sufficient numerical resolution and the numerical scheme in the computational model, all of which are required for accurate calculation for higher order derivatives, leading to misinterpretation of both experimental and numerical data.

Steinman et al. (2009) computed WSS, WSSG, time averaged WSS (TAWSS), oscillatory shear index (OSI) and relative residence time (RRT) on 50 different carotid bifurcation models and performed a pairwise Spearman correlation analysis of these indices and harmonic contents. Himburg and Friedman's dominant harmonic (DH) parameter was computed (Himburg and Friedman, 2006). This parameter quantifies the frequency content of shear variations that occur naturally over a cardiac cycle. Correlations with DH were found to depend on how the WSS was defined in the presence of flow reversals. Interestingly, many of these indices were providing the same information about disturbed flow at the normal carotid bifurcation implying that it was sufficient to compute one index that captured the regions of disturbed flow.

While some numerical studies strongly correlate WSSG to disturbed flow regions, others use the CFD tool to compute the WSS and WSSG, and compare them with experiments designed to study the response of EC to varying WSS and WSSG and in some cases these experiments are also subject to the same errors as in the CFD runs. In the next section we will demonstrate the sensitivity of the WSSG measure, and point out some subtle errors that arise from inadequate mesh resolution, and the meshing scheme used. In order to demonstrate this, we have chosen a simple problem of incompressible flow in pipe of elliptical cross-section, where the velocity solution is known analytically. The details of the derivation of WSS and WSSG will be shown and these analytic results will be systematically compared for varying mesh resolutions, and the type of meshing scheme used.

## 4.2. Numerical Experiment: Flow in an elliptical pipe

Consider flow in an elliptical pipe. The walls are rigid and impermeable. It is a pressure driven flow, and the no-slip condition is imposed at the walls. The flow is in the  $z$ -direction. This is represented in the schematic below.



Figure 4.4. Schematic of flow in an elliptical pipe

$U_z$  is the axial velocity and  $b$  and  $a$  are the minor and major axis respectively. The reference coordinate system is also shown in figure 4.4

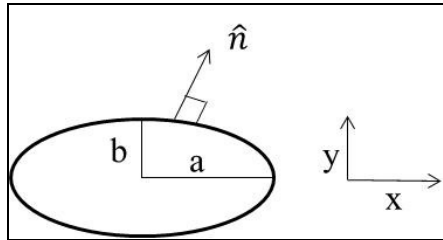


Figure 4.5. Schematic of the cross-section.

The analytic value of  $u_z$  is given by

$$u_z = c \left( 1 - \frac{x^2}{a^2} - \frac{y^2}{b^2} \right), \quad (4.1)$$

where 'c' is given by

$$c = - \frac{\left( \frac{1}{2\mu} \right) \frac{dp}{dz}}{\left( \frac{a^2 b^2}{a^2 + b^2} \right)}, \quad (4.2)$$

where  $\mu$  is the viscosity and  $dp/dz$  is the pressure gradient driving the flow.

From the equation of the ellipse

$$f(x,y) = (x^2/a^2 + y^2/b^2 - 1), \quad (4.3)$$

we can determine the gradient,

$$\nabla f = \frac{2x\hat{i}}{a^2} + \frac{2y\hat{j}}{b^2}, \quad (4.4)$$

and thereby obtain the unit normal,  $\hat{n}$ , which is given by,

$$\hat{n} = \frac{\frac{2x\hat{i}}{a^2} + \frac{2y\hat{j}}{b^2}}{2\left(\frac{x^2}{a^4} + \frac{y^2}{b^4}\right)^{\frac{1}{2}}}. \quad (4.5)$$

The dot product of the symmetric part of the strain rate tensor and the unit normal will then give the WSS,

$$WSS = \frac{1}{2}(\partial_1 u_3 n_1 \hat{k} + \partial_2 u_3 n_2 \hat{k}), \quad (4.6)$$

where  $\hat{k}$  is the unit vector normal to  $\hat{n}$ . By differentiating eqn (4.1) with respect to  $x$  and  $y$ , and substituting in equation 4.6, we get,

$$WSS = -2\mu c \left(\frac{x^2}{a^4} + \frac{y^2}{b^4}\right)^{\frac{1}{2}}. \quad (4.7)$$

To get the WSSG, we now need the other unit vector  $\hat{k}$ , tangential to the surface, but still perpendicular to the unit normal  $\hat{n}$ . That is obtained by the vector cross product of  $\hat{n}$  and  $\hat{k}$ . By doing that we get,

$$\hat{k} \times \hat{n} = -\frac{\left(\frac{2x\hat{j}}{a^2} + \frac{2y\hat{i}}{b^2}\right)}{2\left(\frac{x^2}{a^4} + \frac{y^2}{b^4}\right)^{\frac{1}{2}}}. \quad (4.8)$$

If WSS is denoted by  $s$  then,

$$\frac{\partial s}{\partial x} = -2\mu c \left(\frac{x}{a^4}\right) \left(\frac{x^2}{a^4} + \frac{y^2}{b^4}\right)^{\frac{1}{2}}, \text{ and} \quad (4.9a)$$

$$\frac{\partial s}{\partial y} = 2\mu c \left(\frac{y}{b^4}\right) \left(\frac{x^2}{a^4} + \frac{y^2}{b^4}\right)^{\frac{1}{2}}. \quad (4.9b)$$

And, since the gradient is tangential to the surface, the final formulation of the WSSG is given as,

$$\frac{\partial s}{\partial x} \cdot n_x = -4\mu c \left(\frac{xy}{a^4 b^2}\right) \left(\frac{x^2}{a^4} + \frac{y^2}{b^4}\right), \text{ and} \quad (4.10)$$

$$\frac{\partial s}{\partial y} \cdot n_y = 4\mu c \left(\frac{xy}{a^2 b^4}\right) \left(\frac{x^2}{a^4} + \frac{y^2}{b^4}\right). \quad (4.11)$$

Equations 4.7, 4.10 and 4.11 are the analytic solutions for WSS and WSSG for a flow in an elliptical pipe. These values were computed and were compared against Fluent generated results for various meshes. In the next section some of the key results from the simulations will be discussed.

### 4.3. Numerical Analysis

Of all the tasks in CFD modeling, mesh generation remains among the most difficult. Although a great deal of research has been performed on mesh generation, it still remains a bottleneck in the modeling process, especially for 3D analysis. The fact that no

completely robust solution has been found for unstructured meshing of complex 3D geometries is reflected in the fact that many potential mesh structures exist for the same solution.

The difficulty in using structured meshes is that an extremely large number of mesh elements must be used to obtain good results, which often requires specialized equation solvers that are not available in commercial codes. Thus either approach has its drawbacks. For simple geometries, a structured grid or hexahedral meshing scheme is typically preferred, as a structured grid has higher accuracy, while a tetrahedral meshing scheme or unstructured grid is preferred for more complex geometries as fewer skewed elements exist; however accuracy is compromised when using such a scheme. Figure 4.6 shows a cross section of the ellipse taken at the developed flow region. Note that magnified images of these plots can be found in appendix C. Note the different meshing schemes that have been used to define the computational domain of the elliptical pipe.

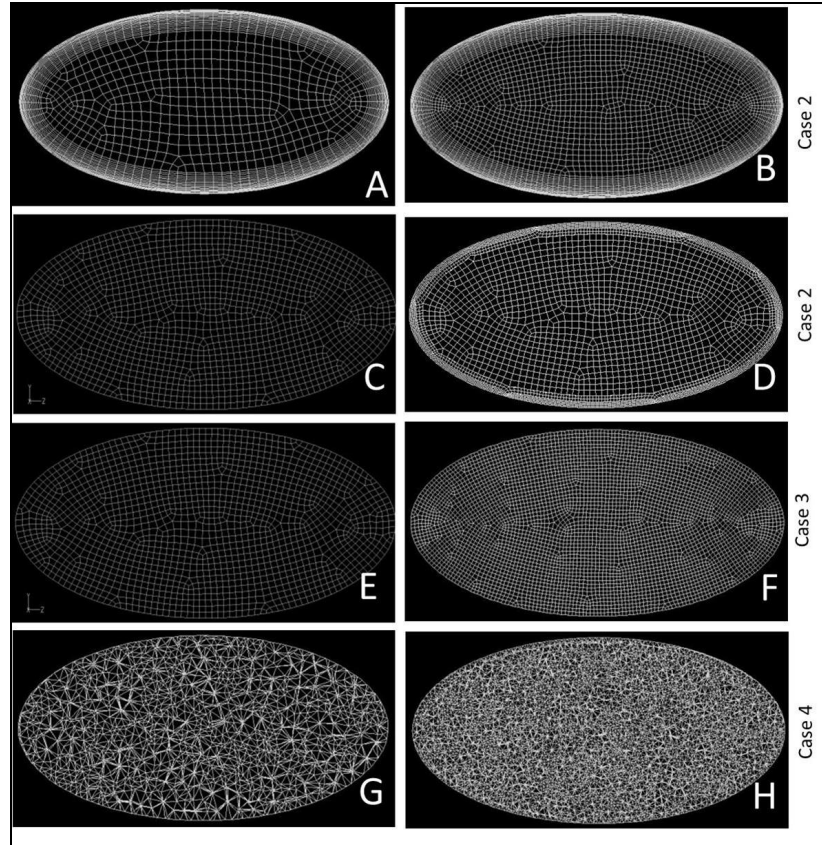


Figure 4.6. Shows different meshes used in the numerical experiment. Case 1(A, B) is the structured mesh with progressively refined boundary layer mesh. Case 2 (C, D) shows hexahedral meshing scheme, but adaptive mesh refinement has been used. Case 3(E, F) shows progressively refined hexahedral elements. Case 4(G, H) is progressive refinement of tetrahedral meshing scheme without the boundary layer mesh.

A combination of structured mesh with boundary layer mesh (BL) is considered the most stable and accurate meshing scheme for numerical calculation. BL meshes are typically used for regions close to a wall (Figure 4.6 A, B). They are highly refined prismatic elements that improve the resolution of the sharp gradients observed near the boundaries. In order to increase the efficiency and optimize the mesh refinement issues, there is another meshing scheme that utilizes the flexibility of the tetrahedral/hexahedral meshing scheme without compromising the accuracy and that is called the adaptive meshing scheme (Figure 4.6 C, D). In this case, first the solution is calculated on an approximate coarse mesh, and regions of highest gradients of critical flow variables, such

as WSS in this case, are noted. Mesh refinement is only done at the regions where sharpest gradients exist. However, one big disadvantage is that mesh refinement done at the boundaries still uses tetrahedral elements as opposed to the structured prismatic elements that one can manually insert using BL scheme, which would mean that the required accuracy may not be achieved. Next, is the structured grid (Figure 4.6 E, F), without the use of a boundary layer mesh and progressive refinement to account for the errors that could happen at the boundaries.

Table 4.1: Details of meshing scheme and refinement procedure and computational costs and times of all the cases run for the numerical experiment.

Meshing Scheme	Methodology	Mesh refinement	Computation Cost and Time
Case 1 Hexahedral Elements with Boundary Layer Mesh	15 layer prismatic elements	240,000 500,000 700,000	Steady case (16 processors) 2hrs 3hrs 4hrs
Case 2 Adaptive Hexahedral 240,000 mesh	Grid adaption at the wall for WSS	Adapted to 700,000 1 million	Steady case (16 processors) 4hrs 8hrs
Case 3 Hexahedral Elements	Progressive refinement	215,000 750,000 2 million	Steady case (16 processors) 2hrs 4hrs 10hrs
Case 4 Tetrahedral Elements	Progressive refinement	215,000 750,000 2 million	Steady case (16 processors) 2hrs 4hrs 10hrs

This is not as effective because to resolve the gradients near the wall would require highly refined mesh, and that would eventually lead to high computational costs. The next is the unstructured tetrahedral meshing scheme. Not only is the accuracy compromised, without the use of boundary layer mesh, one is not entirely sure of the accuracy of the values at the boundaries. However, one big advantage that this scheme offers is the significantly increased flexibility associated with meshing highly complex geometries. Table 4.1 shows details of each of the cases mentioned above and their

computational times. In figure 4.7, plots of WSS computed from the numerical solution are compared against the analytical solution for all the cases shown above. It can be seen that sufficient convergence in WSS is achieved even at the lowest mesh resolution, where approximately 240,000 elements (structured and unstructured) have been used; the error ( $L - \text{infinity} = \max |e_{\text{exact}} - \text{numerical}|$  from  $i = 1$  to  $N$ ,  $N$  being the number of grid points) from the meshing schemes is less than 5% (unstructured tetrahedral meshes). In the case of tetrahedral meshes, the plots are a little scattered, but this is to be expected since it is an unstructured grid.

Most of the studies mentioned in the earlier section either use velocity data for their convergence tests or use WSS data. Going by the results shown above, one might conclude that convergence has been achieved for all the different mesh schemes used, and thereafter proceed with further analysis to compute variables such as WSSG. In figure 4.8, convergence plots based on WSSG are shown and are compared against the analytic solution for WSSG (eqns. 4.10 and 4.11). 4.8a shows comparison of analytic solution of WSSG with structured BL containing 240,000, 500,000 and 700,000 elements respectively. Note how even the coarsest mesh shows convergence for WSSG. However there is an exception at certain localized zones (shown by arrows) where there is a sudden increase in the WSSG values.

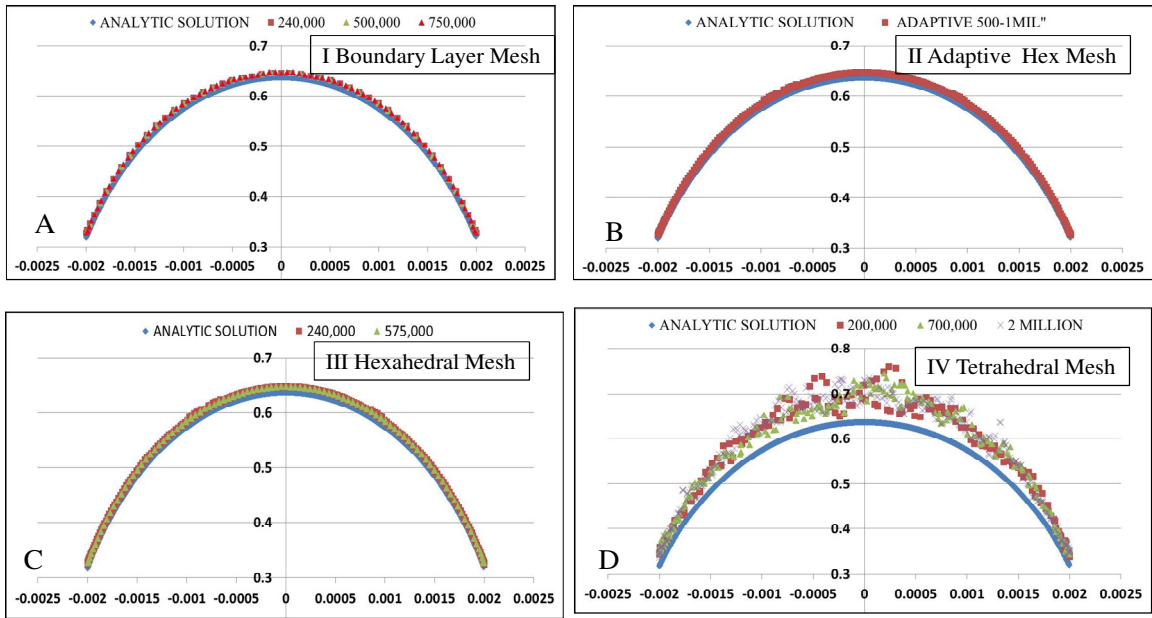


Figure 4.7. Plots A, B, C, D show WSS plots at the circumference of the CS plot shown above for all the Case 1, 2, 3 and 4.

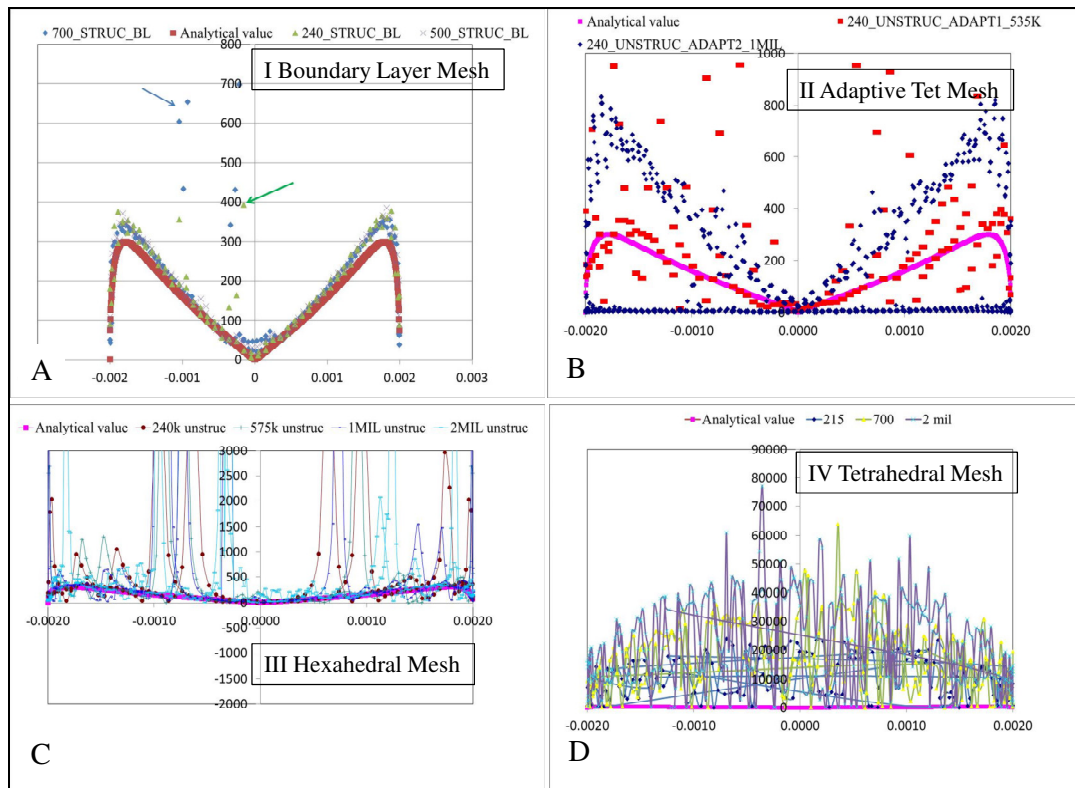


Figure 4.8. Shows convergence plots of WSSG and their comparison with the analytic solution. A,B,C,D are for four cases respectively. Zones of maximum error for BL mesh are indicated by arrows.

Figures 4.8b and 4.8c show really high values of WSSG and do not show any indication of convergence. This could be because of the lack of BL at the boundaries to resolve for the sharp gradients. In addition, figure 4.8c uses an unstructured mesh and is prone to errors generated at the grid near the boundaries. This is particularly intriguing since the WSS obtained from all the meshes is a very smooth function and one would expect a similar trend in WSSG as well. Velocity is a smooth function, and its gradient, although prone to some distortion is still expected to be smooth. However computing the additional gradient of a gradient tends to augment the noises in the data leading to some artificial values as in the case of unstructured mesh. Noise levels always increase in numerical computation of derivatives. In order to avoid this amplification of errors, an adaptive grid meshing was used at the boundaries where gradients of WSS were highest. Coarsest mesh where the WSS converged was used. In this case it was at 500,000 elements. After the solution was obtained, using the built-in algorithm in the software, regions of sharpest WSS gradients were identified and those regions were progressively refined with a tolerance of  $1e-07$ . As a test, a tolerance of  $1e-09$  was also used but that also yielded the same regions as the previous tolerance, and further refinement was not possible. Such a mesh (shown in Figure 4.6), produced fairly reasonable values of WSSG although convergence was hard to quantify even at a resolution of 2 million elements. This implied that the maximum capability of the software to resolve the gradients with the current scheme was highly limited.

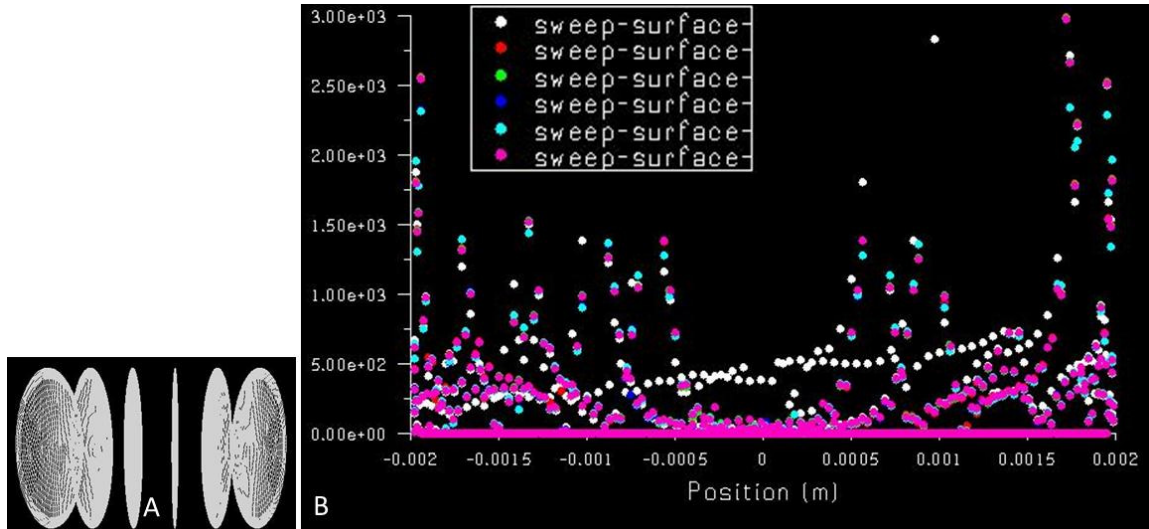


Figure 4.9. (A) shows cross sections along which the WSSG was plotted. (B) plot showing convergence in the axial direction.

To double check, for the unstructured adaptive grid, for any indication of convergence in the axial direction, WSSG was plotted at four cross sections (Fig 4.9). With the exception of very few points, there was indeed convergence in the axial (x-direction) of the grid. This led us to believe that for an unstructured grid more refined algorithms may be required to capture the gradients in the radial direction where sharp changes in both velocity and WSS values are observed.

From these results, we understand that WSSG data obtained from the numerical calculations show there is neither spatial convergence nor any similarity between the trend followed by the analytic solution and the numerically computed solution. In fact, for an unstructured mesh without any BL or adaptive meshing, by mere progressive refinement even till 4 million nodes, errors are only further amplified.

Several studies have demonstrated the effect of WSSG on EC, and used it as a basis to correlate that to the aneurysm formation using commercially available CFD codes. However based on these results, it is hard to predict the WSSG trend based on numerically computed values. A similar result is shown for the arterial geometry in figure

4.10. Contours of WSSG are plotted on a real arterial geometry where an aneurysm eventually formed. Regions of low WSS are seen at the location of eventual aneurysm formation; in addition high WSSG are also present. At first look, the plot of the contours of WSSG would appear to suggest sharp changes in the WSS at the location of eventual aneurysm formation; however it is very uncertain, based on the analysis here, if the magnitude as well as the spatial patterns would indeed reflect the true nature of the spatial variations in WSS.

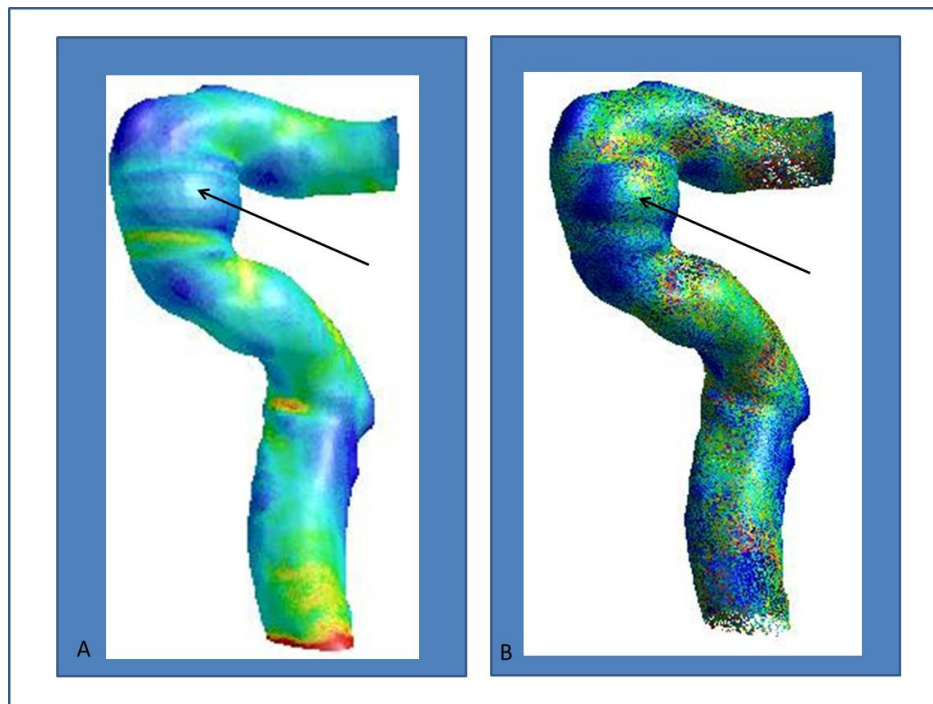


Figure 4.10. (A) Contours of WSS for sidewall case 1 (B) contours of WSSG. Arrows indicate where aneurysm eventually formed. Unstructured meshes with adaptive mesh refinement were used. About 2 Million tetrahedral elements were used to define the computational domain.

#### 4.4. Other issues with WSSG

In addition to the numerical issues with computing WSSG, there are even more complex issues pertaining to simulating flow at the regions where the aneurysm has been artificially removed:

1. The methodology of image acquisition, and the resolution issues associated with it. Low resolution scans can add significant noise and image artifacts.
2. The image development and reconstruction procedures that are used to convert the data obtained from the scans and convert them into a format that can then be imported in the grid generation software generate additional errors.
3. In some studies, where the aneurysm is artificially removed, the process of the arterial reconstruction involves speculation and modeling of the details of the pre-aneurysmal geometric details which can significantly change WSSG.

In this section we will systematically address each of the points discussed above. The most commonly used method for real patient specific data acquisition is 3D-DSA (discussed previously in chapter 1). However, this frequently used method does not have sufficiently high resolution to capture the finer ridges (example figure 4.3a) seen in the arterial wall. These ridges at very fine scales tend to affect the EC behavior when exposed to WSSG and to a lesser extent even WSS. However, such high resolution scans are not clinically feasible as they pose risk to the patient health due to exposure time and radiation. So in effect the best available current modality is indeed the C-arm images. As mentioned earlier, WSSG are very sensitive to the topography of the vessel wall generating very large values near the ridges. However, this effect is reduced in the case of WSS since one less spatial derivative is involved. In light of this, it would be easier and more reliable to use WSS, as opposed to its gradient which may not entirely capture the effect of ECs in the numerical simulations. Figure 4.11 shows a comparison of various resolution and image acquisition techniques for a stent inserted in a PTFE pipe (Ionescu et al., 2011). Note the quality of image obtained for each methodology used.

Illustrated in figure 4.11, Micro-CT provides the highest quality image for which the image reconstruction procedure would involve much smaller noise related errors and motion artifacts. In comparison the MS-CT image is blurry and reconstruction and pre-processing will add more errors. In fact, it is difficult to distinguish between the two planes in figures 4.11a and b, and one cannot be certain of the geometry of the stent struts.

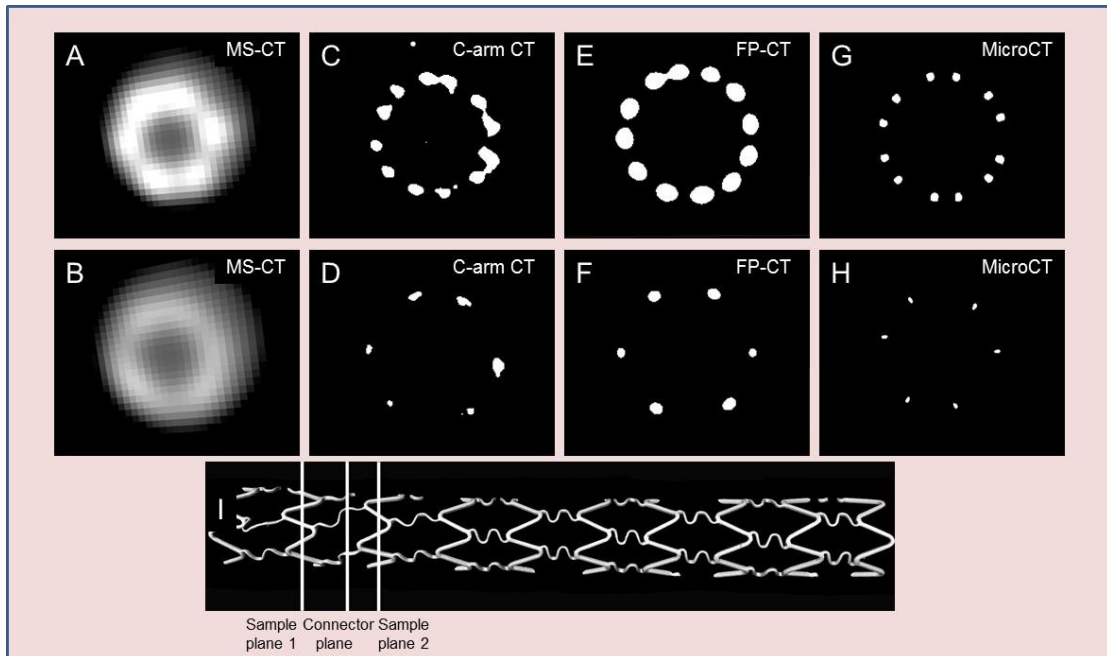


Figure 4.11. Image acquisition through MS-CT, C-arm CT, FP-CT and Micro-CT at two sample planes (near the struts and at the connector plane).

Antiga et al. (2008) developed a novel model for automating the reconstruction and segmentation obtained from the 3D-DSA. They proposed an integrated framework that allowed image segmentation, pre-processing and meshing in a streamlined way.

They aimed at satisfying the following criterion:

1. Minimizing operator intensive tasks, while allowing framework to retain flexibility.

2. Favoring high-level decisions, such as specification of vascular segments through selection of fiducials at their end points followed by automated segmentation.
3. Reducing the number of free parameters that need to be specified at each interval.

In short, they noted that operator related errors are unavoidable, and thus attempted automating the entire process, reducing the errors generated through manual thresholding. As effective as this procedure of arterial segmentation may seem, there is still not a rigorous way to validate it. For example, figure 4.12 (Ionescu et al., 2011) shows the results from the CFD simulations performed on the stent images acquired from the FP-CT and Micro-CT modality. After segmentation and pre-processing the stent image data (see figure 4.11), CFD simulations were performed. The segmentation was done using Amira. The panel on right (Figure 4.12) shows the final images. Note the sharper image reconstruction obtained from the Micro-CT scan. Interestingly, this could be used as a reference for the segmentation for the images obtained through other techniques. In spite of the advantage, note that the image obtained through FP-CT has thicker struts, and a rough interior as a consequence of image artifacts. However, the contours of velocity (right panel, figure 4.12) are relatively similar for both cases away from the wall. If velocity was used as a criterion for successful image segmentation then it would indeed be misleading. The bottom panel shows the contours of WSS for both FP-CT and Micro-CT scans.

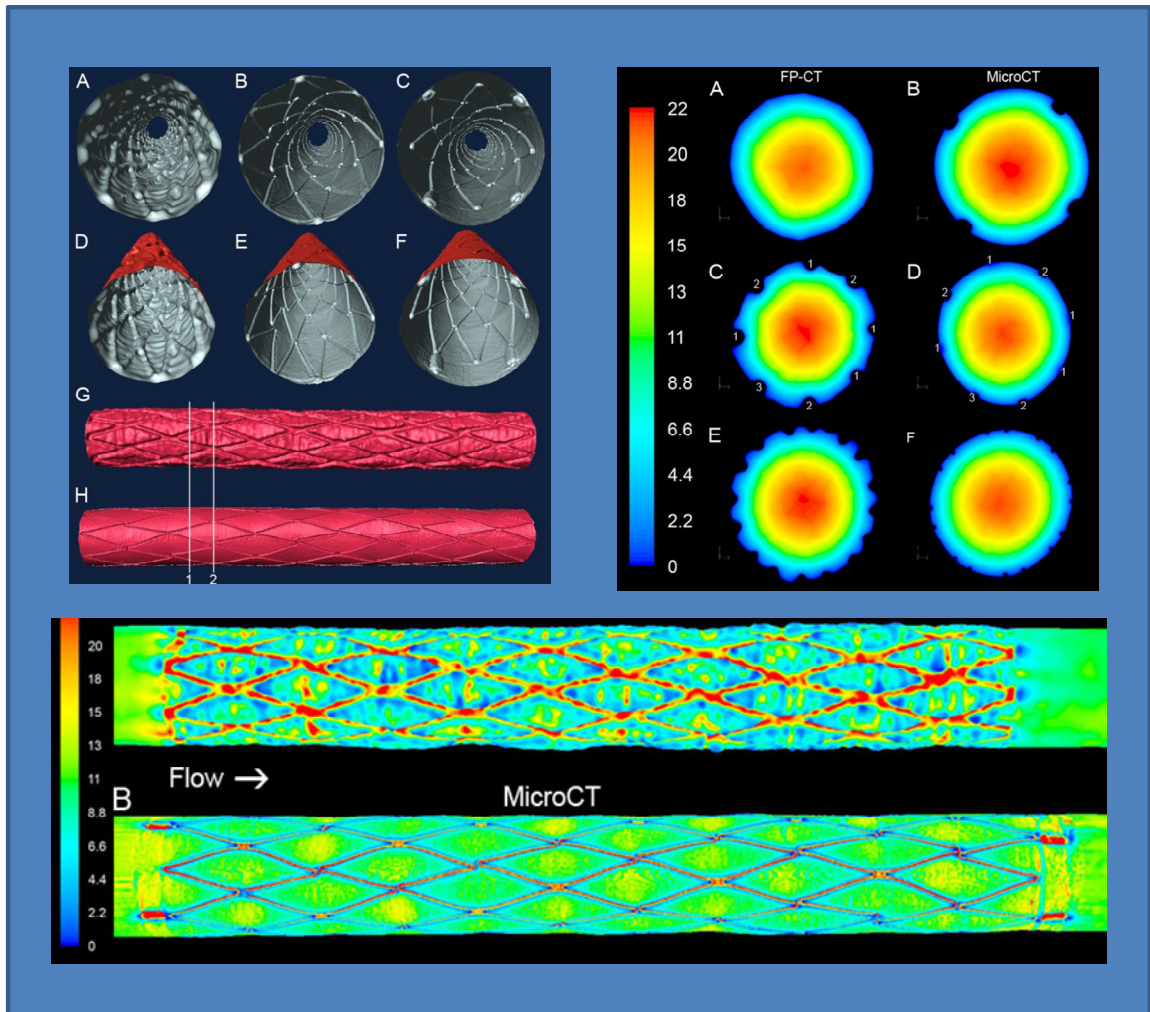


Figure 4.12. Right panel shows magnified image after pre-processing in Amira. Left panel shows contours of velocity. Bottom panel shows contours of WSS for FP-CT and Micro-CT respectively.

It is very clear from this result, how the values of WSS are significantly overestimated in the case FP-CT image, while the WSS are fairly smooth and lower for Micro-CT. WSSG calculations based on FP-CT would be clearly substantially incorrect and highly misleading in this case.

Karmonik et al. (2006) were the first to come up with a smoothing and excision algorithm that artificially removed the aneurysm from the parent artery. The first step in the numerical aneurysm excision procedure was to convert the 3D digital subtraction angiograms into a special format that allowed a quantitative determination of (a) the

aneurysm volume and surface area, and (b) the neck angle (which gives a measure of the extent to which the diameter of the artery extends into the aneurysm). Clinical 3D DSA images were obtained by our collaborators at the Methodist Hospital/Baylor College of Medicine. Three-dimensional projections were used to obtain the orientations of the parent artery and the aneurysm. Subsequently, a set of successive 2D cross-sections were obtained using image reconstruction. These were imported in a suitable format for post-processing. The parent artery was reconstructed at each cross-section by first identifying the boundary points of the lumen. The center of the cross-section was calculated by computing the geometrical centroid, and the arterial radius was obtained by taking the average of all the segments connecting the boundary points to the centroid. This procedure was applied to the cross-sectional planes not containing the aneurysm. For a cross-section containing the aneurysm ostium, a region of interest was defined that contained only those points that belonged to the normal arterial wall and were within a certain radius threshold, determined from the radius of the previous cross-section.

A singular value decomposition algorithm was then used to find the arterial center for this section. The radius of the artery was determined as the average distance of this center point to the reduced set of boundary points. Iteratively applied to all remaining cross-sections, this algorithm determined the center and radius of the artery along the lateral extension of the aneurysm ostium. To determine the neck angle of the ostium, the algorithm traversed the boundary points in an ordered fashion and checked if the distance between a point and the center of the artery exceeded a certain threshold value. The identification of such a location marked one extent of the aneurysm ostium. The algorithm continued to traverse the boundary points until it encountered a distance value

lower than the threshold value. This location defined the other extent of the ostium. This procedure enabled the identification of the two extremal points of the ostium.

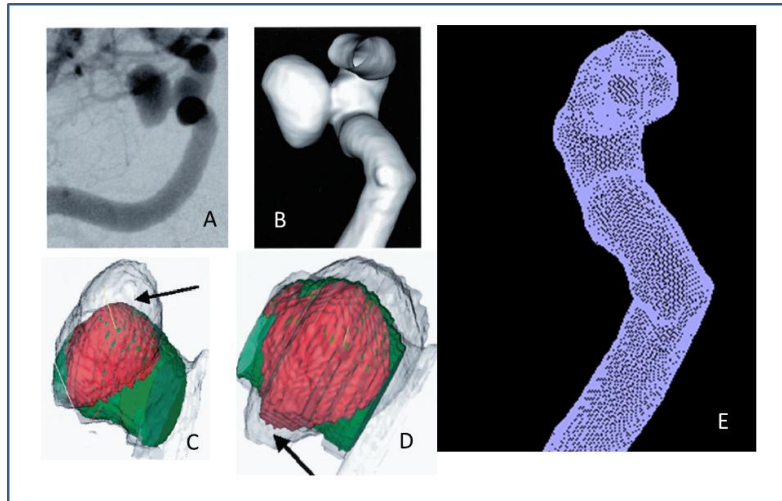


Figure 4.13. Case-I (A) 3D-DSA image directly obtained from human patient. (B) 3D surface reconstruction showing a large side-wall aneurysm. (C,D) Two views showing the reconstructed artery (green) and ostium surface (red) superimposed on the original DSA image. (E) Final mesh of the geometry after excision.

The difference in the angles of these two boundary points was defined as the neck angle (percentage parent artery involvement by the ostium) of the aneurysm. The resulting excised geometries of the aneurysms considered in this study as well as in my M.S. thesis (Mantha 2006) are shown in figures 4.13.

Ford et al. (2009) presented an automated technique (based on Antiga et al., 2009), to digitally remove the aneurysm and reconstruct the parent artery, based on lumen geometries segmented from angio-graphic images. They relied on robust computational geometry concepts, the Voronoi diagrams, of the digitized lumen surface. First, the aneurysm attachment region is defined using the lumen centerlines, and these centerlines are then replaced by smooth interpolations. These interpolations further guide the interpolation of the Voronoi points within the attachment region. Combining these

Voronoi points from outside the attachment region, the parent artery lumen without the aneurysm is constructed. They claimed that images obtained from this procedure were within the uncertainty of the digital reconstruction itself. However, by using an automated technique, it was possible to have a broader platform to systematically quantify aneurysm morphology.

An important issue with the two methods outlined above is that there is no standard way to validate if this reconstruction is correct. It remains unknown if the new parent artery actually resembled the actual pre-aneurysm environment. Due to resolution errors, it is not easy to identify the smaller vessels, and if they belong to the aneurysm. Both the techniques rely on a relatively smooth starting surface (which is not true in most cases), to avoid propagation of spurious surface features along the reconstructed segments. This would significantly affect the calculation of WSSG (as opposed to WSS) as WSSG can be very sensitive to topology features. However, one cannot say with confidence which surface features originally belong to the lumen and which arises from the image acquisition and segmentation and artificial excision of the aneurysm, and these affect the values of WSS to an extent and WSSG to a much greater extent. Smooth interpolations may give unrealistic WSSG values if original endothelin was rough.

Based on the results shown in this section, it is clear that WSSG is complex hemodynamic variable, whose computation is highly susceptible to significant error. Users must exercise their judgment when using this quantity to understand EC behavior. The computation of this variable depends highly on the meshing scheme, the resolution, and modality of image acquisition, segmentation procedure and, in some cases, the algorithm of artificial excision of aneurysm.

## Chapter 5

### 5. Waveform Analysis

Over the last two decades, many groups have attempted to study blood flow waveforms with an aim of understanding disease progression. More realistic simulations are now possible of blood flow in the arteries in order to understand the pathogenesis of flow associated diseases such as atherosclerosis, and more recently of abdominal and cerebral aneurysms. Nagamoto et al. (1992) were the first to study the blood flow velocity waveform in the common carotid artery (CCA), from 99 older adults who had history of either a cardiovascular or orthopedic disease. They classified the waveforms into five types on the basis of the ratio of diastolic to systolic velocity. The key parameters they analyzed were the blood flow volume (ml/min), velocity (cm/s), and heart rate (beats/min) in the right and left CCA. Measurements were taken in both supine and sitting positions. No significant difference in heart rates between the two positions was observed. Total blood flow volumes and mean blood flow velocities fell nearly in direct proportion to the blood flow velocity waveforms in both positions. This suggested that blood flow velocity waveforms correlated with total blood flow volume and mean blood flow velocity.

Holdsworth et al. (1999) characterized flow in the common carotid artery of 17 healthy young individuals. None of the subjects had any history or indication of cardiovascular disease. Two Doppler measurements on the left and right carotid of each of the 17 subjects were taken at 40 minute intervals. They then characterized the waveform based on maximum velocity, point of maximum systolic acceleration and

frequency content; the eventual flow waveform was calculated from the Wormersley solution (Wormersley 1955). The resulting waveform was an ensemble average of the 68 data sets thus collected. Although the results were a good approximation to an average healthy person waveform, they did not reflect the waveform of an aged or a diseased person.

Azhim et al. (2006, 2007) developed a Doppler based telemetry system that enabled simultaneous and synchronized measurement of flow in three different arteries. With this, they were able to acquire flow data of healthy young and older adults, and were able to quantify the positive effect of exercise on the change in the shape of waveform. In addition they were able to show differences in the waveform shape due to gender. However, these differences were not significant.

Yimmen Hoi and Steinman (2010) were among the first to study the internal, external and common carotid artery waveforms in both young and older adults. This time considerable differences in the female older adult vs. male older adult were shown. This could be due to the difference in the tone of the arterial wall changed as a result of post-menopausal changes that happen in women, thereby altering the shape of the waveform.

Kozo and Hirata et al. (2006) also studied the age related variations in the flow waveform of the CCA. 56 healthy subjects from age 22 to 72 years were chosen, and their distension pressure and velocity waveforms were recorded non-invasively and simultaneously from the CCA. Pressure augmentation Index (PAI) was defined as  $(P_1 - P_0)/(P_2 - P_0)$  and Flow Augmentation index (FAI) as  $(V_{sr} - V_{ed})/(V_s - V_{ed})$ . A very good correlation was seen between the velocity and distention waveforms, as well as FAI and

PAI. Changes in the indices due to age were observed, reflecting the biophysical wear and tear of the artery due to aging.

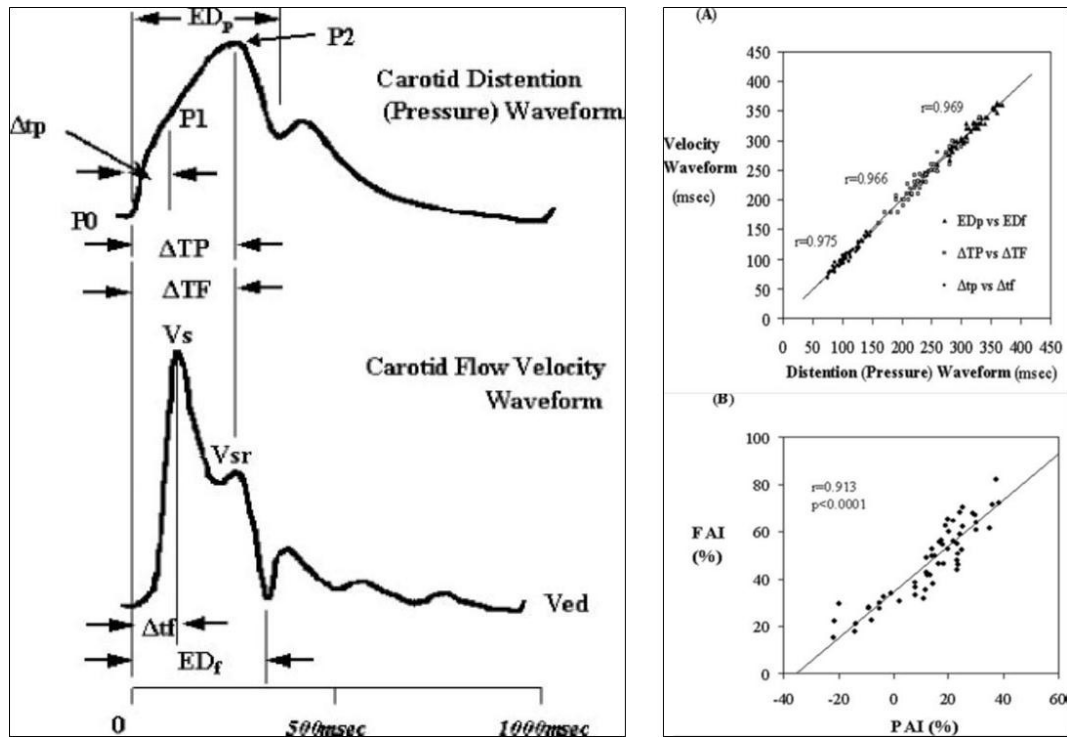


Figure 5.1. Left panel showing pressure and velocity waveform. Right panel shows correlations between velocity and pressure and FAI and PAI.

Based on these studies, blood flow waveform shape can be characterized by its pulse period, peak systolic velocity, end diastolic velocity, slope of acceleration and deceleration, occurrence of Dichrotic notch (a small rise in the velocity during the deceleration phase), and the second peak velocity (at the Dichrotic notch) (Figure 5.2). Thus these features greatly depend on the location of the artery in the vasculature, tone of the arterial wall, and presence of any cardiovascular disease. In addition, the waveform shape is greatly affected by the aging process. Arterial stiffening that occurs due to ageing, results in key changes in the shape of the flow waveform. These are summarized in the table 5.1, below.

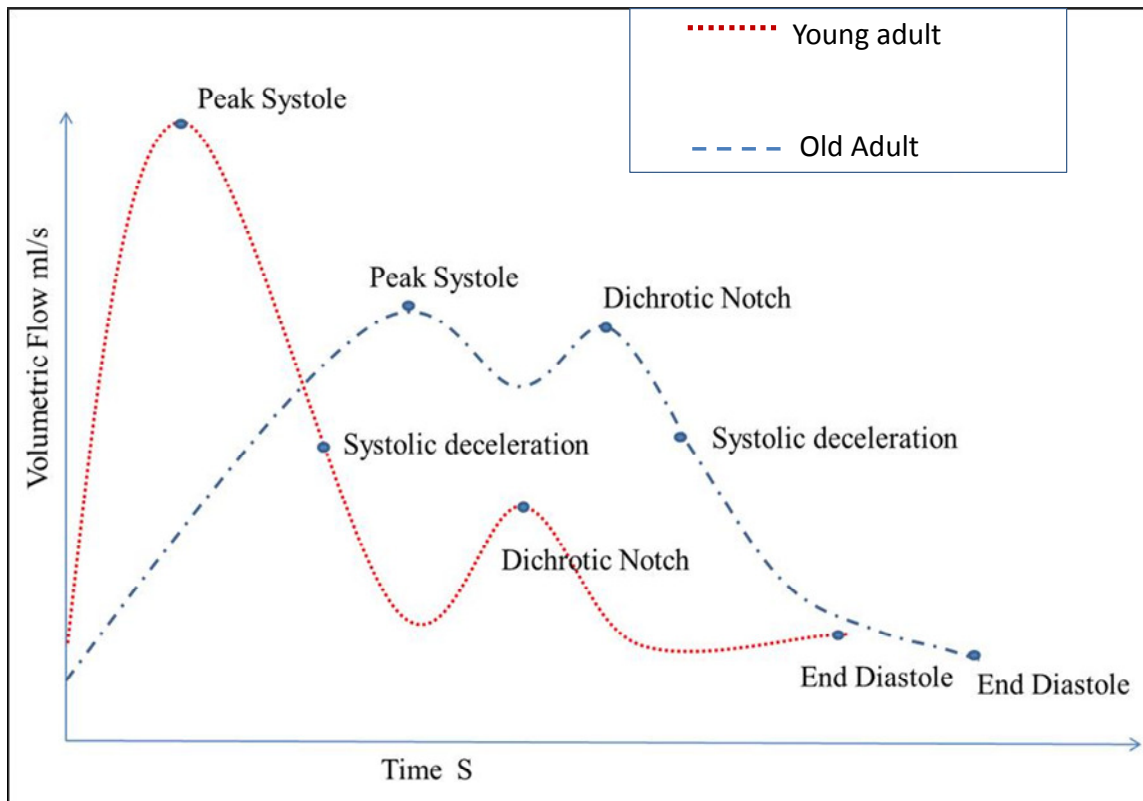


Figure 5.2. A schematic of flow waveform for an old and young adult depicting the key points in the cardiac cycle.

Table 5.1: Key features differentiating old vs. young adult waveform.

Younger Adult (<56)	Older adult (>56)
Higher systolic and diastolic velocities	Decrease in the systolic and diastolic velocities
Late occurrence of Dichrotic notch during the systolic deceleration	Early occurrence of Dichrotic notch after peak systole
Steeper systolic deceleration curve	More blunt systolic deceleration curve.
Change in Heart Rate due to postural change	No significant changes in the HR due to postural change.

In the following sections, we analyze in detail the effect of the differences in the key parameters (shown in figure 5.1) on AFI for sidewall aneurysm case 1 (Figure 3.1 A). The change in the parameters is made to reflect in the waveforms old vs. young adults, and effects of this change on the AFI are noted. Two important points are investigated:

1. The robustness of the indicator
2. Changes in hemodynamic behavior in response to critical changes in the waveform.

Our study focuses on capturing the changes in the key hemodynamic variables, such as the velocity fluctuations and WSS due to aging and correlates these to the biophysical responses that could lead to the initiation of cerebral aneurysms. Therefore, we focus primarily only on the internal carotid artery waveform, obtained from literature representing the waveform of an older adult. Three sidewall aneurysm geometries, where the aneurysm is computationally removed to emulate the environment of the artery before the aneurysm formed, are studied. The analyses are not specific to one geometry whose results have been shown, but generic to all the three geometries analyzed.

## **5.1. The Characteristic Idealized Waveforms**

Based on the brief review presented above, the slope of deceleration differs vastly between aged vs. young adults; the deceleration slope becomes increasingly blunt with age. In these waveforms, the peak velocity, end diastolic velocity and total time period have been kept the same; only the deceleration slope has been modified, to see how this affects the hemodynamic variables (Figure 5.3).

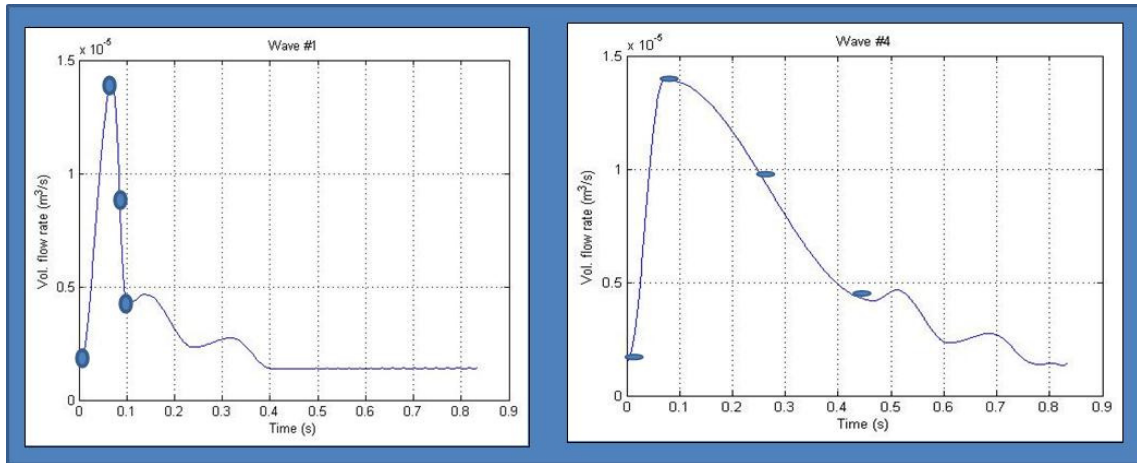


Figure 5.3. Two characteristic waveforms, with different deceleration slope, Wave1 and Wave 4 respectively. The blue circles indicate the important phases in cycle where the results are plotted.

The peak velocity, and end diastolic waveforms are based on a common carotid waveform generated by Ku et al. (1985). The values have been scaled to reflect the flow in the internal carotid artery. Note that these waveforms are not patient specific, but modified in order to simplify the analysis. In wave 1, the deceleration may appear to be steep; however, it would somewhat reflect the waveform of a healthy young individual who exercises regularly. This will be discussed in detail in the following sections. Wave 4 would be typical of an older healthy adult. We will systematically look at various hemodynamic variables like velocity vectors, WSS, WSSG as well as AFI.

Before presenting the results on the secondary flow, we briefly discuss flow in a curved arterial segment, shown in Figure 5.4. As the fluid passes through the curved arterial segment, centrifugal forces push the fluid radially outwards within the tube, resulting in the originally one-dimensional velocity field becoming two-dimensional, with a wall-normal (secondary) flow component. This results in the transport of high-momentum fluid from the arterial centerline towards the outer wall, as well as the transport of low momentum fluid from near the inner wall towards the centerline.

Consequently, the profile at station BB' is deformed from parabolic and acquires a shape similar to that shown in the figure. Note that the streamlines passing close to the inner wall move away from the inner wall and approach the outer wall. Contrarily, near the outer wall, streamlines tend to converge towards one another. There is an adverse contribution to the axial pressure gradient near the inner wall, and a favorable contribution to the axial pressure gradient near the outer wall. If the curvature is sufficiently large, the total pressure gradient along the inner wall can actually become adverse; further, if the adverse pressure gradient is sufficiently large, it can induce flow separation at the inner wall (as shown in the figure). If separation does occur, it creates a region of low and/or reversed WSS.

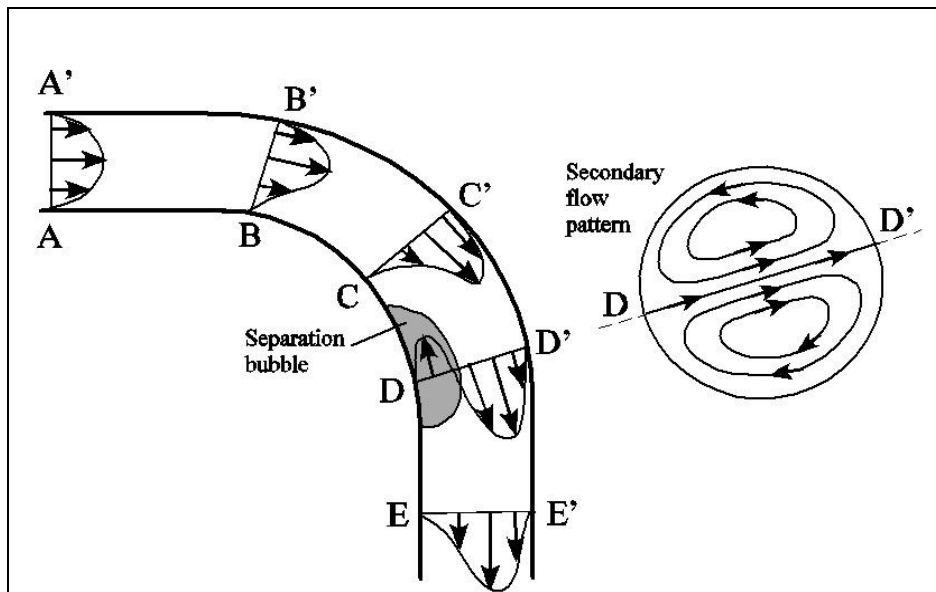


Figure 5.4. Schematic of flow pattern and associated pressure and WSS distributions relevant to arterial hemodynamics: flow in a curved tube.

Associated with these trends the axial flow profiles is the development of secondary flow in the cross-sectional plane, as illustrated at station DD' in the figure. The radially

outward flow induced by curvature impacts the outer wall and is deflected to form two counter rotating eddies.

Figure 5.5 shows contours of velocity magnitude overlaid by secondary flow vectors at the key phases of the cycle, namely: end-diastole (ED), peak systole (PS), systolic deceleration 1 (MSD1) and systolic deceleration 2 (MSD2) for wave 1 and 4 respectively. The cross-section is taken at the location where the aneurysm eventually formed (shown by the inset).

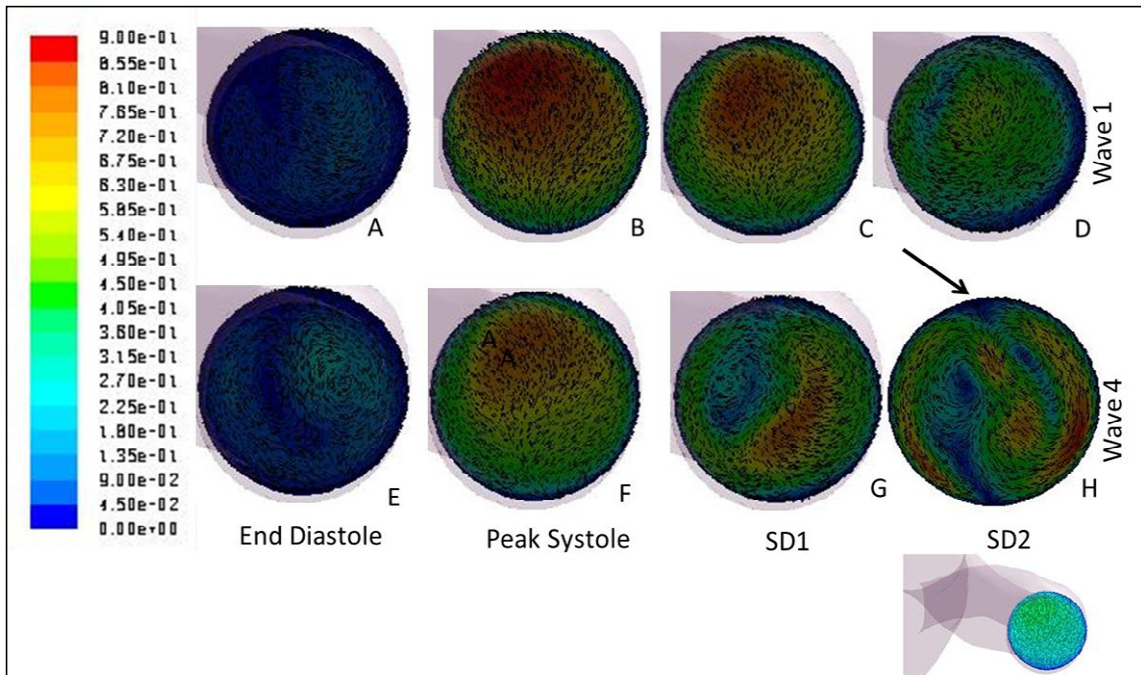


Figure 5.5. Contours of velocity magnitude overlaid with secondary velocity vectors for wave1 and wave 4 taken at ED, PS, and MSD1 AND MSD2 respectively. Inset shows the location of the cross-section. Stagnation zone is shown by the arrow.

Due to the curvature of the artery, strong secondary flow developed at the outer bend of the arterial wall which also coincided with the aneurysm location. Figure 5.5e, shows formation of two eddies at the location. These eddies are more structured for wave 4 compared to wave 1. These counter-rotating eddies get flushed at peak systole and flow is

mostly dominated by the axial flow as shown by figures 5.5b and 5.5f. However, during the deceleration, due to an adverse pressure gradient, the counter-rotating eddies form again, and continue to persist till the end of the cycle as shown in figures 5.5g and h. Note that the aneurysm site is located very close to the stagnation point, where the radially-directed component of the secondary flow impacts the outer arterial wall. Interestingly, the pressure drop in wave 1 is quite abrupt and diastolic flow resumes immediately and persists until the next peak systolic acceleration. This sudden drop does not give enough time for eddies to develop and persist through the cycle, as shown in Figure 5.5c and 5.5d. That is, the secondary flow attains maximum strength during the deceleration part of the systole, and it is particularly larger for Wave 4 than for Wave 1, i.e for wave 4 the secondary flow was greater than 60% of axial flow during systolic deceleration while for wave 1 it was about 50% of the axial flow. This is because during systolic deceleration a fluid particle is subjected to an adverse pressure gradient and required to reduce fluid velocity; the adverse pressure gradient in turn promotes separation from the inner wall, as discussed in Figure 5.4. In Wave 1, the deceleration phase is short-lived and the flow quickly returns to a quasi-steady state with suppressed secondary flow, whereas in Wave 4 the deceleration phase extends over most of the cycle. The attainment of peak secondary flow intensity during flow deceleration is consistent with similar observations in much simpler geometries, e.g. flow in a uniformly curved, circular-cross sectional tube subjected to sinusoidal pulsatility (see Hamakiotes & Berger 1988).

Figure 5.6 shows contours of WSS at the same key times in the cardiac phase for wave 1 and 4. As a result of the formation of eddies, a stagnation zone is seen at the

location of aneurysm. This stagnation zone moves slightly during the pulsatile cycle. This is demonstrated by regions of low WSS at aneurysm site. Regions of low WSS are persistent at the aneurysm site for both Wave 1 and Wave 4 during all the phases of the cardiac cycle. In fact, larger regions of WSS are seen for Wave 1 as opposed to Wave 4. At the distal neck of aneurysm, slightly elevated values of WSS are seen. Note that the maximum WSS attained for both cases has not been greater than  $40 \text{ dynes/cm}^2$ .

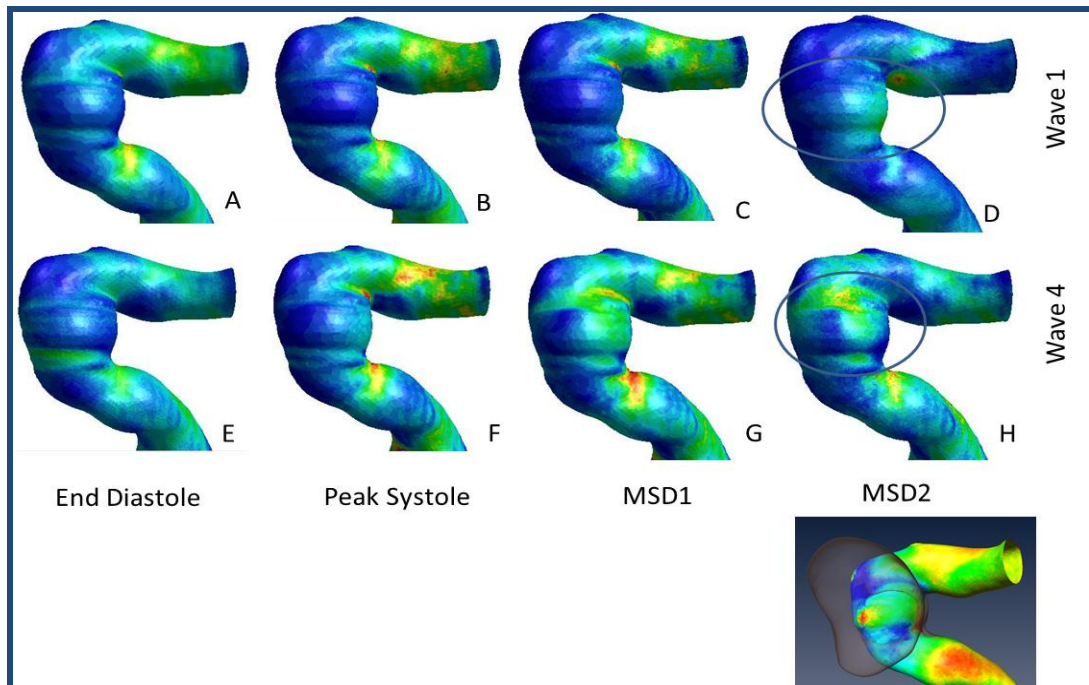


Figure 5.6. Contours of WSS for critical times in cycle for Wave 1 and 4. Inset shows the ostium plane (region connecting the two necks of aneurysm). Accordingly, the region of interest in the pre-aneurysm geometry is indicated by the ovals.

For Wave 4, larger regions of elevated WSS exist and during the deceleration phase of the cycle, these regions even approach the aneurysm site (indicated by the oval). The regions of stagnation flow and low WSS have been found to be less than  $2 \text{ N/m}^2$ . It is believed that shear stresses smaller than approximately  $2 \text{ N/m}^2$  lead to apoptosis in the endothelial cells, which further results in the degeneration of the arterial vessel wall (see

chapter 3 for discussion of related literature). The magnitudes of WSS observed at the location of the aneurysm (in the pre-aneurysm case) are barely  $1.5\text{N/m}^2$  at peak systole; this value seems too low to maintain the regular cellular function of endothelial cells.

In figure 5.7, contours of AFI are shown for Wave 1 and Wave 4. As expected, the AFI is high at the regions of arterial curvature (Neglecting the inlet and outlet boundary conditions that may cause artifacts resulting in higher intensity AFI near the outlet). This is because of the dynamics of the counter-rotating eddies explained earlier. The aneurysm site is at the second curve from the inlet. AFI is particularly persistent for Wave 4, at all the phases of the cycle. Highest reversal in the WSS vector is seen at the critical phases for Wave 4. However, for wave 1, AFI attains its peak negative value, implying a large oscillation in the WSS, during the second half of the deceleration phase and quickly WSS vectors align in the direction of flow, at diastole and peak systole. This sudden oscillation in WSS would be the result of the sudden adverse pressure gradient as opposed to a gradual change in pressure gradient as in the case with Wave 4.

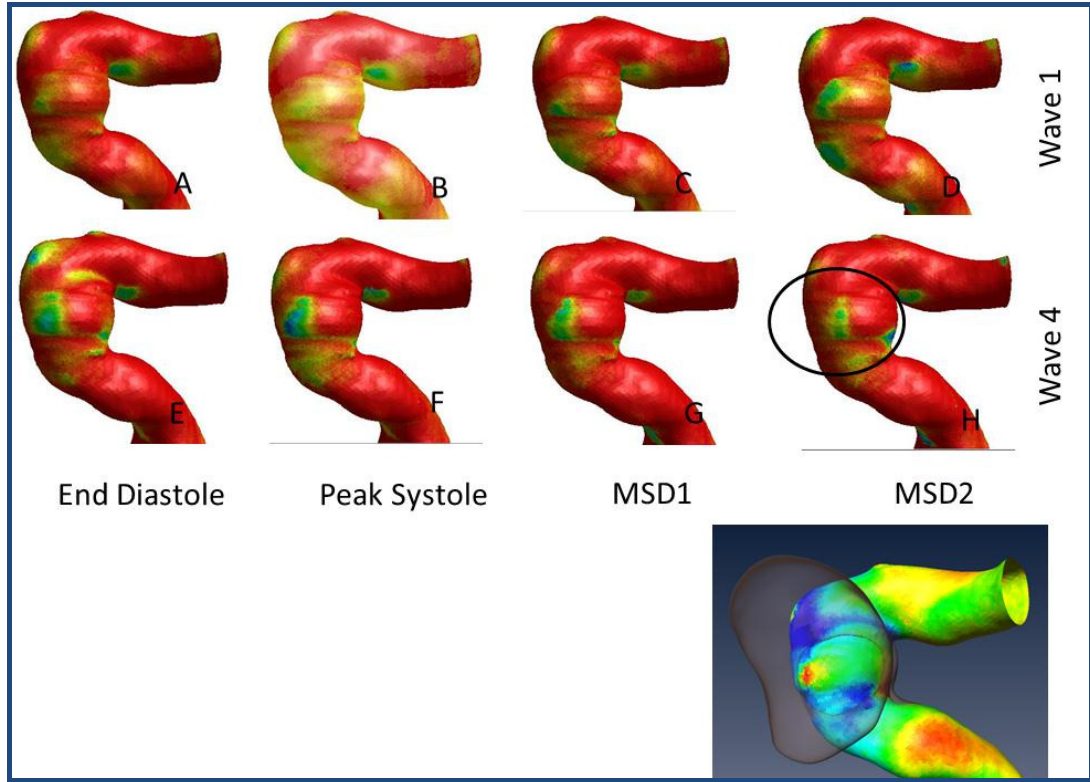


Figure 5.7. Contours of AFI for wave 1 and wave 4. Inset shows the ostium plane(region connecting the two necks of aneurysm). Accordingly, the region of interest in the pre-aneurysm geometry is indicated by the ovals.

This would clearly explain why intermittent high intensity oscillations are present for Wave 1, and more sustained reversal of WSS is observed in Wave 4. This is demonstrated even more clearly when we overlay the WSS vectors on the contours of AFI and observe this pattern particularly for the deceleration phase (Figure 5.5). Figure 5.8 shows a zoomed in view at the aneurysm site. The instantaneous WSS vectors are scaled to have uniform length and are colored in black. The blue color indicates oscillation in WSS.

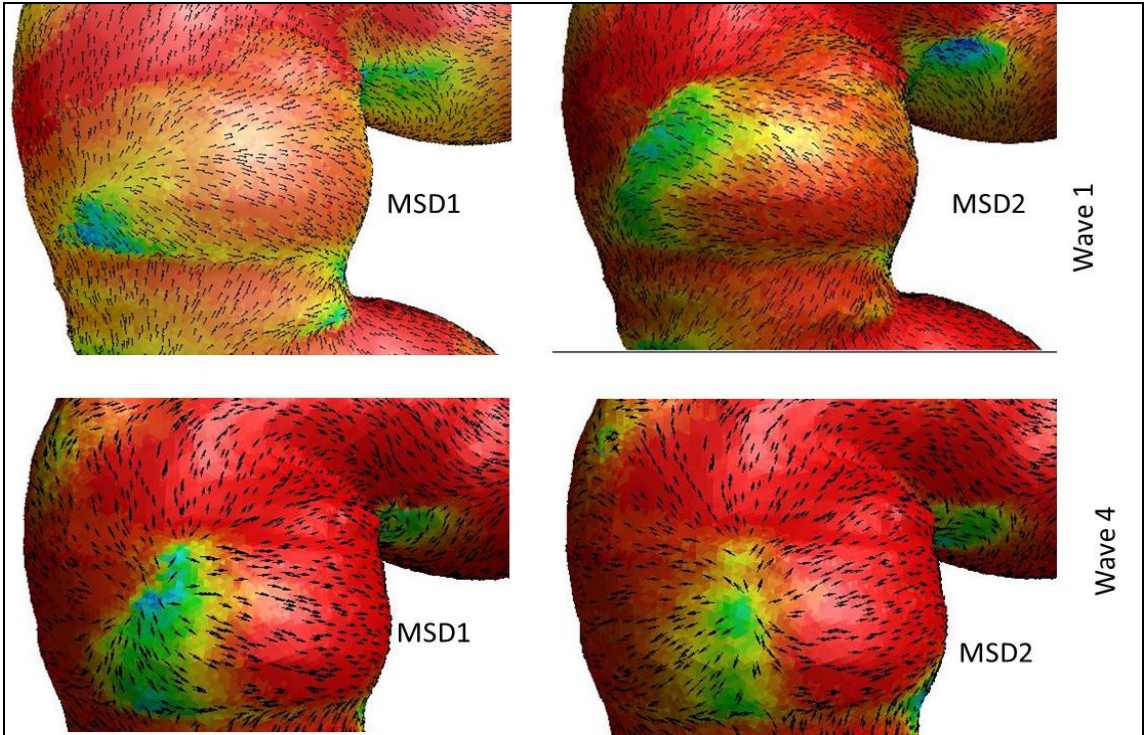


Figure 5.8. Instantaneous WSS vectors overlaid on contours of AFI.

The abrupt change in the pressure gradient over a short period of time acts as a high intensity perturbation to the flow, resulting in reversal of WSS at the regions of aneurysm location. This can be seen by the regions of blue contours, indicating values of  $AFI = -1$ , implying a complete reversal of WSS for wave 1. While the adverse pressure drop is more gradual for wave 4, the reversal is sustained and its intensity is maintained during all phases of the cardiac cycle. The random orientation of WSS vectors for Wave 4 implies a stagnation zone, this stagnation zone seems to move slightly during systolic deceleration. This in fact is the region where high intensity AFI is seen (Wave 4).

Keeping all other key features the same, and by only changing the deceleration slope of systole, we have demonstrated the sensitivity of the flow patterns to the shape of the waveform. This change was made to demonstrate the following: (i) The effect of deceleration slope on flow features, and (ii) differences between old vs. young adult patient waveforms. More importantly, it was to simplify our analyses of the flow features.

In the next sections, we will use measured waveforms from real human data, and demonstrate the consistency of our previous results with the real human data.

## **5.2. The Hoi Waveform: Real Human Data**

Hoi and Steinman (2010) performed measurements of the internal carotid artery (ICA), external carotid artery (ECA) and common carotid artery (CCA), on 94 adults. In addition gender differences were noted (Figure 5.9). They used phase contrast magnetic resonance imaging (PCMRI) to make the measurements. In addition to getting volumetric flow, they also computed FAI. In addition to comparing the waveform against older and younger adult results, they also did an analysis of how the waveform changed with gender. As can be seen from the figure, there is no notable difference in the ICA waveforms between female and male (possibly due to auto regulation), however there are considerable differences in the CCA waveforms of the female and male adults. The slope of deceleration of a female is more blunt when compared to a male adult. This change in the slope, especially for older women, could be explained somewhat by the changes menopause result in hardening of the artery.

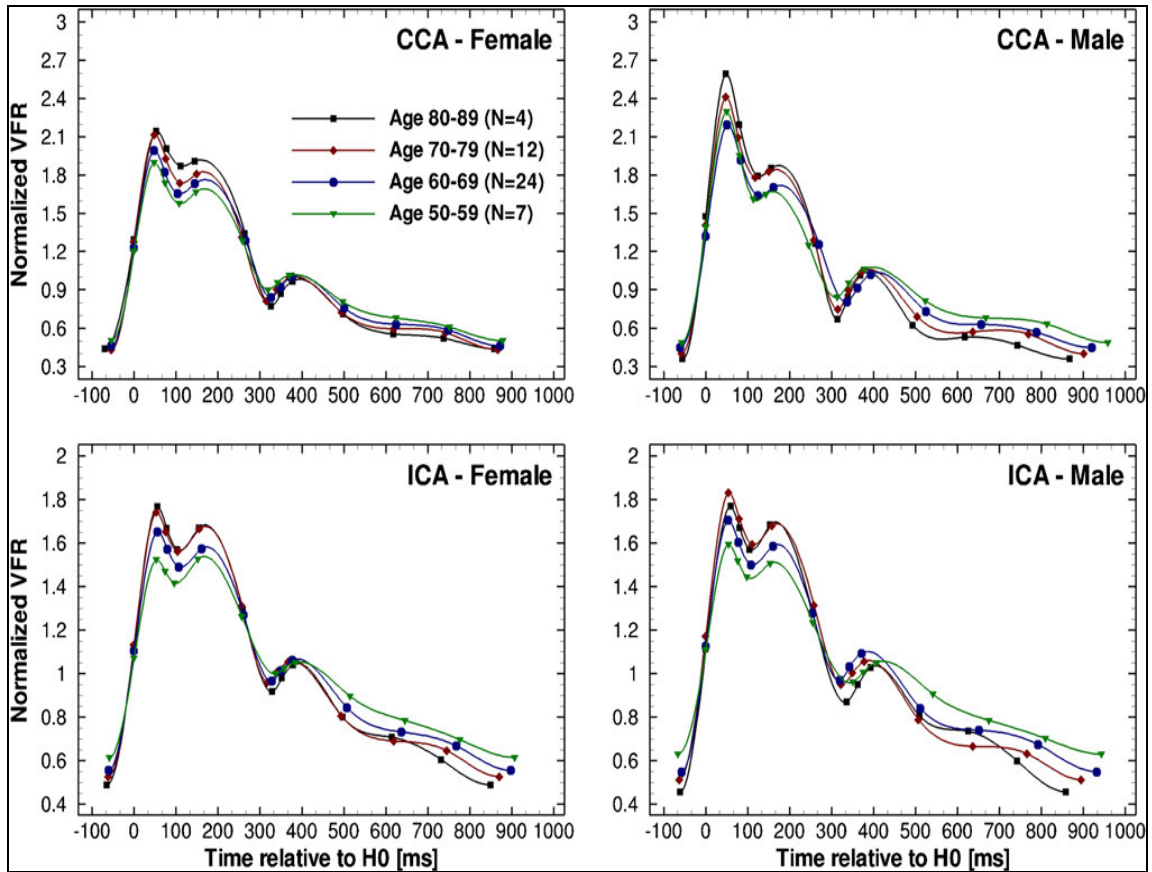


Figure 5.9: Comparison of the CCA and ICA Waveforms for female vs. male.

Figure 5.10 shows the waveform (averaged over the subjects) of the ICA, ECA and CCA. Note that, the deceleration slope of CCA is much steeper than ECA and ICA with ICA having the least steep slope among all. In addition, the peak of the ICA waveform is rounded at systole, compared to ECA and CCA that have a sharp systolic peak. In addition, the Dichrotic notch for the ICA seems to be at the level of peak systole for ICA. These effects will significantly contribute to changes in the hemodynamic variables.

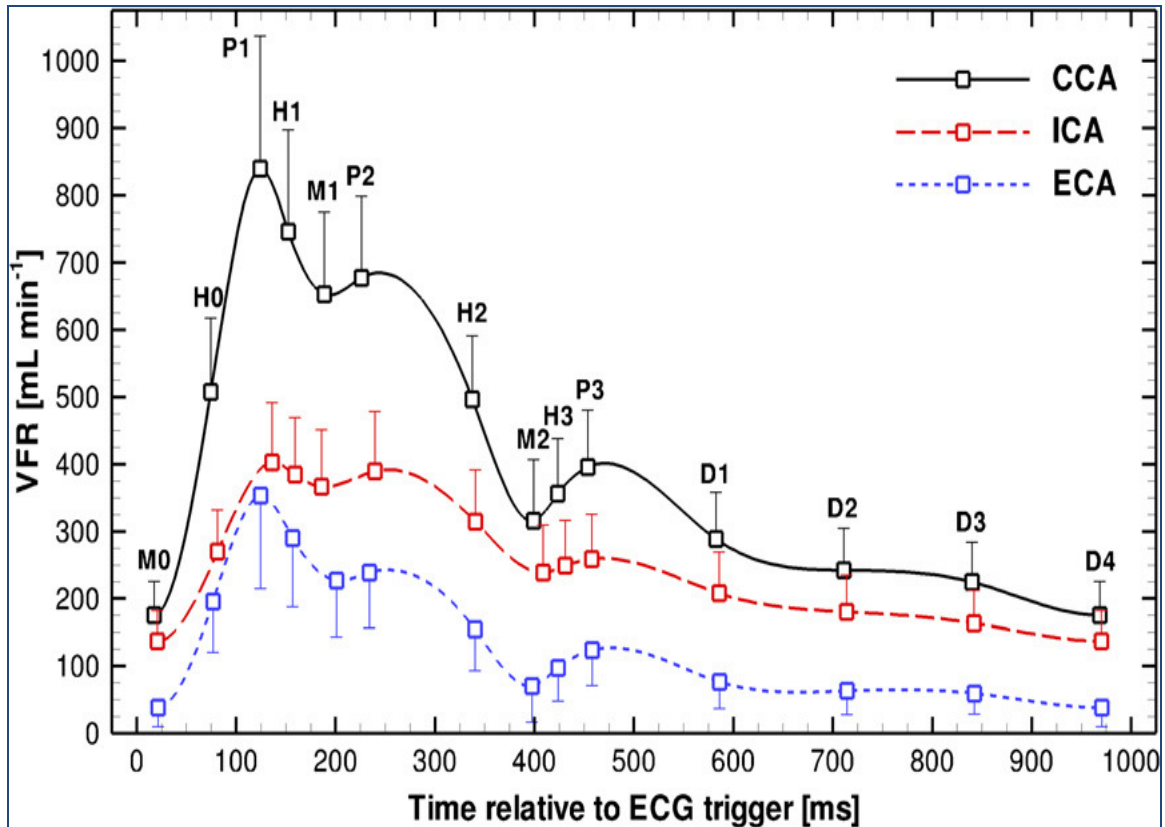


Figure 5.10: The averaged waveform of CCA, ICA and ECA.

Figure 5.11 shows the comparison of older vs. younger adult waveforms. These will be the waveforms we have used for our simulations. The blue and red dots indicate the regions where the data will be plotted. The waveforms have been normalized to match the total volumetric flow. This is to ensure that any variations in the patient physique get cancelled out. This is the reason why the time periods of the cardiac cycle vary while peak systolic values are the same. These waveforms show similar trends as noted in the literature; for example, the diastolic velocity for the older adult is much lower than the younger adult. However, upon closer examination, in particular between the Dichrotic notch and the first deceleration point, the slope is much steeper for the older adult than younger adult. We speculate this could be a result of averaging, and could be an artifact.

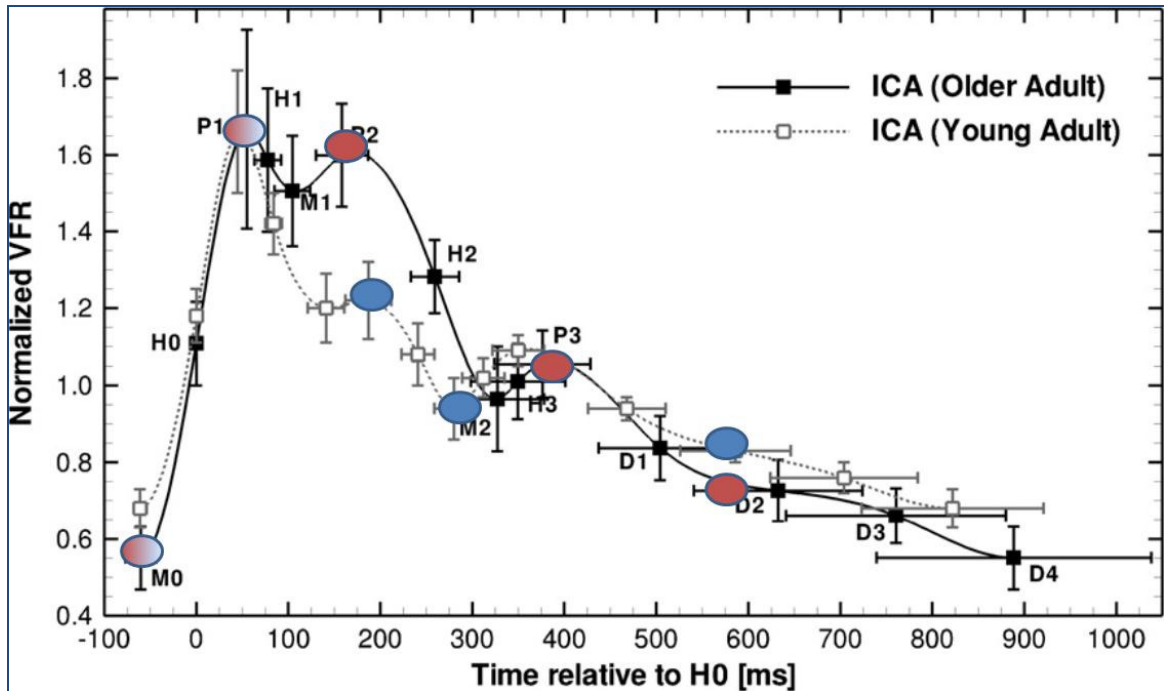


Figure 5.11. Waveform of the ICA for older and younger adult. The blue and red dots indicate regions of interest where the results have been plotted. These will be donated as end diastole, peak systole, second peak, first systolic deceleration 1(SD1), second systolic deceleration (SD2).

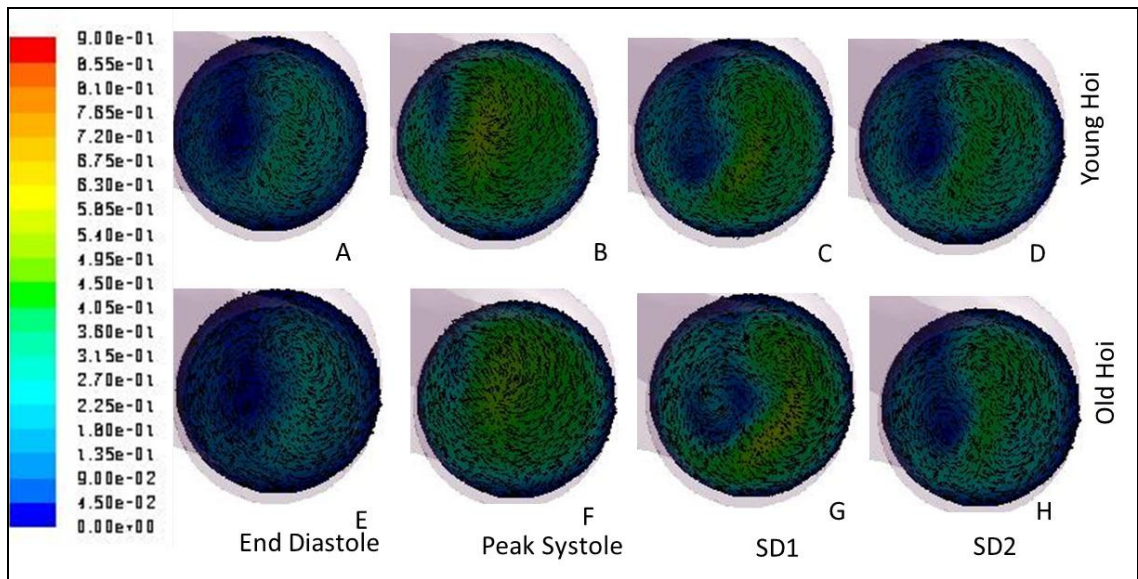


Figure 5.1. Contours of axial velocity overlaid by the secondary velocity for Old and Young waveform at End diastole, Peak systole, SD1 and SD2.

Figure 5.12 shows contours of axial velocity overlaid with secondary velocity vectors. This is similar to the analysis presented in the previous section. The idea is to look at the counter-rotating eddies with the intention of better understanding the spatial changes in the WSS as a result of the formation of stagnation zones. In the top and bottom panels in Figure 5.12, we see similar development and progression of the two counter-rotating eddies and the eventual formation of a stagnation zone at the aneurysm site. Upon closer examination, these plots reveal only slight variations in the velocity at SD1. The old-Hoi waveform has a more developed counter-rotating eddy compared to the young-Hoi waveform. This could be explained by the fact that SD1 and SD2 occur around the same time in the cardiac cycle and have similar volumetric flow rates for both the waveforms. While SD1 for a younger adult is taken at the end of deceleration, the SD1 for the older adult is taken after the slight acceleration that is present during the larger systolic deceleration phase. This results in only slight differences in the plots (Figure 5.12 B and E).

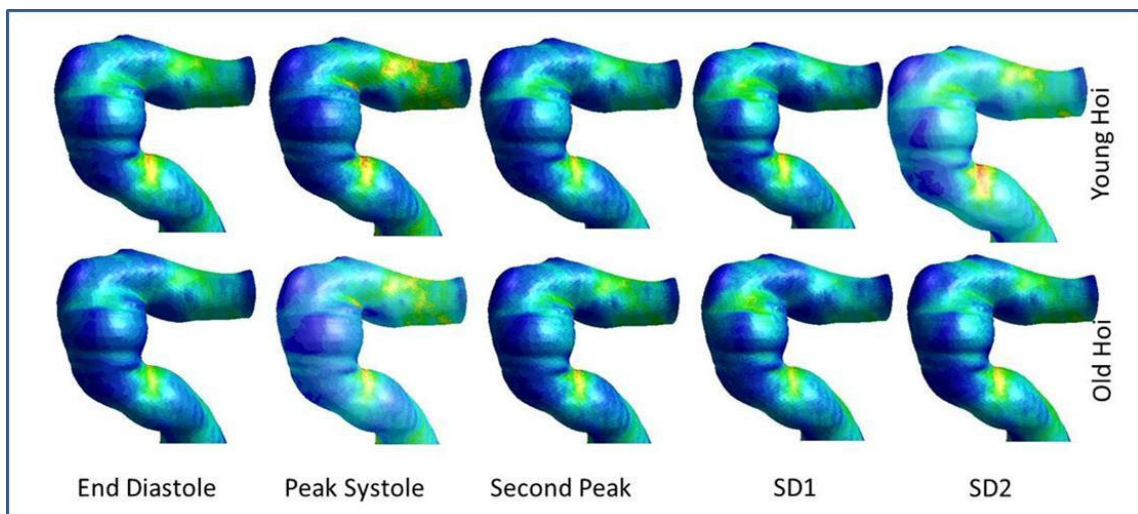


Figure 5.13. Contours of WSS at critical phases of cardiac cycle for Young and Old adult waveform.

Figure 5.13 shows contours of WSS for the two waveforms at the critical phases of the cycle. Similar to the previous results from the idealized waveforms, higher WSS are present at the arterial bends, with a stagnation zone forming at the aneurysm site for both the cases. Again, as a consequence of similar spatial patterns in eddy development and progression, the WSS stresses have similar contour plots.

AFI contour plots are shown in figure 5.14 for both the waveforms. Based on the data from WSS and the velocity, one might expect AFI to show similar contour plots. While there are some similarities in the two waveforms, some significant differences also are present between the two plots (top and bottom panel in Figure 5.10). Reversals in WSS, reflected by blue-green contour plots of AFI, are persistent during the cardiac cycle for both the waveforms. However, higher intensity reversals (shown by AFI) are seen for Old Hoi waveform. These reversals are more intense right after peak systole (Figure 5.10 G and H)

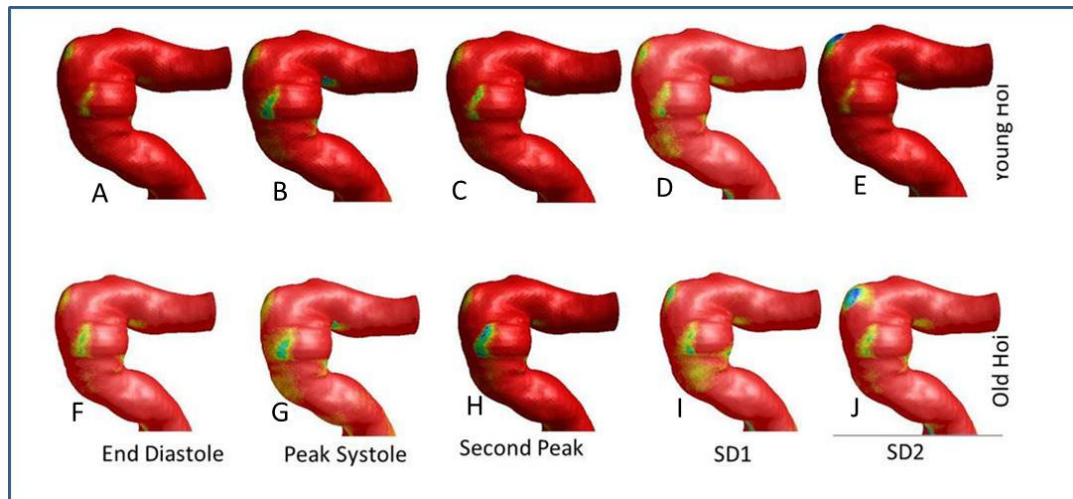


Figure 5.14. Contours of AFI for Older and Young adult.

While reversal is almost negligible during the second systolic deceleration in the case of the young adult, it is persistent in the case of the older adult. Sensitivity of AFI to the subtle changes in WSS, which would not be otherwise captured through mere plots of velocity or WSS contours, makes AFI a more reliable indicator.

We have presented some of the results using the Hoi waveform. Due to very few differences in the shape of the waveform between an older adult and younger adult, the flow patterns were similar. However, AFI was able to successfully capture the subtle changes in flow occurring at the aneurysm site, implying that AFI indeed is a potentially reliable indicator. However, we have used only two sets of waveforms here and under very generic conditions. In the next section, we will present some of the results from another study by Azhim et al. (2009b), in which they not only analyzed the effect of ageing on the waveform, but also show marked differences between the waveforms of adults with and without exercise.

### **5.3. The Azhim Waveform**

Azhim et al. (2009) developed a novel technique that connected electrocardiogram (ECG), Doppler ultrasound and a remote telemetry system together, in order to take synchronized readings of velocity in three different arteries. In this study velocity measurements of 82 men between the ages of 21 to 67 years were taken. The waveforms were characterized by five components as peak systolic (S1), second systolic (S2), incisura between systole and diastole (I), peak diastolic (D) and end-diastolic velocity wave (d) (Figure 5.15).

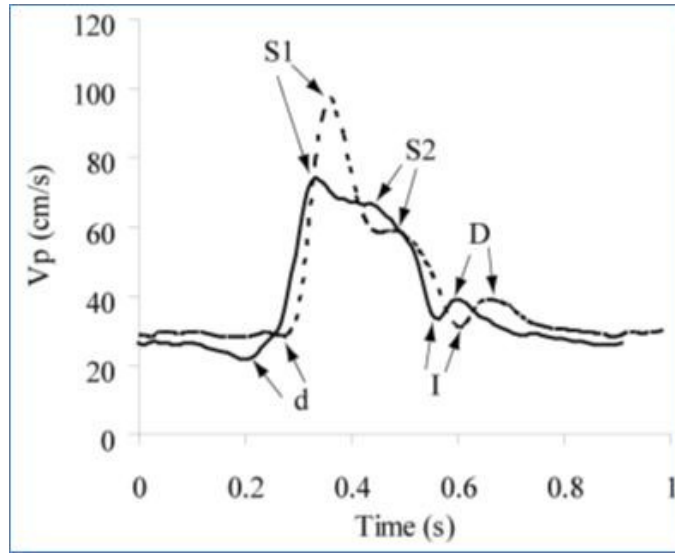


Figure 5.15. A sample waveform characterizing the key features. The dashed line represent young adult and the bold line represents older adult.

By analyzing the changes in these key parameters mentioned above, they concluded that exercise improved the flow waveform in both young and older adults (Figure 5.16). As described earlier, improvement of the arterial tone is reflected by the change in the shape of the waveform. Closer examination of the waveform (bold lines in Figure 5.16) reveals an increase in the peak systolic flow as well as diastolic velocities and a delay in the occurrence of the Dichrotic notch.

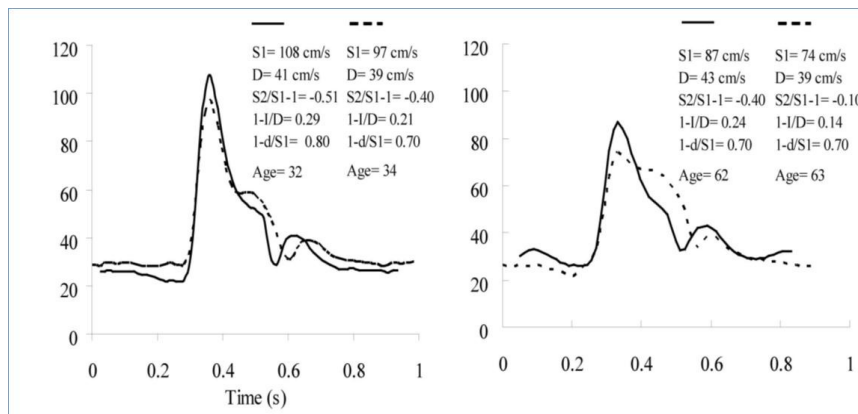


Figure 5.16. Averaged waveform comparing exercise (bold) vs. non exercise (dashed) younger adults (left and older adults (right respectively).

Based on these results, we present an analysis of the change of hemodynamic variables due to exercise. In order to reinforce the effects, we will take a sample waveform of younger adult who exercises regularly and compare that against an older adult leading a sedentary life style (Figure 5.17).

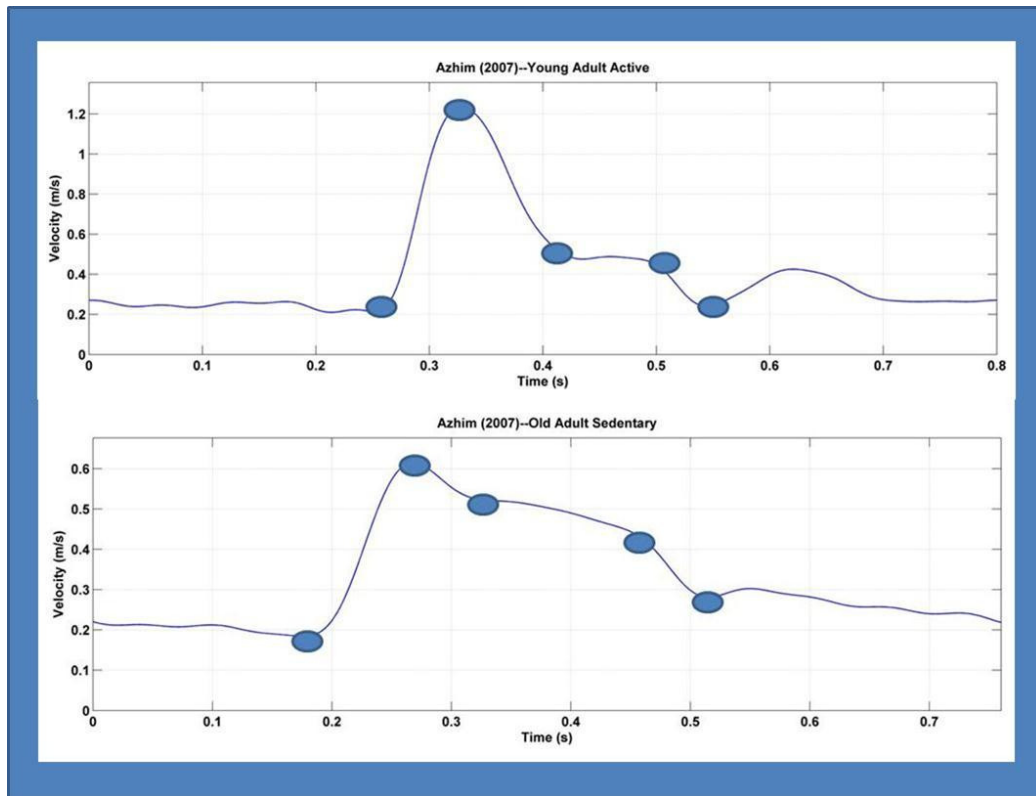


Figure 5.17. Waveform of young active adult and old sedentary adult. The blue dots indicate the key phases in the cardiac cycle where the data will be plotted.

The blue dots indicate the key phases in the cardiac cycle. These are end diastole (ED), peak systole (PS), the dip (DIP), first systolic deceleration (SD1) and second systolic deceleration (SD2). Note the differences in the waveform compared to Hoi; e.g. the Dichrotic notch is almost gone.

Figure 5.18 shows contours of axial velocity overlaid with secondary velocity vectors in order to capture the counter-rotating eddy symmetric eddy that developed during the pulsatile cycle. One common characteristic feature of the curved arterial segments and

pulsatile flow is the development of the counter-rotating eddies seen in all geometries when exposed varying flow waveforms.

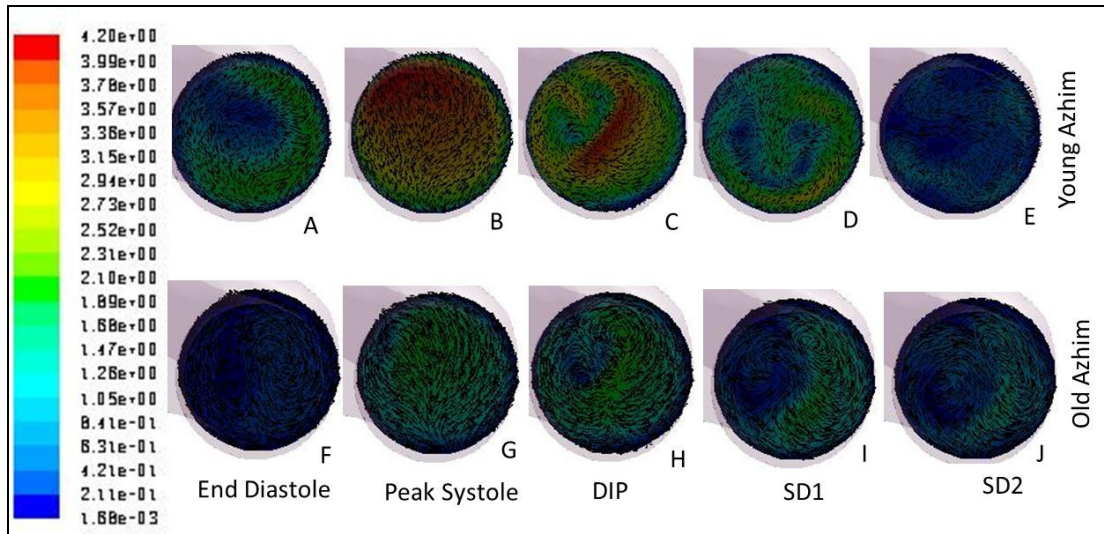


Figure 5.18. Shows contours of axial velocity overlaid with secondary velocity vectors for younger (top panel) and older adults (bottom panel).

The development and progression and even intensity of these eddies varies with the flow and geometry. Only in very few extreme cases of highly tortuous geometries or with waveforms with sharp adverse pressure gradients may eddies not get enough momentum from the flow or perturbation from the gradient to fully develop and sustain them. To some extent this was seen in the case of Wave 1 where the pressure drop was sharp drop (in time) and was not enough to sustain the eddy.

Formation of the counter-rotating eddies happens during the diastolic phase of the cycle, however they get flushed out due to the positive flow during systolic acceleration, as seen Figures 5.18 B and G. The adverse pressure gradient results in the sudden decrease in the axial flow velocity and enhancement of the secondary velocity; as a consequence the eddies gain strength during this phase as seen figure 5.18I (older adult's waveform). In the case when pressure drop is gradual, the eddies have sufficient time to

redevelop and sustain through the diastolic phase. These differences in the older vs. younger waveforms were observed for all the cases so far. The WSS contour plots displayed in Figure 5.19 show similar trends. The regions of elevated WSS are at arterial bends, and low WSS were observed at the location of eventual aneurysm formation.

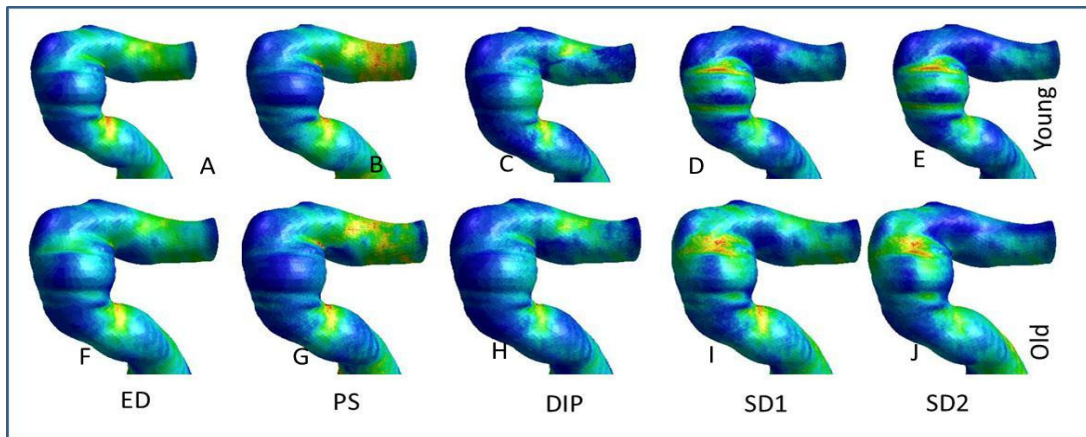


Figure 5.19. Shows contour plots of WSS for active younger and sedentary older adult.

Note the contours of WSS for figure 5.19E and J. The region of stagnation is not present at the aneurysm location, but has moved a little toward the first bend for the active young adult, while the stagnation zone is persistent at the aneurysm site during the entire cardiac cycle for the sedentary older adult. This increase in the WSS at the aneurysm location for the younger adult has an athero-protective effect on the arterial wall (see Chapter 3). This implies that exercise can induce changes in the hemodynamics that positively affect the arterial environment. The changes in WSS patterns are reflected in the AFI contours, shown in Figure 5.20.

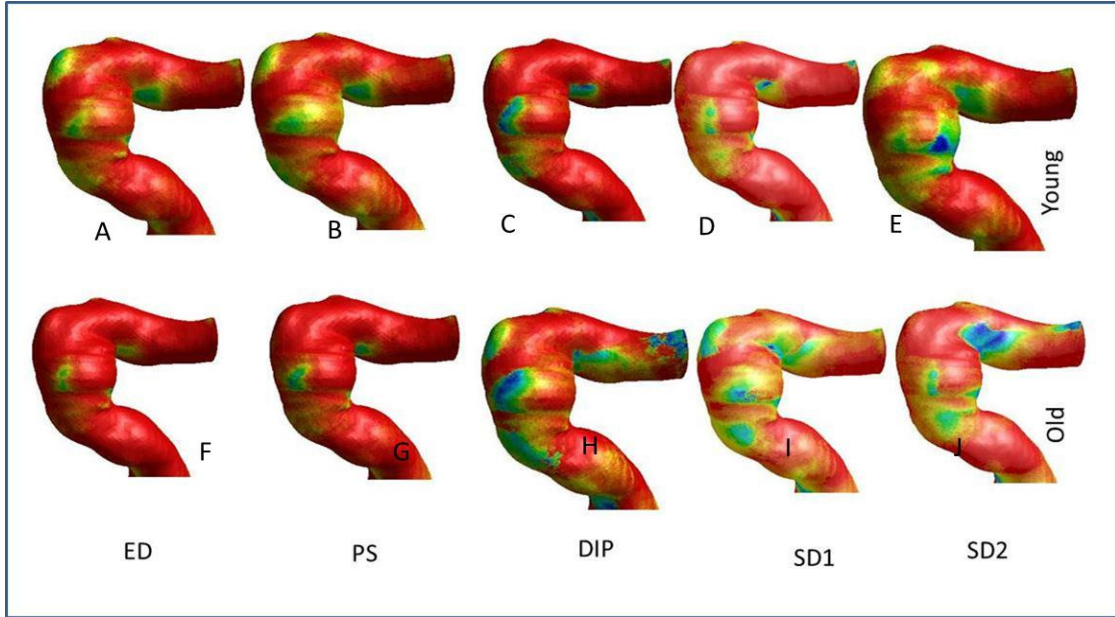


Figure 5.20. Contours of AFI for active younger and sedentary adults respectively.

As expected, high intensity WSS reversals are present for the older adult throughout the cardiac cycle. This does not happen for the younger adult. There is a slight rotation in WSS during ED and PS, and during the second systolic deceleration there is certainly a reversal in WSS. However, when we compare the contour plots with the previous plots of AFI for other waveforms, the AFI is indeed elevated and enhanced for both young and older adults. We do recognize that the AFI contours for the younger adult that exercises regularly are more elevated when compared to the idealized older adult and Hoi waveforms. However, the reversal of WSS, reflected by AFI, is still not persistent throughout the cycle for the younger adult and there is also a change in the location of these slightly elevated values of AFI. It has moved from the aneurysm site, to the first arterial bend, and this elevated level is not present throughout the cycle. In addition we also speculate that deleterious response of the cells due to this high reversal WSS at the second systolic deceleration for the active adult, will be counteracted or nullified by the strong positive effect of the systemic biochemical responses due to exercise.

## 5.4. Discussion

The changes in the shape of the waveform are a result of the gradual degeneration of the vascular bed and therefore to a great extent reflect the character of the vascular bed. In this chapter, we have done a comparative analysis of the effects of ageing on the hemodynamics in an artery and correlated the changes to aneurysm formation. We first used an idealized waveform, in which we changed the deceleration slope (where most changes are seen), in order to simplify the analyses and to see the effect of this change on hemodynamic variables. We found that changing the deceleration slope (making it less steep) significantly affected the AFI. More specifically, making the slope less steep (which models the effect of aging) caused the AFI to be enhanced, showing that AFI correlates well with degeneration of the vascular bed.

Following this, based on the work done by Hoi et al. (2009), we systematically analyzed the effect of ageing on the arterial hemodynamics in order to capture the progressive degeneration of the artery. This was demonstrated by the elevated values of AFI that captured even the subtle changes in WSS. Exercise is known to have a positive effect on the tone of the artery and this was demonstrated by using a waveform of an active young adult and plotting the WSS and AFI. Indeed there was an enhancement in the WSS at the location of the aneurysm formation, which otherwise has low and oscillatory WSS. When we compared this against that of an older adult that led a sedentary lifestyle, AFI values were elevated, even in comparison with the Hoi waveform.

In addition, we believe that AFI successfully captures the subtle changes in WSS as a result of changes in the shape of the waveform which otherwise would not be captured by other indicators. Hoi et al. (2010) performed a study to see the differences between measured and assumed waveform by extracting the carotid artery geometry from nine subjects. Three different waveforms, one young adult, an older adult waveform scaled to measured flow velocities, and measured waveform of an adult were used (Figure 5.21). They computed OSI and relative residence time.

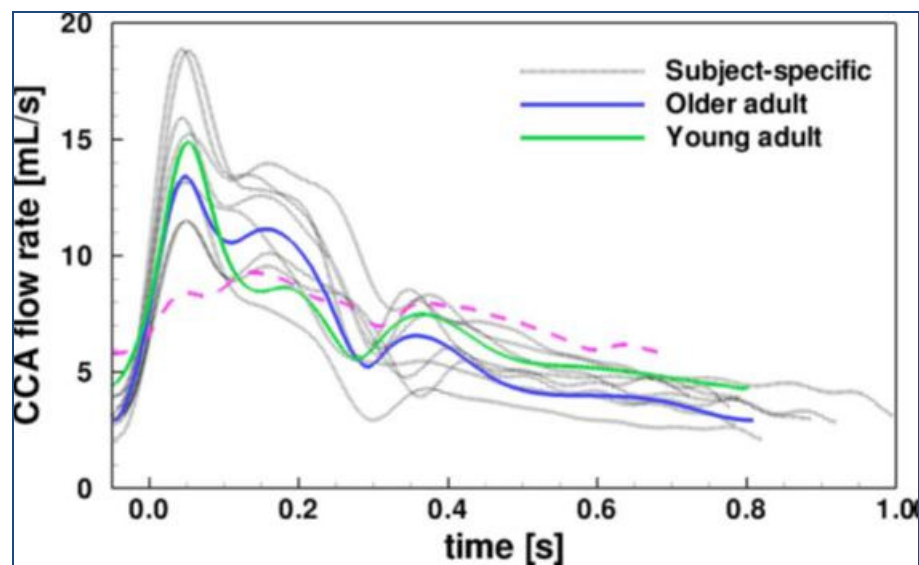


Figure 5.21. Waveform of the CCA showing subject specific, older adult, young adult.

OSI did not show any sensitivity to the waveform shape. Based on those results, they concluded that for large scale studies, using an averaged waveform was sufficient. However, OSI is a value that is averaged over the cardiac cycle, and does not capture the instantaneous effect of WSS on ECs, and it is more sensitive to the flow magnitudes than changes in the shape of the waveforms. The waveform depicted in “pink” was omitted with the rationale that it is a result of some measurement artifact; however, it will be shown that in reality such waveform is seen in unhealthy patients (figure 5.22).

Rohren and Hertzberg (2001) in their pictorial essay presented a spectrum of Doppler waveform in the carotid arteries with severe flow associated diseases. In the diseased patient, the ICA waveforms had a sharp rise in systolic flow and gradual tapering of flow during diastole. In addition, they tended to have a blunted systolic peak and slightly elevated diastolic flow than ECAs. One Doppler spectrum of a 66 year old woman with a high grade stenosis, showed diminished peak systolic velocity values, prolonged systolic acceleration, rounded systolic peak and an absence of Dichrotic notch (Figure 5.22). In 70% of proximal occlusions, flow in the ICA was ante-grade, forming a low resistance waveform with diminished systolic amplitude and delayed systolic upstroke. Aortic regurgitation was seen to introduce flow reversal and several decelerating peaks during the systolic deceleration.

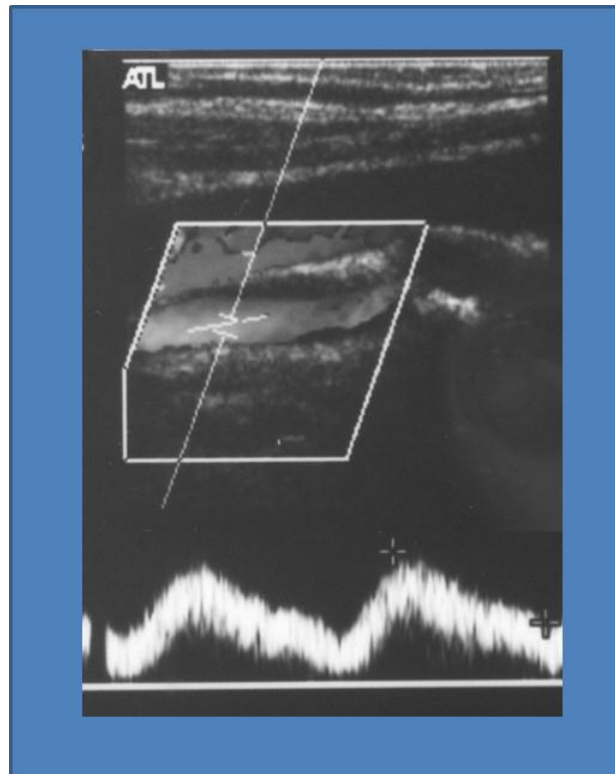


Figure 5.22. 66-year-old woman with high-grade atherosclerotic stenosis of proximal right internal carotid artery and parvus-tardus waveforms in mid internal carotid artery.

It is quite clear that there are indeed variations in the waveforms between an older and younger adult, active vs. sedentary adult, and healthy vs. unhealthy adult. While sophisticated numerical models may be developed that combine the biochemical responses of ageing with hemodynamics, it is much simpler to use patient specific waveforms for simulations as that inherently captures this effect with the change in shape. As cerebral aneurysm initiation and growth happens progressively over time, and is more frequent in older people than younger adults, it would be more effective to use the waveform of an older adult, averaged or patient specific, to model flow in cerebral arteries to better understand hemodynamic flow dynamics.

## **5.5. Conclusions**

The objective of the preceding sections was to clarify the cause-and-effect linkages between hemodynamic factors (such as, wall shear stress) and physiological responses leading to aneurysm formation. First, we emulated the arterial environment before aneurysm formation and performed simulations on an artificially “smoothed” arterial segment. Using a recently developed algorithm for approximating the shape of the artery prior to the aneurysm, we have performed computational hemodynamic simulations on human patient data for arterial flow without the aneurysm present. In addition, we have also shown that the popularly used hemodynamic indicator, WSSG, is exceedingly sensitive to inaccuracies due to mesh resolution, type of meshing scheme, image acquisition modality as well as the methodology of arterial reconstruction. This means that WSSG can be dominated by numerical artifacts and therefore can be misleading.

We have demonstrated the reliability of AFI as an indicator by studying the effect of exercise and ageing on hemodynamics. In the next section we will explore the hemodynamic influences on aneurysm stability via simulations under realistic physiological conditions. We will apply this knowledge of flow patterns towards better design of stents and other flow diverting devices. In addition, potential use of hemodynamic simulations in clinical application is explored.

## Chapter 6

### 6. Stability of Flow inside the aneurysm

The strength and direction of blood flow into and within a cerebral aneurysm are important issues in developing effective surgical intervention strategies to stabilize the aneurysm. In this chapter, some results from the numerical simulations of flow across the ostium plane of an aneurysm are presented. Results show that in many cases there is relatively stable flow structure that is maintained over the phase of the pulsatile flow cycle. Quasi-permanent regions of flow influx and efflux across the ostium plane exist, separated by a “virtual boundary”. The flow pattern within the aneurismal sac is like a helical vortex with swirl in two orthogonal cross-sectional planes. These numerical observations are consistent with clinical data from ultrasound color-Doppler velocimetry. The observed flow patterns are found to occur in different types of aneurysms (basilar and side-wall), and can persist even after flow parameters are perturbed beyond the normal regime of physiological flow conditions. These results suggest that major aspects of the behavior of aneurismal hemodynamics for an important class of aneurysms can be learned from an analysis of steady, non-pulsatile flow, which is much simpler and faster to simulate than time-dependent, pulsatile flow. This fluid dynamical behavior may also prove to be useful in the design and placement of stents, coils and various other interventional flow diverting devices.

The following section describes results obtained from computational hemodynamic simulations (CHD) of six cerebral aneurysms. The main focus was on the characteristics of flow through the ostium plane under pulsatile conditions. Two aneurysm types were

considered: sidewall (paraclinoid) and bifurcation (basilar tip), with three specimens of each obtained from human patients via clinical 3D digital subtraction angiography. The goal was to identify common features of large-scale flow patterns observed in many aneurismal flows.

## **6.1. Previous Work**

The role of hemodynamics - i.e. the nature of blood flow in arteries, and the forces induced by flow on arterial walls - in the genesis and growth of cerebral aneurysms has been the subject of several recent studies. The premise of these investigations has been that the mechanical properties of the arterial wall are pathologically altered in response to sustained exposure to abnormal wall shear stresses and/or pressures, induced by flow of blood through the artery. The motivation of hemodynamic investigations has then been to establish the origin of abnormal wall shear stress or pressures, and to correlate hemodynamic flow patterns with the sites of aneurysm growth and rupture. A secondary motivation is to aid in the design of interventional devices - such as stents - the purpose of which is to alter blood flow into the aneurysm to prevent its further growth and potential rupture, for example by promoting thrombosis within the aneurysm.

Arterial hemodynamics near the ostium of an aneurysm are governed primarily by arterial geometry and flow pulsatility. Curvature can cause the generation of swirl or other secondary flow patterns, which can affect the flow into the aneurysm. The intra-aneurismal flow is also governed by the size of the ostium and the size and shape of the aneurysm itself. Other factors potentially affecting the aneurismal flow include the shape and amplitude of the pulsatile wave form and the size and position of proximate arterial branches.

Studies have been conducted using both "idealized" arterial geometries as well as patient-specific arterial models obtained from clinical imaging. Valencia et al. (2006a) considered an idealized model of a basilar terminal aneurysm and studied the resulting flow at two different "tilt" angles of the ostium plane with respect to the arterial axis. While a tilt angle of 90° generated a symmetric flow pattern in the symmetric aneurysm model, a tilt angle of 23° appeared to generate a single large vortex filling the aneurysm which induced higher peak wall shear stresses compared to the symmetric case. It was concluded that the regulation of these patterns by stents would be important in arresting further aneurysm growth. A similar study was performed by Ford et al. (2008), in which the angle of the aneurysm bulb relative to the parent artery was used to characterize basilar tip aneurysms into two phenotypes and their specific hemodynamic variables were studied. They concluded that the potential use of hemodynamic data in routine clinical decision-making is facilitated by the fact that general features of the flow are predictable through a simple geometric parameter, the parent-bulb angle.

Hoi et al. (2004) focused on other geometrical parameters, namely arterial curvature and aneurysm neck size. They studied idealized geometries and found elevated arterial wall pressure/wall shear stress at the regions of high curvatures, and at aneurysm necks. These effects were seen to amplify with increasing curvature. When a saccular aneurysm was located in the impact zone, the region of elevated hemodynamic forces increased with increasing neck size.

While idealized models permit the systematic variation of geometrical parameters, a number of studies have focused on patient-specific geometries to capture the effects of more typically tortuous geometries often seen in cerebral arteries. Shojima et al. (2005)

conducted a survey of 29 patient-specific cerebral aneurysm models. They found that the pressure elevation at the zone of flow impact on the arterial wall (distal to a region of curvature) was only about 1% of the peak intravascular pressure and did not usually coincide with the location of the aneurysm - thus suggesting there were insufficient increases in wall shear stress and pressure to directly promote aneurysm formation.

The influence of other geometrical features, such as branches, has been investigated by Castro et al. (2006), who used a novel technique to merge multiple rotational angiography images of anterior communicating aneurysms and basilar tip aneurysms. For some aneurysms in the Circle of Willis there can be multiple avenues of inflow and it was found that the presence of merging streams can significantly influence the intra-aneurysmal flow patterns. Their results emphasize the importance of physiologically realistic inflow/outflow boundary conditions in the truncated arterial domains used in simulations. An experimental model of an aneurysm in the internal carotid artery was studied by Tateshima et al. (2003). In this wide-necked model based on tomography images, there were large inflows and outflows from the aneurysm accounting for as much as 43% of the main arterial flow. Using Laser Doppler Velocimetry, they were able to characterize the velocity patterns inside the aneurysm.

This chapter reports some results obtained from computational hemodynamic simulations (CHD) of flow in the internal carotid artery containing a paraclinoid aneurysm. The focus is on the characteristics of flow through the ostium plane and its variation over the pulsatile cycle. This issue is important since it relates to aneurysm hemodynamics, the possibility of thrombus generation and its stability within the

aneurysm, and to potential hemodynamic effects expected after endothelial intervention with a stent or coil or introduction of other flow diverting devices.

As established earlier, many flow patterns in the larger arteries are complex, involving the effects of curvature, branching, and unsteadiness as well as flow pulsatility and other geometric departures from axisymmetry. Two different types of aneurysms are considered: paraclinoid sidewall and basilar, with three different geometries of each type, obtained from human patients using clinical 3D digital subtraction angiograms. The goal is to identify basic common features in large scale flow structures observed in many aneurismal flows.

## **6.2. Identification of Large Scale Structure**

Results for steady state simulations of two cases, sidewall case I (Figure 1A) and bifurcation case II (Figure 1E) (See appendix A), are presented in detail, but are characteristic of features observed respectively in the other 4 cases. Steady-state simulations are very useful for numerical validation (e.g. grid resolution), and preliminary characterization of the flow. Here, steady-state cases are of further interest because the observed flow patterns and large-scale structures (LSS) are very similar to those found under pulsatile conditions.

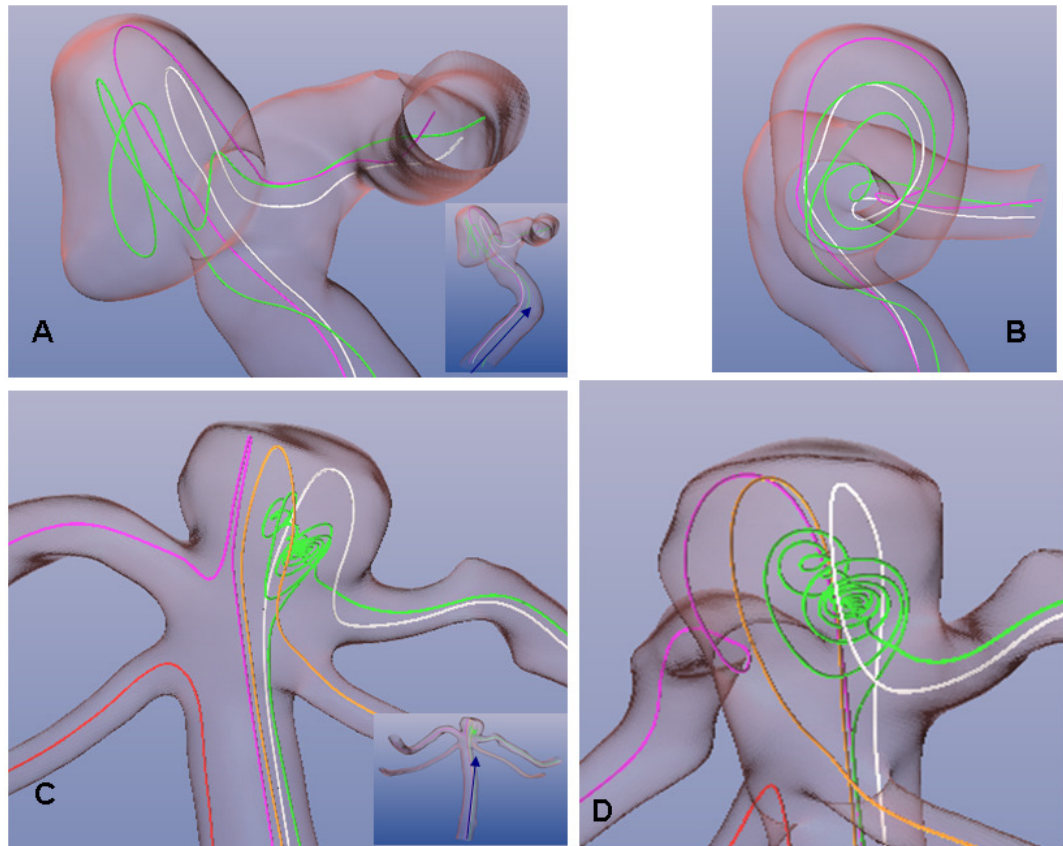


Figure 6.1. Streamlines that have been started from the same points at the inlet plain are shown. (A) Lateral view of the sidewall aneurysm, (B) Figure A rotated anticlockwise by 90o, (C) Anterior Posterior view of Basilar tip, (D) Figure C rotated 90o. Blue arrows indicate flow direction.

Figure 6.1 shows three streamlines starting from the inlet plane, chosen to illustrate the principal flow structure inside the aneurysm. The streamlines are colored according to the normal (perpendicular) velocity magnitude at the point of intersection with the ostium plane: peak influx velocity (pink), peak efflux velocity (white), and very small normal velocity (green). The green streamline passes close to the center of the ostium plane. Two views (one lateral and one frontal view) are shown for a sidewall (Figure 6.1 A, B) and a bifurcation aneurysm (Figure 6.1 C, D). The chosen streamlines all pass through the aneurysm, although in both cases only a small portion of the total arterial flow enters the sac.

While the inlet flow is basically unidirectional, due to the inlet boundary condition, further downstream, for example near the aneurysm, the flow can develop a strong azimuthal component. This swirling motion or secondary flow is a direct result of the curvature of the artery, and is only weakly influenced by the presence of the aneurysm. In the realistic arterial geometries considered in this study, additional complicating factors including aneurysms and variable cross-sectional area and shape are also present.

The effects of arterial curvature and the location of the aneurysm with respect to the point of curvature are both important in determining the flow rate into the aneurysm. It is interesting to note that while the streamlines may appear to enter the aneurysm from the distal end and exit from the proximal end, it is physically impossible for streamlines to cross, so there must be an inherent three-dimensionality to the motion. Nonetheless, the flow pattern near the aneurysm is actually quite simple once its essential geometric features are understood. It is fully three-dimensional and has swirl in two orthogonal planes. Focusing first on the sidewall aneurysm, it is apparent that while the incoming flow follows the principal arterial axis, a swirling component develops proximal to the aneurysm. Fluid enters the sac neither strictly through the proximal nor the distal end, but rather in a lateral fashion, with the green streamline passing through a point of low normal velocity on the “virtual boundary” between the influx and efflux zones (Figure 6.4). This streamline captures the helical motion existing in the aneurysm.

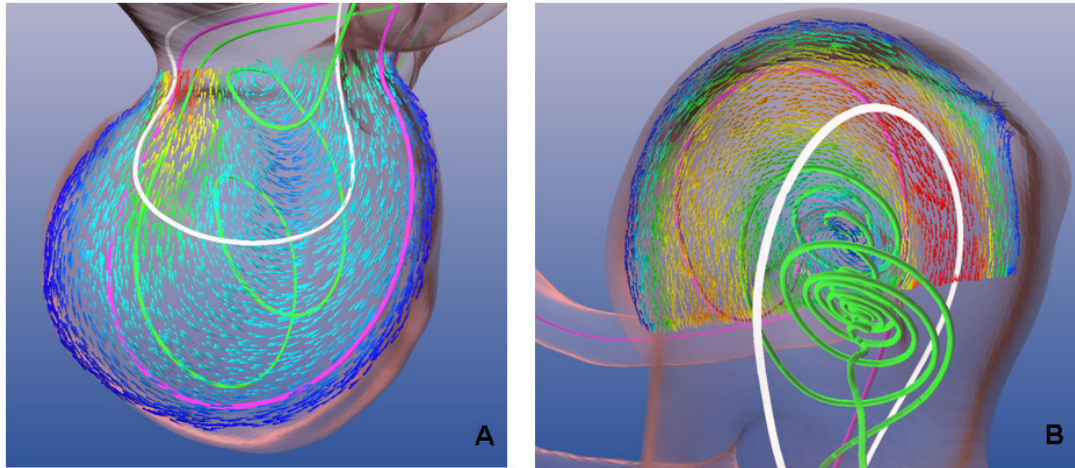


Figure 6.2. The basic aneurysmal flow patterns are characterized by streamlines and velocity vectors for Sidewall Case 1 (A) and Bifurcation Case 2 (B). The three streamlines for each Case are color coded according to their velocity magnitude at their intersection with the ostium plane: peak influx velocity (pink), peak efflux velocity (white), small normal velocity (green). These pink, white and green streamlines are identical to those shown for the two Cases in Figure 2. The velocity vectors are displayed in cross-sectional planes approximately aligned with the peak influx and efflux streamlines. The green streamlines, being closer to the core of the ostium vortex, capture the helical motion of the fluid particles passing through it.

The three-dimensionality of the flow in each case is clearer in magnified views (Figure 6.2). Velocity vectors in Figure 6.2 are approximately tangential to the representative peak influx and efflux streamlines chosen in figure 6.2, thus capturing the essential flow patterns inside the aneurysms. The vectors are color-coded by velocity magnitude to emphasize the centers of swirling motion.

### 6.3. Pulsatile Flow Simulations

Only a small fraction of the total arterial flow enters an aneurysm: 13% in the sidewall aneurysm and 11% in the bifurcation aneurysm (Figure 6.3). This indicates that peak velocities, dynamic pressures, and wall shear stresses in the aneurysm are likely to be significantly smaller than in the artery, except possibly near the ostium neck where the influx jet is strongest.

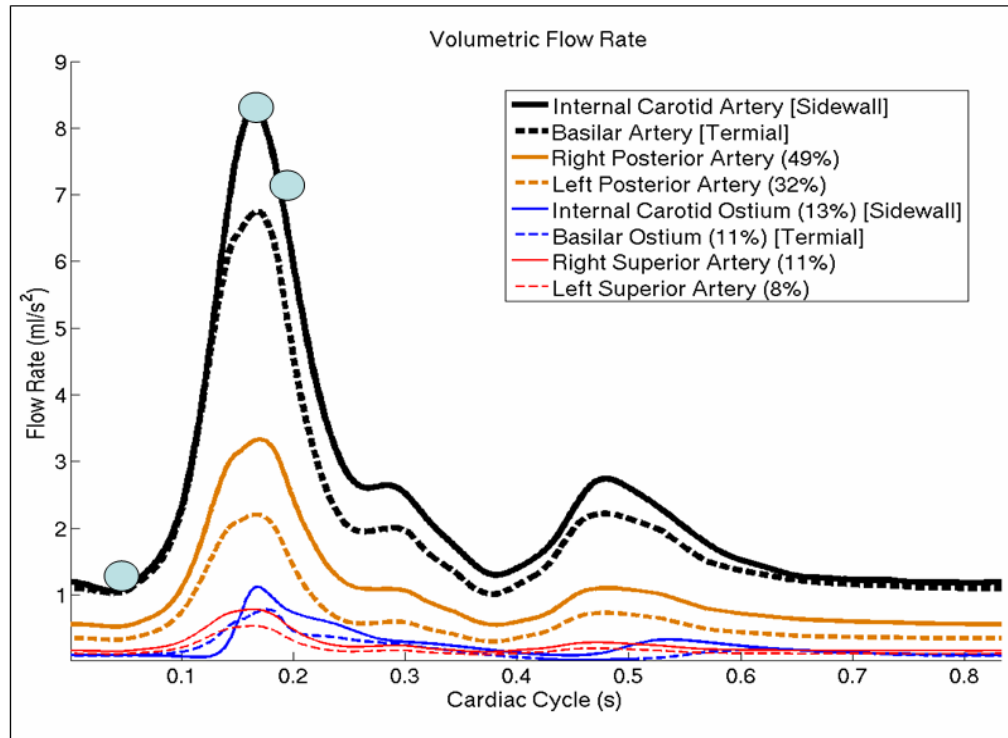


Figure 6.3. Volumetric flow rates across the parent artery, ostium plane, and other arterial branches for Sidewall Case 1 and Bifurcation Case 2.

### 6.3.1. Ostium Flow

Figure 6.4 plots the magnitude of normal velocity across the ostium plane, with negative/blue (positive/red) values indicating fluid entering (leaving) the aneurysm; the top (bottom) row corresponds to the sidewall (bifurcation) aneurysm. The ostium plane approximates the arterial wall prior to aneurysm formation. Thus, the magnitude of the flow across the ostium is a measure of arterial flow disturbance due to the aneurysm.

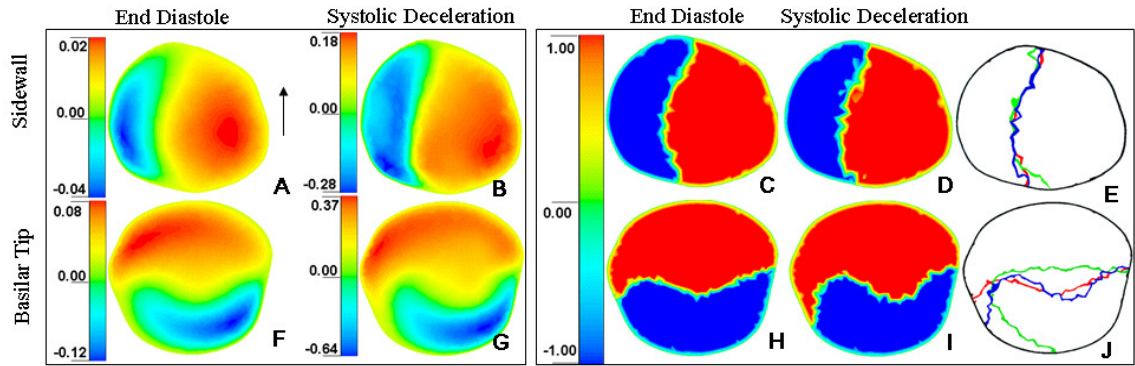


Figure 6.4. Contour plots of flow velocity normal to the ostium plane for Sidewall Case 1 (A – D) and Bifurcation Case 2 (F – I) at end diastole (A,C,F,H) and mid-systolic deceleration (B,D,G,I), with blue indicating influx and red, efflux. Figs. C,D,H, & I are normalized to show the size of the influx & efflux zones and to emphasize the relative stability of these zones over the pulsatile cycle. Figs. E & J show movement of the virtual boundary separating the influx & efflux zones at three times in the pulsatile cycle: end diastole (red), peak systole (green), and mid-systolic deceleration (blue). Black arrow (Fig. 4.4 A) shows parent artery flow direction for Sidewall Case 1. For bifurcation aneurysms, the parent artery flow direction is normal to the viewing plane.

Figures 6.4 (A, B) show contours of normal velocity for the sidewall aneurysm at two extreme phases: end-diastole and systolic deceleration, respectively. Figures 6.4 (F, G) are corresponding plots for the bifurcation aneurysm. In both aneurysms there is a two-zoned flow structure. There is evidence that systolic deceleration corresponds to the point of maximum potential instability in the pulsatile flow cycle (Salsac et al., 2006). However, in all aneurysm cases studied herein, ostium-plane flow shows little structural change in the high velocity influx-efflux regions throughout the pulsatile cycle.

To establish structural steadiness, Figures 6.4 (C, D) and 6.4 (H, I) re-plot the above flow patterns using a different color scheme. There is clearly a separatrix (or a “virtual boundary) across the ostium plane with zero normal velocity, which is minimally perturbed throughout the cycle. Figures 6.4 (E, J) show the virtual boundaries at different phases for each aneurysm case. Although the peak velocity amplitude varies by a factor of  $\sim 5$  over the cycle, the boundary is stable, with relatively minor excursions involving

low-velocity fluid during mid-systolic deceleration. The sidewall aneurysm, especially, shows a nearly fixed virtual boundary which remains aligned in the direction of the mean arterial flow (Figure 6.4A).

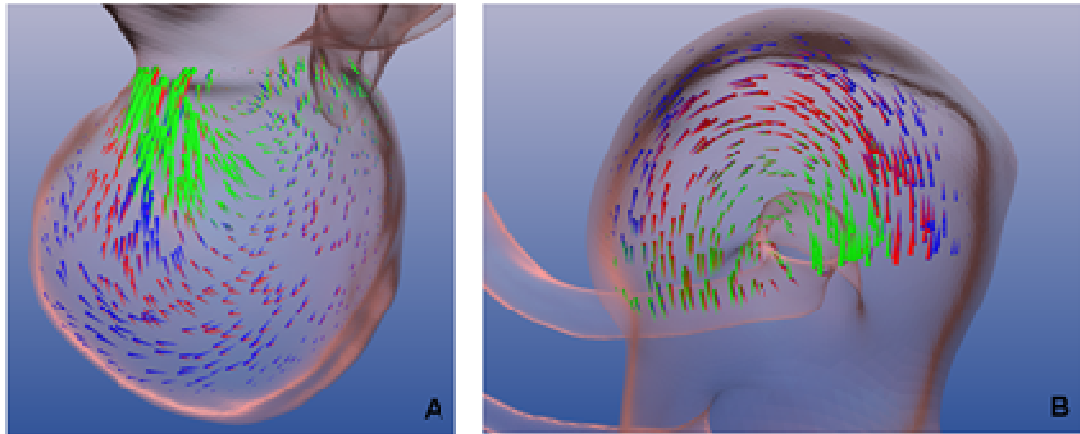


Figure 6.5. Overlaid velocity vectors in the same plane as Figure 4.2 at three different phases of the cycle: end diastole (red), peak systole (green), mid-systolic deceleration (blue) for Sidewall Case 1 (A) and Bifurcation Case 2 (B). There is relatively little change in direction at points of highest velocity over the cycle.

These observations hold for all 6 cases studied here. Structural steadiness of the flow is not restricted to the ostium plane, but applies to the vortical LSS dominating the aneurysmal flow. Overlays of mid-plane velocity vectors at three phases of the pulsatile cycle (Figure 6.5) illustrate that other than the region near the vortex center, which moves slightly during the cycle, the LSS moves very little with time.

### 6.3.2. Waveform Independence

In order to demonstrate that the results are somewhat waveform independent, ostium flux plots for Case 1 sidewall aneurysm model using three different waveforms that have been used in the literature (Cebal et al., Ford et al. and Holdsworth et al.) are shown (Fig 6.6). Not only does the stable segregation of flow exist during both phases of cycle, at

end diastole and peak systole, for all the three waveforms used, but also the spatial flow patterns look similar for the three different waveforms.

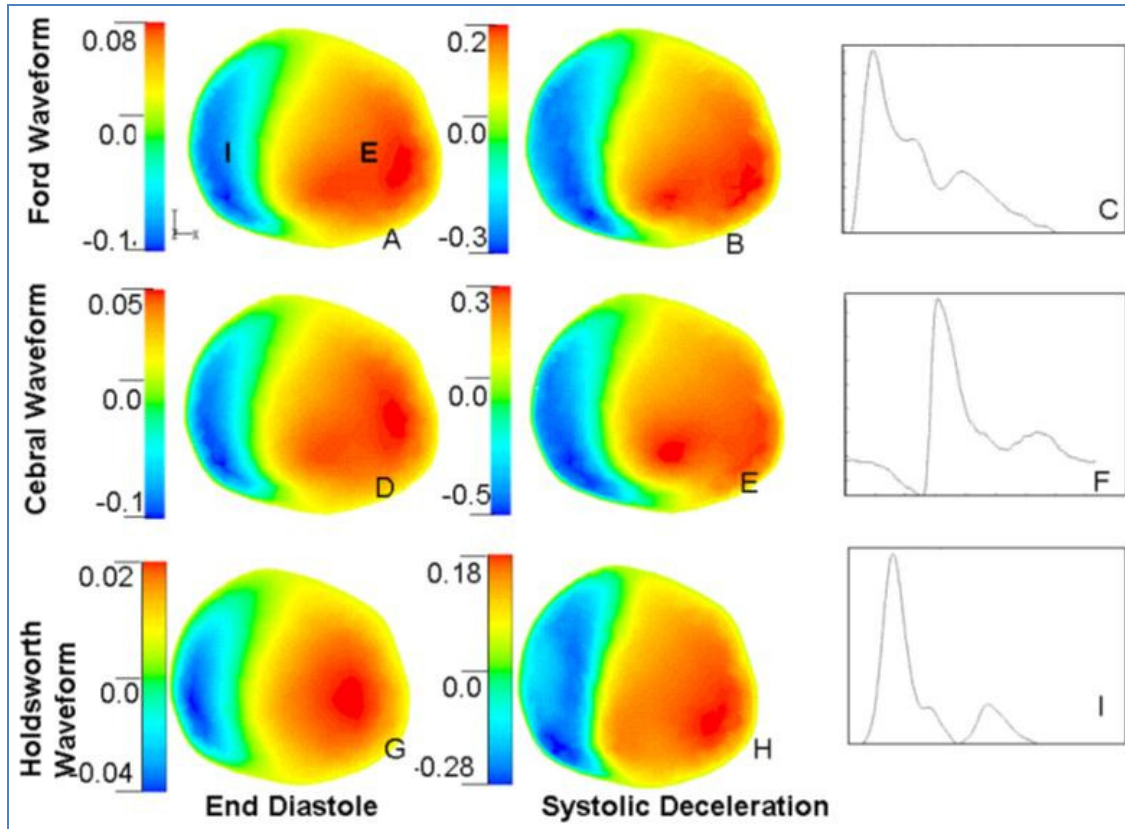


Figure 6.6. Figure A,B,D,E,G,H show the influx and efflux zones for the three sidewall cases respectively. C,F,I show the corresponding waveforms.

### 6.3.3. Additional case

An additional geometry (Fig 6.7) was included in the study of a bifurcation aneurysm that had a very large aspect ratio and the aneurysm extended such that it encompassed the branches, leading to a difficulty in defining the ostium plane. An asymmetric distribution of flow in the branching arteries, development of annular flow (as opposed to bilateral flow observed in other bifurcation and sidewall aneurysm models), reorientation of the

vortical structure, and disruption of the stable ostium flow pattern was therefore observed. However, this only occurred during the systolic phase (during deceleration), when the vortex weakened and shifted slightly; the structure was quickly re-established shortly thereafter. Figure shows the contours of velocity normal to the ostium plane at three different phases of cycle; end diastole, peak systole and systolic deceleration.

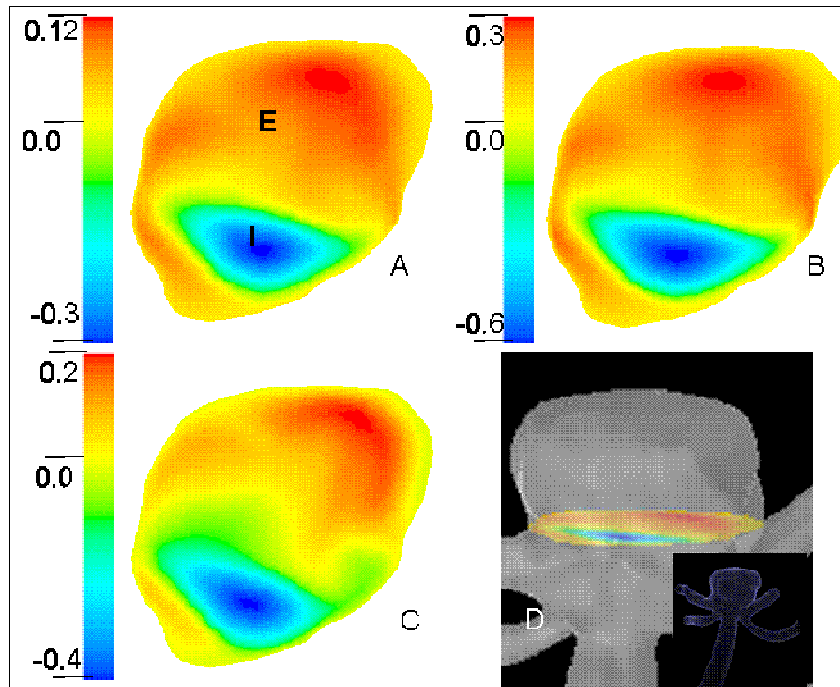


Figure 6.7. A,B,C shows the contours of velocity normal to the ostium plane at three different phases of cycle; end diastole, peak systole and systolic deceleration. Letter I,E on figure 4.7A indicate influx and efflux zone. Figure 4.7 D shows the ostium plane on the aneurysm.

## 6.4. Discussion

Extensive analysis of the aneurismal flow in 3 sidewall and 3 bifurcation aneurysm samples have revealed two principal observations. First, it was found that significantly different aneurysm geometries display qualitatively similar flow patterns; however the simplicity of flow may only be particular to certain class of aneurysm such as those studied here. This simple flow is characterized by stable influx/ efflux zones, generated

by a large eddy near the ostium, which appears to originate from two distinct physical mechanisms (summarized in the figure 6.8 below).

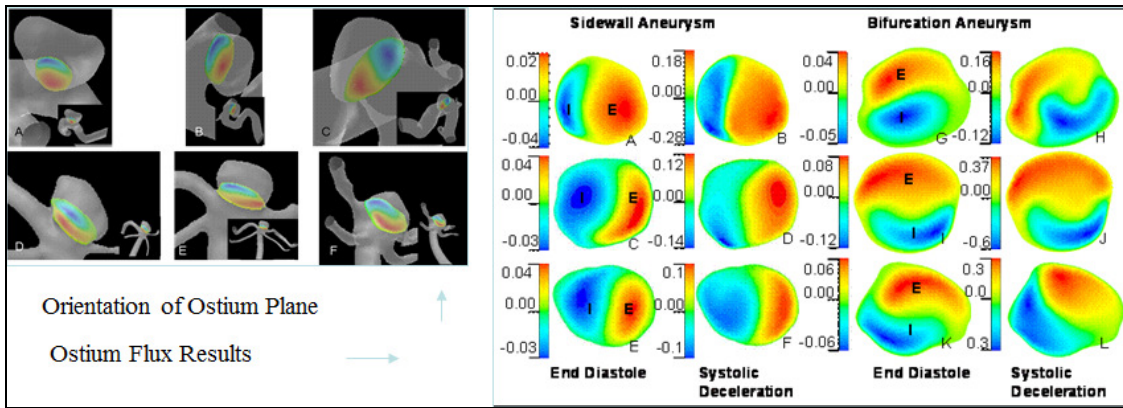


Figure 6.8. Shows the influx and efflux zones of all the aneurysm cases studies herein at the two critical phases of the cycle. To orient the reader, the cross-sectional plots can be seen to the left.

The first is curvature of the main artery proximal to the aneurysm. Swirl is a well-known feature of flows through curved tubes. Centrifugal forces can generate a two-celled pattern of counter-rotating streamwise vortices (Dean, 1927; Dean, 1928; Mantha et al., 2006). For a sidewall aneurysm, fluid from one of the cells of can enter the aneurysm laterally (cf. Figure 3 in Mantha et al., 2006). A second source of swirl can be the geometry of the aneurysm itself. As the flow conforms to the curved surface of the aneurysm wall, there is additional streamline curvature in a plane orthogonal to the arterial cross-sectional plane (Figures 6.2, 6.5). Similar swirling motion occurs in the case of the bifurcation aneurysm. In this case, fluid from the main arterial lumen enters the ostium plane approximately normally, and then is diverted into each of the outgoing arterial branches. Note that specifically *steady* flow was selected in the above discussion, since normally streamlines coincide with fluid particle pathlines only for steady flows (Fox & McDonald, 1992).

For each of the sidewall aneurysms, while peak influx occurs near the distal neck and peak efflux near the proximal neck, the flow actually exhibits a swirling motion with the fluid entering the aneurysm laterally. Note that the streamlines cannot intersect; therefore flow inside the aneurysm is necessarily helical. Note that Figures 6.4 (A, B) are consistent with the in-vitro experimental results of Ujiie et al. (1999), where posterior-*lateral* inflow and anterior-*contralateral* outflow were observed. The region of influx is smaller than the region of efflux, but the net flux through the ostium must be zero by conservation of mass. Segregated flow was also observed for bifurcation aneurysms, although here the influx and efflux zonal areas are more nearly equal. Note that the intrinsic three-dimensionality of these flows limits the usefulness of previous two-dimensional simulations of this problem.

In Strother *et al.* (1992), canine lateral and bifurcating aneurysm flows were studied using ultrasound Doppler velocimetry. They also observed swirling flow and a central vortex within the aneurysm. A sharp segregation between influx and efflux zones was observed, as in Figure 5. Similar observations were made by Yu and Zhao (1999) in their in vitro studies of aneurysm models. Their steady flow analyses found little correlation between aneurysm size and flow characteristics. Radial variations of 50% and 70% in baseline spherical aneurysm models exhibited similar flow characteristics. A single recirculating vortex was observed for Reynolds numbers greater than 700.

The second observation is that the basic flow pattern, viz. a large helical vortex and segregated ostium influx/efflux zones, remains relatively unchanged under steady-state and pulsatile flow conditions. In one of the bifurcation cases, this flow pattern is disrupted briefly during systolic deceleration, but is quickly reestablished by end-systole.

It should be emphasized that “stability” here refers to the large-scale helical structure of the flow, and not the velocity magnitude (which of course varies periodically; Figure 6.3). There are small structural fluctuations (Figure 6.5) due to small shifts in the position of the vortex center, but these appear mainly during deceleration and mainly near the vortex core. Thus, in addition to the stability of the efflux and influx zones through the ostium plane, the principal flow pattern corresponding to the dominant eddy inside the aneurysm exhibits little variation with pulsatility.

Some previous numerical studies find more significant flow variation and suggest dependence of flow patterns on pulsatility (Meng et al., 2004, Tateshima et al., 2003, Valencia et al., 2007, Barath et al., 2004). The reasons for this divergence are not completely clear, but may be related to the size and shape of the aneurysm, angle of ostium plane with respect to the main artery, arterial curvature proximal to the aneurysm, and presence of branches close to the ostium plane. Valencia et al. (2007) considered an aneurysm with an aspect ratio (aneurysm depth/neck width) of about 4, while this study involved much smaller ratios and simpler shapes. Ujiie et al. (1999), using a rabbit aneurysm model, found that flow complexity increased with aneurysm aspect ratio. An additional study was performed on a bifurcation aneurysm, with asymmetric posterior branches very close to the ostium plane. This led to an asymmetric distribution of flow in the branching arteries, reorientation of the vortical structure, and disruption of the stable ostium flow pattern. However, this only occurred during the systolic phase, when the vortex weakened and shifted slightly; the structure was quickly re-established shortly thereafter.

Some studies, e.g. Valencia *et al.* (2006b), have focused on highly symmetric models. Such flow patterns may be unstable to deviations from symmetry, and are therefore rarely observed in reality. More realistic aneurysm geometries, such as those studied here, may display stable LSS. Barath *et al.* (2004) used particle cloud images to deduce a coherent vortical structure in their *in vitro* experiments of an internal carotid artery aneurysm. While this structure did not remain stationary, they noted a periodic motion of the vortex over the pulsatile cycle. Although their aspect ratio was similar to this study, the ostium plane was highly skewed with respect to parent artery.

Also, LSS can be destabilized by large flow reversal, but this is not a common phenomenon in cerebral arteries. The Tatehima study (2003) showed that the locations of peak inflow and outflow at the aneurysm orifice did not vary with phase; velocity patterns inside the aneurysm showed little dependence on pulsatility -- consistent with our results. In a similar study Cebal *et al.* (2005) classified small size aneurysms into four categories based on flow inside the aneurysm. Although the aneurysm showed different flow patterns among the cases studied, it is interesting to note that the position of inflow jet was invariant throughout the pulsatile cycle and these aneurysms did not show variation in spatial flow patterns at different phases of pulsatile cycle. In other words, structural steadiness of flow was maintained in all the small aneurysms throughout the pulsatile cycle. The close resemblance between steady-state and pulsatile flow -- if truly generic (for the specific class of aneurysms and waveforms studied here) -- can be exploited for diagnostic simulations in clinical practice. Steady-state simulations are significantly simpler and easier to analyze than transient simulations.

Another implication of this structural stability relates to stent performance. While Barath et al. (2004) noted a 32% reduction in flow through the ostium in the presence of a stent, the vortex persisted with only a slight perturbation to its pre-stent trajectory. This is consistent with our observations of the stability of aneurismal LSS, and suggests that more vigorous flow diversion may be necessary to disrupt the aneurismal vortex and significantly reduce ostium flux.

## **6.5. Conclusions**

Two specific types of cerebral aneurysms were studied: sidewall and bifurcation, with three samples per type. The principal flow patterns are distinct inflow and outflow zones at the ostium and a coherent vortical structure inside the aneurysm. These patterns are stable throughout the pulsatile cycle; furthermore, pulsatile and steady flows show similar flow patterns.

To the extent that the basic flow patterns are invariant with time, much of this analysis could be based on steady flow simulations alone. The autonomous cerebral blood flow auto-regulation mechanism (Brys et al., 2003) will tend to maintain this flow stability over a wide range of physiological conditions. Knowledge of aneurysmal flow patterns is important in the design of endovascular devices (flow diverters, stents, and coils), and in planning clinical intervention. For example, customized stents with asymmetrical porosity may effectively modify the ostium flow pattern.

The cases discussed here were chosen randomly from clinical data. While this chapter reports observations that are generally applicable to all the cases studied, it has not yet been possible to quantify the detailed effects of aneurysm size, shape, and location on the

observed phenomena. Such analyses are necessary and should include a larger sample of aneurysms selected to provide a wider range of sizes, shapes and locations.

## Chapter 7

### 7. Summary and Conclusions

Having discussed the results and observations from our computational fluid dynamics-based investigation of hemodynamic effects in realistic arterial geometries, we present in this chapter a summary of our key results and conclusions. Following the discussion of our hypothesis, this chapter presents the main aspects of our future research plan. Before proceeding to these, the following section provides a summary of our results so far.

#### 7.1. Key Results and Conclusions

This work is an extension of the paper (Mantha et al., 2006) wherein a conceptual model was developed of how hemodynamic factors can trigger a chain of physiological mechanisms that leads to aneurysm genesis. The hypothesis is synthesized from our observations of the hemodynamics and the AFI measure developed on the basis of these observations. Since the present work has modeled neither the solid mechanics of the arterial wall nor the possible biochemical effects stemming from the hemodynamics, both of which are essential to developing a complete model for aneurysm genesis, we also included various observations from the biological literature to postulate a possible scenario of aneurysm genesis.

In this study, we first did a systematic review of all the major indicators proposed in the literature that have been correlated to the sites of disturbed flow. It was suggested that regions of high speed flow, WSS and WSS gradients lead to weakening of the vessel wall, leading to aneurysm initiation. However, it was shown that the experiments were

not conclusive and the regions of high WSS and high WSSG were very close to regions of low oscillatory WSS which is known to have a deleterious effect on vessel wall. For some indicators that are proposed in the literature like OSI, variations of WSSG are plotted and compared against the AFI (Figure 7.1).

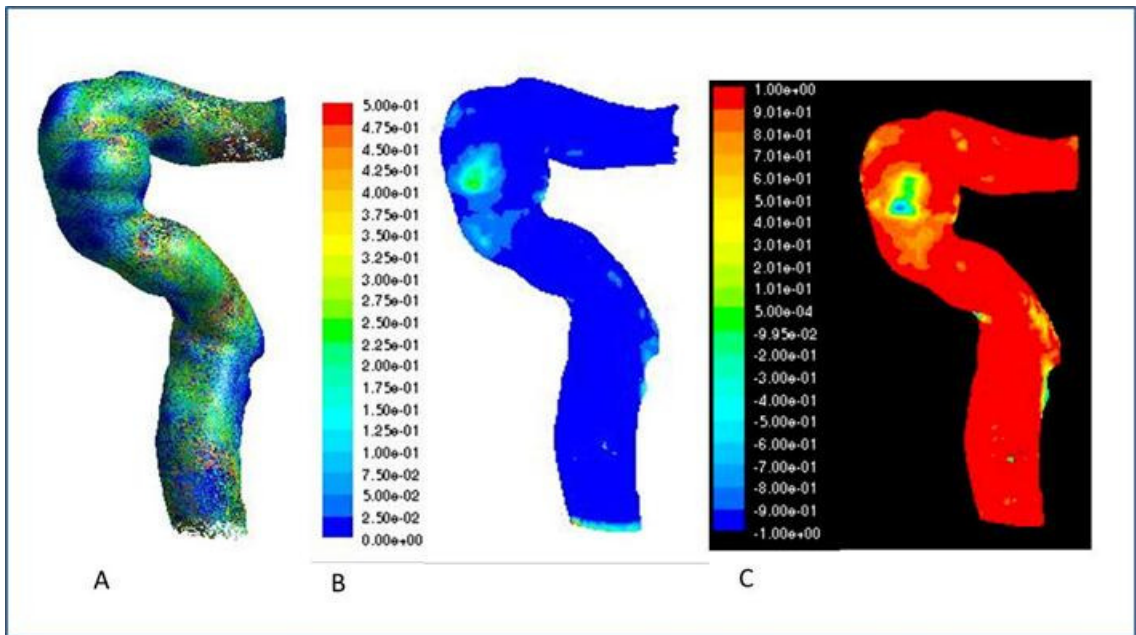


Figure 7.1. Contours of WSSG, OSI and AFI for sidewall aneurysm case 1.

While OSI does correlate with locations of aneurysm sites, it does not capture the instantaneous effects of WSS on the vessel wall and the OSI values were indeed very low (about 0.1). In addition, there are several limitations when using this indicator. In addition it remains to be established if the endothelial cells align with the direction of the temporally averaged WSS vector. It could very well be that the alignment is along the vector direction during diastole, which dominates the heart cycle temporally. Alternatively, the cells could simply align themselves with respect to the geometry, in which case the reference vector direction would correspond to the flow direction in the limit of creeping flow (a low-Reynolds number steady flow, in which the streamlines are

approximately parallel to the axis of the geometry).  $OSI=0$  for unidirectional flow and  $OSI=0.5$  for oscillatory flow, but intermediate OSI values may imply either (a) that there was flow reversal and oscillation for a small portion of the cycle, or (b) sustained rotation of the instantaneous WSS vector throughout the cycle. OSI fails to distinguish these two cases.

Several correlations between arterial diseases and temporal or spatial WSS gradients (WSSG) have been postulated. The WSSG attempts to capture the effects of changing surface forces on the endothelium (Nerem 1986, 1996). These researchers studied the spatial variations in WSS to predict the correlation between endothelial cell dynamics and non-uniform hemodynamic factors. It was postulated that large spatial WSSGs induce morphological changes in the EC, which contribute to elevated wall permeabilities and hence flow associated diseases (DePaolo 1992). However, this hemodynamic indicator can be quite tricky to compute using the commercially available software code such as Fluent. Through our study, it was demonstrated that WSSG is quite sensitive to mesh resolution, meshing scheme, and modality of image acquisition in addition to the errors originating from image segmentation and the reconstruction procedures used. This would explain why regions of high WSSG are seen at most locations in the artery (Figure 7.1a), potentially leading to many false positives.

When we compare these results to the contours of AFI (Figure 7.1c), not only does AFI capture the instantaneous effects of WSS, it correlates well with the location of aneurysm site. What makes AFI more reliable is that it is based on a simpler hemodynamic variable, the WSS which is not as sensitive to meshing scheme or resolution; thus the reason there are fewer false positives associated with this indicator.

Having established AFI as a potential aneurysm formation indicator, we performed a parametric study of the effect of change in waveforms to hemodynamics in the artery and whether or not AFI can really capture those subtle changes. We first used an idealized waveform and varied the slope of deceleration; the steeper slope representing a healthy young adult and a more blunt representing that of an older adult. By keeping everything else fixed and changing the slope of deceleration, we could isolate this phenomenon and simplify the analysis. This component of flow waveform is important because it has been shown that most instability occurs during post systolic peak deceleration.

Subsequent to this analysis, four different waveforms from two separate studies were investigated: Old and Young adult waveforms (Hoi et al. 2010) and those of active and sedentary older adults (Azhim et al. 2009). We found subtle changes in development and progression of counter-rotating eddies, thereby effecting the formation of stagnation zone and the WSS patterns. As these changes were subtle, it could be misinterpreted as the shape has no effect on the hemodynamics. However, upon more careful examination of contours of AFI, these effects were clearer making AFI a sensitive indicator. Furthermore, distinct differences between young active and sedentary older adults were also seen. The changes with age in the shape of the waveform is a result of the gradual degeneration of the vascular bed and therefore to a great extent reflect vascular health. These changes were well captured by AFI, establishing AFI as a reliable indicator. Although results of only one sidewall aneurysm model were presented in the analysis, Figure 7.2 shows contours of AFI for wave 4 for all the three cases studied. It should be noted that the preceding ramification (elevated AFI at sites of aneurysm formation) of arterial geometry and associated hemodynamic factors are always present. However, with

the presence of additional factors, such as hypertension and higher heart rates (during exercise or other stressful activities), oscillation and suppression of WSS are augmented, providing impetus to vascular degenerative processes associated with these hemodynamic factors. At these locations, repetitive and sustained exposure to high pressures and low, oscillatory WSS will cause a local weakening of the vessel wall. A weakened wall may subsequently be incapable of withstanding the physiological temporal pressure gradients experienced by any normal artery, particularly under the condition of elevated systolic pressure, causing it to deform and bulge into aneurysm.

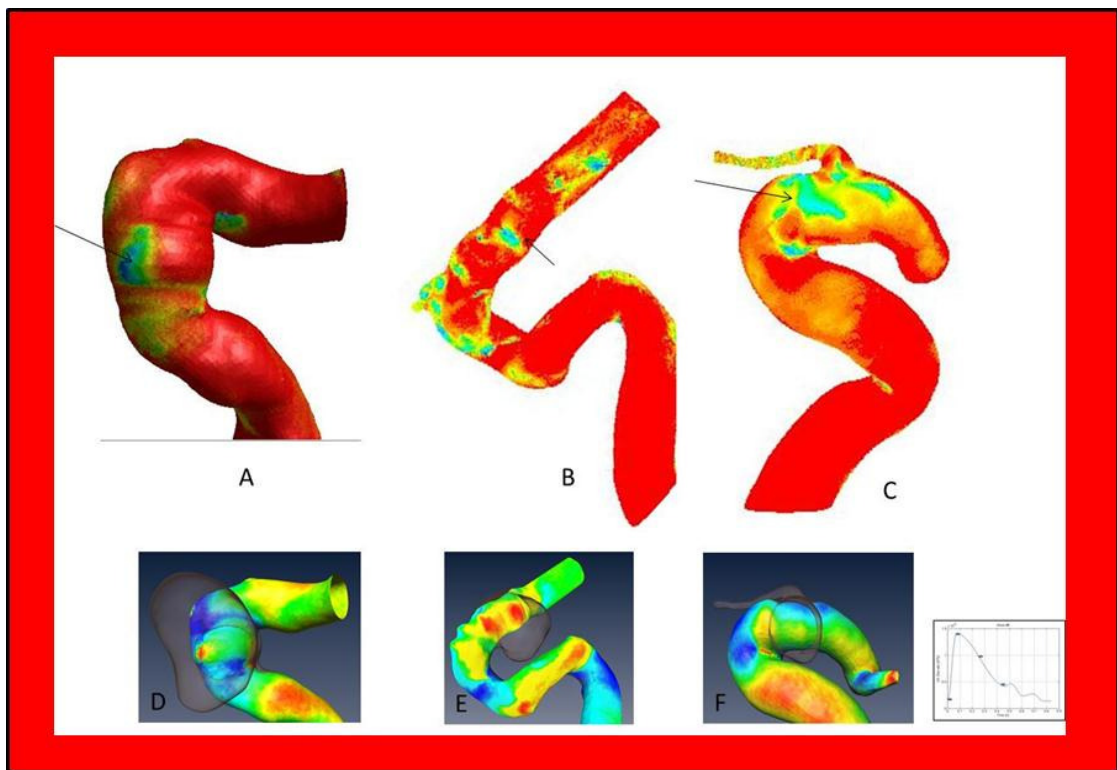


Figure 7.2. Contours of AFI was the three cases studies here in. D, E, F show the pre-aneurysmal artery overlaid with the artery where aneurysm is present to clearly indicate the region of interest. Regions of aneurysm sites (A, B, C) are indicated by black arrows. Inset shows Wave 4.

Having proposed a possible hypothesis of aneurysm initiation, the focus of the next study was to characterize the flow across the neck of an aneurysm (i.e. ostium plane), and its variation over the pulsatile cycle. Hemodynamically generated normal and shear stresses can affect the location of aneurysm formation, as well as the evolution of the aneurysm. Thus, specific flow patterns may be important in the design and the application of stents, coils and other remedial strategies. 3D-DSA data from three sidewall and a bifurcation aneurysm were used to perform computation hemodynamic simulations. Analysis of flow across the ostium plane of these aneurysm shows, somewhat unexpectedly, that there is virtually no change in the flow structure throughout the phase of the pulsatile flow cycle. Quasi-permanent regions of flow influx-efflux across the ostium plane exist, separated by a virtual wall (Figure 7.3).

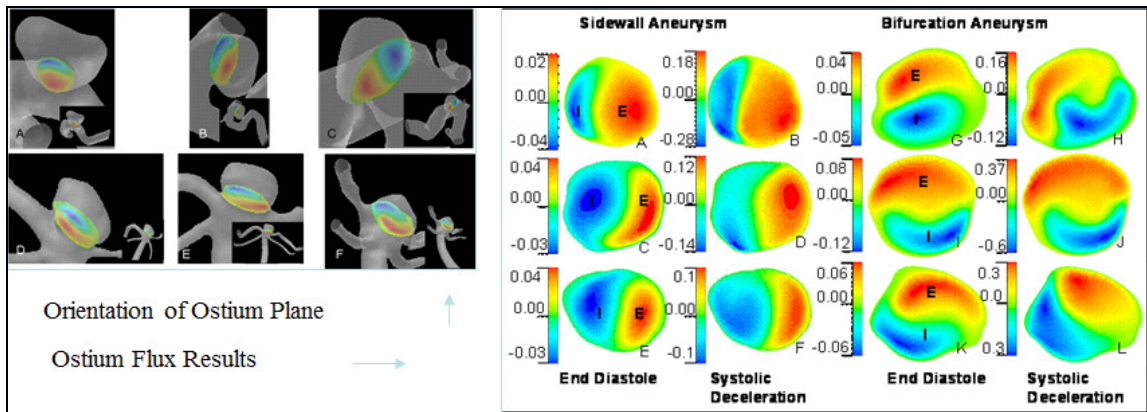


Figure 7.3. Shows the influx and efflux zones of all the aneurysm cases studies herein at the two critical phases of the cycle. To orient the reader, the cross-sectional plots can be seen to the left.

These observations, based on numerical simulations, are consistent with clinical data from ultrasound Doppler velocimetry, suggesting that many aspects of intracranial hemodynamics can be analyzed through steady state simulations- much simpler than simulating pulsatile flow. This study helped understand the hemodynamic influences on aneurysm stability enabling better stent design and other flow diverting devices.

## 7.2. Recommendations for Future Work

In this section some potential extensions of our current research towards a more complete description of the blood flow-related arterial diseases are described. In the present work, we used three different models of intra-cranial sidewall aneurysms. In reality, there are three other major types of aneurysms, of which bifurcation aneurysms are the most common. From our results, we speculate that the etiology of sidewall and bifurcation aneurysms may have common elements, both being in the regions of low WSS. This hypothesis of common etiology requires confirmation, through simulations of bifurcation aneurysms under similar conditions as in the present work, i.e. in pre- and post-aneurysmal situations. Further, the correlations we have observed among the three cases studied here need to be unambiguously established to hold for aneurysms appearing in other arterial segments and having different geometries. This can be done by considering a larger sample size of real patient data. In addition these results should be validated with carefully planned experiments and also longitudinal studies in real patients who have cardiovascular disease.

Real arterial geometries involve many extraneous complicating factors, such as variations of arterial cross-sectional area, non-uniform and irregular curvatures. These significantly affect the quantities of interest, but it can be difficult to characterize the flow. To alleviate this problem, an idealized arterial geometry should be considered, featuring uniformly circular cross-section and segments with uniform curvature. It is interesting to note that the arterial models we used feature *two* bends, with the aneurysm in each case appearing at the second bend. This is probably an important geometrical detail that needs to be included in the model, since the incoming profiles at the second

bend are controlled by the curvature experienced by the fluid at the first bend. Therefore, first an idealized pipe model that is the closest approximation to the real artery should be studied. Second, the flow should be characterized in terms of the controlling parameters (such as, the Dean number and the Womersley number). Eventually, a database of simulations over a realistic range of these governing parameters could form the basis for an automated software tool that can be quickly customized to simulate specific, individual patient data, enabling the physician to be aware of arterial segments that are vulnerable. This should be recognized as an intermediate step toward the ultimate goal of performing accurate, patient specific geometric or waveform similarities to the relevant indicators as this work has shown. A major factor in reaching this goal is the development of sufficiently accurate clinical arterial scanners.

As discussed earlier, blood is a colloid, containing several types of particulate materials. While the homogenous, single-phase, Newtonian fluid assumption is legitimate as a first approximation, two-phase, non-Newtonian physics may be needed to capture certain subtle features. Perhaps the most important of these is the deposition of monocytes in certain regions (e.g. corresponding to low or oscillatory WSS). Such deposition, controlled by fluid mechanical effects, has important biological ramifications. Wherever platelet deposition occurs, it tends to cause degeneration of arterial tissue, as discussed earlier. Arterial tissue degeneration, by affecting the mechanical properties of the wall, is an important parameter in determining the susceptibility to cardio-vascular diseases. To study particle deposition, two-phase simulations involving particles suspended in a homogeneous fluid should be performed. A variety of numerical approaches are possible, with varying degrees of computational effort involved. As a first

approximation, fluid containing homogeneous, neutrally buoyant particles should be modeled to capture this effect. Furthermore, it is important to validate these simulations through careful experiments.

In order to better understand the effect of WSS on endothelial cells, a more sophisticated model needs to be developed. Currently (and also in this study), the hemodynamic analysis is performed and then, based on the literature available, correlations between the flow and EC behavior are obtained. An important goal of a more sophisticated model would be to capture the EC response. We propose to do this in the following way:

Highly accurate geometric data of the artery capturing the ECs topology (cell lining at the lumen) has to be obtained using high resolution Micro-CT scans. This can be achieved by first performing flow experiments on EC lined in a phantom model of an artery and extracting the geometric data using Micro-CT that can capture the topology of the EC alignment in the phantom model. Experiments have been performed in glass tubes where ECs have been cultured and straining has been used to determine to see if the cells are viable after 24,36,48 and 72 hour periods. (Kenneth et al., 2006). A similar technique can be used to align EC in more complex geometries such as the phantom model of the artery and exposing them to varying flow.

Since the geometric data is available, the next step is to extract this geometric data and defining the computational domain. It is important to incorporate the biomechanics of the arterial wall based on the existing literature. Some studies have demonstrated the feasibility of this technique wherein arterial wall properties have been used as the

boundary conditions at the wall and incorporate wall motion and pulse waves. (Watton et al., 2010)

Model EC behavior in response to WSS based on the experimental data. For example, WSS derived from hemodynamic analysis at the aneurysmal level could be used in NO generation models in ECs, which could then be coupled with apoptosis models of SMCs. Loss of SMCs leads to a weakened wall and changes lumen diameters and, thus, affects WSS and wall remodeling. This modeling cycle encompasses multiple spatial and temporal scales at different levels of biological organization.

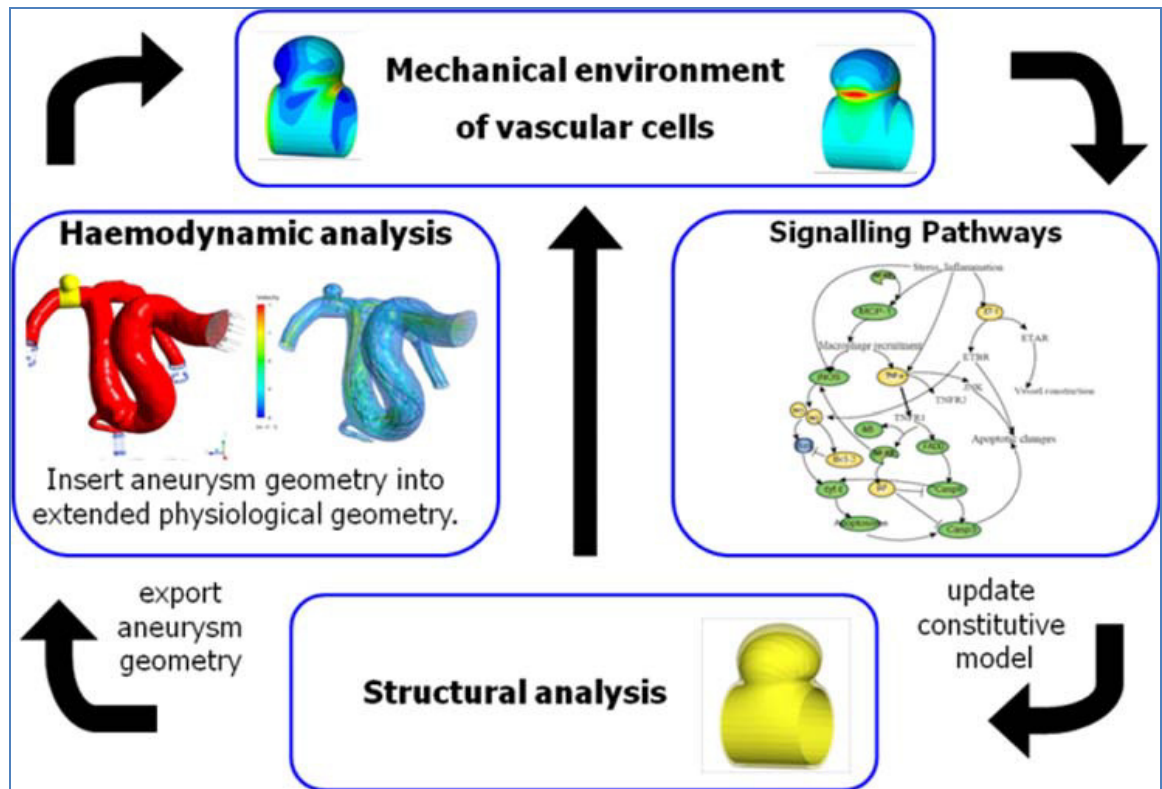


Figure 7.4. Multiscale modeling framework for IA evolution combining structural, hemodynamic, and signaling pathway analysis. (Adapted from Ho et al., 2011).

While it is imperative to validate this model with experiments, once this approach has been demonstrated to be accurate enough to capture EC behavior in response to flow, it would provide flexibility to systematically analyze the relevant phenomenon occurring at the disturbed flow regions. Incorporating the EC behavior in the computational model could link the biochemical responses of the arterial wall to fluid flow with the aim to better understanding flow associated diseases such as atherosclerosis and aneurysms.

The ultimate goal of all these efforts would be to develop a computational model that incorporates physiological responses of the vessel wall to hemodynamic stimuli, on a patient-specific basis. The model should not only be capable of predicting the present state of the artery, but also by taking as input factors such as age, gender, state of health, and genetic make-up, be able to (a) predict the risk of future arterial degeneration, (b) diagnose the locations most prone to disease, and (c) provide recommendations for the most suitable therapeutic measures. Such a tool would facilitate efficient early diagnosis or prevention, reducing the need for expensive and risky surgical procedures.

## 8. References

- Alberding, J. P., Baldwin, A. L., Barton, J. K., & Wiley, E. (2004). Onset of pulsatile pressure causes transiently increased filtration through artery wall. *American journal of physiology. Heart and circulatory physiology*, 286(5), H1827-35.
- Alnaes, M. S., Isaksen, J., Mardal, K.-A., Romner, B., Morgan, M. K., & Ingebrigtsen, T. (2007). Computation of hemodynamics in the circle of Willis. *Stroke; a journal of cerebral circulation*, 38(9), 2500-5.
- Alnæs, M. S., & Isaksen, J. (2007). Computation of Hemodynamics in the Circle of Willis. *Clinical Hemorheology*, 2500-2505.
- Antiga, Luca. (2002). *Patient-Specific Modeling of Geometry and Blood Flow in Large Arteries*.
- Antiga, Luca, Piccinelli, M., Botti, L., Ene-Iordache, B., Remuzzi, A., & Steinman, D. a. (2008). An image-based modeling framework for patient-specific computational hemodynamics. *Medical & biological engineering & computing*, 46(11), 1097-112.
- Azhim, A, Katai, M., Akutagawa, M., Hirao, Y., & Yoshizaki, K. (2007). Exercise Improved Age-associated Changes in the Carotid Blood Velocity Waveforms. *Pharmaceutical Engineering*, 1, 17-26.
- Azhim, Azran, Akioka, K., Akutagawa, M., Hirao, Y., Yoshizaki, K., Obara, S., Nomura, M., et al. (2007). Effect of gender on blood flow velocities and blood pressure: role of body weight and height. *Conference proceedings*: ... *Annual International Conference of the IEEE Engineering in Medicine and Biology Society. IEEE Engineering in Medicine and Biology Society. Conference, 2007*, 967-70

- Azhim, Azran, Akioka, K., Akutagawa, M., Hirao, Y., Yoshizaki, K., Obara, S., Nomura, M., et al. (2007). Effects of aging and exercise training on the common carotid blood velocities in healthy men. *Conference proceedings*: ... *Annual International Conference of the IEEE Engineering in Medicine and Biology Society. IEEE Engineering in Medicine and Biology Society. Conference, 2007*, 989-93.
- Azhim, Azran, Akutagawa, M., Yoshizaki, K., Obara, S., Nomura, M., Tanaka, H., & Kinouchi, Y. (2008). Wireless blood velocity spectra measurement system for healthcare evaluation: reference data. *Conference proceedings*: ... *Annual International Conference of the IEEE Engineering in Medicine and Biology Society. IEEE Engineering in Medicine and Biology Society. Conference, 2008*, 1427-30.
- Azhim, Azran, Katai, M., Akutagawa, M., Hirao, Y., Yoshizaki, K., & Obara, S. (2006). Measurement of Blood Flow Velocity Waveforms in the Carotid , Brachial and Femoral Arteries during Postural Change. *Pharmaceutical Engineering*, 438-442.
- Bacabac, R. G., Smit, T. H., Cowin, S. C., Van Loon, J. J. W. a, Nieuwstadt, F. T. M., Heethaar, R., & Klein-Nulend, J. (2005). Dynamic shear stress in parallel-plate flow chambers. *Journal of biomechanics*, 38(1), 159-67.
- Bao, X., Lu, C., & Frangos, J. A. (1999). Temporal Gradient in Shear But Not Steady Shear Stress Induces PDGF-A and MCP-1 Expression. *Blood*, 996-1003.
- Berger, S. A., & Jou, L. (2000). Flows in Stenotic Vessels. *Annual review of fluid mechanics*, 32, 347-382.
- Bullitt, E., Rahman, F. N., Smith, J. K., Kim, E., Zeng, D., Katz, L. M., & Marks, B. L. (2009). The effect of exercise on the cerebral vasculature of healthy aged subjects as visualized by MR angiography. *AJNR. American journal of neuroradiology*, 30(10), 1857-63.

- Byun, H. S., & Rhee, K. (2004). CFD modeling of blood flow following coil embolization of aneurysms. *Medical engineering & physics*, 26(9), 755-61.
- Cantón, Gador, Levy, D. I., & Lasheras, J. C. (2005). Hemodynamic changes due to stent placement in bifurcating intracranial aneurysms. *Journal of neurosurgery*, 103(1), 146-55.
- Cantón, Gádor, Levy, D. I., & Lasheras, J. C. (2005). Changes in the intraaneurysmal pressure due to HydroCoil embolization. *AJNR. American journal of neuroradiology*, 26(4), 904-7.
- Cantón, Gádor, Levy, D. I., Lasheras, J. C., & Nelson, P. K. (2005). Flow changes caused by the sequential placement of stents across the neck of sidewall cerebral aneurysms. *Journal of neurosurgery*, 103(5), 891-902.
- Castro, M a, Putman, C. M., & Cebral, J. R. (2006). Patient-specific computational fluid dynamics modeling of anterior communicating artery aneurysms: a study of the sensitivity of intra-aneurysmal flow patterns to flow conditions in the carotid arteries. *AJNR. American journal of neuroradiology*, 27(10), 2061-8.
- Castro, M a, Putman, C. M., & Cebral, J. R. (2006). Computational fluid dynamics modeling of intracranial aneurysms: effects of parent artery segmentation on intra-aneurysmal hemodynamics. *AJNR. American journal of neuroradiology*, 27(8), 1703-9.
- Castro, Marcelo a, Putman, C. M., & Cebral, J. R. (2006). Patient-specific computational modeling of cerebral aneurysms with multiple avenues of flow from 3D rotational angiography images. *Academic radiology*, 13(7), 811-21.
- Cattaruzza, M., Dimigen, C., Ehrenreich, H., & Hecker, M. (2000). Stretch-induced endothelin B receptor-mediated apoptosis in vascular smooth muscle cells. *FASEB journal*: official publication of the Federation of American Societies for Experimental Biology, 14(7), 991-8.

- Cebral, Juan R, Castro, M. a, Burgess, J. E., Pergolizzi, R. S., Sheridan, M. J., & Putman, C. M. (2005). Characterization of cerebral aneurysms for assessing risk of rupture by using patient-specific computational hemodynamics models. *AJNR. American journal of neuroradiology*, 26(10), 2550-9.
- Cebral, Juan R, Pergolizzi, R. S., & Putman, C. M. (2007). Computational fluid dynamics modeling of intracranial aneurysms: qualitative comparison with cerebral angiography. *Academic radiology*, 14(7), 804-13
- Cebral, Juan R, Yim, P. J., Löhner, R., Soto, O., & Choyke, P. L. (2002). Blood flow modeling in carotid arteries with computational fluid dynamics and MR imaging. *Academic radiology*, 9(11), 1286-99.
- Cha, K. S., Balaras, E., Lieber, B. B., Sadasivan, C., & Wakhloo, A. K. (2007). Modeling the interaction of coils with the local blood flow after coil embolization of intracranial aneurysms. *Journal of biomechanical engineering*, 129(6), 873-79.
- Chen, J., & Lu, X.-Y. (2006). Numerical investigation of the non-Newtonian pulsatile blood flow in a bifurcation model with a non-planar branch. *Journal of biomechanics*, 39(5), 818-32.
- Cheng, C., Tempel, D., van Haperen, R., van der Baan, A., Grosveld, F., Daemen, M. J. a P., Krams, R., et al. (2006). Atherosclerotic lesion size and vulnerability are determined by patterns of fluid shear stress. *Circulation*, 113(23), 2744-53.
- Comerford, a, Plank, M. J., & David, T. (2008). Endothelial nitric oxide synthase and calcium production in arterial geometries: an integrated fluid mechanics/cell model. *Journal of biomechanical engineering*, 130(1), 011010.
- Dean WR.(1927) Note on motion of fluid in a curved pipe. *Phil Mag* 4: 208

Dean WR. (1928)The stream line motion of fluid in a curved Pipe. *Phil Mag* 5: 673

Ding, Z., Wang, K., Li, J., & Cong, X. (2001). Flow field and oscillatory shear stress in a tuning-fork-shaped model of the average human carotid bifurcation. *Journal of biomechanics*, 34(12), 1555-62.

Deng X, King MW and Guidoin R (1994): Localization of atherosclerosis in arterial junctions: Concentration distribution of LDL at luminal surface in regions of disturbed flow, *ASAIO J*, 41:58-67

Deng X, Marois Y, How T, Merhi Y, King MW and Guidoin R (1995): Luminal surface concentration of LDL and its effects on the wall uptake of cholesterol on canine carotid arteries, *J Vasc Surg*, 21:135-145,

Deng XY and Karino T (1989): Effects of steady laminar re-circulation flows on mass transfer from a flowing fluid to a semi-permeable vessel wall. *7 th Int. Congr. of Biorheology Abstracts* 26(3): 604

Depaola N, Gimbrone MA, Davies PF and Dewy CF (1992): Vascular endothelium response to fluid shear stress gradients, *Arteriosler. Thromb.* 12(11): 1254-1257

Donovan Jr, Mcciwain, R.W: Experimental Correlations to predict fluid resistance of Fluid (1994). *Biomedical Engineering* 1116:516-521

Doenitz, C., Schebesch, K.-M., Zoepfel, R., & Brawanski, A. (2010). A mechanism for the rapid development of intracranial aneurysms: a case study. *Neurosurgery*, 67(5), 1213-21; discussion 1221.

Dolan, J. M., Meng, H., Singh, S., Paluch, R., & Kolega, J. (2011). High fluid shear stress and spatial shear stress gradients affect endothelial proliferation, survival, and alignment. *Annals of biomedical engineering*, 39(6), 1620-31.

- Feldman, C. L., Coskun, A. U., Yeghiazarians, Y., Kinlay, S., Wahle, A., Olszewski, M. E., Rossen, J. D., et al. (2006). Remodeling characteristics of minimally diseased coronary arteries are consistent along the length of the artery. *The American journal of cardiology*, 97(1), 13-6.
- Feldman, C. L., Ilegbusi, O. J., Hu, Z., Nesto, R., Waxman, S., & Stone, P. H. (2002). Determination of in vivo velocity and endothelial shear stress patterns with phasic flow in human coronary arteries: A methodology to predict progression of coronary atherosclerosis. *American Heart Journal*, 143(6), 931-939.
- Finol, E. a, & Amon, C. H. (2002). Flow-induced wall shear stress in abdominal aortic aneurysms: Part I--steady flow hemodynamics. *Computer methods in biomechanics and biomedical engineering*, 5(4), 309-18.
- Finol, E. a, & Amon, C. H. (2002). Flow-induced wall shear stress in abdominal aortic aneurysms: Part II--pulsatile flow hemodynamics. *Computer methods in biomechanics and biomedical engineering*, 5(4), 319-28.
- Fisher, C., & Rossmann, J. S. (2009). Effect of non-newtonian behavior on hemodynamics of cerebral aneurysms. *Journal of biomechanical engineering*, 131(9), 091004.
- Ford, M D, Hoi, Y., Piccinelli, M., Antiga, L., & Steinman, D. a. (2009). An objective approach to digital removal of saccular aneurysms: technique and applications. *The British journal of radiology*, 82 Spec No, S55-61.
- Ford, Matthew D, Lee, S.-W., Lownie, S. P., Holdsworth, D. W., & Steinman, D. a. (2008). On the effect of parent-aneurysm angle on flow patterns in basilar tip aneurysms: towards a surrogate geometric marker of intra-aneurismal hemodynamics. *Journal of biomechanics*, 41(2), 241-8.

Gao, Ling, Hoi, Y., Swartz, D. D., Kolega, J., Siddiqui, A., & Meng, H. (2008). Nascent aneurysm formation at the basilar terminus induced by hemodynamics. *Stroke; a journal of cerebral circulation*, 39(7), 2085-90.

Glor, F. P., Ariff, B., Hughes, a D., Crowe, L. a, Verdonck, P. R., Barratt, D. C., Thom, S. a M., et al. (2004). Image-based carotid flow reconstruction: a comparison between MRI and ultrasound. *Physiological Measurement*, 25(6), 1495-1509.

Gosgnach, W., Messika-zeitoun, D., Gonzalez, W., Philipe, M., Michel, J.-baptiste, Liu, R., Hotta, Y., et al. (2012). Shear stress induces iNOS expression in cultured smooth muscle cells: role of oxidative stress Shear stress induces iNOS expression in cultured smooth muscle cells: role of oxidative stress. *American Journal Of Physiology*, 279, 1888-2000.

Grinberg, L., & Karniadakis, G. E. (2008). Outflow boundary conditions for arterial networks with multiple outlets. *Annals of biomedical engineering*, 36(9), 1496-514.

Grotberg, J. B., & Jensen, O. E. (2004). Biofluid Mechanics in Flexible Tubes. *Annual Review of Fluid Mechanics*, 36(1), 121-147.

Guo, X., & Kassab, G. S. (2009). Role of shear stress on nitrite and NOS protein content in different size conduit arteries of swine. *Acta physiologica (Oxford, England)*, 197(2), 99-106.

Glynn LE (1940): Medical defects in the circle of Willis and their relation to aneurysm formation. *J Pathol* 51:213-222

Goldman (1999): Cecil Textbook of Medicine. 21st ed. Philadelphia, Pa: W B Saunders Co;

Gonzalez CF, Cho YI, Ortega HV, Moret J (1992) Intracranial aneurysms: Flow analysis of their origin and progression. *American Journal of Neuroradiology* 13(1): 181-188

- Groden C, Laudan J, Gatchell S, Zeumer H (2001) Three-dimensional pulsatile flow simulation before and after endovascular coil embolization of a terminal cerebral aneurysm. *Journal of Cerebral Blood Flow & Metabolism*; 21(12): 1464-1471
- Hartley CJ, Reddy AK, Madala S, Entman ML, Michael LH and Taffet GE (2004), Non-invasive ultrasonic measurement of arterial wall motion in mice, *Am J. Physiol. Heart Circ. Physiol.* 287: H1426-1432 He X, Ku DN (1994). Unsteady entrance flow development. *Journal of Biomedical Engineering* ;116:302-310
- Helmlinger G, Geiger RW, Shrek S and Nerem RM (1991): Effects of pulsatile flow on cultured vascular endothelial cell morphology. *J Biomech Eng*, 113: 123-131
- Hashimoto, N, Kim, C., Kikuchi, H., Kojima, M., Kang, Y., & Hazama, F. (1987). Experimental induction of cerebral aneurysms in monkeys. *Journal of neurosurgery*, 67(6), 903-5.
- Hashimoto, T., Meng, H., & Young, W. L. (2006). Intracranial aneurysms: links among inflammation, hemodynamics and vascular remodeling. *Neurological research*, 28(4), 372-80.
- Hassan, T., Timofeev, E. V., Saito, T., Shimizu, H., Ezura, M., Tominaga, T., Takahashi, A., et al. (2004). Computational replicas: anatomic reconstructions of cerebral vessels as volume numerical grids at three-dimensional angiography. *AJNR. American journal of neuroradiology*, 25(8), 1356-65.
- Hazama, F., Kataoka, Y., K, K., Hashimoto, N., Kojima, M., & Kim, C. (1986). Early changes of Experimentally Induced Cerebral Aneurysms in Rats. *Journal of Pathology, The*, 399-404.
- Himburg, H. a, Grzybowski, D. M., Hazel, A. L., LaMack, J. a, Li, X.-M., & Friedman, M. H. (2004). Spatial comparison between wall shear stress measures and porcine arterial endothelial permeability. *American journal of physiology. Heart and circulatory physiology*, 286(5), H1916-22.

- Hirabayashi, M., Ohta, M., Rüfenacht, D., & Chopard, B. (2003). Characterization of flow reduction properties in an aneurysm due to a stent. *Physical Review E*, 68(2), 1-6.
- Hirata, K., Yaginuma, T., O'Rourke, M. F., & Kawakami, M. (2006). Age-related changes in carotid artery flow and pressure pulses: possible implications for cerebral microvascular disease. *Stroke; a journal of cerebral circulation*, 37(10), 2552-6.
- Hoi, Yiemeng, Gao, L., Tremmel, M., Paluch, R. a, Siddiqui, A. H., Meng, H., & Mocco, J. (2008). In vivo assessment of rapid cerebrovascular morphological adaptation following acute blood flow increase. *Journal of neurosurgery*, 109(6), 1141-7.
- Hoi, Yiemeng, Meng, H., Woodward, S. H., Bendok, B. R., Hanel, R. a, Guterman, L. R., & Hopkins, L. N. (2004). Effects of arterial geometry on aneurysm growth: three-dimensional computational fluid dynamics study. *Journal of neurosurgery*, 101(4), 676-81.
- Hoi, Yiemeng, Wasserman, B. a, Lakatta, E. G., & Steinman, D. a. (2010). Carotid bifurcation hemodynamics in older adults: effect of measured versus assumed flow waveform. *Journal of biomechanical engineering*, 132(7), 071006.
- Hoi, Yiemeng, Wasserman, B. a, Xie, Y. J., Najjar, S. S., Ferruci, L., Lakatta, E. G., Gerstenblith, G., et al. (2010). Characterization of volumetric flow rate waveforms at the carotid bifurcations of older adults. *Physiological measurement*, 31(3), 291-302.
- Holdsworth, D W, Norley, C. J., Frayne, R., Steinman, D. a, & Rutt, B. K. (1999). Characterization of common carotid artery blood-flow waveforms in normal human subjects. *Physiological measurement*, 20(3), 219-40.

Hoogstraten, H. W., Kootstra, J. G., Hillen, B., Krijgert, J. K. B., & Wensing, P. J. W. (1996). Numerical Simulation of Blood Flow in Artery with Two successive bends, *29(X)*.

Imai, Y., Sato, K., Ishikawa, T., & Yamaguchi, T. (2008). Inflow into saccular cerebral aneurysms at arterial bends. *Annals of biomedical engineering*, *36(9)*, 1489-95.

Imai, Y., Sato, K., Ishikawa, T., Comerford, A., David, T., & Yamaguchi, T. (2010). ATP transport in saccular cerebral aneurysms at arterial bends. *Annals of biomedical engineering*, *38(3)*, 927-34.

Ionescu, M., Metcalfe, R. W., Cody, D., Alvarado, M. V. Y., Hipp, J., & Benndorf, G. (2011). Spatial resolution limits of multislice computed tomography (MS-CT), C-arm-CT, and flat panel-CT (FP-CT) compared to MicroCT for visualization of a small metallic stent. *Academic radiology*, *18(7)*, 866-75.

Jeng, J., & Shu, C. (2011). Effects of Disturbed Flow on Vascular Endothelium: Pathophysiological Basis and Clinical Perspectives. *Physiological Reviews*, 327-387.

Jou, L.-D., Wong, G., Dispensa, B., Lawton, M. T., Higashida, R. T., Young, W. L., & Saloner, D. (2005). Correlation between luminal geometry changes and hemodynamics in fusiform intracranial aneurysms. *AJNR. American journal of neuroradiology*, *26(9)*, 2357-63.

Jung, J., Lyczkowski, R. W., Panchal, C. B., & Hassanein, A. (2006). Multiphase hemodynamic simulation of pulsatile flow in a coronary artery. *Journal of biomechanics*, *39(11)*, 2064-73.

Kadirvel, Ramanathan, Ding, Y.-H., Dai, D., Zakaria, H., Robertson, A. M., Danielson, M. a, Lewis, D. a, et al. (2007). The influence of hemodynamic forces on

biomarkers in the walls of elastase-induced aneurysms in rabbits. *Neuroradiology*, 49(12), 1041-53.

Kamm, Roger D. (2002). Cellular fluid mechanics. *Annual review of fluid mechanics*, 34, 211-32.

Karmonik, Christof, Arat, A., Benndorf, G., Akpek, S., Klucznik, R., Mawad, M. E., & Strother, C. M. (2004). A technique for improved quantitative characterization of intracranial aneurysms. *AJNR. American journal of neuroradiology*, 25(7), 1158-61.

Kolega, John, Gao, L., Mandelbaum, M., Mocco, J., Siddiqui, A. H., Natarajan, S. K., & Meng, H. (2011). Cellular and molecular responses of the basilar terminus to hemodynamics during intracranial aneurysm initiation in a rabbit model. *Journal of vascular research*, 48(5), 429-42.

Komai, Y., & Tanishita, K. (1997). Fully developed intermittent flow in a curved tube. *Journal of Fluid Mechanics*, 347, 263-287.

Krex, D., Schackert, H. K., & Schackert, G. (2001). Genesis of cerebral aneurysms--an update. *Acta neurochirurgica*, 143(5), 429-48; discussion 448-9.

J. M. Wardlaw and P. M. White (2000), The detection and management of unruptured intracranial aneurysms. *Brain*, Vol. 123, No. 2, 205-221, 2000

Karino T, Motomiya M and Goldsmith HL (1990), Flow patterns at the major T-Junctions of the dog descending aorta, *J Biomech* 23(6): 537-548, 1990

Kataoka N, Ujita S and Sato M (1998): Effect of flow direction on the morphological responses of cultured bovine aortic endothelial cells, *Med Biol Eng Comp*, 36: 122-128

- Komai, Y. and Tanishita, K., 1997. Fully developed intermittent flow in a curved tube. *J. Fluid Mech.*, 347: 263-287.
- Konno, T. Satoh, Y. & Tanishita K (1994). Secondary flow augmentation in the diastolic phase of physiologically intermittent flow in a curved tube. *VDI 17 107*, 205
- Ku D.N (1997): Blood flow in Arteries. *Ann, Rev, Fluid Mech* 29:399-434
- Ku DN, Giddens DP, Zarins CD, Glagov S (1985) Pulsatile flow and atherosclerosis in the human carotid bifurcation. *Arteriosclerosis* 5: 293-302
- Ku DN, Giddens DP, Zarins CK and Glagov S (1998): Pulsatile flow and atherosclerosis in the human carotid bifurcation: Positive correlation between plaque location and low and oscillating WSS , *Atherosclerosis* , 5:293-302,
- Ku, D. N. (1997). Blood Flow in Arteries. *Annual Review of Fluid Mechanics*, 29(1), 399-434.
- Kulcsár, Z., Ugron, a, Marosfoi, M., Berentei, Z., Paál, G., & Szikora, I. (2011). Hemodynamics of cerebral aneurysm initiation: the role of wall shear stress and spatial wall shear stress gradient. *AJNR. American journal of neuroradiology*, 32(3), 587-94.
- Lasheras, J. C. (2007). The Biomechanics of Arterial Aneurysms. *Annual Review of Fluid Mechanics*, 39(1), 293-319.
- Lee, S.-W., & Steinman, D. a. (2007). On the relative importance of rheology for image-based CFD models of the carotid bifurcation. *Journal of biomechanical engineering*, 129(2), 273-8.
- Li, Y.-S. J., Haga, J. H., & Chien, S. (2005). Molecular basis of the effects of shear stress on vascular endothelial cells. *Journal of biomechanics*, 38(10), 1949-71.
- Liang, Y. L., Teede, H., Kotsopoulos, D., Shiel, L., Cameron, J. D., Dart, a M., & McGrath, B. P. (1998). Non-invasive measurements of arterial structure and

function: repeatability, interrelationships and trial sample size. *Clinical science (London, England)*: 1979), 95(6), 669-79.

Lieber, B. B., Livescu, V., Hopkins, L. N., & Wakhloo, A. K. (2002). Particle Image Velocimetry Assessment of Stent Design Influence on Intra-Aneurysmal Flow. *Annals of Biomedical Engineering*, 30(6), 768-777.

Liu, B., Liu, X.-yue, & Ding, Z.-rong. (2009). The Effects of Physiological Flow Waveform on Wall Shear Stress in Carotid Bifurcation Model. *Journal of Hydrodynamics, Ser. B*, 21(5), 669-674.

Longest, P. W., Kleinstreuer, C., Truskey, G. a., & Buchanan, J. R. (2003). Relation Between Near-Wall Residence Times of Monocytes and Early Lesion Growth in the Rabbit Aorto–Celiac Junction. *Annals of Biomedical Engineering*, 31(1), 53-64.

Lu, D., & Kassab, G. S. (2011). Role of shear stress and stretch in vascular mechanobiology. *Journal of the Royal Society, Interface / the Royal Society*, 8(63), 1379-85.

Lu, X., & Kassab, G. S. (2004). Nitric oxide is significantly reduced in ex vivo porcine arteries during reverse flow because of increased superoxide production. *The Journal of physiology*, 561(Pt 2), 575-82.

Mantha, A. R., Benndorf, G., Hernandez, A., & Metcalfe, R. W. (2009). Stability of pulsatile blood flow at the ostium of cerebral aneurysms. *Journal of biomechanics*, 42(8), 1081-7.

Mantha, A., Karmonik, C., Benndorf, G., Strother, C., & Metcalfe, R. (2006). Hemodynamics in a Cerebral Artery before and after the Formation of an Aneurysm. *Ajnr. American Journal Of Neuroradiology*, 27, 1113-18.

- Marzo, A., Singh, P., Larrabide, I., Radaelli, A., Coley, S., Gwilliam, M., Wilkinson, I. D., et al. (2011). Computational hemodynamics in cerebral aneurysms: the effects of modeled versus measured boundary conditions. *Annals of biomedical engineering*, 39(2), 884-96.
- Meckel, S., Stalder, A. F., Santini, F., Radü, E.-W., Rüfenacht, D. a, Markl, M., & Wetzel, S. G. (2008). In vivo visualization and analysis of 3-D hemodynamics in cerebral aneurysms with flow-sensitized 4-D MR imaging at 3 T. *Neuroradiology*, 50(6), 473-84
- Meinders, J. M., & Hoeks, A. P. G. (2004). Simultaneous assessment of diameter and pressure waveforms in the carotid artery. *Ultrasound in medicine & biology*, 30(2), 147-54.
- Meng, H, Wang, Z., Kim, M., Ecker, R. D., & Hopkins, L. N. (2006). TECHNICAL NOTE Saccular Aneurysms on Straight and Curved Vessels Are Subject to Different Hemodynamics□: Implications of Intravascular Stenting. *Illinois Research*, 1861-1865.
- Meng, Hui, Metaxa, E., Gao, L., Liaw, N., Natarajan, S. K., Swartz, D. D., Siddiqui, A. H., et al. (2011). Progressive aneurysm development following hemodynamic insult. *Journal of neurosurgery*, 114(4), 1095-103.
- Meng, Hui, Swartz, D. D., Wang, Z., Hoi, Y., Kolega, J., Metaxa, E. M., Szymanski, M. P., et al. (2009). A Model System for Mapping Vascular Responses to Complex Hemodynamics at Arterial Bifurcations In Vivo. *Neuroradiology*, 59(5), 1094-1101.
- Meng, Hui, Wang, Z., Hoi, Y., Gao, L., Metaxa, E., Swartz, D. D., & Kolega, J. (2007). Complex hemodynamics at the apex of an arterial bifurcation induces vascular remodeling resembling cerebral aneurysm initiation. *Stroke; a journal of cerebral circulation*, 38(6), 1924-31.

- Metaxa, E., Meng, H., Kaluvala, S. R., Szymanski, M. P., Paluch, A., Kolega, J., & Paluch, R. A. (2008). Nitric oxide-dependent stimulation of endothelial cell proliferation by sustained high flow. *Physiology*, 736-742.
- Metaxa, E., Meng, H., Kaluvala, S. R., Szymanski, M. P., Paluch, R. a, & Kolega, J. (2008). Nitric oxide-dependent stimulation of endothelial cell proliferation by sustained high flow. *American journal of physiology. Heart and circulatory physiology*, 295(2), H736-42.
- Moncada, S, Palmer R.M.J, H. E. . (1991). Nitric Oxide: Physiology, Pathophysiology, and Pharmacology. *Pharmacological Reviews*, 43(2), 109-134.
- Morgan, A. J., & Hosking, S. L. (2007). Non-invasive vascular impedance measures demonstrate ocular vasoconstriction during isometric exercise. *The British journal of ophthalmology*, 91(3), 385-90.
- Myers, J. G., Moore, J. a., Ojha, M., Johnston, K. W., & Ethier, C. R. (2001). Factors Influencing Blood Flow Patterns in the Human Right Coronary Artery. *Annals of Biomedical Engineering*, 29(2), 109-120.
- Nagatomo, I., Nomaguchi, M., & Matsumoto, K. (1992). Blood flow velocity waveform in the common carotid artery and its analysis in elderly subjects. *Clinical autonomic research*: official journal of the Clinical Autonomic Research Society, 2(3), 197-200.
- Nelson, M. R., Stepanek, J., Cevette, M., Covalciuc, M., Hurst, R. T., & Tajik, a J. (2010). Noninvasive measurement of central vascular pressures with arterial tonometry: clinical revival of the pulse pressure waveform *Mayo Clinic proceedings. Mayo Clinic*, 85(5), 460-72.
- Nerem RM, Levesque MJ and Cornhill JF (1981): Vascular endothelial morphology as an indicator of the pattern of blood flow, *J Biomech. Eng*, 103: 172-176,

- Nerem RM, Levesque MJ and Sato M (1986): Vascular dynamics and endothelium, Endothelium, (ed)Schmid-Shonbeine et al., Springer Verlag, New York 23: 324-341,
- Newell DW, Elliott JP, Eskridge JM (1999): Endovascular therapy for aneurysmal vasospasm. *Crit Care Clin* 15(4): 685-99
- Nixon, A. M., Gunel, M., & Sumpio, B. E. (2010). The critical role of hemodynamics in the development of cerebral vascular disease. *Journal of neurosurgery*, 112(6), 1240-53.
- Ohno, M., Cooke, J. P., Dzau, V. J., & Gibbons, G. H. (1995). Fluid shear stress induces endothelial transforming growth factor beta-1 transcription and production. Modulation by potassium channel blockade. *The Journal of clinical investigation*, 95(3), 1363-9.
- Ohta, M., Nakayama, T., Takahashi, a., & Rufenacht, D. a. (2007). Three-Dimensional Reconstruction of a Cerebral Stent using Micro-CT for Computational Simulation. *Journal of Intelligent Material Systems and Structures*, 19(3), 313-318.
- Okano M and Yoshida Y (1993): Influence of shear stress on endothelial cell shapes and junction complexes at flow dividers of aortic bifurcations in cholesterol-fed rabbits, *Front Med. Biol. Eng.*5(2): 95-120,
- Okano M and Yoshida Y (1994): Junction complexes of endothelial cells in atherosclerosis-prone and atherosclerosis-resistant regions on flow dividers of brachio-cephalic bifurcations in the rabbit aorta, *Biorheology* 31(2): 155-161
- Ortega, J., Hartman, J., Rodriguez, J., & Maitland, D. (2008). Post-treatment hemodynamics of a basilar aneurysm and bifurcation. *Annals of biomedical engineering*, 36(9), 1531-46.

- Oshima, M., & Torii, R. (2006). Numerical evaluation of elastic models in blood flow–arterial wall interaction. *International Journal of Computational Fluid Dynamics*, 20(3-4), 223-228.
- O'Rourke, M. F., & Seward, J. B. (2006). Central arterial pressure and arterial pressure pulse: new views entering the second century after Korotkov. *Mayo Clinic proceedings. Mayo Clinic*, 81(8), 1057-68.
- Paál, György, Ugron, Á., Szikora, I., & Bojtár, I. (2007). Flow in simplified and real models of intracranial aneurysms. *International Journal of Heat and Fluid Flow*, 28(4), 653-664.
- Penn, D. L., Komotar, R. J., & Sander Connolly, E. (2011). Hemodynamic mechanisms underlying cerebral aneurysm pathogenesis. *Journal of clinical neuroscience* □: *official journal of the Neurosurgical Society of Australasia*, 18(11), 1435-8.
- Perktold K and Rappitsch G (1995): Computer simulation of local blood flow and vessel mechanics in a compliant carotid artery bifurcation model. *J Biomech* 27(8): 845-856m
- Perktold K, Gruber K, Kenner T, Florian H Calculation of pulsatile flow and particle paths in an aneurysm model. *Basic Research in Cardiology* 79(3): 253-261
- Perktold K, Kenner T, Hilbert D, Spork B, Florian H (1988) Numerical blood flow analysis: arterial bifurcation with a saccular aneurysm. *Basic Research in Cardiology* 83(1): 24-31
- Pivkin, I. V., Richardson, P. D., Laidlaw, D. H., & Karniadakis, G. E. (2005). Combined effects of pulsatile flow and dynamic curvature on wall shear stress in a coronary artery bifurcation model. *Journal of biomechanics*, 38(6), 1283-90.

- Poulin, M. J., Syed, R. J., & Robbins, P. a. (1999). Assessments of flow by transcranial Doppler ultrasound in the middle cerebral artery during exercise in humans. *Journal of applied physiology (Bethesda, Md. □: 1985)*, 86(5), 1632-7.
- Prosi, M., Zunino, P., Perktold, K., & Quarteroni, a. (2005). Mathematical and numerical models for transfer of low-density lipoproteins through the arterial walls: a new methodology for the model set up with applications to the study of disturbed luminal flow. *Journal of biomechanics*, 38(4), 903-17.
- Qiao, a K., Guo, X. L., Wu, S. G., Zeng, Y. J., & Xu, X. H. (2004). Numerical study of nonlinear pulsatile flow in S-shaped curved arteries. *Medical engineering & physics*, 26(7), 545-52.
- Ramaswamy, S. D., Vigmostad, S. C., Wahle, a, Lai, Y. G., Olszewski, M. E., Braddy, K. C., Brennan, T. M. H., et al. (2004). Fluid dynamic analysis in a human left anterior descending coronary artery with arterial motion. *Annals of biomedical engineering*, 32(12), 1628-41.
- Rayz, V. L., Lawton, M. T., Martin, A. J., Young, W. L., & Saloner, D. (2008). Numerical simulation of pre- and postsurgical flow in a giant basilar aneurysm. *Journal of biomechanical engineering*, 130(2), 021004.
- Rhee, K., Han, M. H., & Cha, S. H. (2002). Changes of Flow Characteristics by Stenting in Aneurysm Models: Influence of Aneurysm Geometry and Stent Porosity. *Annals of Biomedical Engineering*, 30(7), 894-904.
- Rohren, E. M., Kliwer, M. a, Carroll, B. a, & Hertzberg, B. S. (2003). A spectrum of Doppler waveforms in the carotid and vertebral arteries. *AJR. American journal of roentgenology*, 181(6), 1695-704.
- Rossi, J., Jonak, P., Rouleau, L., Danielczak, L., Tardif, J.-C., & Leask, R. L. (2011). Differential response of endothelial cells to simvastatin when conditioned with steady, non-reversing pulsatile or oscillating shear stress. *Annals of biomedical engineering*, 39(1), 402-13.

- Sadamasa, N., Nozaki, K., Takagi, Y., Moriwaki, T., Kawanabe, Y., Ishikawa, M., & Hashimoto, N. (2007). Cerebral aneurysm progression suppressed by blockage of endothelin B receptor. *Journal of neurosurgery*, 106(2), 330-6.
- Sangalli, L. M., Secchi, P., Vantini, S., & Veneziani, A. (2009). A Case Study in Exploratory Functional Data Analysis: Geometrical Features of the Internal Carotid Artery. *Journal of the American Statistical Association*, 104(485), 37-48.
- Sangalli, L. M., Secchi, P., Vantini, S., & Veneziani, A. (2009). Efficient estimation of three-dimensional curves and their derivatives by free-knot regression splines, applied to the analysis of inner carotid artery centrelines. *Journal of the Royal Statistical Society: Series C (Applied Statistics)*, 58(3), 285-306.
- Santis, G., De Beule, M., Van Canneyt, K., Segers, P., Verdonck, P., & Verhegghe, B. (2011). Full-hexahedral structured meshing for image-based computational vascular modeling. *Medical engineering & physics*, 33(10), 1318-25. Institute of Physics and Engineering in Medicine.
- Schieviniki, W. I. (1997). Intracranial Aneurysms. *New England Journal of Medicine*, 336(1), 28-40.
- Scotti, C. M., Shkolnik, A. D., Muluk, S. C., & Finol, E. a. (2005). Fluid-structure interaction in abdominal aortic aneurysms: effects of asymmetry and wall thickness. *Biomedical engineering online*, 4, 64.
- Seo, T., Schachter, L. G., & Barakat, A. I. (2005). Computational Study of Fluid Mechanical Disturbance Induced by Endovascular Stents. *Annals of Biomedical Engineering*, 33(4), 444-456.
- Sforza, D. M., Putman, C. M., & Cebal, J. R. (2009). Hemodynamics of Cerebral Aneurysms. *Annual review of fluid mechanics*, 41, 91-107.

- Shadden, S. C., & Taylor, C. a. (2008). Characterization of coherent structures in the cardiovascular system. *Annals of biomedical engineering*, 36(7), 1152-62.
- Shi, Z.-D., & Tarbell, J. M. (2011). Fluid flow mechanotransduction in vascular smooth muscle cells and fibroblasts. *Annals of biomedical engineering*, 39(6), 1608-19.
- Shimano, H., Nagasawa, S., Miyatake, S.-I., Kawanishi, M., Yamaguchi, K., Kawabata, S., & Kuroiwa, T. (2006). Model analysis of coil embolization of cerebral aneurysms: prediction of thrombus formation in aneurysms based on the coil embolization rate. *Neurological research*, 28(2), 172-6.
- Shimogonya, Y., Ishikawa, T., Imai, Y., Matsuki, N., & Yamaguchi, T. (2009). Can temporal fluctuation in spatial wall shear stress gradient initiate a cerebral aneurysm? A proposed novel hemodynamic index, the gradient oscillatory number (GON). *Journal of biomechanics*, 42(4), 550-4.
- Shojima, M., Oshima, M., Takagi, K., Torii, R., Hayakawa, M., Katada, K., Morita, A., et al. (2004). Magnitude and role of wall shear stress on cerebral aneurysm: computational fluid dynamic study of 20 middle cerebral artery aneurysms. *Stroke; a journal of cerebral circulation*, 35(11), 2500-5.
- Shojima, M., Oshima, M., Takagi, K., Torii, R., Nagata, K., Shirouzu, I., Morita, A., et al. (2005). Role of the bloodstream impacting force and the local pressure elevation in the rupture of cerebral aneurysms. *Stroke; a journal of cerebral circulation*, 36(9), 1933-8.
- Singh, P. K., Marzo, A., Howard, B., Rufenacht, D. a, Bijlenga, P., Frangi, A. F., Lawford, P. V., et al. (2010). Effects of smoking and hypertension on wall shear stress and oscillatory shear index at the site of intracranial aneurysm formation. *Clinical neurology and neurosurgery*, 112(4), 306-13.

- Stahlhofen, a. a, & Nimtz, G. (2006). Evanescent modes are virtual photons. *Europhysics Letters (EPL)*, 76(2), 189-195.
- Stamenović, D., & Ingber, D. E. (2002). Models of cytoskeletal mechanics of adherent cells. *Biomechanics and modeling in mechanobiology*, 1(1), 95-108.
- Stehbens WE (1960): Focal intimal proliferation in the cerebral arteries. *Am J Pathol* 36:289-301,
- Stehbens WE (1963): Histopathology of Cerebral Aneurysms. *Arch Neurol* 8:272-285,
- Stehbens WE (1962): Hypertension and Cerebral Aneurysms. *Med J Aust* 2:4-10,
- Stehbens WE (1959): Medial defects of the cerebral arteries of man. *J Pathol Bacteriol* 78:179-185,
- Steinman, David a, Milner, J. S., Norley, C. J., Lownie, S. P., & Holdsworth, D. W. (2003). Image-based computational simulation of flow dynamics in a giant intracranial aneurysm. *AJNR. American journal of neuroradiology*, 24(4), 559-66.
- Stone, P. H., Coskun, A. U., Kinlay, S., Clark, M. E., Sonka, M., Wahle, A., Ilegbusi, O. J., et al. (2003). Effect of endothelial shear stress on the progression of coronary artery disease, vascular remodeling, and in-stent restenosis in humans: in vivo 6-month follow-up study. *Circulation*, 108(4), 438-44.
- Strother CM, Graves Vb, Rappe (1992) A, aneurysm hemodynamics - an experimental-study, *American Journal Of Neuroradiology* 13 (4): 1089-1095
- Sugiyama, S.-I., Meng, H., Funamoto, K., Inoue, T., Fujimura, M., Nakayama, T., Omodaka, S., et al. (2011). Hemodynamic Analysis of Growing Intracranial Aneurysms Arising from a Posterior Inferior Cerebellar Artery. *World neurosurgery*, 4(Figure 2), 1-7.

- Suh, G.-Y., Les, A. S., Tenforde, A. S., Shadden, S. C., Spilker, R. L., Yeung, J. J., Cheng, C. P., et al. (2011). Quantification of particle residence time in abdominal aortic aneurysms using magnetic resonance imaging and computational fluid dynamics. *Annals of biomedical engineering*, 39(2), 864-83.
- Szikora, Istvan, Paal, G., Ugron, A., Nasztanovics, F., Marosfoi, M., Berentei, Z., Kulcsar, Z., et al. (2008). Impact of aneurysmal geometry on intraaneurysmal flow: a computerized flow simulation study. *Neuroradiology*, 50(5), 411-21.
- Szymanski, M., & Metaxa, Elena, Meng, Hui, Kolega, J. (2008). Endothelial Cell Layer Subjected to Impinging Flow Mimicking the Apex of an Arterial Bifurcation. *Annals of biomedical engineering*, 36(10), 1681-1689.
- Tada, S., & Tarbell, J. M. (2002). Flow through internal elastic lamina affects shear stress on smooth muscle cells (3D simulations). *American journal of physiology. Heart and circulatory physiology*, 282(2), H576-84.
- Takizawa, K., Brummer, T., Tezduyar, T. E., & Chen, P. R. (2012). A Comparative Study Based on Patient-Specific Fluid-Structure Interaction Modeling of Cerebral Aneurysms. *Journal of Applied Mechanics*, 79(1), 010908.
- Tanishita, K, Omura, H., & Villablanca, J. P. (2007). Intra-Aneurysmal Hemodynamics during the Growth of an Unruptured Aneurysm: In Vitro. *Ajnr. American Journal Of Neuroradiology*, 1-6.
- Tateshima, S., Viñuela, F., Villablanca, J. P., Murayama, Y., Morino, T., Nomura, K., & Tanishita, K. (2003). Three-dimensional blood flow analysis in a wide-necked internal carotid artery-ophthalmic artery aneurysm. *Journal of neurosurgery*, 99(3), 526-33.
- Taylor, C a, Hughes, T. J., & Zarins, C. K. (1999). Effect of exercise on hemodynamic conditions in the abdominal aorta. *Journal of vascular surgery*: official

*publication, the Society for Vascular Surgery [and] International Society for Cardiovascular Surgery, North American Chapter, 29(6), 1077-89.*

Torii, Ryo, Oshima, M., Kobayashi, T., Takagi, K., & Tezduyar, T. E. (2007). Numerical investigation of the effect of hypertensive blood pressure on cerebral aneurysm — Dependence of the effect on the aneurysm shape. *Blood Pressure*, (April), 995-1009.

Trachet, B., Renard, M., De Santis, G., Staelens, S., De Backer, J., Antiga, L., Loeys, B., et al. (2011). An integrated framework to quantitatively link mouse-specific hemodynamics to aneurysm formation in angiotensin II-infused ApoE <sup>-/-</sup> mice. *Annals of biomedical engineering*, 39(9), 2430-44.

Uchida, S. (1956). The Pulsating Viscous Flow Superposed on the Steady Laminar Motion of Incompressible Fluid in a Circular Pipe.

Valencia, A. (2005). Simulation of unsteady laminar flow in models of terminal aneurysm of the basilar artery. *International Journal of Computational Fluid Dynamics*, 19(4), 337-345.

Valencia, A. a, Guzmán, A. M., Finol, E. a, & Amon, C. H. (2006). Blood flow dynamics in saccular aneurysm models of the basilar artery. *Journal of biomechanical engineering*, 128(4), 516-26.

Valencia, A., & Solis, F. (2006). Blood flow dynamics and arterial wall interaction in a saccular aneurysm model of the basilar artery. *Computers & Structures*, 84(21), 1326-1337.

Valencia, A., Morales, H., Rivera, R., Bravo, E., & Galvez, M. (2008). Blood flow dynamics in patient-specific cerebral aneurysm models: the relationship between wall shear stress and aneurysm area index. *Medical engineering & physics*, 30(3), 329-40.

- Valencia, A., Zarate, A., Galvez, M., & Badilla, L. (2006). Non-Newtonian blood ow dynamics in a right internal carotid artery with a saccular aneurysm. *International Journal for Numerical Methods in Fluids*, (September 2005), 751-764.
- Wada, S., & Karino, T. (2002). Theoretical Prediction of Low-Density Lipoproteins Concentration at the Luminal Surface of an Artery with a Multiple Bend. *Annals of Biomedical Engineering*, 30(6), 778-791.
- Wang, C., Pekkan, K., de Zélicourt, D., Horner, M., Parihar, A., Kulkarni, A., & Yoganathan, A. P. (2007). Progress in the CFD modeling of flow instabilities in anatomical total cavopulmonary connections. *Annals of biomedical engineering*, 35(11), 1840-56.
- Watton, P N, Selimovic, a, Raberger, N. B., Huang, P., Holzapfel, G. a, & Ventikos, Y. (2011). Modelling evolution and the evolving mechanical environment of saccular cerebral aneurysms. *Biomechanics and modeling in mechanobiology*, 10(1), 109-32.
- Weir, B., Amidei, C., Kongable, G., Findlay, J. M., Kassell, N. F., Kelly, J., Dai, L., et al. (2003). The aspect ratio (dome/neck) of ruptured and unruptured aneurysms. *Journal of neurosurgery*, 99(3), 447-51.
- Wenderoth, J. D., Khangure, M. S., Phatouros, C. C., & Apsimon, H. T. (2003). Case Report Basilar Trunk Occlusion during Endovascular Treatment of Giant and Fusiform Aneurysms of the Basilar Artery. *Ajnr. American Journal Of Neuroradiology*, (July), 1226-1229.
- White, C. R., Stevens, H. Y., Haidekker, M., & Frangos, J. a. (2005). Temporal gradients in shear, but not spatial gradients, stimulate ERK1/2 activation in human endothelial cells. *American journal of physiology. Heart and circulatory physiology*, 289(6), H2350-5.
- Womersley, J. R. (1954). Method for the calculation of velocity, rate of flow and voscous drag in arteries when the pressure gradient is known. *Journal of Physiology*, 127, 553-563.

- Yamaguchi, R., Ujiie, H., Haida, S., Nakazawa, N., & Hori, T. (2008). Velocity profile and wall shear stress of saccular aneurysms at the anterior communicating artery. *Heart and vessels*, 23(1), 60-6.
- Younis, H F, Kaazempur-Mofrad, M. R., Chan, R. C., Isasi, a G., Hinton, D. P., Chau, a H., Kim, L. a, et al. (2004). Hemodynamics and wall mechanics in human carotid bifurcation and its consequences for atherogenesis: investigation of inter-individual variation. *Biomechanics and modeling in mechanobiology*, 3(1), 17-32.
- Younis, H. F., Kaazempur-Mofrad, M. R., Chung, C., Chan, R. C., & Kamm, R. D. (2003). Computational Analysis of the Effects of Exercise on Hemodynamics in the Carotid Bifurcation. *Annals of Biomedical Engineering*, 31(8), 995-1006.
- Yutaka Komai And Kazuo Tanishita (1997): Fully developed intermittent flow in a curved tube. *J. Fluid Mech.* 347: 263-287.
- Yu, S. C., & Zhao, J. B. (1999). A steady flow analysis on the stented and non-stented sidewall aneurysm models. *Medical engineering & physics*, 21(3), 133-41.
- Zakaria, H., Robertson, A. M., & Kerber, C. W. (2008). A parametric model for studies of flow in arterial bifurcations. *Annals of biomedical engineering*, 36(9), 1515-30.
- Zarins C, Giddens DP, (1983). Carotid bifurcation Atherosclerosis: Quantitative correlation of plaque localization with flow velocity profiles and wall shear stress. *Circulation Research* 53:502-514
- Zeng, Z., Kallmes, D. F., Durka, M. J., Ding, Y., Lewis, D., Kadirvel, R., & Robertson, a M. (2011). Hemodynamics and anatomy of elastase-induced rabbit aneurysm models: similarity to human cerebral aneurysms? *AJNR. American journal of neuroradiology*, 32(3), 595-601.

## Appendix A

### Flow in Curved pipes

There have been various studies of flows (steady and unsteady) in curved tubes. The motivation of these studies has been that pathological studies indicated that curved portions of arterial vessels are one of the favored sites for any blood flow associated diseases such as atherosclerosis and aneurysms. This section is a brief overview of the simulations that have been performed in the past using the idealized curved pipe geometries. This survey would be useful in trying to understand the complex flow patterns associated with the real arterial geometries.

W.R. Dean was the first scientist to study steady flow in a curved pipe in the year 1927. He proposed that the secondary flows in curved tubes arise primarily from centrifugal forces, which in turn originate due to the curvature effects of the pipe (curvature ratio,  $\delta = a/R$ ; where  $a$ = Radius of the pipe and  $R$ =radius of curvature). To characterize the combined effects of the inertial, viscous and centrifugal forces, he also proposed a non-dimensional number, now called the Dean number, which is given by,  $2Re_m \delta^{1/2}$ ; here  $Re_m$  is the Reynolds number. The magnitudes of the secondary motion are affected by the curvature ratio,  $\delta$  and because  $\delta$  is a direct measure of the pipe geometry it influences the balance between the three forces; inertial, viscous and centrifugal.

The complexity of unsteady flows in curved pipes arises from both pulsatility and curvature. The flow has quite widely studied due to its prevalence in many practical problems. The study of unsteady flow in curved tubes was initiated by Lyne (1971) and its relevance to hemodynamical problems was highlighted by Pedley (1980). Various

pathological studies indicated that there was a marked tendency for atherosclerosis in arterial segments with curvature (Wesolowski et al. 1965). A synthesis fluid mechanical analyses and biological surveys suggest that hemodynamics plays a major role in the genesis of atherosclerosis (Gessner 1973).

Pulsatile flows in curved tubes have been investigated theoretically, experimentally, and of late numerically. The analysis of Smith (1975) showed that secondary flows occur even at small Reynolds numbers when sinusoidal pulsatility is imposed (whether with large or small frequency). Blood flow in a curved artery was characterized as developing flow. Talbot & Gong (1983) used Laser Doppler Velocimetry (LDV) to measure pulsatile entrance flow in a curved tube. They found flow reversal and flow separation during primary flow deceleration, at a frequency parameter  $\alpha = 12.5(a/\nu)^{1/2}$ , where  $a$ ,  $\nu$  and  $\omega$  are the radius of the tube, the kinematic viscosity of the fluid, and the angular frequency of pulsation in a systole, respectively. Separation occurred at the inner bend, where mean flow deceleration due to centrifugal effects causes an adverse pressure gradient to develop.

Rindt et al. (1991) calculated the velocity profile in the entrance flow for steady, oscillatory, and pulsatile flow conditions. The secondary flow was found to depend mainly on the mean component of the mean flow. For sinusoidal pulsatility, the flow during the systolic phase was found to be unaffected by the flow patterns occurring at diastole, when the secondary flow exhibits a complex three-dimensional structure. For more intermittently pulsatile flow, this may not necessarily be the case (discussed later). The aortic flow waveform is characterized by intermittent flow rather than by sinusoidal flow (i.e. the flow waveform in the aorta consists of pulse-like systolic flow followed by

the stationary diastolic period). Chandran & Yearwood (1993) measured three-dimensional flow distributions for conditions of intermittent flow. Further experimental studies (Konno, Sato & Tanishita 1994) showed that the secondary flow amplified during diastole.

The curvature of an aortic arch (i.e.  $\delta=1/3$ ) strongly influences the WSS and causes it to oscillate (Naruse et al.1990). Therefore, blood flow in an aortic arch can be simulated as intermittent flow in a strongly curved tube (Berger & Talbot []). The numerical results of Chang & Tarbell (1985) exhibited complex secondary flow patterns, with up to seven vortices in the upper half cross-section of the arterial segment. Komai & Yanishita (1997) studied the intermittent flow in a curved tube; their goal was to understand the flow patterns in the aortic arch, simulating a physiological flow waveform. Physiological pulsatile flow in the aorta was simulated as intermittent flow (figure A.1), with a waveform consisting of a pulse-like systolic flow period followed by a stationary diastolic period.

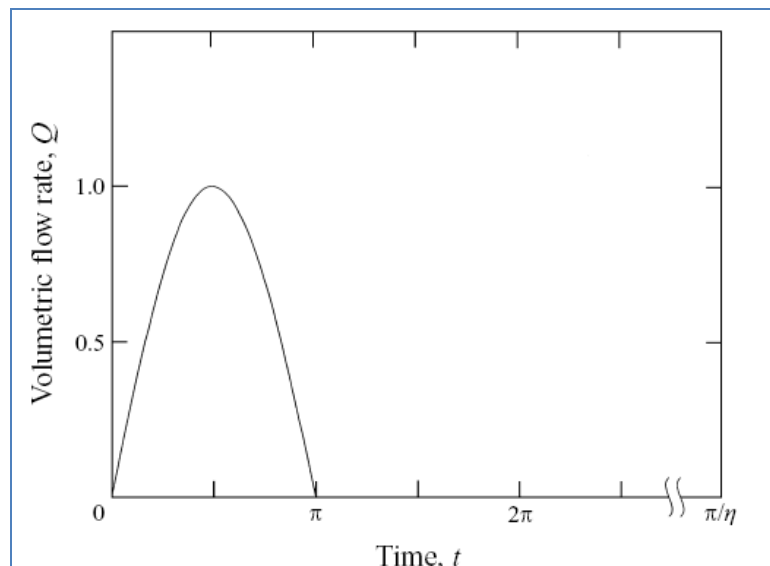


Figure A.1. Flow form used by Tomai & Yanishita (1997) for simulating intermittent flow in curved tubes.

Numerical simulations were carried out for the following conditions: Dean number,  $\kappa = 393$ , frequency parameter  $\alpha = 4$ , curvature ratio  $\delta = 1/2, 1/3$  and  $1/7$ , and intermittency parameter  $\eta = 0$  and  $1/2$ , where  $\eta$  is the ratio of a systolic time to the cycle period. For  $\alpha = 18$  and  $27$  the axial-flow profile became close to that of a sinusoidally oscillatory flow. Figure 3.2 shows the secondary flow streamlines for  $\kappa = 393, \alpha = 27, \eta = 0$  and  $\delta = 1/2$ . During systole, axial velocity reversed in the vicinity of the tube wall. The reversal is due to the extremely large negative axial pressure gradients that are imposed at this stage of the cycle (Figure A.2). (Such large adverse pressure gradients are not encountered in the physiological conditions characteristic of intra-cranial arteries; consequently, no reversed flow is observed in our simulations.)

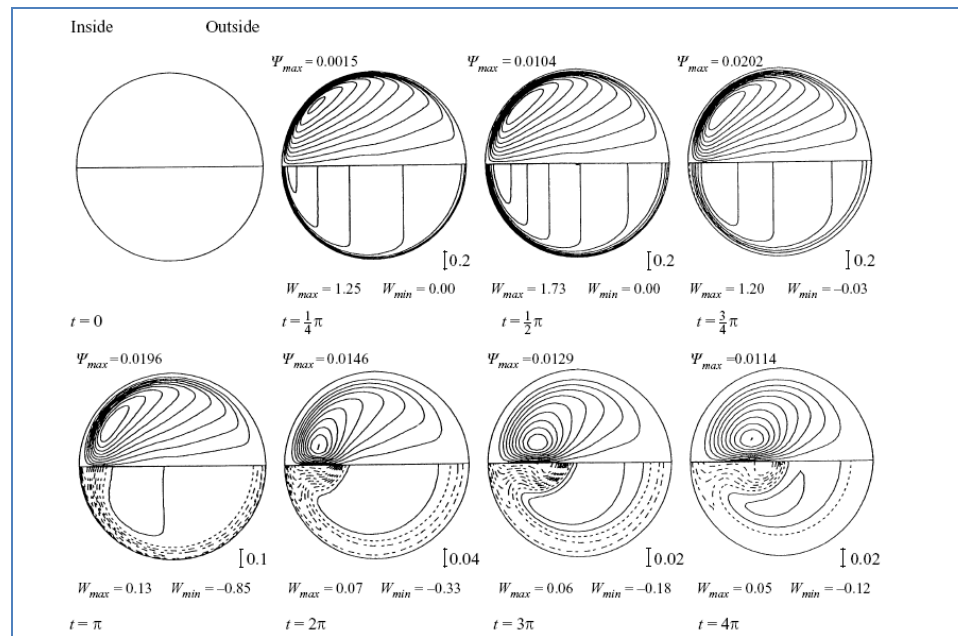


Figure A.2. Secondary flow streamlines for  $\kappa = 393, \alpha = 27, \eta = 0$  and  $\delta = 1/2$ . (From Tomai & Yanishita 1997).

Hoogerstraten et al. (1996) performed numerical simulations of steady blood flow in a pipe with two successive bends. The shape of the curved pipe was made to emulate that of the femoral artery (Figure A.3). They observed strong and complicated three-

dimensional effects in the secondary flow patterns. In particular, in the second bend, for relatively small values of Reynolds number ( $Re < 240$ ) the flow turned out to be drastically different from that for larger  $Re$  values. The flow in the first bend exhibited two secondary vortices. The flow behavior in the second bend depended strongly on the Reynolds number.

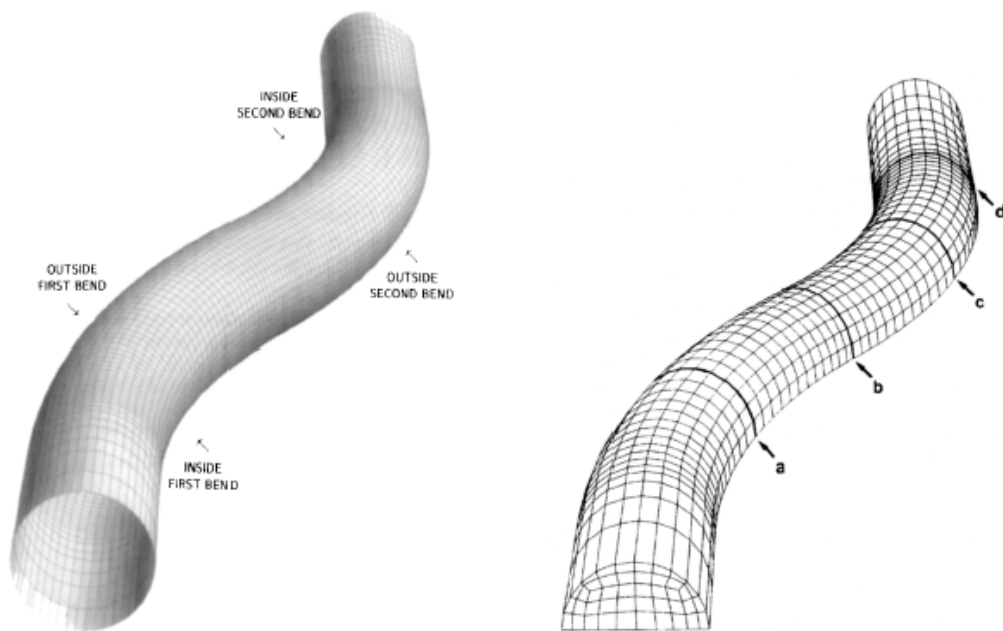


Figure A.3. (a) The vessel segment. The inflow plane is at the front. (b) The finite-element mesh. Four representative cross-sections have been indicated: (a) halfway down first bend, (b) end of first bend/beginning of second bend, (c) halfway down second bend and (d) end of second bend. Hoogerstraten et al. (1996).

For  $Re < 240$  the secondary vortices that were created in the first bend were not visible at the end of second bend where the flow pattern was seen to be dominated completely by the (counter-rotating) secondary vortices generated in the second bend. On the other hand, for larger  $Re$  values ( $Re > 300$ ), the secondary flow created in the first bend remained visible at the end of the second bend, resulting in a complex flow pattern

characterized by a flat axial velocity profile and four-vortex secondary flow field. They concluded that relatively low WSS will occur near the transition between the bends.

Qiao et al. (2004) studied pulsatile flow in S-shaped pipes. The temporal and spatial distributions of hemodynamic variables during the cardiac cycle such as velocity field, secondary flow, pressure, and WSS were analyzed. They used two different diameters, but with the same radius of curvature of the two bends for the curved pipes (Figure A.4).

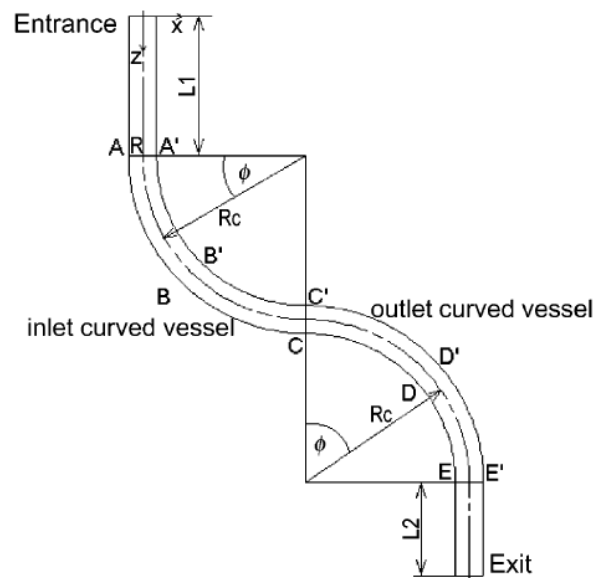


Figure A.4. The geometric model of the S-shaped artery.

Their results showed that the secondary flow in the larger S-shaped curved artery, called LVM (large vessel model), is more complex than that in the smaller one, SVM; stronger eddy flow occurred in the inner bends of curved arteries; pressure and wall shear stresses changed violently in the larger artery. To capture the effects of WSS on endothelial cells, Ku & He (1994) proposed a non-dimensional number called the oscillatory shear index (OSI), which is given as,

$$OSI = 0.5 \left[ 1 - \frac{\left| \int_0^T \bar{\tau}_w dt \right|}{\int_0^T |\bar{\tau}_w| dt} \right]. \quad (A.1)$$

Flow is purely oscillatory for OSI=0.5 and unidirectional for OSI=0. They computed the OSI for the two curved pipes (emulating the femoral artery of a dog). The computed OSI values are shown in the table A.1.

Table A.1: OSI values computed at different cross-sections (refer Figure A.4).

	A	B	C	D	E	A'	B'	C'	D'	E'
OSI of SVM	0.2085	0.0648	0.0219	0.3315	0.3748	0.1631	0.3093	0.4851	0.1470	0.0408
OSI of LVM	0.3774	0.2409	0.0736	0.4833	0.4900	0.1576	0.3977	0.2909	0.2814	0.0906

LVM exhibited larger OSI than SVM, and OSI at the inner bends was larger than that at the outer bends. The physiological blood flow at the inner bends of LVM was observed to be more complex and non-uniform. They correlated these important effects of hemodynamic variables in curved arteries with the function of arterial endothelium in the region. For instance, it was speculated that low WSS in the regions may lead to the proliferation of smooth muscle cells and the thickening of the intima, and cardiovascular diseases such as atherosclerosis may develop in such regions.

Wada and Karino (2002) performed numerical simulations to study the effects of various physical and hemodynamic factors on transport of atherogenic low-density lipoproteins (LDL) from blood to the wall of an artery with a multiple bend, under the conditions of a steady flow. They reconstructed an idealized artery from a picture of a right human coronary artery, as shown in figure A.5.

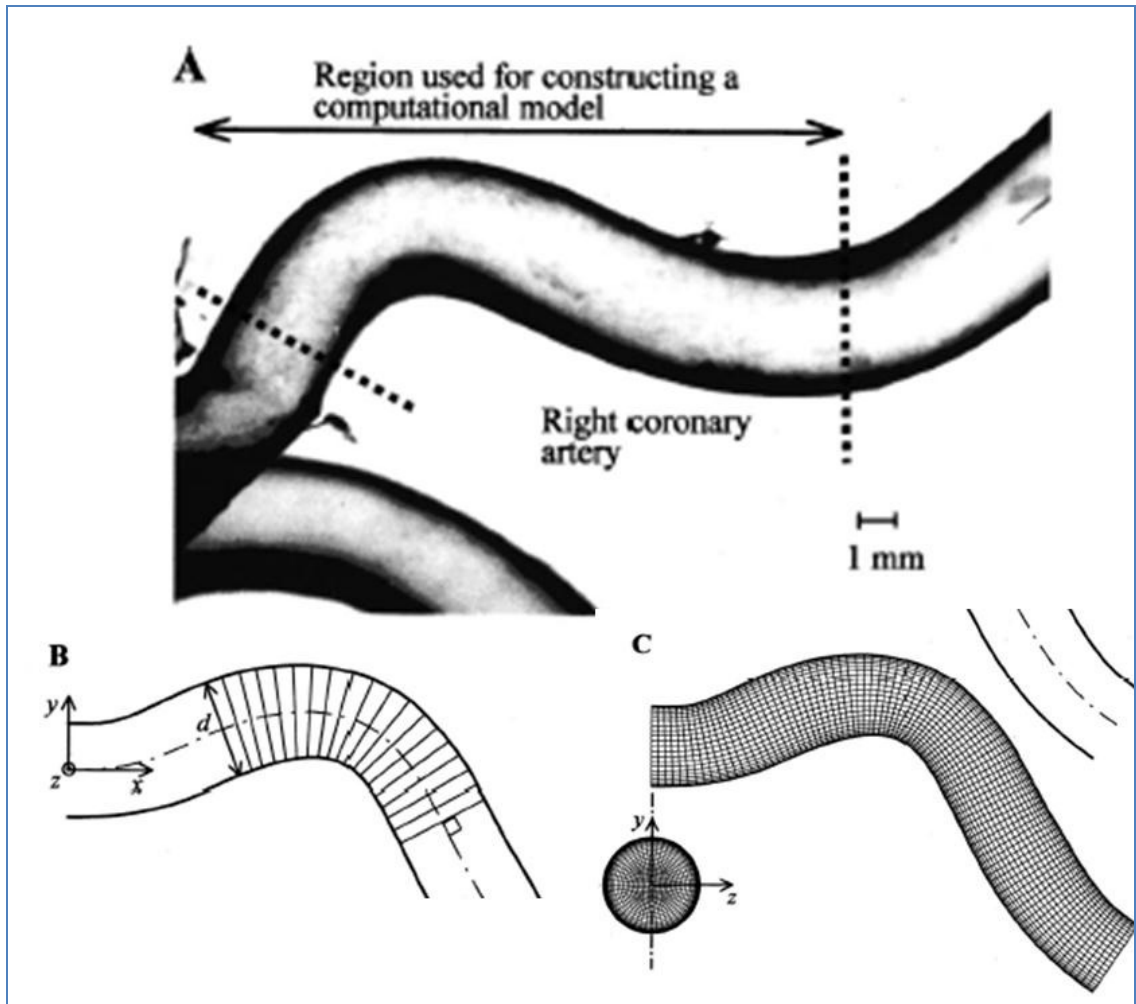


Figure A.5. A photograph of a transparent human right coronary artery (panel A) from which the shape of the multiple bend adopted in the present study was traced out (panel B), and a three-dimensional mesh model of the vessel used in the computational analyses of blood flow and transport of LDL from flowing blood to the vessel wall (panel C).

In order to incorporate the porosity of the blood vessel, they also prescribed a velocity normal to the wall, called the water infiltration velocity. This parameter has never been considered before in any of the previous simulations. Calculations of various hemodynamic properties of blood flow through a multiple bend of a human right coronary artery were carried out at various Reynolds numbers evaluated at the inlet of the vessel, assuming a physiological level of water filtration velocity at the vessel wall.

Regions of high LDL concentrations were found distal to the apex of inner wall of each of the two bends, where there was formation of secondary and recirculation zones (Figure A.6). The highest surface LDL concentration was however, found distal to the acute second bend. This region has shown susceptibility to various flow associated diseases.

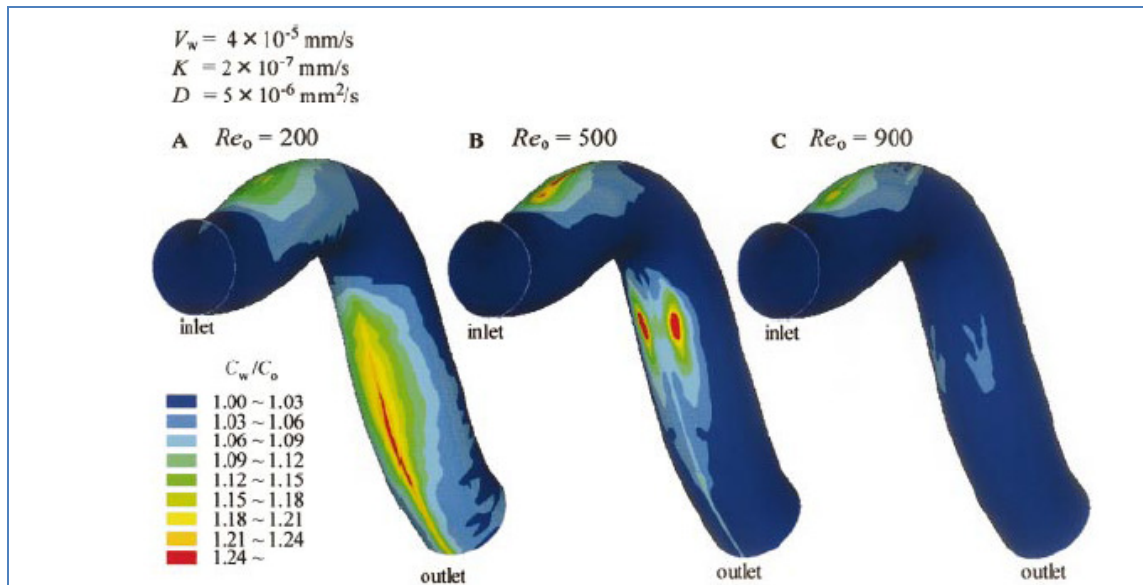


Figure A.6. The effect of Reynolds number on the distribution of LDL concentration at the luminal surface of the multiple bend. Note that at  $Re=200$  at which no adverse flow formed distal to the apex of the inner wall of the acute second bend, the highest LDL surface concentration appeared as a long stripe in the common median plane of the multiple bend, whereas at  $Re=500$  and  $900$  at which an adverse flow formed as a result of flow separation at the apex of the inner wall of the bend, the highest LDL surface concentration appeared as a pair of spots located symmetrically on both sides of the common median plane.

## Appendix B

### The Models and Assumptions

Arterial hemodynamics involves many complex phenomena, such as intricate geometry, unsteadiness, complex rheology, wall compliance, mass transfer effects and, of course, biochemical and cellular biological mechanisms. This necessitates that several simplifying assumptions be made when simulating the flow, in order to make computational study feasible.

#### B.1 Assumptions

Since our primary focus in this study is to isolate possible fluid mechanical aspects of aneurysm genesis and growth, we have designed our simulations using the following simplifying assumptions.

1. Blood is treated as a single-phase, homogenous, Newtonian fluid, having constant viscosity (0.004 kg/m-s). In reality, blood is a colloid and non-Newtonian. The viscosity depends on the diameter of the artery and erythrocyte concentration. Further, viscosity can be inhomogeneous; e.g. viscosity can be larger close to the vessel wall, where platelet deposition may occur. While this may seem a drastic simplification, various studies (Cokelet et al. 1992, Chein et al. 1970, Whitmore 1968, Fahreus and Lindquist in 1931, Perktold et al. 1994) show that the Newtonian assumption is acceptable when modeling flow in relatively large arteries, i.e. having diameter greater than 5 mm. The major arteries that supply blood to the brain are relatively large (diameter approximately 5 mm). Newtonian fluid simulations of the internal carotid artery conducted in this study are therefore providing a good representation of the true fluid mechanics.

**2.** The arterial walls are taken to be rigid. This means that there is no change of vessel diameter in response to pressure change within the flow, as may occur in reality. Further, any possible effects of wall compliance, such as feedback of wall flexure to the flow, are excluded. Comparative studies in the literature of rigid versus compliant wall (Perktold et al.1994) hemodynamics indicate that wall compliance effects are small: for instance, it was found that velocity magnitudes change by only a few percent when the rigid wall assumption is not made. However, it is still possible that under certain circumstances (e.g. when modeling flow in hypertensive conditions, where shear stresses can change drastically) that the patterns of flow may be significantly sensitive to wall compliance. While the rigid wall assumption is an acceptable first approximation, compliant wall simulations should be pursued, and are planned in the future.

**3.** Impermeable boundary conditions are applied at the wall. In physiological flow, the arterial wall is semi-permeable, with normal mass flux (and non-zero normal velocity). However, normal velocity magnitudes are extremely small (reported to be about four orders of magnitude smaller than the mean) and will not affect the main flow.

**4.** The simulated arterial segment is of course a small section of the arterial length. When a localized segment is simulated, it is unavoidable that the flow profiles close to the inlet will not match reality, where the inlet flow profiles are dependent on all upstream effects. Since different flow profiles will result in different shear stresses at the wall, values of the wall shear stress values close to the inlet may very well contain modeling artifacts. However, in all the geometries studied herein critical regions of the arterial segment (i.e. arterial bends and aneurysms) are sufficiently downstream of the inlet (approximately 10

diameters) that inlet flow artifacts are not likely to affect flow patterns and wall shear stress values in these regions.

## **B.2 Numerical Method and Models**

Simulations were performed using version 6.1.22 of the commercially available fluid dynamics package, Fluent. The software uses the finite volume method. This method has become increasingly popular in recent years due to its suitability for complex geometries. Each grid cell is regarded as a control volume over which the Navier-Stokes equations are integrated. In the present study, the 3D segregated solver and 2<sup>nd</sup>-order implicit formulation in time were selected. Spatial discretization schemes were chosen to be first order upwind for momentum and SIMPLE for pressure-velocity coupling.

### **B.2.1 Geometry**

The overall research effort of which this thesis forms a part is being conducted in collaboration with medical doctors at the Baylor College of Medicine/Methodist Hospital. Dr. C. M. Strother, a professor in the radiology department at Methodist, treats patients with cerebral aneurysms. He made available to us three-dimensional digital subtraction angiograms obtained from real patients. Six such images were extensively studied in the present study. The data we obtained was in a form that is not recognizable by any of the standard image processing tools. Therefore, angiogram data was converted to stereolithography, or STL, format before further processing.

The STL format was then read into Fluent's Gambit software package within which the pre-processing of the geometry was conducted. This stage involves the three-dimensional meshing of the images. In general, either hexahedral or tetrahedral meshing

can be used. While hexahedral meshes are more structured and result in better accuracy, we have chosen tetrahedral meshing, which is more suitable to complex geometries. This meshing procedure well approximates the three-dimensional arterial geometry and the approximation can be improved by choosing progressively higher resolutions.

### **B.2.2 Convergence tests for discretization**

First, a coarse mesh of the geometry was constructed within Gambit and the wall, inlet, and outlet boundaries were defined. Steady simulations on the coarse mesh were used to guide the mesh refinement procedure. That is, the mesh was progressively refined using the in-built algorithms of Gambit and the procedure was stopped when sufficient global accuracy of the simulations was obtained. Such a procedure ensures that adequate resolution is obtained while minimizing the total number of mesh points, and hence the computational effort. Further remeshing of the grid was discontinued once the difference in WSS between the current and previous mesh was less than 1% for the same boundary conditions. The final computational meshes of the three aneurysm models are shown in figure B.1. The grid file was then exported to Fluent as a case file.

A similar procedure of progressive refinement was used to determine the optimal time-step increment to be employed for the unsteady flow cases. Figure B.2 shows the time-variation of velocity at a fixed location in the computational domain, as the time-step is progressively reduced.

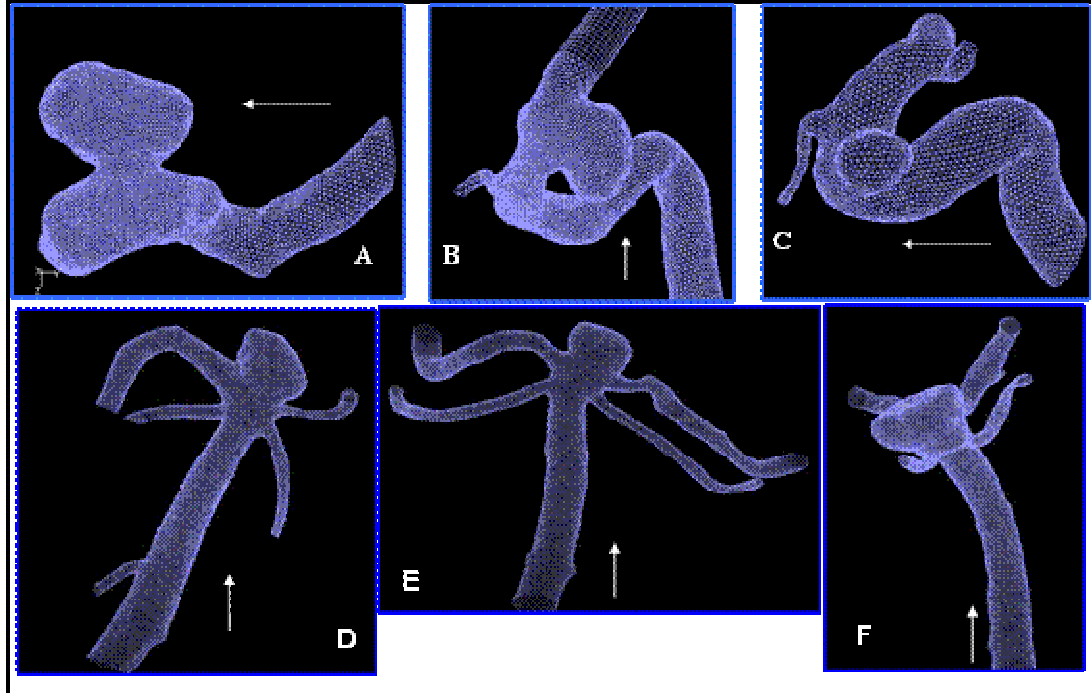


Figure B.1. Final meshes of the 6 different aneurysm models used on the study.

Table B.1: Shows the cases and various meshes used for each case.

Cases	Parent Diameter (m)	Number of Tetrahedral Elements	Diastolic Reynolds number	Systolic Reynolds number
Sidewall Case 1 (Fig 1A)	0.0052	569938	136	790
Sidewall Case 2 (Fig 1B)	0.0064	477022	158	608
Sidewall Case 3 (Fig 1C)	0.005	429209	130	740
Bifurcation Case 1 (Fig 1D)	0.0041	584350	178	745
Bifurcation Case 2 (Fig 1E)	0.0037	616504	178	775
Bifurcation Case 3 (Fig 1F)	0.0034	458392	178	775

Results are shown over one pulsatile flow cycle. Asymptotic convergence can be clearly seen, with the  $\Delta t=0.0005$  and  $\Delta t=0.001$  solutions being visually indistinguishable

(note that the two curves fall on top of each other in the figure). Since the computational effort increases with decreasing time-step size,  $\Delta t=0.001$  was chosen for subsequent solutions.

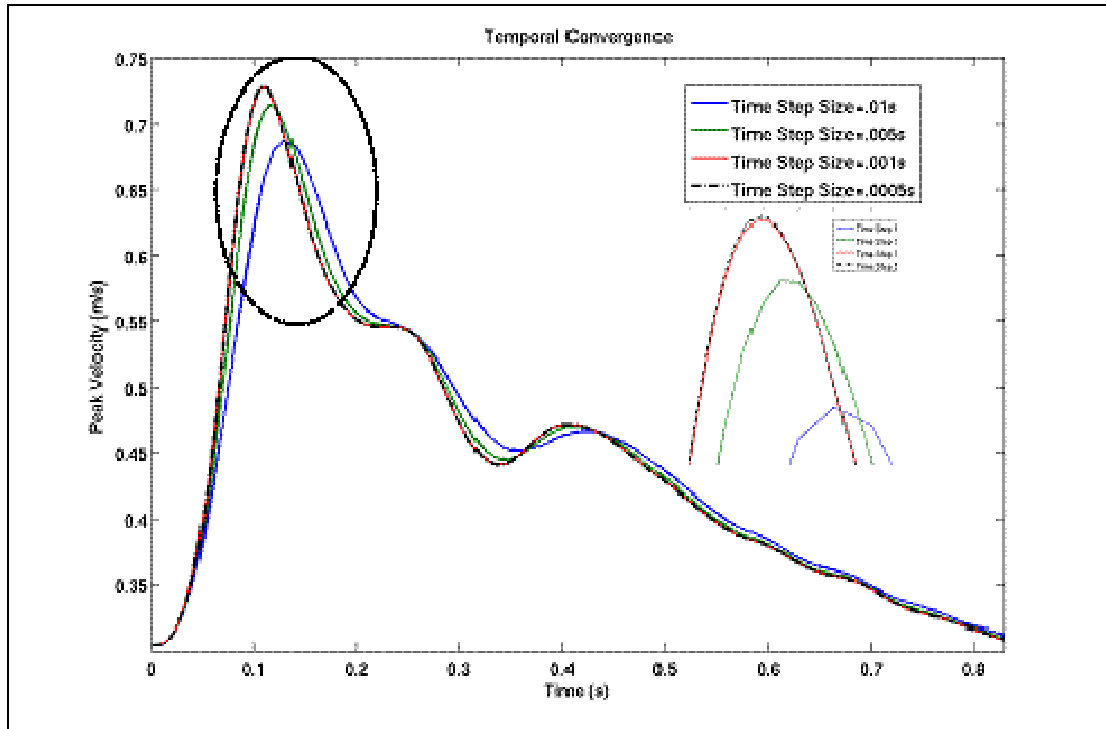


Figure B.2. Temporal convergence plot.

### B.2.3 Boundary Conditions

All simulations presented in the chapters used identical boundary conditions. Pressure values were prescribed at the outlet planes and mass-flux was prescribed at the inlet. The outlet plane pressure value was set (without loss of generality) to zero, and the inlet mass-flux value was adjusted to obtain the desired flow rates. Unsteady simulations were initialized from a steady-state solution based on end diastolic flow rates; no data were analyzed until after the two cardiac cycle since it was determined by computational

comparison that two initial cycles was sufficient to minimize transient effects. The minimum time-step was 0.001s (for a 0.83 sec cycle).

The heart beat cycle comprises two distinct phases: the diastolic and the systolic. Diastolic refers to the phase when the flow rate is close to minimum, and in fact nearly constant. Systolic refers to the phase with large flow rates, and includes both the accelerating and decelerating phases. Note that the diastolic phase occupies nearly 70% of the cardiac cycle. We use the two extreme phases, i.e. end diastolic and peak systolic, and an intermediate phase, i.e. the mid-systolic deceleration, are used extensively as the critical times to display results from hemodynamic simulations.

For the second part of the thesis where flow inside aneurysm has been studied, a time-dependent pressure gradient was imposed to match the flow waveform, for example,  $Q(t)$ , given in Holdsworth *et al.* (1999). For the bifurcation aneurysms, the pressure outlet boundary condition at the left posterior cerebral artery was adjusted to match the mean velocity at this artery to that provided in literature by Valencia *et al.* (2006) and Owega *et al.* (1998). The change in volumetric flow rate between the basilar and posterior artery was then extrapolated to obtain the flow rates for the remaining arteries and the pressure boundary conditions were then adjusted to obtain those extrapolated flow rates.

In some instances where a pressure boundary condition was applied, that would result in the desired volumetric flow rate, the following procedure was used. Since approximately 70% of the total flow in the common carotid artery flows through the internal carotid artery, the Ku waveform (Ku *et al.*, 1985) was first scaled accordingly. For pulsatile flow through tubes, Uchida has developed a theory (Uchida, 1956) based on temporal profiles of pressure and flow rate. It should be noted that there is a phase lag

between the two quantities, which must be accurately represented. Since Uchida's formulas involve frequency-dependent parameters, fast Fourier transforms were used to solve for the pressure waveform. The heart rate was taken to be 84 beats per minute (the normal physiological range being 60 to 100 beats per minute). Assuming linear variation of pressure with axial distance, the inlet pressure was then obtained from the pressure gradient. The pressure boundary conditions so obtained were verified to reproduce the expected flow rate profiles when applied in numerical simulation. As a further check, it was verified that the pressure gradient difference between the times of maximum (42mm Hg) and minimum pressures (2mm Hg) corresponded closely with those observed physiologically (120-80 mm Hg, i.e. 40mm Hg difference).

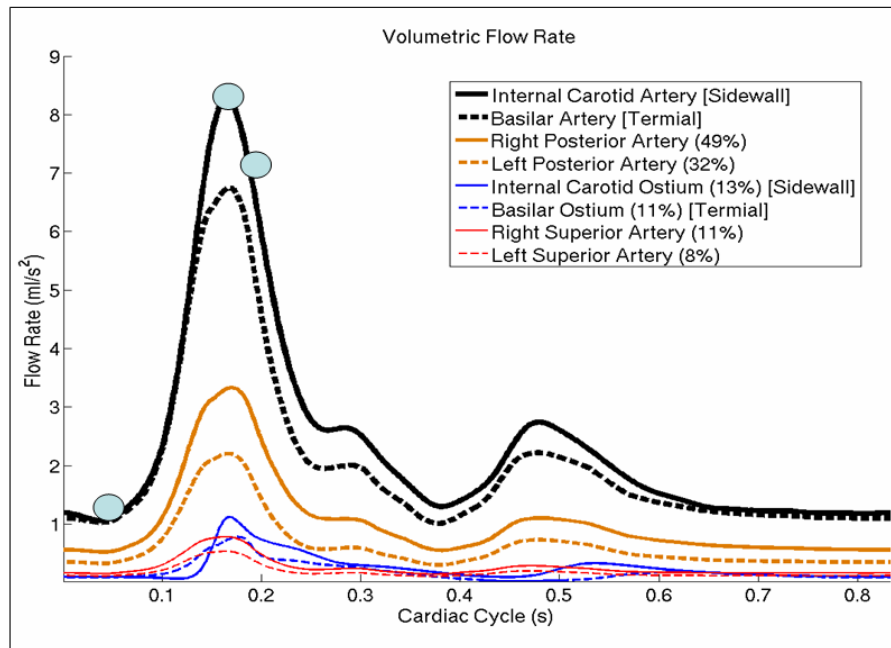


Figure B.3. Shows the volumetric flow waveform used for the simulations.

For steady flow simulations, pressure gradients ranging from 2-4 mm Hg, corresponding to 2.5 ml/sec were used. These conditions approximate flow during diastole. In unsteady simulations, results obtained from steady flow simulations were used for initialization. On the arterial walls, no-slip and impenetrable boundary conditions were applied.

# Appendix C

## Enlarged Plots from Chapter 4

In this appendix, enlarged plots from chapter 4 are presented for better understanding of grids used for the numerical experimental done to demonstrate the sensitivity of the WSSG. Note that figure numbers have been kept the same for ease of reference.

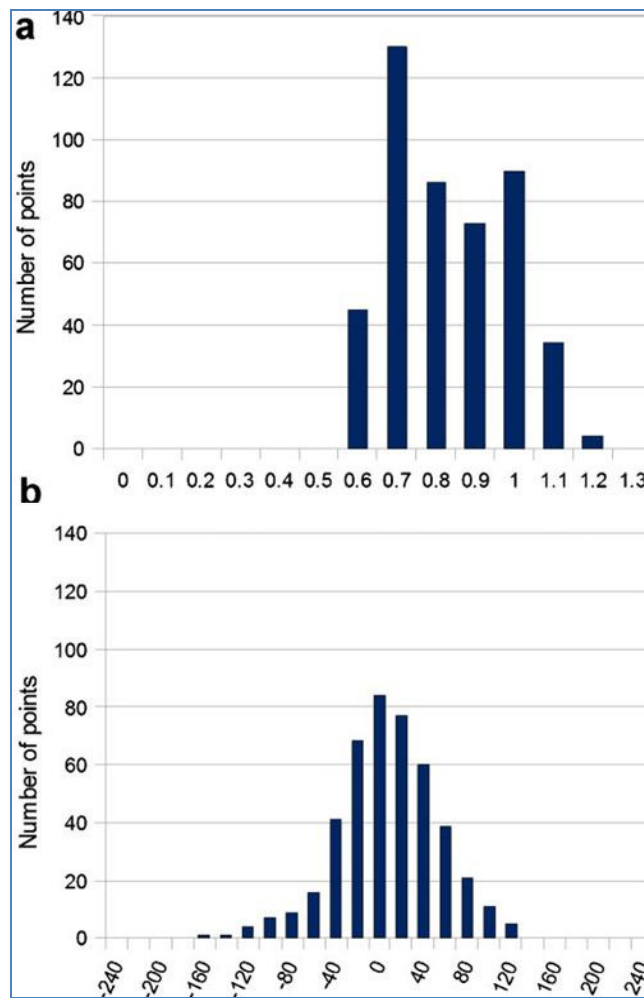


Figure 4.3. Top panel shows a sample topography map, middle panel shows the values of shear stresses and bottom panel shows the histograms of the WSS and WSSG from the CFD model.

**Figure 4.6 Hexahedral Grid with Boundary Layer Case 1**

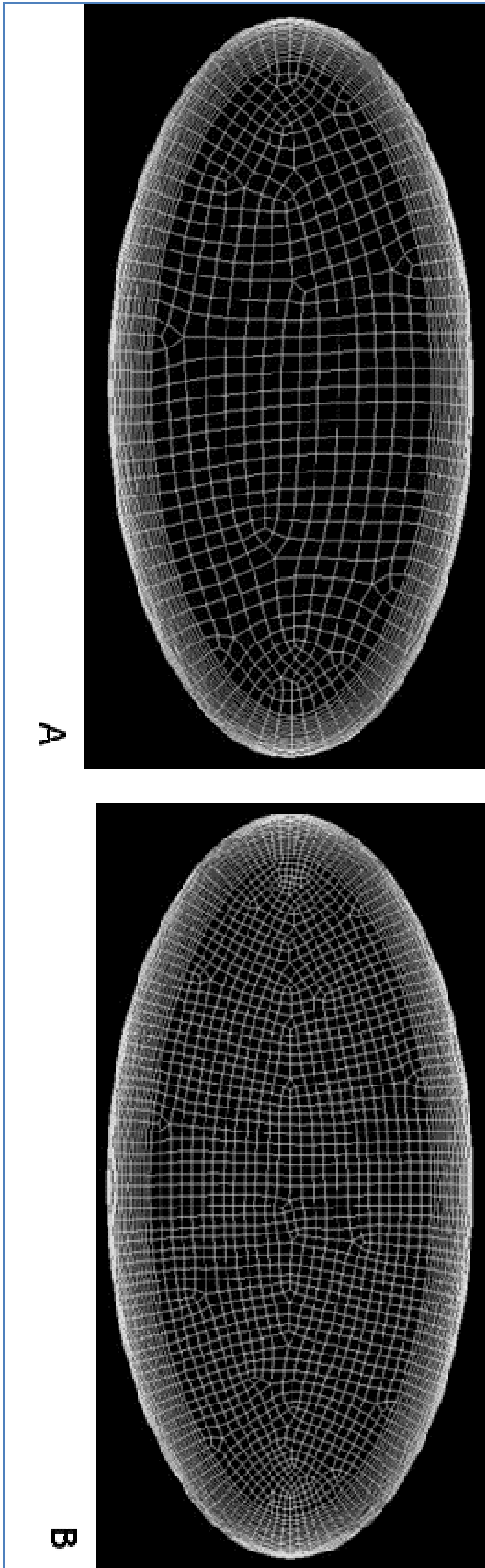
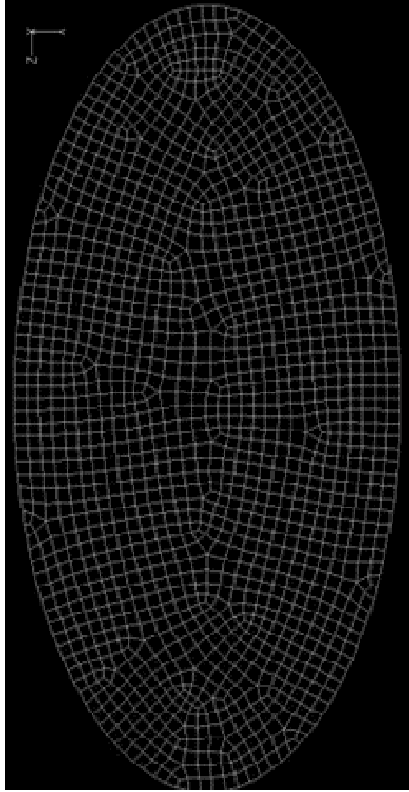
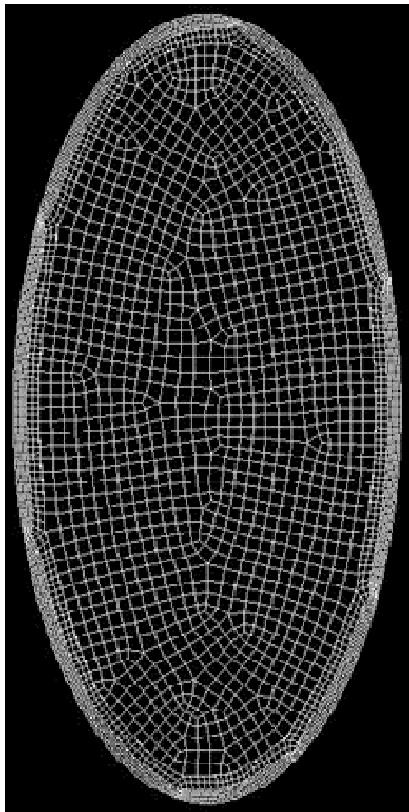


Figure 4.6 Hexahedral Grid with adaptive mesh Case 2

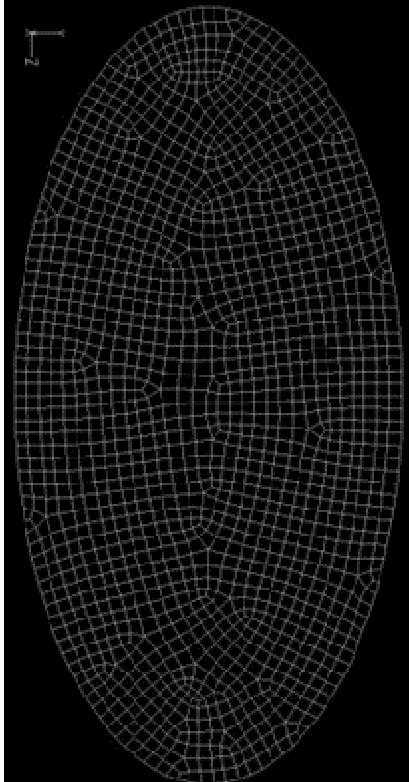


C

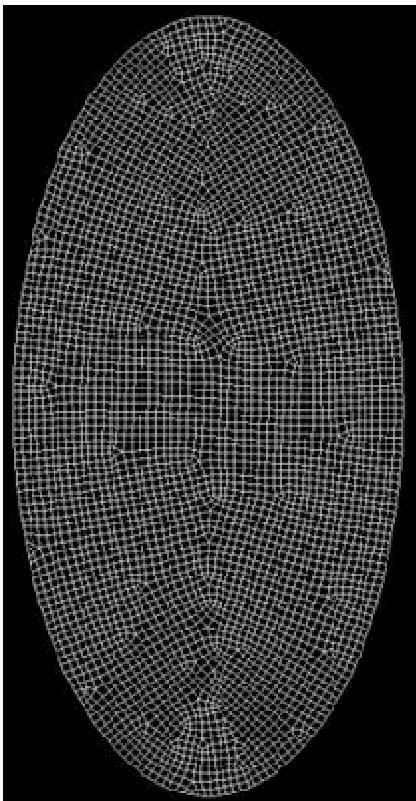


D

Figure 4.6 Hexahedral Grid with progressive refinement Case 3



E



F

Figure 4.6 Tetrahedral Grid with progressive refinement Case 4

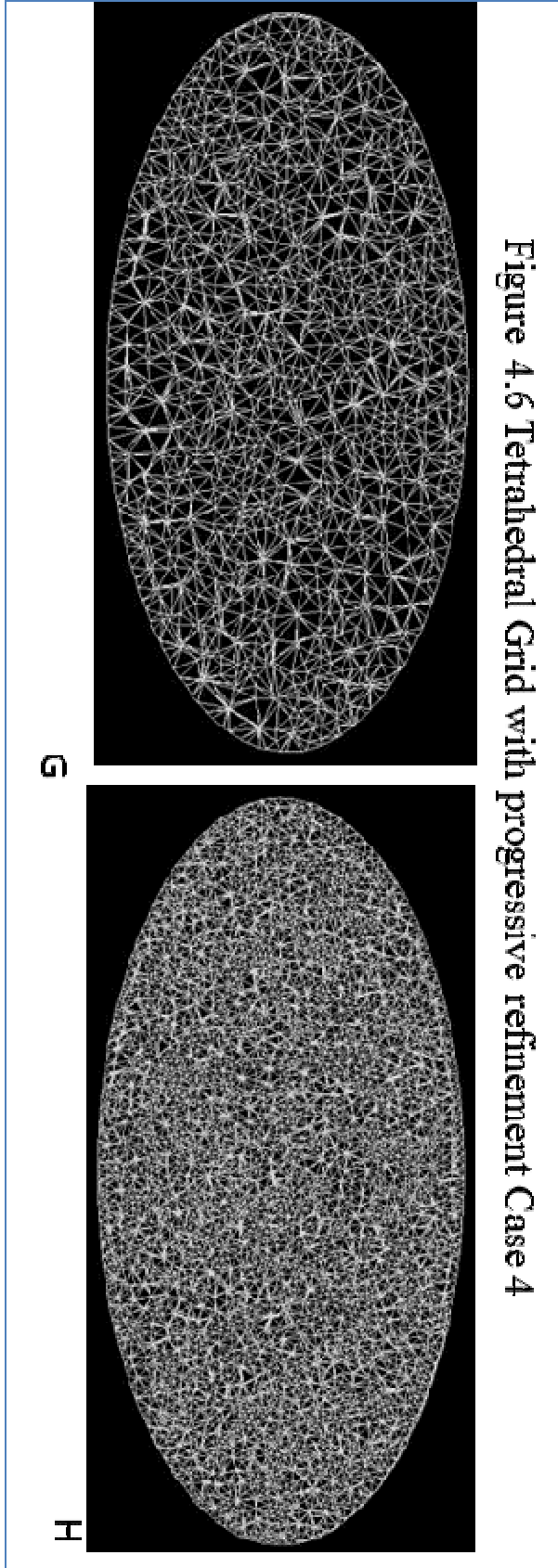


Figure 4.7 WSS plots at the circumference of the CS plot shown above for Case I

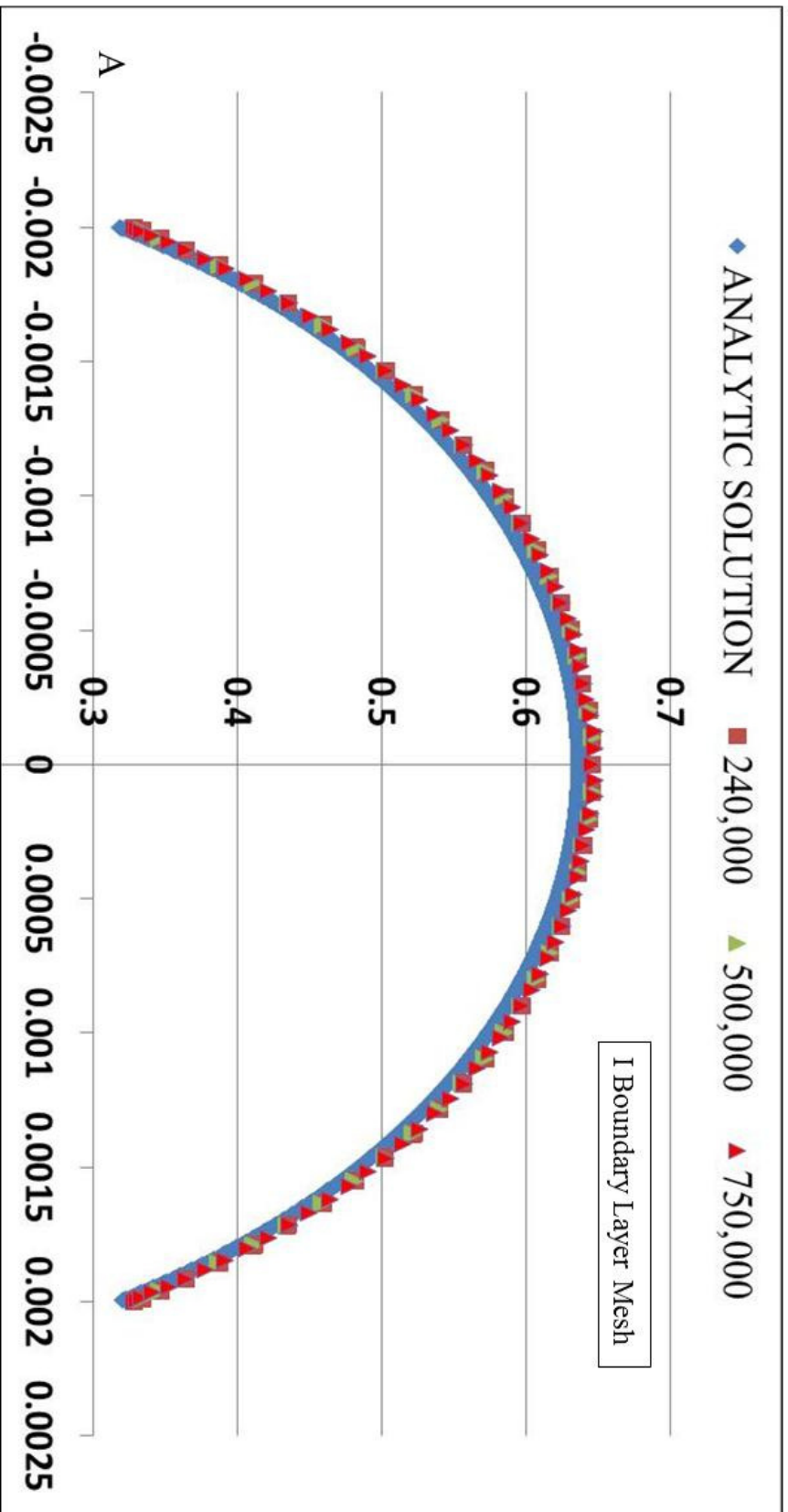


Figure 4.7 WSS plots at the circumference of the CS plot shown above for Case 2

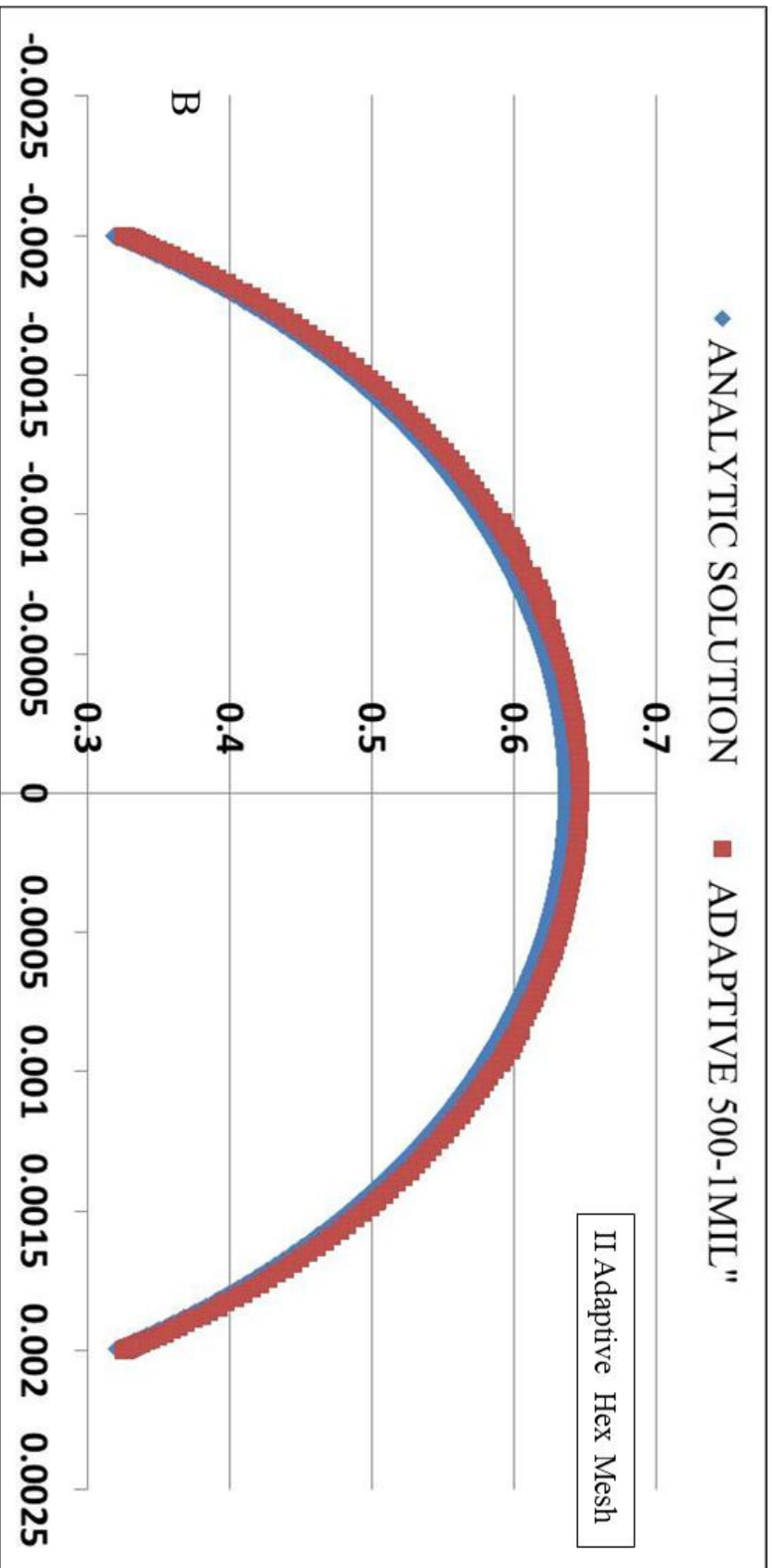


Figure 4.7 WSS plots at the circumference of the CS plot shown above for Case 3

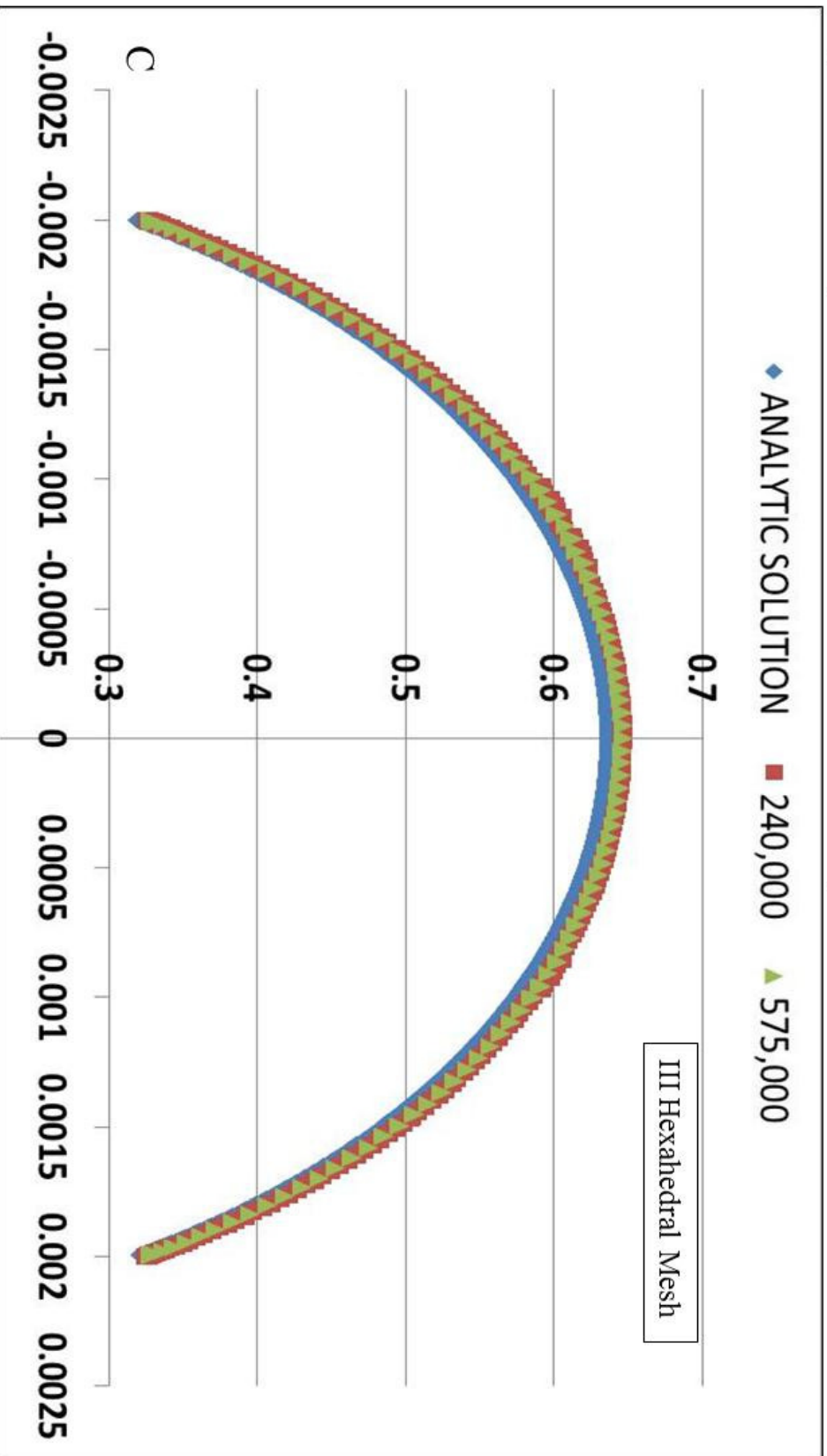


Figure 4.7 WSS plots at the circumference of the CS plot shown above for Case 3

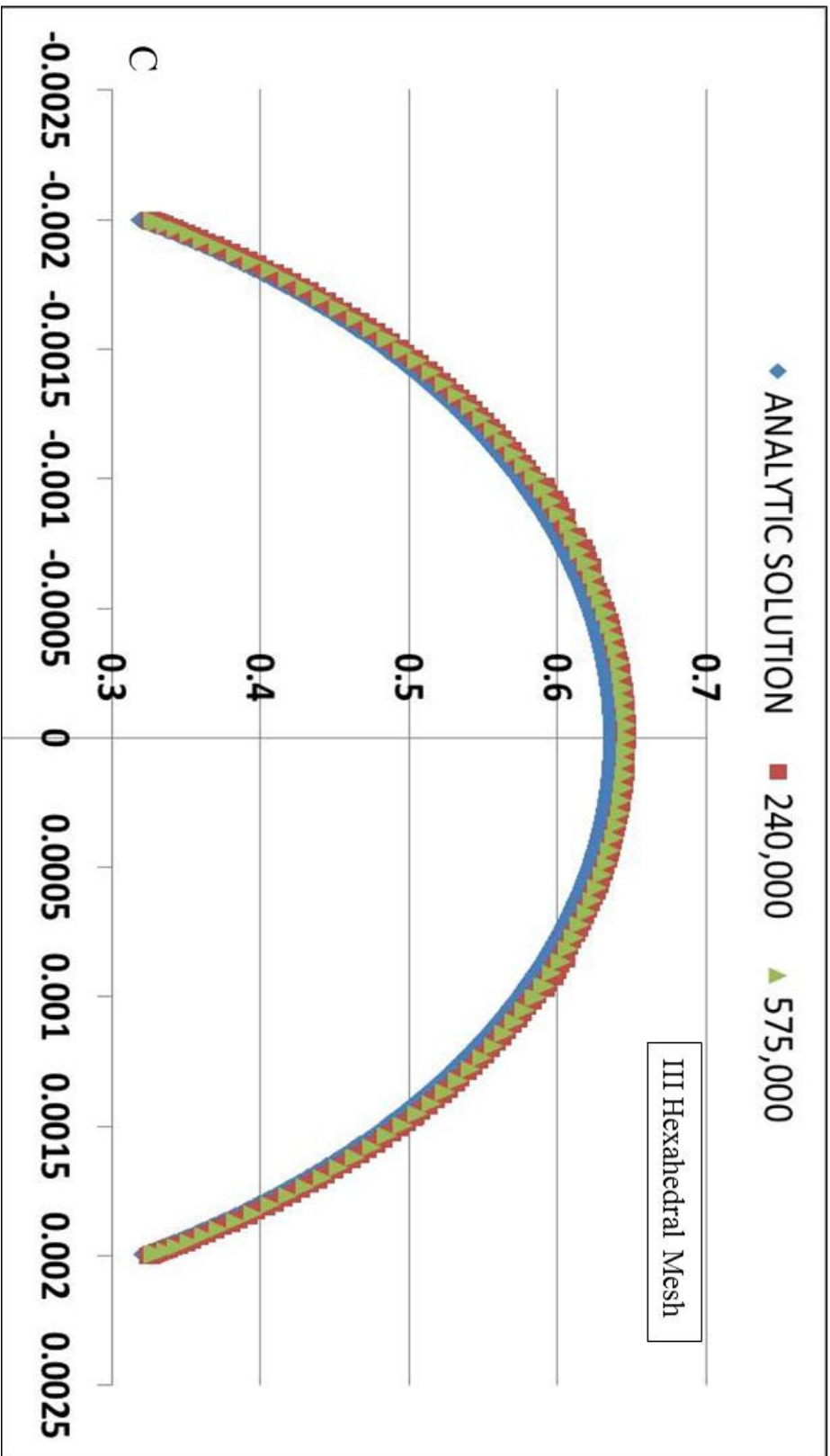


Figure 4.8: Convergence plots of WSSG and their comparison with the analytic solution. Case 1. Zones of maximum error for BL mesh are indicated by arrows.

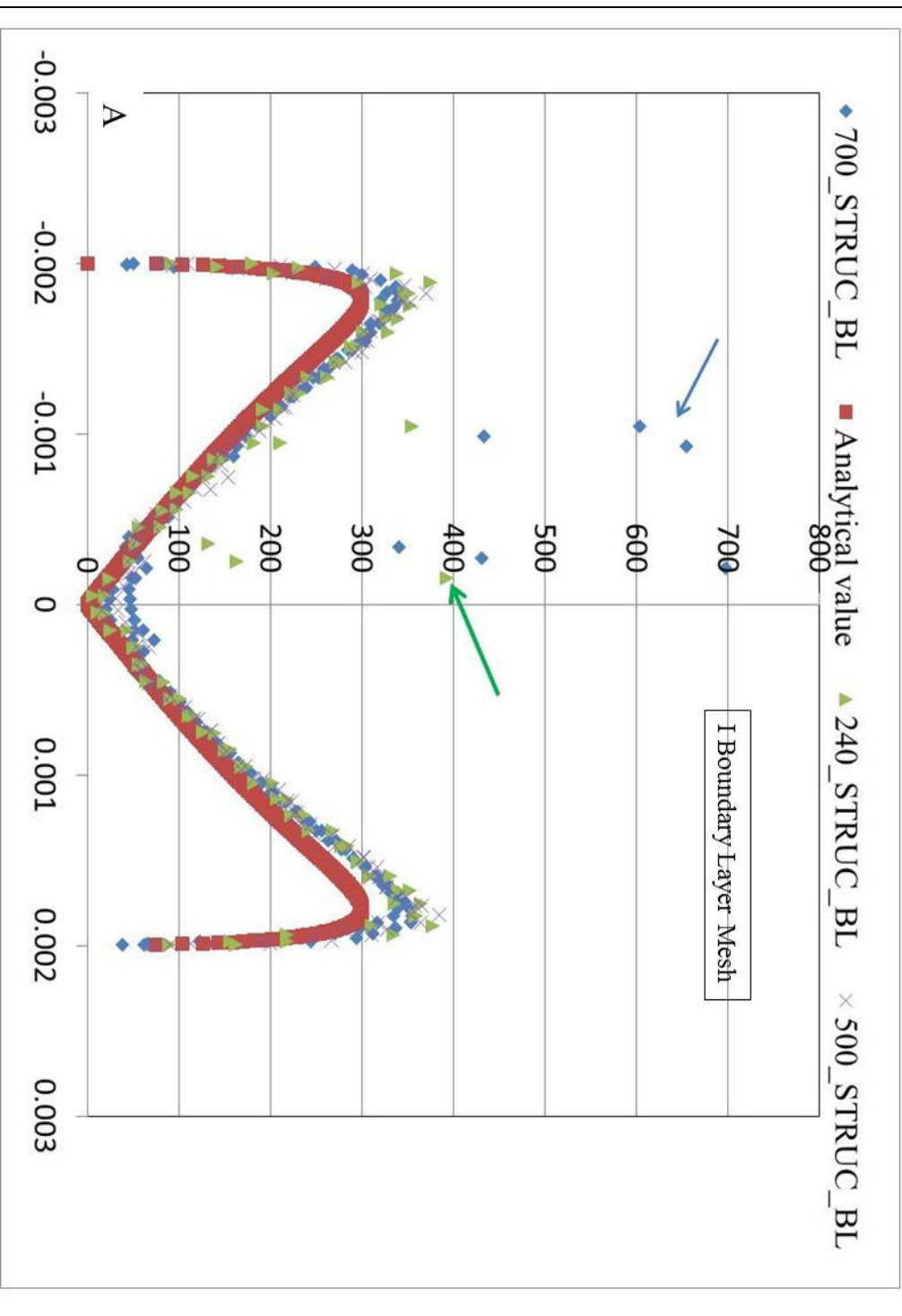


Figure 4.8: Convergence plots of WSSG and their comparison with the analytic solution. Case 2.

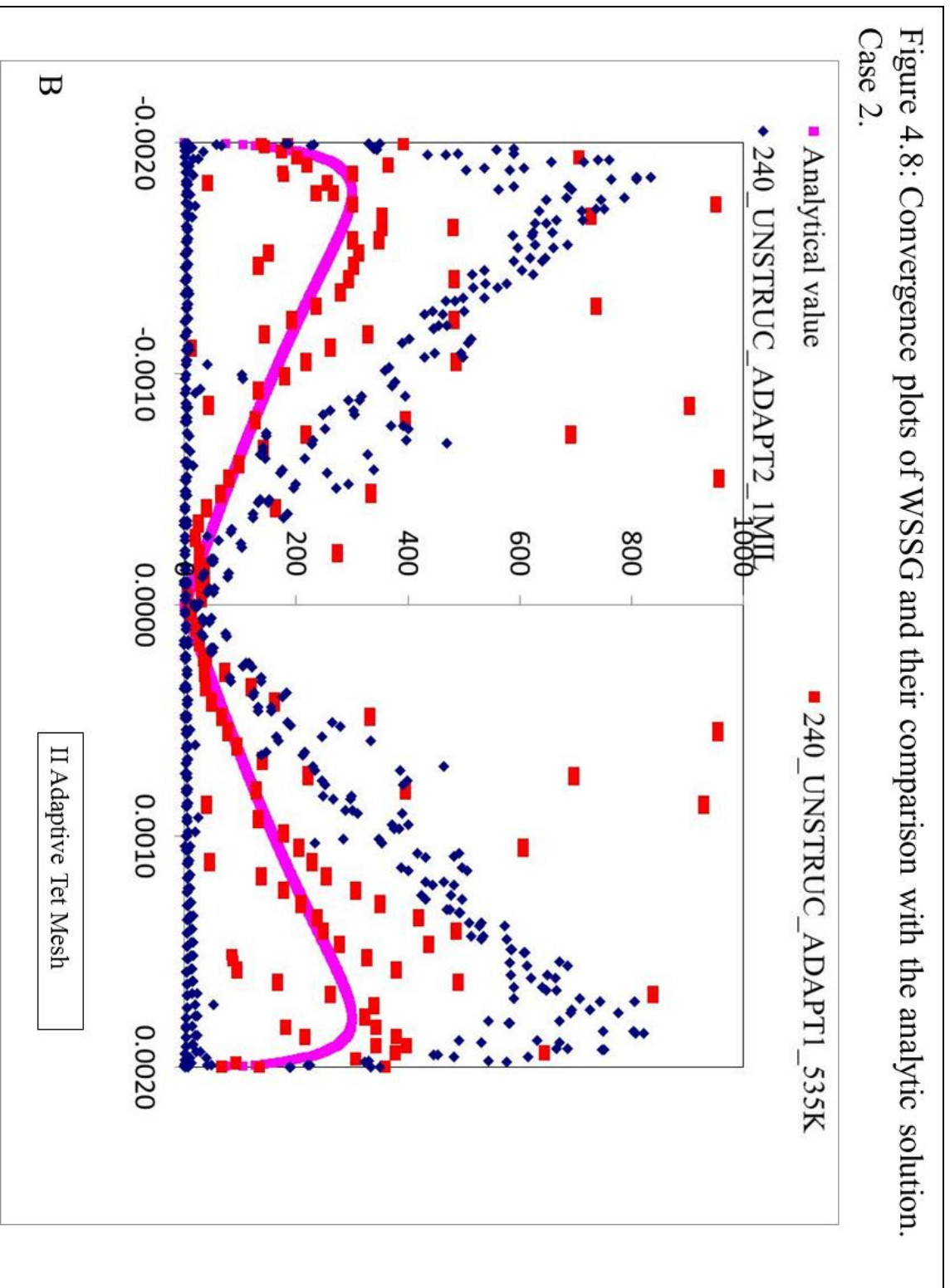


Figure 4.8: Convergence plots of WSSG and their comparison with the analytic solution. Case 3.

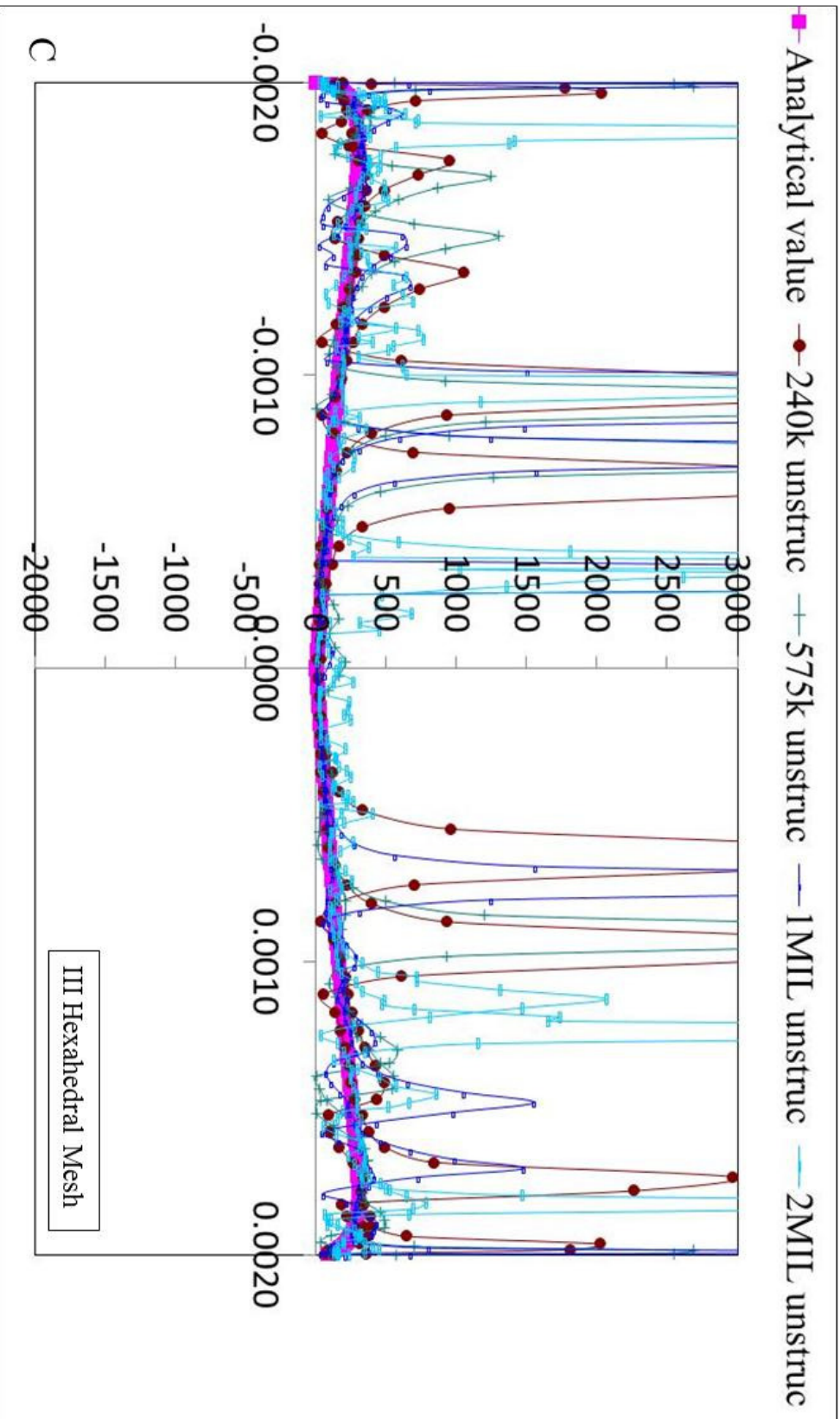


Figure 4.8: Convergence plots of WSSG and their comparison with the analytic solution. Case 4.

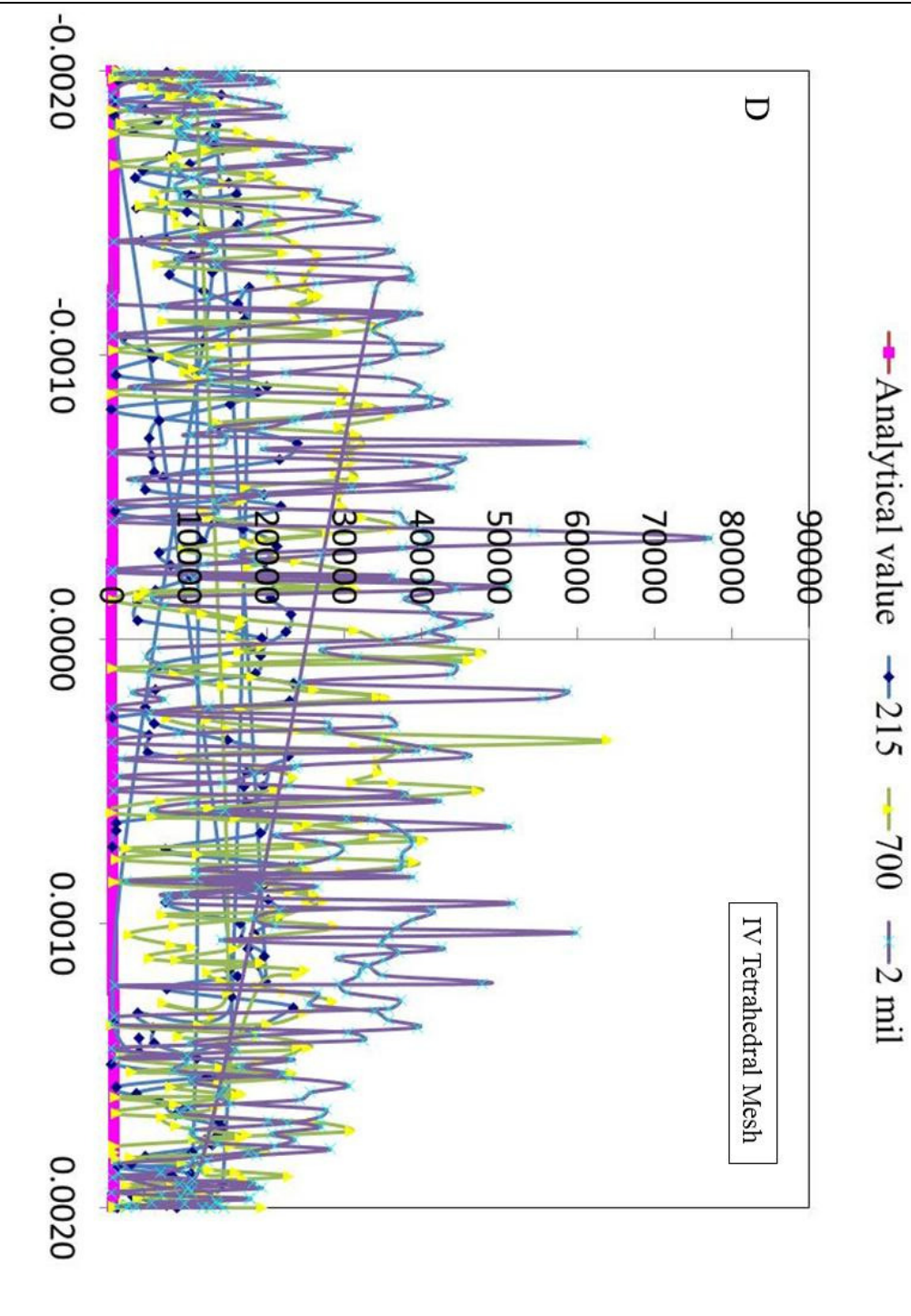


Figure 4.12 Right panel shows magnified image after pre-processing in Amira. Left panel shows contours of velocity. Bottom panel shows contours of WSS for FP-CT and Micro-CT respectively.(Ref Ionescu et al, 2011)

